Non-wetting drops : from impacts to self-propulsion

Dan Soto

THESE DE DOCTORAT

Spécialité : Physique

Présentée par

Dan Soto

pour obtenir le grade de

DOCTEUR DE L'UNIVERSITE PIERRE ET MARIE CURIE

Non-wetting drops: from impacts to self-propulsion

Soutenue le 17 octobre 2014 devant le jury composé de :

M.	Christophe Clanet	Directeur de thèse
M.	Robert Cohen	Rapporteur
M.	Jean-François Joanny	
M.	Hamid Kellay	Rapporteur
M.	Detlef Lohse	
M.	David Quéré	Directeur de thèse

Merci !

After several months of manuscript writing, the time has finally come to thank everyone that has made this work possible.

First of all I would like to thank all the jury members, Jean-François Joanny (who I hope enjoyed the drops' racing-track), Detlef Lohse (who was kind enough to come from Netherlands on the eve of his journey to Shanghai), and my thesis referees Robert Cohen (who crossed the atlantic from Boston) and Hamid Kellay (who I first met talking about amazing tornados in soap bubbles) for their enlightening remarks and for their careful reading of the manuscript.

As the saying goes, "It takes a village to raise a child". In my case, the village was the PMMH lab at ESPCI in Paris, as well as the Ladhyx at Ecole Polytechnique. In this rich environment, I want to thank first my PhD advisors Christophe Clanet and David Quéré. Christophe, thank you for your constant availability, your tireless thirst for models and of course your sense of humour. David, thank you for your endless encouragements and your communicative enthusiasm. Your advice was always distilled in a way that gave me extreme freedom.

Thank you to all the members of the "Compagnie des interfaces" with whom I have shared my daily work. The "Elders": Keyvan Piroir, who kindly welcomed me in my first days in the group; Alexandre Ponomarenko and his incredible (but true) stories; Marie Le Merrer, who I first met as my internship advisor at Polytechnique and Jacopo Seiwert (and his friendly outspokenness and shared passion for the sea). The generation of "The famous Five" who were for me a key reference point: Caroline Cohen (an amazing surfer), Baptiste Darbois Texier (a tireless joker with bulletproof optimism), Pascal Raux (who could talk for hours over lunch and who showed us Lyon by night... and by bike!), Pierre-Brice Binten (with whom we spend as much time working in the "soute" as choosing which music to listen to) and Guillame Dupeux (who was as much worried by my carbon footprint as he was generous with his time to initiate me to the Leidenfrost world and share with me his passion for Matlab). The crucial link between this two generations was Adrien Benusiglio, an engaging person always up front with everything. I had the

pleasure to spend my three years with Raphaële Thevenin. Thank you for your help with your "white room skills", for all our discussions and for making me travel all around the world when sharing your holidays.

As time went on, we welcomed in the group Manu du Pontavice (with whom I shared several adventure racings, but never got to finish them), Anaïs Gauthier (a formidable cards opponent with a cheerful personality) and Philippe Bourrianne (who may never forget the soccer defeat of France against Spain but may find some confort when recalling that to win a bet it takes a lot of sacrifice!). In my last year, three new PhD students arrived: Eline Dehandschoewercker (as conscientious as outgoing), Thimothé Mouterde (always with a big smile and who I loved to tease with his rowing activities) and Hélène de Maleprade (with whom I had the pleasure to work on our air-levitated objects while enjoying her constant giggles.) Around this time, two Post-docs also joined the group: Cunjing Lv (who was always eager to share a moment with us) and Evan Spruijt (whose kindness was synonym of infinite patience).

I want to specially thank Aurelie Borel de Larivière, a master thesis intern with whom I worked on drop impacts and who carried out an outstanding work. I thank all the interns with whom I have crossed paths with, with a special mention to Maxime "Costa". Martin and Hadrien, good luck with your PhD!

I also thank you all because I am leaving with wonderful memories of our time shared outside the lab: may it be in California (where we could play cards in uncommon places), in Pittsburg (where the snow took us by surprise), in Copenhagen (where soccer and swimming was as important as the conferences), in Twente (where we discovered what Evan had usually for breakfast), in Rome (where we enjoyed a thrilling soccer game), during our skiing adventures or the different evenings spent in each other homes.

I want to thank the PMMH director Philippe Petitjeans (and his predecessor José Eduardo Wesfreid) for welcoming me in their lab. Frédérique Auger, Amina Mialet and Claudette Barez, thank you for making so much things happen. I spent a lot of time in the workshop and I want to thank all their members, with a special mention to Guillaume Clermont (who took the time to initiate me to the numerical mill) and Xavier Benoit-Gonin (who taught me all the secrets of the laser cutter). Thank you to all the other members of the lab with whom I had the pleasure to live with for three years (and six months internship). I will not forget the friendly atmosphere of Ladhyx and the incredible soccer games!. Thank you all.

Robert Cohen spent six months in the lab and we had a great pleasure working with him on drops and grids. Thank you for your kindness and for being always so thoughtful (such as with the organisation of my trip to Boston). I also thank Xavier Boutillon, Stef-

fen Hardt, Tobias Baier and Stephane Dorbolo with whom we collaborated at Palaiseau, Darmstadt or Liège.

Finally, I would like to thank everyone who has not been mentioned above but accompanied me all along this adventure. My friends, who will forgive me for not attempting an exhaustive enumeration. My parents, who proofread my manuscript and gave me the taste for science. My brother, who has always led the way. All my family, who never doubted the value of a PhD on water drops.

And Marion.

Contents

Introduction

In 1959, the Belgian surrealist artist Magritte finished his masterpiece entilted "Le Château des Pyrénées" (The Castle of the Pyrenees) shown in figure 1. This painting embodies

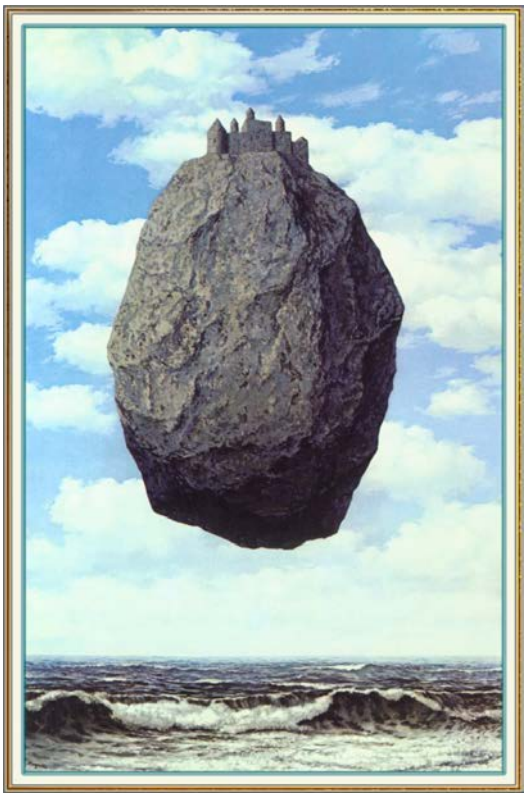

Figure 1 – Le Château des Pyrénées (The Castle of the Pyrénées), René Magritte, 1959. Oil on canvas, 200 x 145 cm. Gift of Harry Torczyner to the American Friends of the Israel Museum.

the artist's typical disturbing juxtaposition of familiar objects, combined with captivating poetry and mystery. A gigantic boulder, topped by a castle, is immobilized in the air between an azure sky (dotted with clouds) and a pristine sea (whose waves reflect the gray nuances of the rock). After a first impression, the gap between the rock (emphasized by the tiny relative size of the top castle) and the sea attracts our attention. Magritte

works in the artistic dimension - where imagination rules and we do not have to satisfy physical laws. However, we can adopt a more realistic point of view, and wonder how an object could possibly levitate.

A first answer was proposed in 1756 by the German physician Johann Gottlob Leidenfrost. In [68], he studied the behavior of a water droplet deposited over a hot substrate (typically 400 °C). Placing a candle behind the drop, Leidenfrost could observe with the naked eye that light passes between the hot solid and the liquid, revealing the existence of a film of vapor below the drop as shown in figure 2, in a very similar way than what Magritte represented in "Le Château des Pyrénées". However, contrasting with Magritte's masterpiece, the Leidenfrost levitation has an explanation: it results from a balance between evaporation (that nourishes the vapor cushion on which the drop levitates) and the drop's weight (which presses on this vapor layer). Since then, other methods have been proposed to generate levitation. Among them, levitation by blowing air - somehow like an hovercraft.

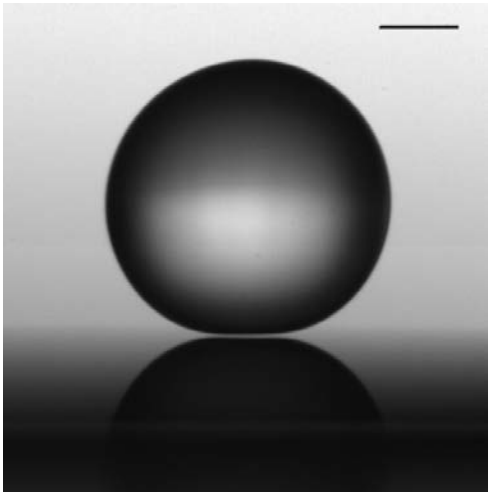

Figure 2 – Millimetric drop levitating over a hot plate. Backlighting is used, which helps to distinguish the interval between the drop and its reflection owing to the presence of vapor. The scale bar shows 1 mm.

A levitating body avoids any contact with the substrate, which makes it highly mobile. In this work, we focus on the special dynamics associated with this mobility. We exploit this situation to generate self-propulsion (allowing us to put a resting object into motion). Conversely, frictionless objects are difficult to stop. We consider situations where a moving liquid drop can be stopped by different means: from substrate texturation, to an impact on a solid wall through impact on a mesh (an intermediate situation between

a solid wall, able to stop a movement, and no obstacle at all).

These various situations will stress, I hope, the novel physics that arise in this lively field of hydrodynamics without contact.

Chapter I

The non-wetting world

Contents

1 Generating non-wetting objects

1.1 The super-hydrophobic state

The lotus plant has been considered as a sacred plant several centuries before our era. It was held to be the symbol of truth, auspiciousness and beauty, always remaining untainted despite its surroundings. As Veda Vyasa points out in his ancient sanskrit scripture Mahabharata[1], a lotus leaf never gets wet even though it is always in water:

"ब्रह्मन्य् आदाय कर्माणि
सङ्गम् त्यक्त्वा करोति यह
लिप्यते न स पापेन
पद्म-पत्रम् इवाम्भसा "

"One who performs his duty without attachment,
surrendering the results unto the Supreme God,
is not affected by sinful action,
as the lotus leaf is untouched by water."

Despite this ancient text, it is only recently (in the 90's) that the lotus mystery has been solved thanks to the use of Scanning Electron Microscope (SEM) in the work of W. Barthlott and C. Neinhuis [5]. They describe how the combination of microtextures and proper chemistry makes lotus actively repel water. From that time on, the lotus has moved from a religious, sacred dimension to a scientific one, where we try to mimic its properties. If we look at the surface of a lotus leaf through an SEM (figure I.1), we can observe a highly sophisticated double texturation: the leaf is covered by micrometric posts, themselves covered by nanometric wax crystals.

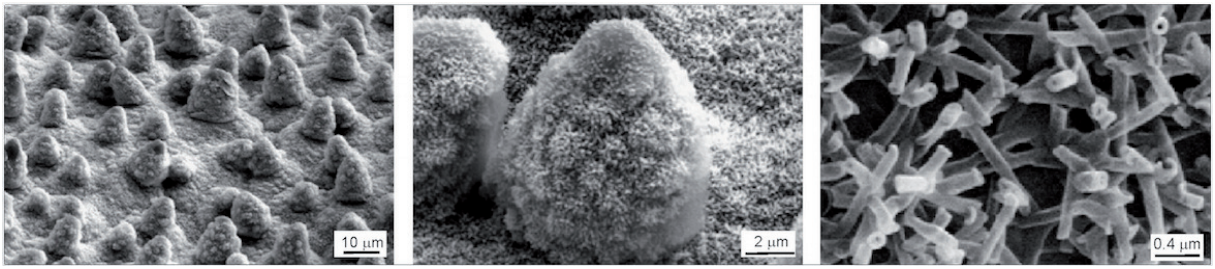

Figure I.1 – SEM picture of the surface of a lotus leaf. We can see that each pillar is likewise structured because it is covered by small wax crystals. Figure from [9].

[1]probable composition period: between the fifth and the second century BCE.

If we want to imitate this effect artificially, nature tells us that we need to satisfy two requirements:

(i) have a hydrophobic surface (from the ancient Greek ὑδρόφοβος: has fear of water). The affinity of a liquid towards a substrate can be characterized by its contact angle θ_c as defined in figure I.2. At the contact line, we have three interfaces: solid-liquid, liquid-gas and gas-solid. Since each one has its own surface tension, the static equilibrium is determined by Young's equation: $\cos\theta_c = \frac{\gamma_{sl}-\gamma_{sg}}{\gamma_{lg}}$.

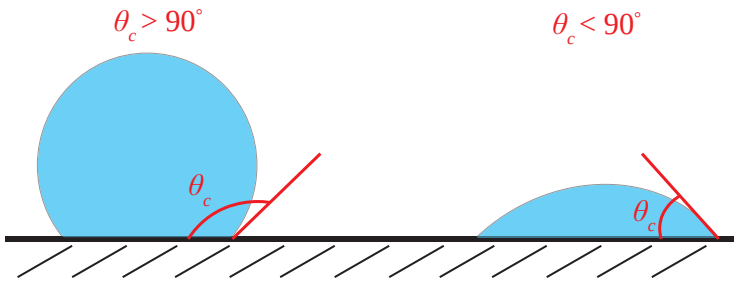

Figure I.2 – Hydrophobic (left) and Hydrophilic drop (right).

If $\theta_c < 90°$, the substrate is hydrophilic. Conversely, if $\theta_c > 90°$, the substrate is hydrophobic. Wax, oils, fats, long carbon chains and fluorinated molecules are usually hydrophobic.

(ii) have a textured surface to enhance hydrophobicity and achieve a super-hydrophobic effect. It is observed that surface chemistry alone fails to achieve contact angles above $\theta_c = 120°$ [99]. In nature, we can find other examples of super hydrophobicity in plants (Ginkgo Biloba, Brassica Oleracea) or animals (water strider, dragonfly, collembola). They all share a common feature: they have a tailored surface. In order to outreach an angle of 160° or even above, we need to add surface roughness. As explained by A. Cassie [18], when adding roughness, the drop does not wet the whole projected surface beneath it but only the top of the summit topography, like a fakir on a bed of nails. Locally, the drop satisfies Young's equation on top of each pillar. However, the macroscopic contact angle θ_c^* (also called the apparent contact angle) is much larger (figure I.3). In other words, the drop will mainly face air beneath it (the top pillars represent only a very low percentage of the total projected area) and will be in a non-wetting state.

Experimentally, we can generate well-controlled roughness by micro-engineering an array of pillars such as those in figure I.4a. Although different techniques exist to manufacture such refined structures, they all require advanced skills and high technology equipment. Easier methods that allow greater areas to be treated have been proposed, such as the one by Larmour and collaborators [65]. This two-steps method (where the

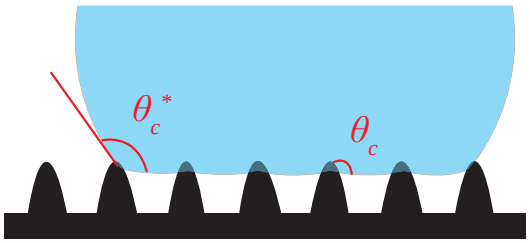

Figure I.3 – Textured surface, with a drop sitting on it as a fakir on a bed of nails. On the top of each pillar, the local angle of contact θ_c satisfies Young's equation. However, the macroscopic angle of contact θ_c^* is much larger.

precise geometry of the texture can not be controlled) begins by plunging the substrate in a solution of silver nitrate. The surface darkens owing to the deposition of small silver particles that generate micrometric roughness. Then, the surface is treated with an alcoholic solution of 3,3,4,4,5,5,6,6,7,7,8,8,9,9,10,10,10-*heptadecafluoro*-1-*decanethiol* (HDFT) that will graft these long fluorinated molecules to the surface of the silver texture, making it chemically hydrophobic. This method is limited to metallic substrates, such as copper or brass. More recently, industrial liquid coatings (such as UltraEverDry^{TM} or Glaco^{TM}) have appeared on the market as an easy alternative (as easy as spraying the liquid on the surface) to achieve both chemical hydrophobicity and physical roughness. After coating a sample with this industrial solutions made of hydrophobic colloids, we can see through an SEM a disordered roughness at very small scale (see figure I.4b). Another method for treating large areas of complex geometry (such as a mesh shown in figure I.4c), is for example used in the group of R. Cohen by spray-coating or dip-coating the sample from 50/50 wt% mixture of poly(methyl methacrylate) and hydrophobic molecules $1H,1H,2H,2H-heptadecafluorodecyl$ polyhedral oligomeric silsesquioxane (commonly called fuorodecyl POSS, see [23, 105, 60]), providing a high degree of hydrophobicity.

1.2 The Leidenfrost state

Leidenfrost experiment

The key to generating a non-wetting state is to prevent contact between liquid and solid. In the super-hydrophobic state, the pillars succeeded in artificially trapping an air layer between drop and substrate. However, because the weight of the drop has to be compensated, it needs to rest on top of each pillar: although marginal, contact still exists. If we

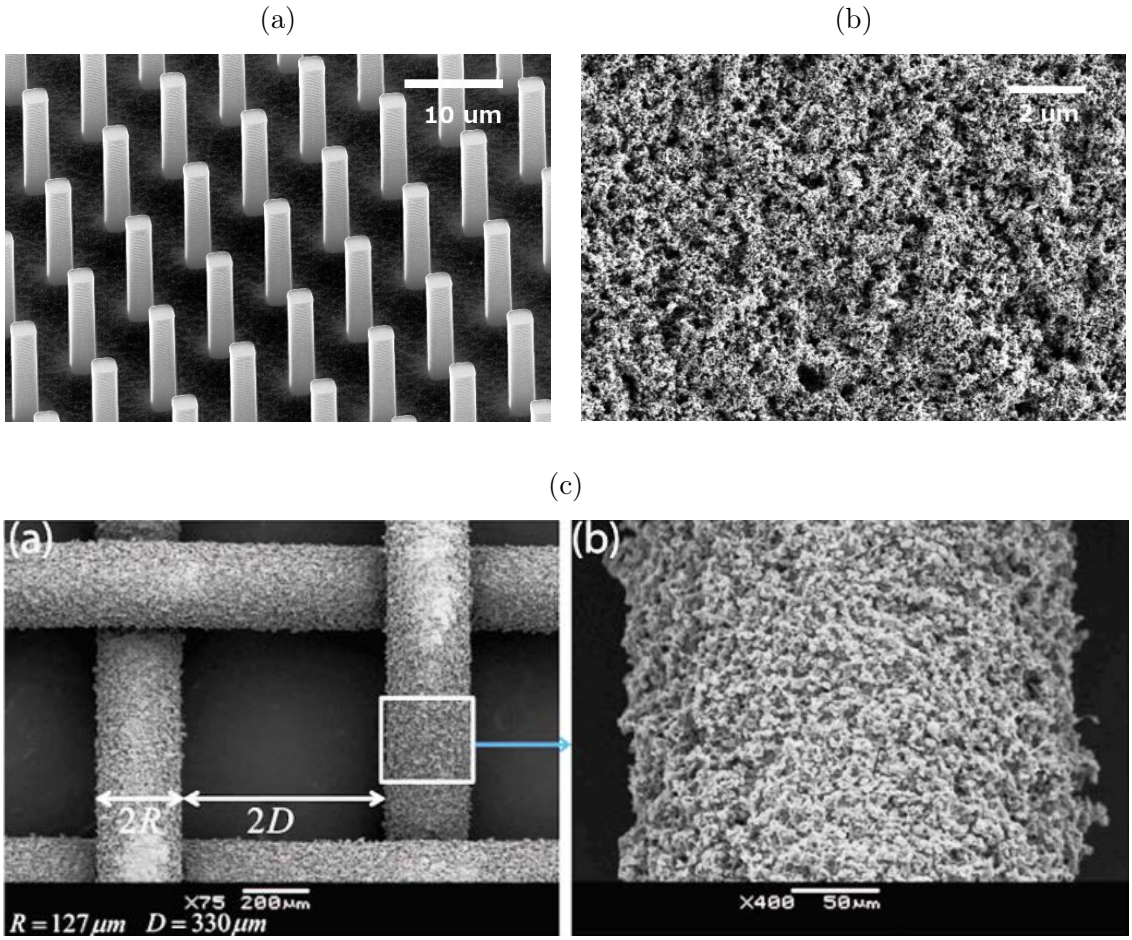

Figure I.4 – SEM views of three artificial super hydrophobic surfaces. (a) Array of micro pillars of height 10 µm, diameter 2 µm, and pitch 10 µm. Scale shows 10 µm, courtesy of M. Reyssat. (b) Surface treated with Glaco^{TM}. Scale shows 2 µm. Courtesy of C. Willem. (c) Scanning electron micrographs at different magnifications of dual-textured spray-coated super-hydrophobic mesh surfaces. Figure from [105].

wish to completely eradicate this contact, we have to go back to Germany in 1756[2], and read J. G. Leidenfrost's paper "On the fixation of water in diverse fire" [68]:

> "*At the instant when the drop touches the glowing iron, it is spherical. It does not adhere to the spoon, as water is accustomed to do, which touches colder iron.*"

Through this observation, we understand that a Leidenfrost water droplet is in a non-wetting state. By looking from the side at water sitting on a hot plate (figure I.5, experiment sketched in figure I.6), Leidenfrost was able to see a beam of light passing between the liquid and the plate, thus demonstrating a pure non-wetting state.

[2]The Dutch scientist H. Boerhaave was the first to mention the levitation of a drop over a hot substrate in his 1732 publication: Elementa Chemiae [13].

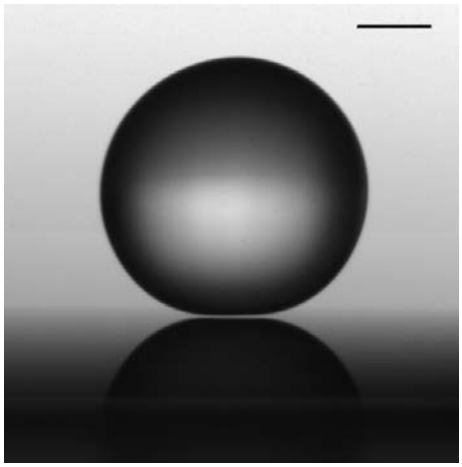

Figure I.5 – Side view of a water droplet on a hot substrate (400°C). The gap between the drop and the substrate (visible because of the back light passing through it) has a typical height $h \sim 100$ µm. The bar shows 1 mm.

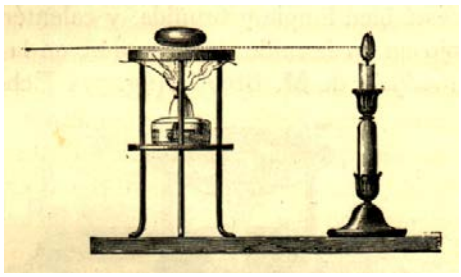

Figure I.6 – Experimental set up used by J. G. Leidenfrost to observe vapor cushions between a drop and its hot substrate.

As the drop approaches the hot substrate it evaporates at a rate fast enough to form a stable vapor film beneath it (visible in figure I.5). The droplet is sitting on top of a cushion of its own vapor, squeezing it and generating a vapor flow permanently compensated by evaporation, hence achieving an equilibrium levitation height h of typically 10 to 100 µm.

Drop lifetime

A way to characterize the Leidenfrost effect consists in measuring the lifetime evolution τ of a drop sitting on a substrate, as a function of the substrate temperature. At high temperature, the vapor provides thermal insulation and the drop can last over several tenths of a second. However, as we decrease temperature, we observe a sharp transition. The temperature corresponding to this lifetime discontinuity is called the Leidenfrost Temperature T_L. At this point (typically between 150 and 200 °C for water), the substrate is not hot enough to sustain the necessary evaporation rate. Consequently, the peaceful non-wetting state (described in figure I.8 as film boiling regime) disappears and is replaced

by a violent boiling regime (first, transition boiling and then, nucleate boiling, again shown in figure I.8). As expected when direct contact between liquid and substrate occurs, drops lifetime falls drastically.

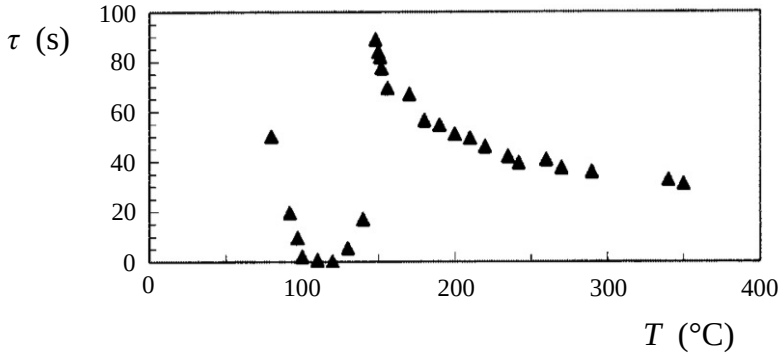

Figure I.7 – Lifetime τ of a millimetric water droplet of radius $R = 1$ mm, as a function of the temperature T of the Duralumin plate on which it is deposited. Leidenfrost temperature T_L is around 150 °C. Above this temperature, we are in the film boiling regime. Right below it, the drop experiences the transition boiling regime. If we further decrease the temperature, we go thorough the nucleate boiling regime before arriving to the single phase (see figure I.8). Figure adapted from [11].

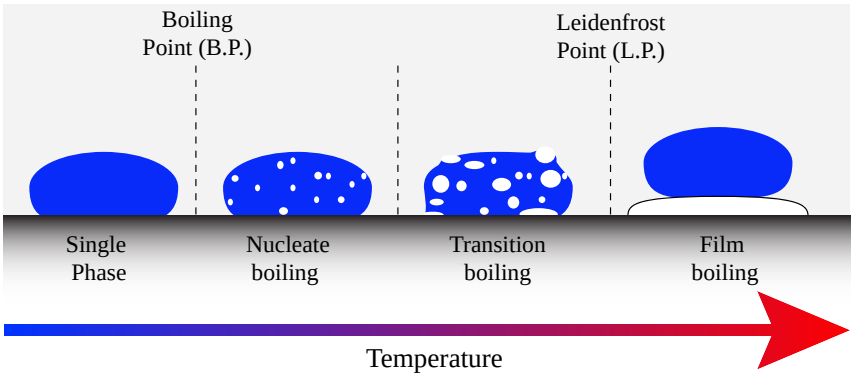

Figure I.8 – Sketch of different boiling regimes ranging from single phase to film boiling (Leidenfrost state) going through the boiling point (B.P.) and the Leidenfrost point (L.P.). Figure adapted from [112].

The Leidenfrost temperature depends on the nature of the liquid, the substrate and its roughness. Water on a clean smooth substrate will levitate at lower temperature than on a dirty rough one. It has been shown [58, 57, 59] that a fine texture (at the scale of 0.1–10 μm) considerably increases the Leidenfrost temperature. Characteristic metal roughness ranges from 0.05 µm to 10 µm (rusted metal even reaching 100 µm). Typical vapor thickness being 100 µm, the greater the characteristic roughness length scale the

shorter the distance between the liquid and the tip of a local crest topography. Any vibration of the interface will therefore easily put the liquid in contact with the roughness protuberance, instantaneously nucleating boiling. We have previously seen that if textures were hydrophobic, they would achieve super-hydrophobicity. Conversely, if they were hydrophilic, they would achieve super-hydrophility. Thereby, textures role can be seen as an enhancer of liquid substrate affinity. In the Leidenfrost state, something similar happens and roughness does not always necessarily result in a Leidenfrost temperature increase. If textures are hydrophobic they can be used to stabilize the Leidenfrost vapor layer as shown by Vakarelski et al. [124].

1.3 The air-levitated state

From Leidenfrost to air-levitated drops

We just saw that we can achieve complete levitation by constantly nourishing a vapor cushion between a drop and its hot substrate. The vapor is created by using heat to transform liquid into gas phase. This inevitably means that our drop has a limited lifetime as it is consuming itself in order to levitate. The time limited (or even deadly!) nature of this levitation can be avoided by replacing vapor by external injected air as done with air hockey tables. In 1986, M. Goldshtik carried out a thorough comparison between Leidenfrost and air-levitated drops [48]. A strong similarity arises from the close analogy between the symmetry and hydrodynamic mechanisms of both types of suspension (see figure I.9). In the end, the critical parameter that governs air-levitation is the differential pressure on a porous surface, as is the temperature in the thermal counterpart.

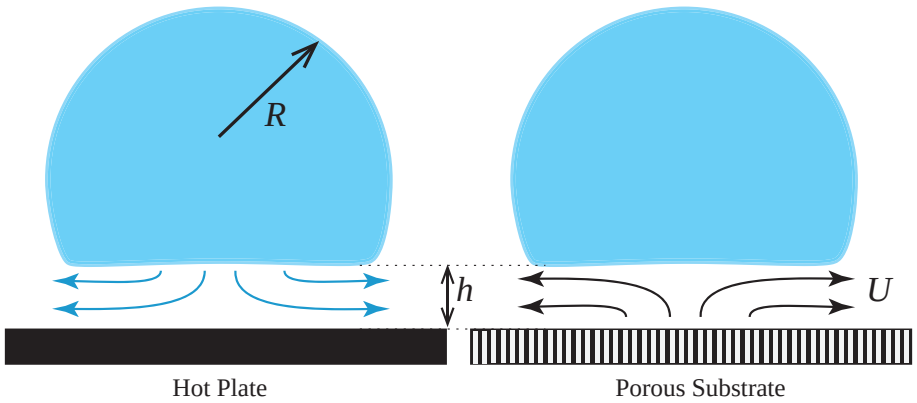

Figure I.9 – Leidenfrost drop (left) and air-levitated drop (right). We can see how striking is the analogy between these two situations.

The deformable case

In the Leidenfrost state, it is experimentally difficult to reach high vapor flow rates due to temperature limitations. This contrasts with the air-levitated state where we can easily adjust the differential pressure through the porous substrate, hence freely varying the air injection rate on a wide range of values. Therefore, we can reach airflows that are strong enough to change the underlying levitation mechanism.
To understand this transition, we have to compare the role of inertial forces versus viscous ones. By denoting ρ_a the air density, η_a its viscosity and U its speed, a first ratio of these two forces can be constructed with the drop radius as a characteristic distance, which yields for this Reynolds number:

$$Re = \frac{\rho_a U R}{\eta_a} \tag{I.1}$$

We experimentally see that the bottom of the drop is deformed and flattened by the vapor pressure as sketched in figure I.9. In this region, inertial forces will scale as $\rho_a U^2/R$ and viscous ones as $\eta U/h^2$. Their ratio, sometimes called the lubrication Reynolds number, is:

$$Re_L = \frac{\rho_a U h^2}{\eta_a R} = Re\ \frac{h}{R} \tag{I.2}$$

For a millimetric drop with $h \approx 100$ µm and small flow rate ($U \approx 0.1 - 1$ m/s), we expect $Re_L < 0.1$: viscous effects clearly dominate within the air cushion.

The non-deformable case

Previous mechanism of levitation involved the deformation of the interface of the object. However, a non-deformable solid object (such as a ping-pong ball) can also be maintained in levitation by blowing air beneath it. We address here the situation of a levitated drop for which deformation can be neglected. A moving sphere experiences drag from its surrounding liquid (or gas). If the drag is strong enough to compensate the drop's weight, it will result in levitation - like a free falling object experiences in its own frame. Depending on the Reynolds number, several regimes can be observed:

(i) For small Reynolds number (i.e. Re < 1), the sphere will experience a viscous stress $\eta_a U/R$ integrated over its whole surface R^2. It will be subjected to the Stokes drag force:

$$F_{Stokes} \sim \eta_a R U \tag{I.3}$$

By compensating it with the drop weight $\rho R^3 g$ (where ρ denotes the liquid density),

we immediately get a critical levitation speed:

$$U^* \sim \frac{\rho R^2 g}{\eta_a} \tag{I.4}$$

We can insert this speed in the Reynolds number expression (I.1), $Re^* = \frac{\rho_a \rho R^3 g}{\eta_a^2}$ and build a characteristic length R_L:

$$R_L = (\frac{\eta_a^2}{\rho_a \rho g})^{1/3} \tag{I.5}$$

Using this characteristic length, the Reynolds number can be re-expressed as: $Re = (R/R_L)^3$. As previously said, this regime only applies if Re < 1: hence a maximum droplet radius: $R^* = R_L$. For a water droplet surrounded by air, this means very small droplets: $R < R^*$=30 µm.

(ii) If we continue increasing the flow rate, we will enter the intermediate Reynolds number regime: $1 < Re < 10^3$. When a body is put into motion in a viscous fluid, a boundary layer develops around the object with a characteristic thickness $\delta \sim \sqrt{\nu_a t}$. Here $\nu_a = \eta_a/\rho_a$ denotes the kinematic viscosity of air and t the time of development of the boundary layer [3]. For an object of size R, t naturally scales as R/U, hence: $\delta \sim \sqrt{\nu R/U}$. The resulting stress being $\sigma \sim \eta_a U/\delta$, the skin drag force is:

$$F_{skin} \sim \sqrt{\eta_a \rho_a}[RU]^{3/2} \tag{I.6}$$

Analogous reasoning leads to a critical levitation speed:

$$U^* \sim R(\frac{\rho g}{\sqrt{\eta_a \rho_a}})^{2/3} \tag{I.7}$$

Using the same characteristic length R_L than defined in equation I.5, the Reynolds number will now be: $Re = (R/R_L)^2$. As $Re \in$ [1,1000] this leads to drop radius R ranging from 30 µm to 1000 µm, that is, still relatively small drops.

(iii) Finally, we consider drag at high flow rates: Re $>$ 1000, yet below turbulent regimes. If the characteristic length scale of the object is R, it has to displace an initially resting mass of air $\rho_a R^3$ at a speed U in a characteristic time R/U in order to move forward. This leads to an inertial drag force:

$$F_{aero} \sim \rho_a R^2 U^2 \tag{I.8}$$

In most everyday situations (car, plane, soccer ball), we have to fight against this force

[3] This equation is characteristic of diffusive events and in this case the diffused quantity is momentum.

in order to move. However, as done in the two previous regimes, we can use this drag force to levitate a body by compensating its weight - the same way a skydiver would do in a wind tunnel. The critical speed at which we will be able to sustain a drop in air being:

$$U^* \sim \sqrt{\frac{\rho R g}{\rho_a}} \tag{I.9}$$

In this case the Reynolds number can be rewritten as: Re$=(R/R_L)^{3/2}$. To satisfy the relationship Re > 1000, a last critical radius arises: $R^* = 1000^{2/3}\, R_L$. Once again, for a water droplet in air this means $R > R^* = 1$ mm. In the case of rain, this is the most common regime as everyday drops are usually larger than a millimeter. If we think of a falling drop, after a short acceleration (initially it will accelerate as free fall), drag will increase until it compensates the weight and the drop reaches its terminal speed U_∞ (described in I.9)- typically 10 m/s. In a simple way, we can see a falling drop at terminal speed (from the drop frame point of view) as a non-wetting object.

1.4 A wide range of other possibilities

A great variety of other approaches have been used to generate levitation [84]. Besides the air injection through a porous medium, alternative solutions have been proposed to nourish the air film.

In [27], Couder et al. deposit a liquid drop on top of a vibrating bath of the same liquid. If the oscillation period and amplitude are well chosen, the air cushion can be renewed between two oscillations before it has time to drain, hence avoiding coalescence.

Another solution to generate liquid levitation consists on putting a drop above a spinning disk where solid/liquid contact will be prevented by the thin air boundary layer entrained by the disk. As a consequence, the drop levitates and is slightly deformed as shown in figure I.10.

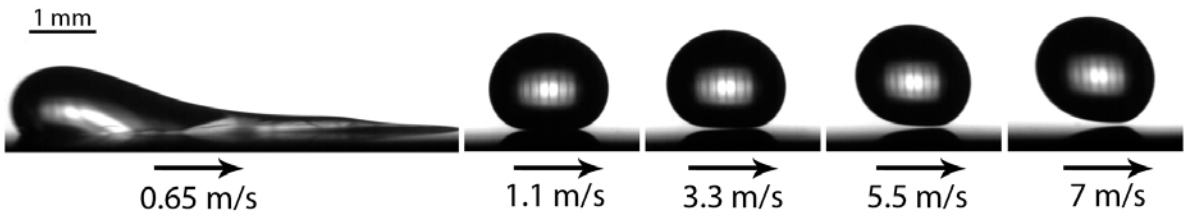

Figure I.10 – Shape of a millimetric silicone-oil drop (viscosity 100 cSt) levitating over a rotating disk. If rotation speed is not high enough (left image), entrained air is not strong enough to overcome the drop's weight and avoid contact. The higher the rotation speed seen by the drop, the more the drop deforms. Figure courtesy of A. Gauthier.

Also based on a moving substrate, levitation can be induced by depositing a liquid droplet on an hydraulic jump as discussed in [104, 39]. Indeed, a thin layer of air is entrained underneath the drop by the flow of liquid preventing coalescence.

In [84, 81, 35], Neitzel and collaborators use thermocapillarity effects to drive a lubricating gas film between a heated droplet and a cooled substrate. By heating the top interface of a drop, they increase the local temperature, hence decrease the local surface tension. As a consequence, liquid is pulled along the interface from the top to the bottom of the drop. Due to this Marangoni flow, surrounding air is entrained in the same direction, so that air is also injected at the bottom of the drop generating levitation. For instance, if we take two drops of the same liquid and put them in contact they will coalesce. However, if the two drops are at different temperature [34] Marangoni flows will drag air between the droplets suppressing coalescence as shown in figure I.11.

(a) (b)

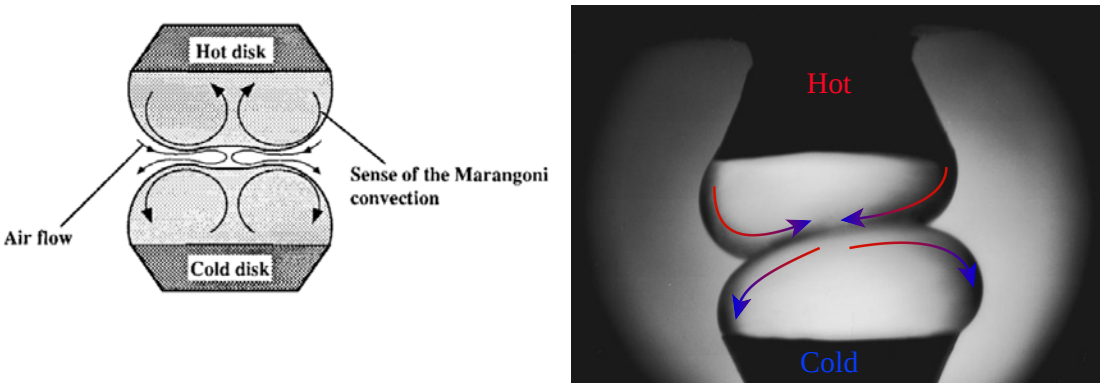

Figure I.11 – (a) Sketch of the flow field for two non-coalescing drops held at different temperatures. The gap thickness is exaggerated to display the direction of motion in the entrained air film. (b) Non-coalescnece of two 5 cST silicone oil drops of different temperature around 15 °C. Arrow shows the direction of the Marangoni flow along the interface. Figures from [34].

Other approaches include Bernoulli levitation, magnetic, electrostatic or even acoustic levitation [85].

2 Shape

2.1 The static shape

Surface tension

A physical consequence of being non-wetting is the appearance of a quasi-spherical shape. As we suppress contact (or, in the super-hydrophobic state, almost suppress it), a drop is only subject to gravitational forces (scaling as $\rho R^3 g$) and liquid-gas surface tension forces (scaling as γR, where γ denotes from now on the liquid-gas surface tension). A first characteristic length called the capillary length is obtained by balancing this two forces:

$$\ell_c = \sqrt{\frac{\gamma}{\rho\, g}}$$

In the case of water, we have $\ell_c = 2.7$ mm at ambient temperature and $\ell_c = 2.5$ mm at 100°C. Another convenient liquid is acetone, for which ℓ_c is smaller, namely 1.6 mm near its boiling point at 60°C. In figure I.12, we show two drops: on the left side (figure I.12a) a spherical drop smaller than the capillary length; on the right side (figure I.12b) a flattened puddle larger than ℓ_c. We clearly see that the capillary length sets the limit between small droplets modeled by surface tension and large ones globally deformed by gravity.

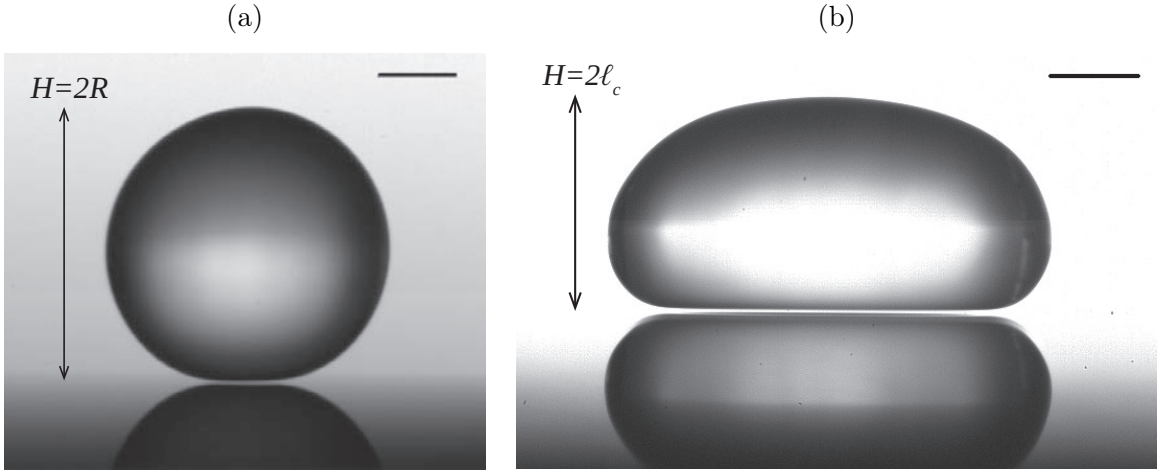

Figure I.12 – (a) Small droplets are mainly shaped by surface tension, hence having a quasi-spherical shape. Scale shows 1 mm. (b) Large drops are flattened by gravity, of maximum height twice the capillary length ℓ_c. Scale shows 2mm.

Droplets: $\mathbf{R < \ell_c}$

We refer to small drops when $R < \ell_c$ so that surface tension dominates gravity, as shown in figure I.12a. If we take a fixed amount of liquid (small enough to be in this capillary world), surface tension selects the geometry that minimizes the surface area. For example, if we consider a pyramidal geometry, corners are not very efficient since we can put very little liquid in them although we need a lot of surface to generate them. This example tells us that surface tension avoids sharp geometries, hence naturally selecting the spherical shape (mathematically known to minimize surface area for a given volume). In 1805, Pierre Simon de Laplace showed [64] that a consequence of curved interfaces, is the existence of a difference of pressure ΔP between the inside and the outside of the interface: $\Delta P = \gamma C$ (known as the Young-Laplace equation). Here, C represents the interface curvature defined as the sum of two curvatures in perpendicular planes. For a Leidenfrost droplet, the geometry is that of a sphere, and we have $\Delta P = 2\gamma/R$, about 100 Pa for millimetric drops.

Puddles: $\mathbf{R > \ell_c}$

We refer to big drops or puddles when $R > \ell_c$, so that gravity effects have to be taken into account. As we can see in figure I.12b, the drop is flattened by gravity. R will further on denote the equatorial radius of a puddle and H its thickness. Laplace pressure on the curved side can be written as: $P_L = \gamma(2/H + 1/R)$, where R and $H/2$ are the curvature in the horizontal and vertical plane, respectively. In the big drop limit ($H << R$), it reduces to $P_L \approx 2\gamma/H$. From a hydrostatic point of view, the inner pressure at half height is $P_H = \rho g H/2$. By balancing these two pressures, we get an expression for puddle thickness. It is independent of the radius R, and writes $H = 2\ell_c$.

If we want to have an exact solution for the drop's shape, we have to solve the differential equation similarly obtained by pressure arguments. The pressure at any height z of the drop can be written following two different methods based on the two different paths sketched in figure I.13 (the horizontal position is not relevant in this problem since we are in a hydrostatic state):

(i) the first path sketched in figure I.13 by a red arrow, where we simply cross the drop's interface at height z, implies a pressure jump $\Delta P_1 = \gamma C(z)$.

(ii) the second one (sketched in figure I.13 by a blue arrow), where we follow an imaginary path that crosses first the interface on the axis of symmetry at the top of the drop (with a pressure jump γC_0) and then goes down along the z-axis until reaching height z (hence a hydrostatic pressure $\rho g z$). The corresponding pressure jump is: $\Delta P_2 = \gamma C_0 + \rho g z$.

Introducing the capillary length, equality between these two pressures $\Delta P_1 = \Delta P_2$

gives us the following equation for the local curvature:

$$C(z) = C_0 + \frac{z}{{\ell_c}^2} \tag{I.10}$$

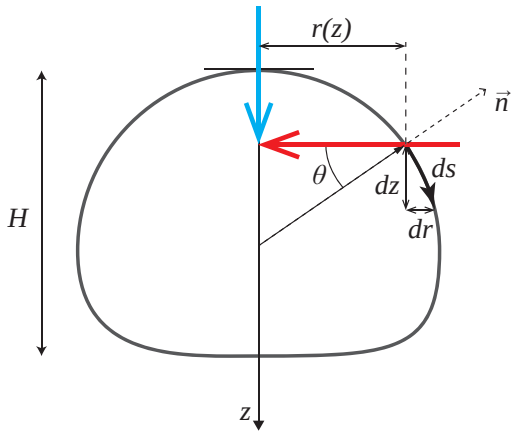

Figure I.13 – Shape of a non-wetting drop. Two different paths allow to access two different expression for the pressure inside the drop at height z: red arrow show path number one while blue arrow shows path number two.

Introducing s as the curvilinear coordinate, $r(z)$ as the horizontal radius at height z and θ as the angle between the tangent to the interface and the vertical plane (see figure I.13), the two orthogonal curvatures can be written: $C_1(z) = \frac{\cos\theta}{r}$, $C_2(z) = -\frac{d\theta}{ds}$. In addition, geometrical observation shows that $\mathrm{d}r{=}\mathrm{d}s\,\sin\theta$, $\mathrm{d}z{=}\mathrm{d}s\,\cos\theta$ and $\dot{r} = \frac{dr}{dz} = \tan\theta$. By re-expressing $\cos\theta$ as $1/\sqrt{1+\dot{r}^2}$, we immediately get $C_1(z) = \frac{1}{r\,(1+\dot{r}^2)^{\frac{1}{2}}}$ and $C_2(z) = -\frac{d\theta}{dz}\,\frac{dz}{ds} = -\frac{d\theta}{dz}\,\frac{1}{\sqrt{1+\dot{r}^2}}$. By calculating $\ddot{r} = \frac{d\tan\theta}{dz} = \frac{d\theta}{dz}\,\frac{1}{1+\dot{r}^2}$ we obtain the expression of $\frac{d\theta}{dz}$ equal to $\frac{\ddot{r}}{1+\dot{r}^2}$. We now have all the elements to re-write equation I.10 as the following second order differential equation for $r(z)$:

$$\frac{1}{r\,(1+\dot{r}^2)^{1/2}} - \frac{\ddot{r}}{(1+\dot{r}^2)^{3/2}} = C_0 + \frac{z}{{\ell_c}^2} \tag{I.11}$$

There is no analytical solution to this equation, which must be solved numerically. The only physical parameters that we have to set are the curvature at the top of the drop C_0 and the capillary length. We show in figure I.14 the shape of several drops for water ($\ell_c = 2.7$ mm) and curvature radius at the drop's apex ranging from 1 mm (smallest radius of curvature, hence almost spherical drop) to 10 mm (biggest radius of curvature, hence the more flattened drop).

The model assumes homogeneous stress on the bottom of the drop (as we can get in super-hydrophobic states). In the Leidenfrost (or air-levitated) situation, gas escapes from the axis of symmetry towards the external edge, indicating that maximum pressure point is located right below the center of drop. We will therefore have a local higher

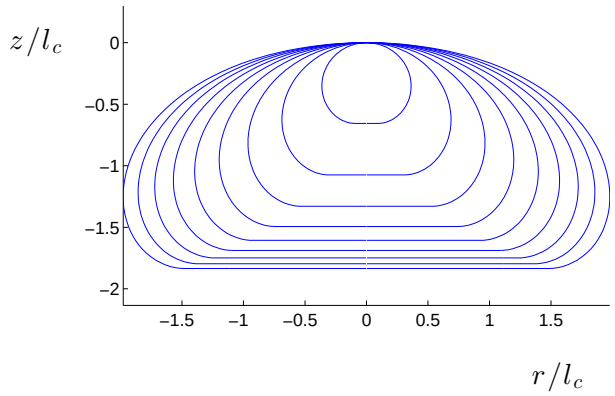

Figure I.14 – Numerical resolution of equation I.11 rescaled by capillary length (set to ℓ_c = 2.7 mm). Curvature radius at the apex of the drop ranging from 1 mm (smallest radius of curvature, corresponding to an almost spherical drop) to 10 mm (biggest radius of curvature, corresponding to the most flattened drop). As explained above, the maximum height H for a puddle tends towards $2\,\ell_c$ as the drop volume increases.

thickness of vapor at this point, as experimentally observed [17, 19]. A correction can be introduced in the Leidenfrost state (as well as the air-levitated state) to take into account the underlying vapor film as done in [103] or [38] for the air-levitated situation. We will see in section 2.3 that this deformation can be the cause of an instability.

Volume of a non-wetting drop

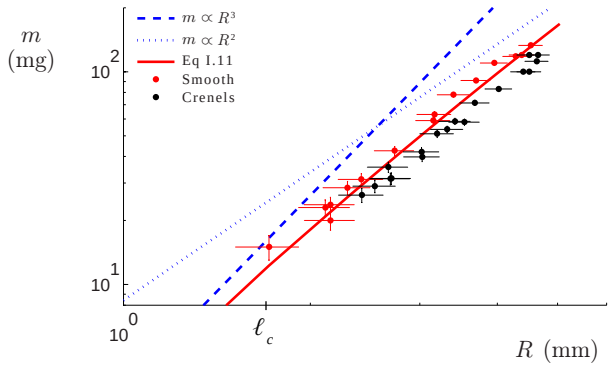

Figure I.15 – Drop mass as a function of the equatorial radius for acetone. Red dots show experiments done on a smooth surface while black dots show experiments done on a crenelated surface (see section 2.4). Plain red line: numerical solution from equation I.11. Dashed blue line shows spherical drop approximation for which m varies as R^3. Dotted blue line shows disk approximation for which m scales as R^2.

From the 2D numerical solution of the shape we can easily compute the volume Ω and mass m of a drop as a function of its equatorial radius R. We show in red in figure I.15 the comparison between experiments (red dots) and numerical solution (red line) for acetone. We also draw in dashed blue an approached solution in the small drop's regime where we assume perfect spherical drops, hence $m = \rho\frac{4}{3}\pi R^3$ is proportional to R^3. In the puddle regime (dotted blue), assuming disk shapes we would get $m = \rho 2\,\ell_c\,\pi R^2$, hence varying as R^2. This volume approximation, although in qualitative agreement, always tends to overestimate the data.

Falling drops: analogy with Leidenfrost drops

Free falling drops bigger than 1 mm are in the aerodynamic regime (see section 1.3). Assuming spherical shapes, we previously deduced their terminal velocity by balancing drag and weight forces. However, for bigger droplets (i.e. bigger than the capillary length), the interface can be deformed and a new geometrical variable is added to the problem. In order to understand this new drop geometry, we show in figure I.16 the air flow around the drop.

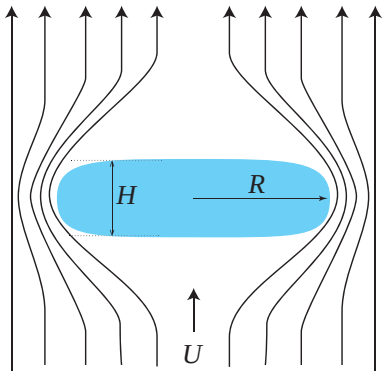

Figure I.16 – Falling drop of equatorial radius R and terminal speed U in the aerodynamic regime. Owing to the Bernoulli effect, the drop deforms perpendicularly to its vertical trajectory. Once the drop has reached its terminal speed, its thickness H scales as the capillary length ℓ_c - exactly as in the Leidenfrost scenario.

In the drop's frame, the flow is slowed down on the top and bottom of the drop. On the sides, the streamlines get nearer to each other having a local higher speed. In the case of a permanent, irrotational and inviscid flow, Bernoulli theorem gives us the following relationship between speed and pressure: $\rho_a U^2/2 + P = cst$. This relation states that high speed points are low pressure ones. In our situation, pressure is lower on the sides than on the top and bottom of the drop. This radial depression pulls the drop's edge

outwards, leading to a puddle shape. At equilibrium, the pulling pressure $\rho_a U^2$ must be balanced by Laplace pressure γ/H (we assume $H << R$). The new drop's thickness H now scales as $\gamma/\rho_a U^2$. Denoting R_0 as the drop radius in the original spherical geometry, volume conservation leads to the following equatorial radius:

$$R \sim \sqrt{\frac{R_0^3 \rho_a U^2}{\gamma}} \tag{I.12}$$

The terminal speed of this falling puddle is obtained by balancing drag $\rho_a R^2 U^2$ with the drop's weight $\rho R_0^3 g$:

$$U \sim \sqrt{\frac{\rho g \ell_c}{\rho_a}} \tag{I.13}$$

We now see how the terminal speed for a big drop (equation I.13) is analogous to the one obtained for small drops (equation I.9), provided that drop radius replaces the capillary length. In addition, if we plug this terminal speed in I.12, we obtain the equatorial radius for a free falling drop in terminal speed: $R^2 \sim \frac{R_0^3}{\ell_c}$. In other words, thickness scales as in a Leidenfrost situation:

$$H \sim \ell_c \tag{I.14}$$

Through this double analogy, we see how free falling drops and levitated drops are alike[4]. Indeed, we shown in figure I.17 three free falling drops: on the left side, the smaller one (below the capillary length) is spherical, in the middle, a bigger one (above the capillary length) is a flattened puddle and on the right side, a big drop that is being destabilized (see section 2.3). Again, all mechanisms seen for the Leidenfrost drops are visible in the free fall regime.

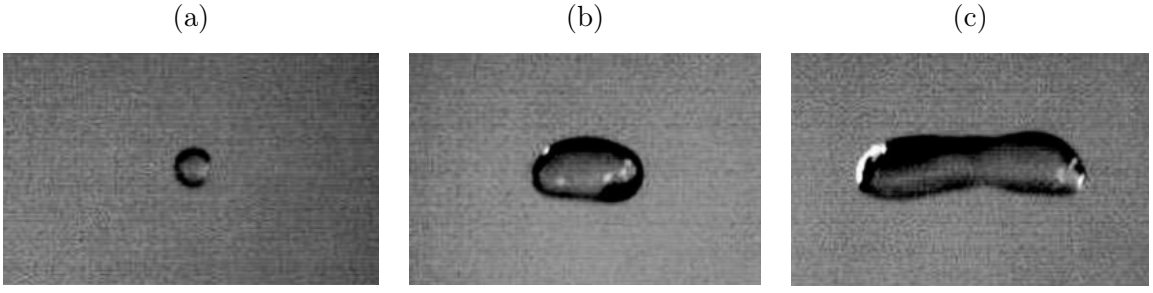

Figure I.17 – Free falling water drops of different volume. The drop in (b) has a horizontal dimension $2R = 1$ cm. Pictures (a) and (c) have the same scale as (b). Photos from [92].

[4]Reyssat et al. showed in [92] how speed and thickness equations are in good agreement with experiments.

2.2 The vapor cushion

Recent studies have focused on the thickness h of the vapor cushion beneath the drop. Burton and collaborators have been able to experimentally access the profile of the vapor layer under a Leidenfrost drop[5] [17, 19]. Although they showed that the interface is slightly concave, in what follows we assume a uniform deformation, i.e. a flat bottom surface. As evoked earlier, h is fixed by the balance between the drop's weight and the horizontal flow overpressure. Once more, two different scenarios are to be considered depending on the drop's size.

Puddles, $\mathbf{R} > \ell_c$

Vapor flow below drops comes from the evaporation of the liquid. Gottfried et al. showed in [50] that the heat transfer at temperatures of 200-500 °C is dominated by conduction. The heat obeys the Fourier law and it can be written per unit area: $\kappa\frac{\Delta T}{h}$ where we denote the thermal conductivity of the vapor as κ and the difference between the substrate and liquid temperature as ΔT. After a transient regime (where the drop uses the heat energy to reach its boiling temperature), all the incoming heat flux is used to transform liquid into vapor, hence a consumed flux of energy per unit area: $\mathcal{L}\dot{m} = \mathcal{L}\rho_v\, c$ where we denote the density and latent heat of evaporation as ρ_v and $\mathcal{L}$, respectively, and the rate of evaporation as c.

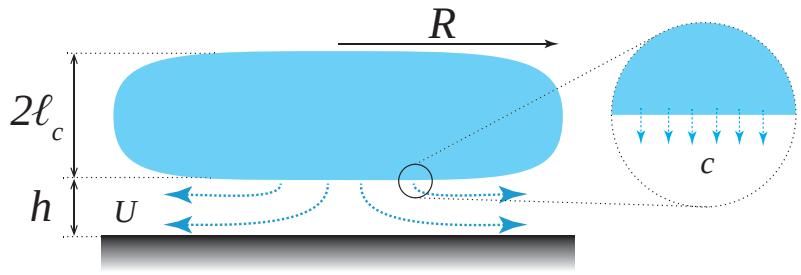

Figure I.18 – Sketch describing evaporation mechanism for a Leidenfrost puddle.

As sketched in figure I.18, c can also be seen as the vertical speed of vapor injected into the cushion. Balancing consumed and incoming energy, we get a first equation for the expression of vapor injection speed c:

$$c = \frac{\kappa\,\Delta T}{\rho_v\,\mathcal{L}\,h} \tag{I.15}$$

A second equation is obtained from a mass balance. As the equilibrium height h is

[5] They have used similar interferometric techniques than initially used to observe the evolution of the air layer between an impacting drop and its substrate [125, 122].

attained, the vapor injected at rate c from the bottom of the drop is balanced by the lateral escaping flux (of horizontal speed U in figure I.18). Hence we have:

$$U = \frac{1}{2} c \frac{R}{h} \tag{I.16}$$

Equation I.16 tells us that given a typical height h of levitation around 100 μm, the horizontal escaping speed U for a several millimeters drop is ten times greater than the injection speed c.

A last expression is obtained from the Navier-Stokes equation. Since the Reynolds number is small, we can neglect inertial effects in the vapor cushion flow. Laplacian associated to viscosity stress $\eta \frac{U}{h^2}$ is balanced by the horizontal pressure gradient $\frac{\Delta P}{R}$, leading to:

$$\eta \frac{U}{h^2} \sim \frac{\Delta P}{R} \tag{I.17}$$

Combining equations I.15, I.16 and I.17, we get the equilibrium levitation height h as a function of the different parameters of the problem:

$$h \sim [\frac{\eta \kappa \, \Delta T}{\rho_v \, \mathcal{L} \Delta P}]^{1/4} R^{1/2} \tag{I.18}$$

In the case of liquid puddles, the overpressure below the drop is the drop's hydrostatic pressure due to its weight: $\Delta P = \rho g H = \rho g 2 \ell_c$. We finally get:

$$h \sim [\frac{\eta \kappa \, \Delta T}{\rho_v \mathcal{L} \rho g \ell_c}]^{1/4} R^{1/2} \tag{I.19}$$

For a water droplet, the liquid's physical parameters have to be taken at 100 °C: $\rho = 960$ Kg/m^3 and $\ell_c = 2.5$ mm. The substrate temperature for a Leidenfrost experiment being typically 400 °C ($\Delta T = 300$ °C), the vapor's physical parameters are taken at an average temperature of 250 °C: $\eta = 1.8\,10^{-5} Pa \cdot s$, $\rho_v = 0.4$kg/m^3 and $\kappa = 36$mW/m/K. Finally, the latent heat of evaporation is set to $\mathcal{L} = 2300$ kJ/kg. With these values and for a drop of radius $R \approx 1$ cm, the typical vapor thickness is about 100 μm. This expression also shows that film thickness h has a very slow dependence regarding the substrate temperature, since it varies as $\Delta T^{1/4}$. In order to double the thickness we would need to multiply the temperature by a factor of 16. For water, it would imply temperatures around 5000 °C: despite all the experimental difficulties involved in reaching this temperature (being way above pyrolysis temperature), the heat flux would no longer be dominated by diffusion but by radiation. We can now foresee the advantage of the air levitation technique as it allows us to vary more easily h.

Exact solution This whole argument can be solved analytically by calculating the exact geometric prefactors, as done in [11]. Owing to the circular symmetry of the problem, equation I.17 can be written as: $12\eta\frac{U}{h^2} = \nabla P$. Taking into account the conservation of mass $div(hU) = c$ and assuming h homogeneous, if we take the divergence of the Poiseuille equation we get: $\frac{12\eta c}{h^3} = div(\nabla P) = \frac{1}{r}\frac{\partial(r\frac{\partial P}{\partial r})}{\partial r}$. After integrating twice between the bottom center of the drop $r = 0$ (pressure P_2) and the outside edge at $r = R$ (pressure P_0), we get the following expression for the overpressure: $P(r) - P_0 = \frac{3\eta c}{h^3}(R^2 - r^2)$. Balancing the integral of this overpressure over the bottom surface of the drop with the hydrostatic one (and using equation I.15), we get an exact expression for the vapor thickness:

$$h = [\frac{3}{4}\frac{\eta\kappa\,\Delta T}{\rho_v\,\mathcal{L}\rho g\ell_c}]^{1/4} R^{1/2} \tag{I.20}$$

Lifetime We can also evaluate a puddle's lifetime τ by calculating the ratio between the droplet's mass $m \sim \rho\ell_c R^2$ and its mass flow rate $\dot{m} \sim \rho_v R^2 c$, which yields:

$$\tau \sim \frac{\rho\ell_c}{\rho_v c} \sim \frac{\ell_c\rho\,\mathcal{L}\,h}{\kappa\,\Delta T} \tag{I.21}$$

For a centimetric puddle, this lifetime is around 100 s - long enough to observe it. It has been calculated under the assumption that almost all the evaporation is done through the bottom of the drop. This point has been experimentally demonstrated by obtaining similar lifetimes with droplets covered at their top with a thin aluminium film to avoid any evaporation other than from the bottom [88].

Droplets, $\mathbf{R < \ell_c}$

We now focus on the second size regime concerning small drops. The main difference dwells in the area through which evaporation takes place. For big flattened drops, evaporation was assumed to occur at the bottom area R^2 (see figure I.18). For small droplets, evaporation takes place through the entire surface R^2 as sketched in figure I.19.

Moreover, the bottom is deformed by gravity over a characteristic length scale $l \sim R^2/\ell_c$ [31]. Since the new horizontal characteristic lengthscale is now l we have to replace R by l in equations I.16 and I.17. The pressure exerted on the vapor flow due to the droplet is now dominated by the Laplace pressure (not the weight anymore). In equation I.17 the pressure gradient has to be replaced by $\Delta P/l \sim \frac{\gamma}{R}/l$, hence a vapor thickness h scaling as:

$$h \sim [\frac{\eta\kappa\,\Delta T}{\rho_v\,\mathcal{L}\gamma\ell_c^2}]^{1/4} R^{5/4} \tag{I.22}$$

These different theoretical predictions have been experimentally tested and checked

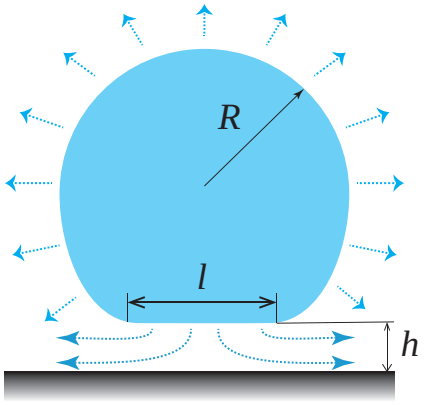

Figure I.19 – Evaporation mechanism for a small drop takes place through its entire area R^2. Contact area where drop's bottom is flattened is noted as l.

by Biance et al. [11, 12].

We can now calculate the lifetime of a drop assuming that the temperature gradient is established over the whole drop on the length scale R, leading to: $\dot{m} \sim \frac{\kappa \Delta T}{\mathcal{L} R} R^2$. Hence:

$$\tau \sim \frac{\rho \mathcal{L} R^2}{\kappa \Delta T} \tag{I.23}$$

For a water droplet of radius R equal to 0.6 mm, equation I.23 gives a lifetime of 80 s. This value overestimates the lifetime as experimentally seen by Biance et al. [11] who got a value around 10 s. Despite this overestimation, the model gets the experimental ΔT^{-1} dependency. As the drops become very small ($R << \ell_c$), capillary effects completely dominate and the bottom droplet does not deform at all, remaining spherical. For droplets as big as the characteristic vapor thickness ($h \lesssim 100$ µm) the lubrication theory no longer applies. Celestini et al. [21] have theoretically and experimentally shown that the droplet in this regime lifts and takes off from the substrate.

Additional remark

The main ingredient in Leidenfrost levitation is the need of high evaporation rates. We can consequently contemplate changing the type of liquid in order to lower the Leidenfrost temperature as done by using ethanol or even acetone. Almost all our subsequent Leidenfrost experiments will therefore be done with acetone. More exotic liquids can also be used: for example, liquid nitrogen and oxygen (whose boiling point is -196 °C and -183 °C, respectively) are already in Leidenfrost levitation at ambient temperature. We can even play with special solids that sublimate at ambient temperature as dry ice or camphor [3, 41].

2.3 Instabilities

Since the drop has a deformable interface, shape instabilities can appear for numerous reasons. In what follows we discuss three main different causes.

Vapor chimney

The vapor cavity beneath the drop becomes unstable for large drops. The gas forms a chimney rising at the center of the puddle and forming (transiently) a dome at the top as shown in figure I.20 [11].

Figure I.20 – Side view of a Leidenfrost drop puddle deformed by a chimney instability. Vapor underneath is less dense than liquid on top. As the interface is deformable, buoyancy effects make the vapor try to escape upwards and form a dome before bursting. Scale shows 5 mm.

The dome then bursts, which leaves a liquid torus that closes, generating strong oscillations before a new chimney forms. Similar instabilities were predicted for large puddles levitating on air-blown porous materials [74]. This instability can be seen as an inverse Rayleigh-Taylor instability [113]: instead of having a dense film on a ceiling destabilizing downwards [113], here we have a light film of gas destabilizing upwards. Gravitational force dominates surface tension when the drop radius is larger than a threshold critical radius $R^* = 4.3\ell_c$ [103], in good agreement with observations [11][6]. The case of even larger drops, a few centimeters or more, is also of interest: multiple chimneys form with a preferential distance, such as in the Rayleigh-Taylor instability [11]. We will see that this effect limits the maximum drop size in our experiments.

Spontaneous oscillations

In both Leidenfrost [111, 110, 121, 108, 101] and air-levitated states [15], it was reported that an instability leads to spontaneous oscillations, eventually inducing a breaking of symmetry and the appearance of "star drops" as shown in figure I.21 [16].

[6] Kozyreff et al. also looked at the instabilities in the case of viscous liquids, as discussed in [61].

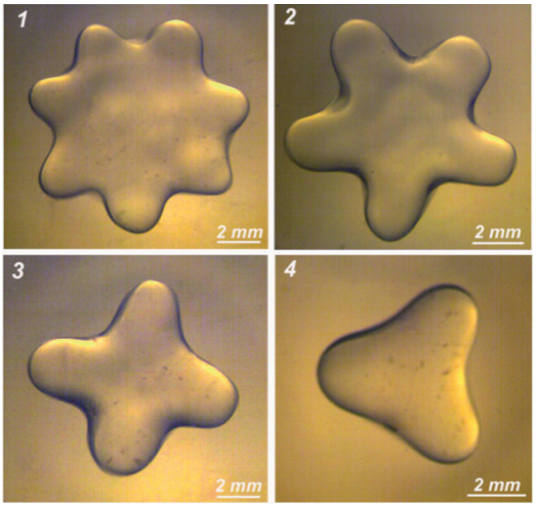

Figure I.21 – Star-shaped drops obtained with liquid nitrogen. A levitating droplet can oscillate with several different modes. Figure from [101].

The characteristic oscillation time is given by the competition between surface tension (γR) and inertial effects ($\rho R^3 \frac{R}{\tau^2}$):

$$\tau \sim \sqrt{\frac{\rho R^3}{\gamma}} \tag{I.24}$$

For a water droplet, this time is between 0.01 s and 0.1 s. The instability appears for flattened drops yet smaller than the critical radius of chimney apparition. This instability take some time to appear and in none of our experiments we observed these star-shaped drops.

Aerodynamic breakup

A free falling drop can become unstable in an analogous way, even though its environment is not initially turbulent. Falling puddles face an airflow coming towards them at speed U. They experience a pressure force proportional to $\rho_a U^2 R^2$ (acting on the axis of symmetry of the drop). This force can deform the drop, making an invagination over a characteristic distance δ as sketched in figure I.22.

Surface tension opposes this deformation. The local curvature due to a vertical deformation δ scale as δ/R^2, resulting in a Laplace pressure $\gamma\delta/R^2$. This pressure is opposed by the aerodynamic pressure $\rho_a U^2$, resulting in:

$$\delta \sim \frac{\rho_a U^2 R^2}{\gamma} \tag{I.25}$$

Drops are unstable if this vertical deformation becomes on the same order of magnitude

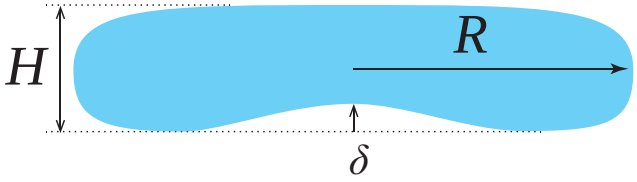

Figure I.22 – Deformation along the axis of symmetry of a falling puddle due to air pressure.

as the initial thickness of a falling puddle, that is, if $\delta > \ell_c$. Inserting this condition in equation I.25, and using the expression of the terminal speed of a falling puddle (equation I.13), we conclude that puddles are unstable for:

$$R > \ell_c \tag{I.26}$$

This problem can be seen as a variation of the previous chimney instability, highlighting once more the strong analogy between air-levitated (or free falling drops) and Leidenfrost drops as previously shown in figure I.17c. By analogy with the Rayleigh-Taylor instability, the numerical coefficient in these criteria should be on the order of π, resulting in critical radius of about the centimeter.

2.4 Crenelated surfaces

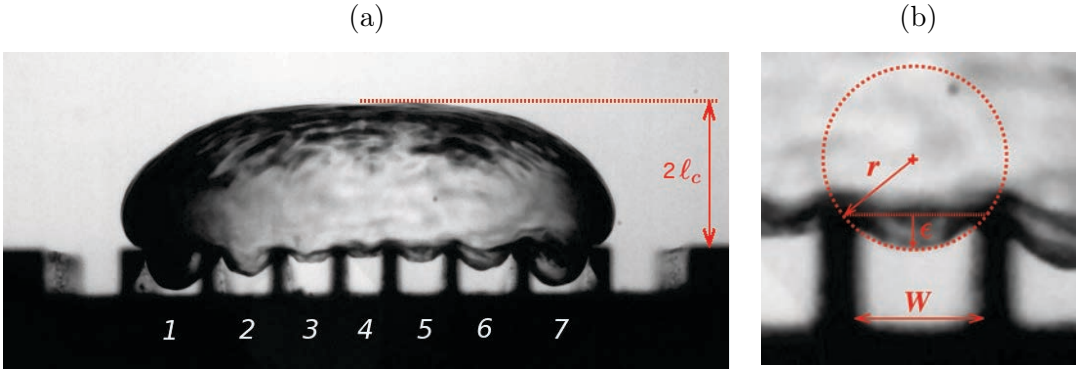

Figure I.23 – (a) Drop of acetone on a hot substrate (T = 400°C) with straight crenels of various widths W. W is 1.4 mm for crenels 1 and 7, 1.2 mm for 2 and 6, 1 mm for 3 and 5 and 0.8 mm for 4. The depth H is 1 mm to make clear the transition between levitation (crenels 2 to 6) and impalement (crenels 1 and 7). (b) Zoom on crenel 5 with the definitions of the distances related to the curvature of the liquid/vapor interface.

We discussed how vapor or air pressure can deform a drop's interface if it is strong

enough to overcome surface tension effects. Here, we explore the deformation due to a physical constraint such as a texture. For that purpose, we etch parallel grooves on a brass plate, heat it, and deposit on it a water puddle as shown in figure I.23a. It is important to know whether the crenellations can support the liquid sitting on them or not. Three geometrical parameters defining the grooved texture must be explored: the distance W between walls, the thickness λ of the walls and the depth H of the grooves.

Width dependency

We denote as ϵ the sagging distance of the drop into the groove, as defined in figure I.23b. We expect a small sagging if the groove is narrow, and a full penetration if it is wide enough. To be more quantitative, we show in figure I.24 how ϵ experimentally varies as a function of crenel width W.

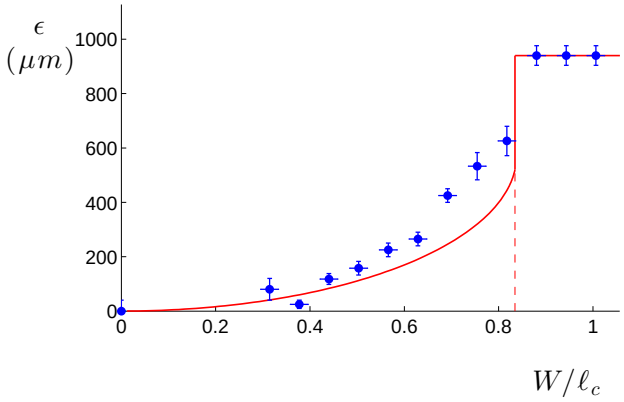

Figure I.24 – Penetration ϵ of an acetone drop ($\ell_c = 1.6$ mm) in a groove as a function of the width W of this groove rescaled by the capillary length. Vertical red dashed line is placed at the critical width value $W_c = 2(\sqrt{2}-1)\ell_c$ calculated from the model I.31. Plain red line show numerical solution of equation I.29. Wall thickness is $\lambda = 0.2$ mm and depth H is 1 mm.

A critical width W_c separating two different regions clearly appears in the data (vertical red dashed line in figure I.24). For $W > W_c$, we have a plateau regime where full impalement in the texture occurs. The drop falls into the grooves and reaches the bottom - set here to 1 mm. For $W < W_c$, the wider the groove, the deeper the drop penetration in the texture, but the liquid/vapor interface remains suspended above the bottom of the groove. In order to understand this dependency we use a hydrostatic argument. Assuming a depth H big enough, we can consider that the bottom of the channel does not perturb the sagging part of the drop (for the sake of simplicity, we can even assume H infinite). In such case, the local curved interface between two walls (of radius r defined in figure I.23b) can be at equilibrium if the Laplace pressure γ/r (we neglect the other perpendicular curvature assuming $r << R$) is balanced by the hydrostatic pressure $\rho g(2\ell_c + \epsilon)$, hence:

$$r = \frac{\ell_c^2}{2\ell_c + \epsilon} \tag{I.27}$$

The interface radius r and the sagging ϵ (figure I.23b) are geometrically related through:

$$2r\epsilon = \epsilon^2 + W^2/4 \tag{I.28}$$

We can deduce from I.27 and I.28 an equation for ϵ:

$$2\ell_c^2\epsilon = (\epsilon^2 + \frac{W^2}{4})(2\ell_c + \epsilon) \tag{I.29}$$

Since there is no analytical solution, we solve it numerically and draw the solution with a plain red line in figure I.24. Although we have a good qualitative agreement, the model near W_c tends to underestimate the data. This may be due to the approximation done when assuming tangent interface at the corners' tops. In other words, the interface deformation is supposed to be in first approximation circular, however a catenoid shape may be more accurate.

Approached solution to I.29 can be obtained in the limit of small ϵ ($\epsilon << \ell_c$ and $\epsilon << W$):

$$\epsilon \approx W^2/4\ell_c \tag{I.30}$$

The sagging ϵ logically increases when making the crenellations wider, and the critical width W_c at which the liquid fully penetrate a crenel ($r \approx \epsilon$) is obtained for $r = W/2$, which yields:

$$W_c = 2(\sqrt{2} - 1)\ell_c \tag{I.31}$$

With acetone, we have $W_c/\ell_c = 0.84$ - in perfect agreement with experiments as shown in figure I.24 where the red vertical dashed line is placed at this theoretical value. W_c is expected to be 2 mm for water and 1.3 mm for acetone whose smaller surface tension makes it impale more easily in the crenels. To go further in our model comparison we show in figure I.23a a side view of a drop sitting on hot straight channels of width W varying from 0.8 mm at the drop center to 1.4 mm at its periphery. The critical value W_c fits with what can be seen in figure I.23a, where acetone only penetrates crenels 1 and 7, the only crenels of width $W = 1.4$ mm above $W_c = 1.3$ mm.

Depth dependency

We show in figure I.25 a set of images of a drop sitting on a hot surface textured with parallel crenels of width W= 1 mm and wall thickness is λ= 0.2 mm. A different crenel

depth H has been fixed for each picture ranging (from left to right) from 200 μm to 1200 μm. For deep crenels, the sagging part of the drop ϵ remains unaffected by the bottom of the groove. However, as shown in the first left image of figure I.25, ϵ is smaller for shallow crenels.

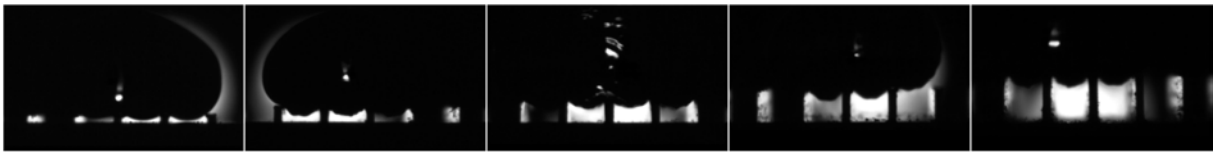

Figure I.25 – Side zoom view of a Leidenfrost puddle drop sitting on crenels of fixed width $W = 1$ mm and wall thickness $\lambda = 0.2$ mm. Depth H from left to right is 200 μm, 400 μm, 600 μm, 800 μm and 1200 μm. On the left image, where $H = 200$ μm $< h$, ϵ is smaller due to the vapor cushion overpressure.

In order to be more quantitative, we plot in figure I.26 ϵ as a function of H :

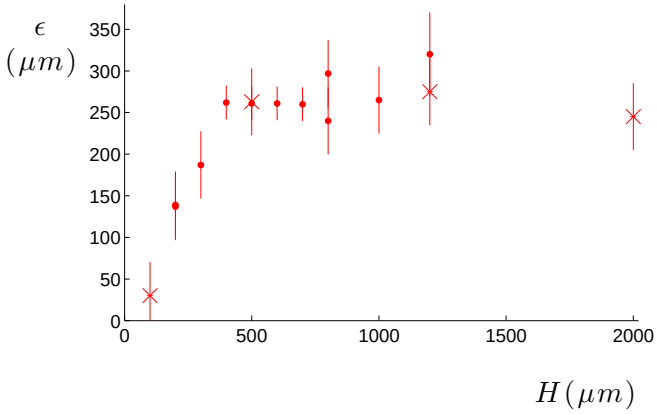

Figure I.26 – Sagging distance ϵ of the drop in the groove as a function of the depth H of the groove. In this series of experiments, width is $W = 1$ mm ($W/\ell_c \approx 0.6$), and wall thickness is $\lambda = 0.2$ mm.

Two asymptotic regimes can be observed and explained. When H is small compared to the vapor thickness h on a smooth substrate, everything happens as if there were no texture, hence $\epsilon \approx 0$. When $H >> h$ (regime corresponding to the plateau seen for $H >$ 400 μm in figure I.26), the bottom of the groove does not play any role in the deformation: we are in the situation studied above and ϵ obeys equation I.29. In the particular case of figure I.26, the expected theoretical value is $\epsilon \approx 190$ μm - as explained above, slightly underestimating the experimental value. In between ($H/h \sim 1$), a more detailed model should be produced to take into account that below the interface we are not anymore at atmospheric pressure: we have to include the overpressure due to the confined flow.

Wall thickness dependency

The final geometrical substrate parameter to be explored is the wall thickness. In all the previous experiments, we have set wall thickness to $\lambda = 0.2$ mm. We have tried to see what happens with a texture of same aspect ratio $\lambda/W = 0.2$, but half smaller ($W = 0.5$ mm, $\lambda = 0.1$ µm). The experimental observation was that we could not avoid frequent boiling events, even at high temperature and using acetone.

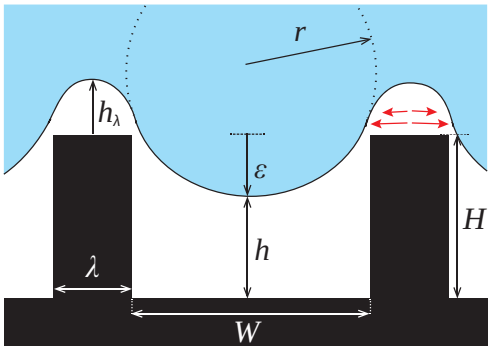

Figure I.27 – Zoom on a single crenel for a drop sitting on a grooved hot surface deep enough to neglect evaporation at the bottom of the sagging part. For visibility, h_λ and ϵ are not at scale. In red arrows, the escaping flow from the top of a crenel is horizontal and perpendicular to the grooves direction.

In the limit where the vapor film thickness h is smaller than the texture height H (and with $\lambda < W < W_c$), the drop is suspended at the top of the walls. The whole weight of the drop has to be sustained by the overpressure present on these tops (the bottom of the channel being too far away to contribute through the sagging part). The corresponding vapor thickness on top of each channel (denoted as h_λ and defined in figure I.27) is calculated by balancing the drop weight by the pressure arising from the escaping flow, whose direction is from the middle of a wall top, towards the outside (i.e. perpendicular to the wall over the distance λ, as sketched with red arrows in figure I.27). We reproduce the same argument used to calculate the equilibrium thickness of an evaporating drop on a flat surface (section 2.2) where we simply replace R by λ and h by h_λ in the previous equations I.15, I.16 and I.17. In addition, the weight of the liquid column is now being compensated by the surface area corresponding to the top of the walls, hence only over a surface fraction $\phi \sim \frac{\lambda}{W+\lambda}$. In the former Poiseuille equation (I.17), the overpressure has to be replaced by $\rho g \ell_c/\phi$. The result is a vapor thickness solution analogous to I.19: $h_\lambda \sim [\frac{\eta\kappa\,\Delta T}{\rho_v \mathcal{L} \frac{\rho g \ell_c}{\phi}}]^{1/4} \lambda^{1/2}$, hence:

$$\frac{h_\lambda}{h} \sim [\frac{\lambda}{R}]^{1/2} \phi^{1/4} \tag{I.32}$$

In all our experiments, we have $\phi \approx 0.17$. In the case of a 5 mm radius puddle and

$\lambda = 0.2$ mm, we get $\frac{h_\lambda}{h} \approx 10\%$, hence $h_\lambda \approx 20$ μm. Through this simple model, we can see that the drop interface on each wall is close to the substrate. Any small perturbation due to the vibration of the interface will therefore easily result in a temporary boiling event. Equation I.32 also tells us that even with a fixed aspect ratio, a decrease of 50 % in wall thickness will result in a local thickness reduction by 30%. This explains why it was much more difficult to avoid boiling on wall tops with a half-thick texture (keeping the aspect ratio constant). Because we want to stay in a film boiling Leidenfrost regime, from now on we fix $W = 1$ mm and $\lambda = 0.2$ mm, values for which we have experimentally tested that we avoid the formation of vapor bubbles.

Relationship between mass and radius on a crenelated surface

We showed in figure I.15 (section 2.1) the volume of a non-wetting drop sitting on a smooth substrate as a function of its equatorial radius. As a consequence, we were able to deduce the drop volume from the only observation of its radius (without having to directly measure it). In order to also be able to access the volume of a drop sitting on a crenelated surface (here of depth $H = 200$ μm) we add to figure I.15 the corresponding curve. It can be seen in figure I.15 (black data) that for a fixed volume, a drop on a crenelated surface has a bigger equatorial radius. To understand this radius increase, we can assume that thickness from top to bottom of the sagging part of the drop remains unchanged compared to that on a smooth substrate (a reasonable assumption as far as the drop is sustained by the top of the walls, i.e. $W < W_c$). As a consequence, the volume occupied by the walls is relocated in the bulk, which yields a larger equatorial radius.

3 High mobility and special friction

If we pour liquid nitrogen on the floor, the resulting drops glide by very large distances, most often comparable to the size of the room (a few meters) where the experiment was performed. The absence of a contact line around a levitating drop makes it "adhering nowhere," as noted by Leidenfrost himself. It generates original dynamical behaviors, which are also observed in super-hydrophobic situations. These drops move nearly without friction [42], and bounce when impacting solids [10, 56, 128]. This section presents some of these special dynamics.

Unexpectedly, it appears that there is no comprehensive study in the literature devoted to these frictionless motions, maybe because of the simplicity of the friction laws expected in this limit. The details of the corresponding laws depend on the shape of the liquid, and for simplicity we consider here the puddle case (large drops of thickness $2\ell_c$ and radius R). Several scenarios can be expected depending on where the dissipation takes place: in the vapor cushion beneath the drop, in the air surrounding the drop or in the liquid itself.

3.1 Viscous friction in the vapor film

If we consider that dissipation takes place in the vapor cushion, we are in the situation described in figure I.28. The "contact" area of a gliding puddle is comparable to its surface

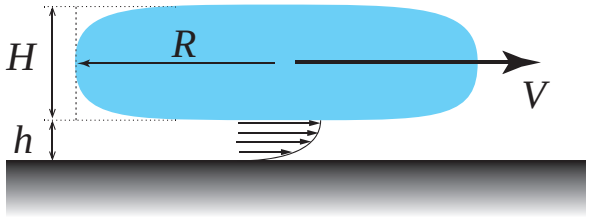

Figure I.28 – Viscous friction in vapor film beneath a gliding levitating drop.

area R^2 so that the viscous friction F_η scales as:

$$F_\eta \sim \frac{\eta_a V}{h} R^2 \tag{I.33}$$

The vapor thickness h was evaluated in section 2.2. Taking its value as independent of V, we find a friction of typically 1 μN for a velocity $V \approx 1$ m/s, that is, approximately 0.1% of the drops' weight. This is very different from liquids on common substrates, for which pining forces are comparable to the weight (sticking the drops to tilted plates) and for which viscous forces opposing the liquid puddle motion (for velocities in the range 0.1 - 1 m/s) can be even larger, also because of the existence of contact lines [102].

3.2 Inertial friction in the surrounding air

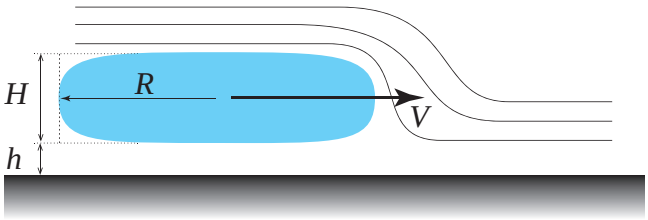

Figure I.29 – Aerodynamic friction around a gliding levitating drop.

In general, the main force resisting the motion of levitating drops moving on a plate is the inertia of air. It is similar to the one discussed in section 1.3, except that the corresponding cross section is not R^2, but $RH \sim R\ell_c$ as shown in figure I.29. Hence we get:

$$F_i \sim \rho_a V^2 R\ell_c \tag{I.34}$$

For $V \approx 1$ m/s, F_i typically is 10 μN, 10 times larger than F_η. For a drop running down a solid tilted by an angle θ relative to the horizontal direction, balancing F_i with the weight $mg\sin\theta$ we obtain a terminal velocity V $\sim [\rho/\rho_a Rg\sin\theta]^{1/2}$, typically a few meters per second. Conversely, if we throw drops of liquid nitrogen on the floor, they will decelerate until friction stops them. The corresponding distance L_i is given by Newton's equation $mV^2/L_i \sim F_i$, from which we get:

$$L_i \sim \rho R/\rho_a \tag{I.35}$$

If we put numbers in this equation, the characteristic stop length is a thousand times the drop's radius - several meters. For liquid nitrogen, these distances are so large that the time L_i/V to stop is often on the order of (or even smaller than) the evaporation time τ evaluated in section 2.2.

3.3 Special friction on a crenelated surface

Frictionless drops can be seen as untamable mobile objects. It is worth thinking of more efficient ways to slow them down and even try to trap them. This can be done by creating a texture at the solid surface. For large textures, comparable to the liquid scale (0.1–1 mm) (see figure I.30a) Dupeux et al. [42] showed that a levitating drop meeting a series of crenelations perpendicular to its way decelerates on centimeter-size distances, instead of meters.

This strong effect has been proposed to result from the successive impacts of the

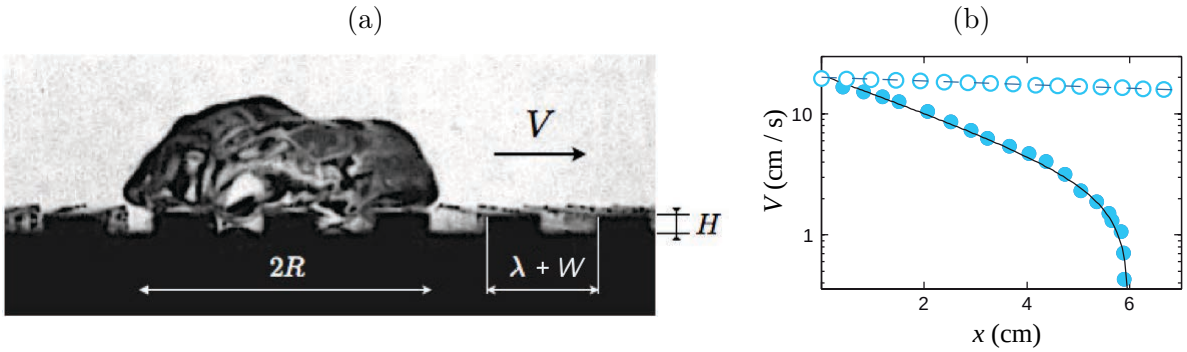

Figure I.30 – (a) Leidenfrost drop running on a plate with crenelations. (b) The drop slows down on centimeter-size distances (solid dots), instead of meters on a flat solid (empty dots). This enhanced friction is attributed to the successive (soft) impacts of the bumps below the drop onto the side of the crenelations. The distance $\lambda + W$ between two crenels is 1.5 mm, and their depth is $H = 250$ μm. Figure from [42].

sagging liquid on the crenel sides [42]. The liquid deforms in crenelations, and as the drop slides, each bump hits the side of the crenel without contacting it (no boiling is observed). As known from impact literature [56], normal shocks are most often soft, despite the absence of an obvious source of dissipation (such as contact lines). Kinetic energy is transferred in vibrations that later decay owing to liquid viscosity [10]. This inertial method of slowing down a drop is efficient because it involves the liquid density, instead of vapor density.

For crenelations of depth H and wavelength $\lambda + W$, we have $R/(\lambda + W)$ crenels below the liquid. Each step is hit over a surface area scaling as ϵR (ϵ being the sagging distance in the crenel). If $W > W_c$, the drop fully penetrates the texture and we get $\epsilon \sim H$. The corresponding crenel friction force scales as:

$$F_c \sim \rho V^2 R^2 \frac{H}{\lambda + W} \tag{I.36}$$

Crenelations increase the friction by a factor $\frac{\rho}{\rho_v}\frac{H}{\lambda+W}$ compared to the aerodynamic flat situation (seen in I.34). Because the density of a liquid is 3 orders of magnitude higher than that of air, the resisting inertial force is increased approximatively 100 times for $H \approx 0.1\ (\lambda+W)$. The efficiency of the trap relies on the fact that dissipation mostly takes place in the liquid and only marginally in the surrounding air. More precisely, balancing this inertial friction with the drop deceleration $\rho R^2 \ell_c \frac{d(V^2)}{dx}$ provides an exponential decrease of the velocity along the direction of motion, with a characteristic length:

$$L_c \sim \ell_c \frac{\lambda + W}{H} \tag{I.37}$$

For a puddle, L_c is a few cm, to be compared to the several meters expected previously

on a flat solid with inertial air friction (equation I.35). This exponential regime is visible in figure I.30b and followed by an abrupt trapping in the crenels, possibly due to gravity [42].

Chapter II

Self-Propulsion in the Leidenfrost state

Contents

1 The texture revolution

In 2006, Linke et al. found the first system where a Leidenfrost drop could self-propel. This effect is obtained by texturing a substrate with a ratchet geometry. Linkes' experiment has been a stimulating starting point for a rich theoretical and experimental research. A wide range of scenarios has been evoked to explain the propelling mechanism, ranging from local thermal effects, surface waves, to rocket effect and viscous mechanisms. To sort them out, several complementary experiments have been proposed. We first do a short review of these works in order to understand the underlying mechanisms which have generated elegant novel experiments and configurations. Then, we discuss how all this experiments lead us to achieve a new texture, easier to model and to optimize.

1.1 The ratchet: a seed is sown

The Linke experiment

As reported by Linke et al., liquids can self-propelled when placed on a hot horizontal ratchet [73]. Indeed, a drop levitating above saw-teeth (as shown in figure II.1) will accelerate perpendicular to the texture, in the direction of the slow local slope of a tooth, from left to right in the case shown in figure II.1, before reaching a terminal speed. Such a motion is observed provided that the drop is larger than the tooth size.

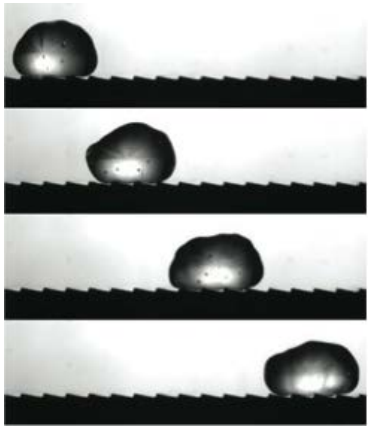

Figure II.1 – A liquid drop (radius $R = 2$ mm) is placed on a hot ratchet with teeth of depth $H = 0.2$ mm and length $\lambda = 1.5$ mm. For ratchet temperatures larger than the Leidenfrost temperature T_L, the drop self-propels, from left to right in the figure. The interval time between successive pictures is 40 ms. (Courtesy of Marie Le Merrer).

Linke also reported that two regimes can be observed, depending on the substrate temperature:

Low temperature regime (L in figure II.2). Droplets on a ratchet are not fully supported by a vapor layer: nucleate boiling events introduce fluctuations. We show in figure II.2 drop's acceleration as a function of substrate temperature. In this narrow regime (L), accelerations are large, around 1 m/s^2. A study focusing on this nucleate boiling propulsion has been done by a British team in Bath [1] by analyzing the sound produced by their boiling. However, nucleate boiling greatly increases the evaporation rate of the liquid, and as a consequence, induces the drop to vanish much faster.

High temperature regime (H in figure II.2). The drop is sitting on a vapor cushion avoiding direct contact with the textures and generating self-propelled Leidenfrost drops. After a short time of acceleration (on the order of 10 cm/s^2), typical terminal speed is observed around 10 cm/s. This terminal regime is the signature of an equilibrium between a propelling force (experimentally calculated by multiplying the drop's mass by its acceleration at zero speed) and a resistive friction. Typical values of acceleration being 50 times smaller than gravity g, the propulsion force is 50 times smaller than the drop's weight. Although small, propelling forces (several μN) are high enough to generate quick motion: this is a direct consequence of the high mobility in the non-wetting state. Linke and colleagues suggested the following explanation for this movement: the film of vapor directly below the region of the drop that is on top of the ridge is most compressed. This causes the vapor to flow away from that spot, both backwards and forwards. But, thanks to the asymmetrical shape of the surface, only the flow in the forward direction creates a viscous force on the drop, capable of moving it [112].

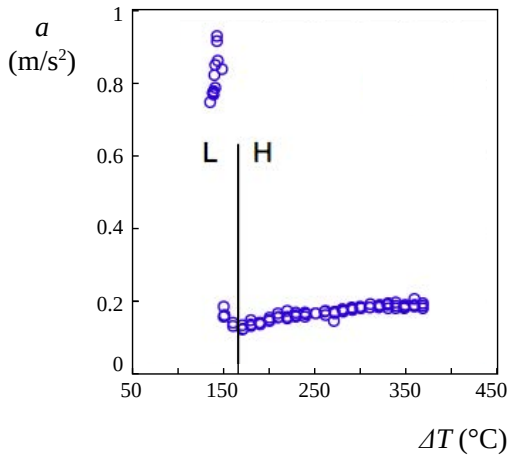

Figure II.2 – Droplet acceleration as a function of the difference of temperature between liquid water and ratchet substrate. Two regimes are separated by a vertical black line. "H" is the High temperature regime where we have Leidenfrost self-propulsion. "L" is the Low temperature regime where nucleate boiling generates greater accelerations but faster evaporation of the liquid. Figure adapted from [73].

The Dry ice experiment: sorting propulsion scenarios

Other mechanisms explaining this self-propulsion have been considered, possibly relying on the deformable character of the liquid/vapor interface. Indeed, experiments performed by Daniel et al. [29] showed that when a liquid drop is subjected to an asymmetric lateral vibration on a non-wettable surface, a net inertial force causes it to move. Others scenarios based on the liquid nature of the object are to be found among Marangoni effects [81], spontaneous oscillation of the drop or surface waves. However, Lagubeau et al. showed in 2011 that self-propulsion on hot ratchets can also be achieved with dry ice (see section 2.2, chapter 1): the dry ice platelet both levitates and is set into motion by the hot substrate ratchet texture in the same direction as observed for the drop. It is made clear by this simple experiment that propulsion does not need the deformable and liquid nature of drops [41, 4].

Visualizing the flow: self-propulsion scenario

Two remaining opposite scenarios might however still remain. A first one, based on a rocket effect and momentum ejection, where the vapor escape would propel the drop in the direction opposite to this ejection. A second one, where the vapor flows in the same direction as the drop, which gets entrained by (vapor) viscosity. We see how crucial it is to know the direction of the vapor flow to distinguish between inertial and viscous propulsion. In order to make this question clear, Dupeux et al. put small glass bead tracers in the vapor flow to assess its direction [43]. The 3D vapor flow was found to have a complex 3D geometry, but it emerges from this work that the flow starts at the teeth tops, flows down the teeth, and gets perpendicularly evacuated along the bottom of the steps, as sketched in figure II.3.

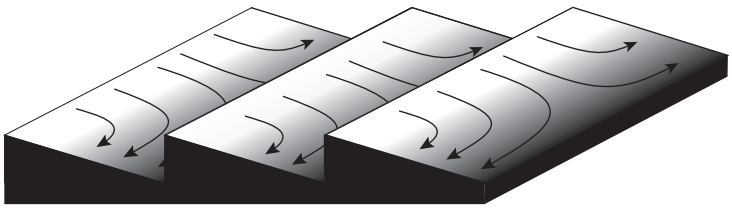

Figure II.3 – Sketch of vapor flow below a Leidenfrost drop or solid on a hot ratchet. The vapor flow is cellular: each tooth carries a vapor in the down slope direction, which gets perpendicularly evacuated along the bottom of the step.

This experience establishes that the main vapor flow direction is the same as the levitating object motion, validating the viscous entrainment scenario. As previously seen in Chapter I (section1.3), the Reynolds number in the vapor cushion is small and Dupeux et al. [43] propose the following model based on scaling law arguments. Denoting h as

the mean thickness of vapor, we expect a propelling force scaling as:

$$F \sim \frac{\eta U}{h} R^2 \tag{II.1}$$

The Poiseuille equation gives a relationship between shear stress and pressure gradient:

$$\frac{\eta U}{h} \sim \frac{\Delta P}{R} h \tag{II.2}$$

Combining equation II.1 and II.2 yields:

$$F \sim \Delta P R h \tag{II.3}$$

Since the underlying pressure ΔP has to compensate the pressure generated by the objects weight mg/R^2 (where m is the object mass) we finally get:

$$F \sim mg\frac{h}{R} \tag{II.4}$$

The ratio h/R is typically $1/50$, in good agreement with the experimental results previously discussed where propelling force was 50 times smaller than the drop's weight.

A fertile starting point

A whole zoology of new studies has been developed by this Linke experiment. Two main directions of work have been privileged:

Scale reduction Marin et al. [49] have worked on ratchets with a texture almost 10 times smaller compared to Linke's original experiment: their horizontal pitch being 140 µm and the crest height ranging between 10 µm and 32 µm. This vertical scale is to be compared to the typical vapor thickness beneath water droplets on flat substrates shown in figure II.4 and ranging from 30 µm to 90 µm [12]. In Marin's experiments, droplets have a radius $R \in [0.7, 3]$ mm so that they mostly are in the capillary-dominated regime where the texture height is comparable to the vapor thickness. For big puddles, vapor thickness can be 10 times bigger than the texture used by Marin so that we expect a less effective rectification of the vapor flow. They have shown that the viscous mechanism proposed by Dupeux et al. fits reasonably well with experiments performed on micro-ratchets, not only for big droplets, but also for capillary droplets, for which the scaling of the force with the droplet radius is inverted [49].

Ok et al. went a step further in size reduction and manufactured micro- and sub-micron ratchets [86]. They showed that sub-micron ratchets yield water droplet velocities reaching 40 cm/s if brought at a temperature range slightly above the threshold of droplet

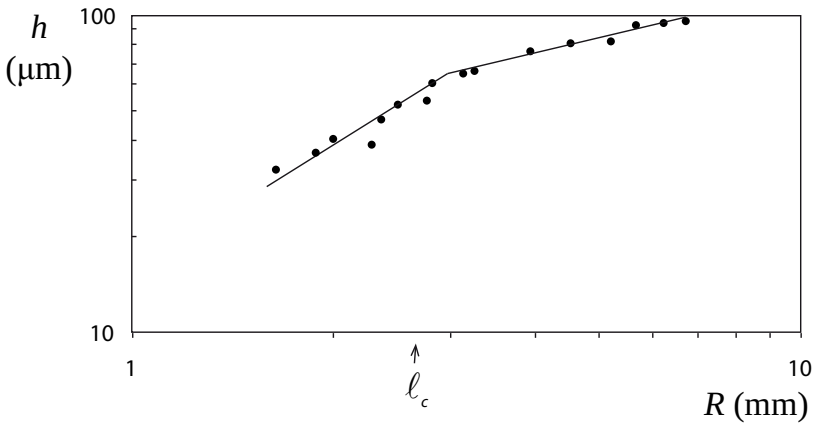

Figure II.4 – Vapor thickness h of a Leidenfrost drop on a smooth surface as a function of its equatorial radius R. As discussed in chapter I (section 2.2), two regimes are observed depending on the drops radius: if the drop is smaller than the capillary length, thickness increases as $R^{5/4}$; if it is larger, it goes as $R^{1/2}$. Capillary length ℓ_c is marked on the R-axis, with a value of 2.5 mm for water at 100°C. Figure from [12].

motion. This dramatic increase in the droplet velocity is attributed to an enhanced heat transfer through the local contacts between ratchet tips and bottom of the droplet - close to the observations of Linke in the L-regime of figure II.2.

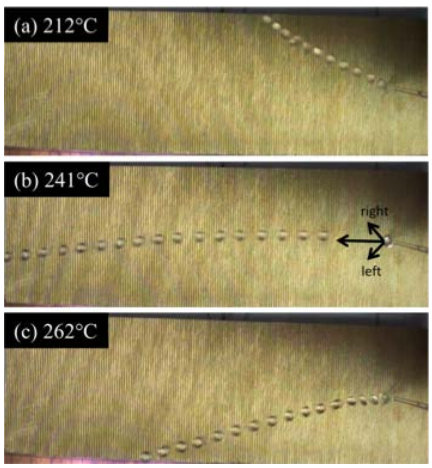

Figure II.5 – Chronophotographies of droplet trajectories on a brass ratchet in the transition boiling regime (where direct contact is observed between liquid and texture) for three different temperatures. (a) Brass temperature at 212 °C. A strong deviation perpendicular to the main direction is observed due to boiling events and interaction with sub-structures. (b) Brass temperature at 241°C, deviation in the opposite direction is observed. (c) Brass temperature at 262 °C. By increasing the temperature, we modify the nature of the contact with the sub-structures, hence changing the deviation. The horizontal pitch is 1 mm and the sloping parts of teeth are at 30°(hence a crest teeth at 600 μm from the bottom-deep structures). Figure from [1].

Finally, Grounds et al. focused their study on the transition boiling regime [1]. While observing the drops' trajectories on a ratchet, they recorded the sound produced by boiling. From sound intensity they could assess wether they were in the Leidenfrost regime or in the transition boiling regime. They showed that the later regime can be induced even at high surface temperatures with acute protrusions. In this regime, droplets can climb steeper inclines perpendicular to the ratchet texture. They also observe that sub-structures (generated by the milling process and of typical length scale of a few μm) generate movement in the direction perpendicular to the motion due to boiling events. As shown in figure II.5, this lateral motion can be tuned by varying the temperature of the surface: the drop does not only moves in the same direction as seen in the Leidenfrost regime, but it also has a slow motion along the teeth direction. Grounds et al. showed how two different propelling mechanisms can be combined. In our study, we will only concentrate on the viscous drag regime, hence avoiding by all means nucleate boiling.

Looking for new texture geometries Cousins et al. [115] produced a new texture geometry by exploiting the ratchet effect to construct a "circular ratchet trap" for Leidenfrost drops: a surface with concentric circular ridges, each asymmetric in cross section as shown in figure II.6. This new texture was used to study drops' trajectories as a function of the initial speed, and to observe how drops get gradually trapped at the center of the device due to a combination of propulsion and friction in the textures. They also looked at big drops deformations, large enough to generate binary fission of puddles owing to important internal movements.

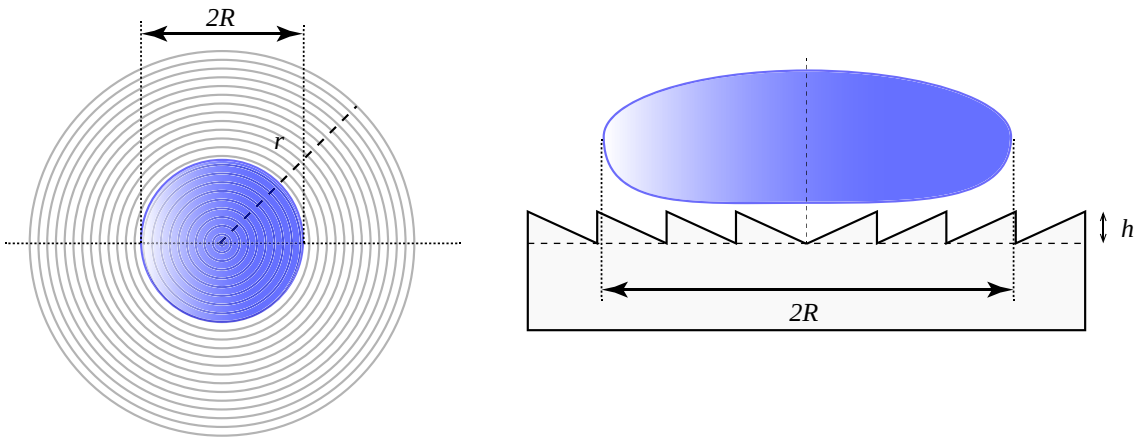

Figure II.6 – Sketch of a circular ratchet with a drop trapped in the middle. (Left) Top view. (Right) Side view. Figure adapted from [115].

Limitations

The previous scaling argument qualitatively captures the propulsion mechanism and it is in good agreement with the measurements. However, it does not provide the force dependency towards the substrate geometrical parameters such as tooth angle and horizontal pitch. In order to take them into account, we have to produce a more sophisticated model by adding two more equations to the Poiseuille one: conservation of mass and thermal balance, as previously done to calculate the thickness of the vapor cushion on a flat surface. All three equations depend on the vertical characteristic distance fixed by the vapor thickness h. If we have a closer look at a single tooth (see figure II.7), we observe that the thickness beneath the drop interface ranges from H (the height of a step) at point 2 to almost zero (at the crest) at point 1. The first limitation of this model dwells on the need to somehow "arbitrary" choose h between 0 and H.

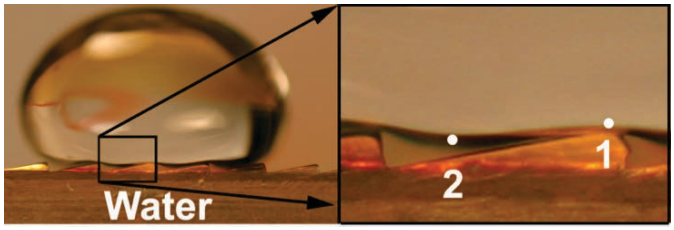

Figure II.7 – Side view of a Leidenfrost droplet on a ratchet. If we focus on a single teeth, we clearly observe that the vapor film thickness ranges from $h \approx H$ (near point denoted 2) to $h << H$ (around point denoted 1). Figure from [112].

A second limitation of the ratchet geometry is that, although we rectify in average the flow in the main propulsion direction, the detailed 3D flow is rather complex (as shown in the recent numerical study by Baier et al. [4]), making a rigorous analytical model probably impossible.

A third limitation dwells on the fact that the ratchet geometry makes it difficult to predict beforehand how the flow will be rectified. We put the evaporating object on it, and then observe the vapor direction. Meanwhile, the vapor pattern is free to choose its own escape path. Hence, it is not easy to understand how the ratchet geometry impacts the vapor flow, and how it can be optimized.

1.2 The herringbone: time to reap

Lead by previous work, we propose here to create a new self-propelling texture in order to reach a double aim: (i) to produce an experiment that would validate the viscous entrainment scenario, (ii) to further explore the possibility of novel textures, and optimize them.

The herringbone Texture

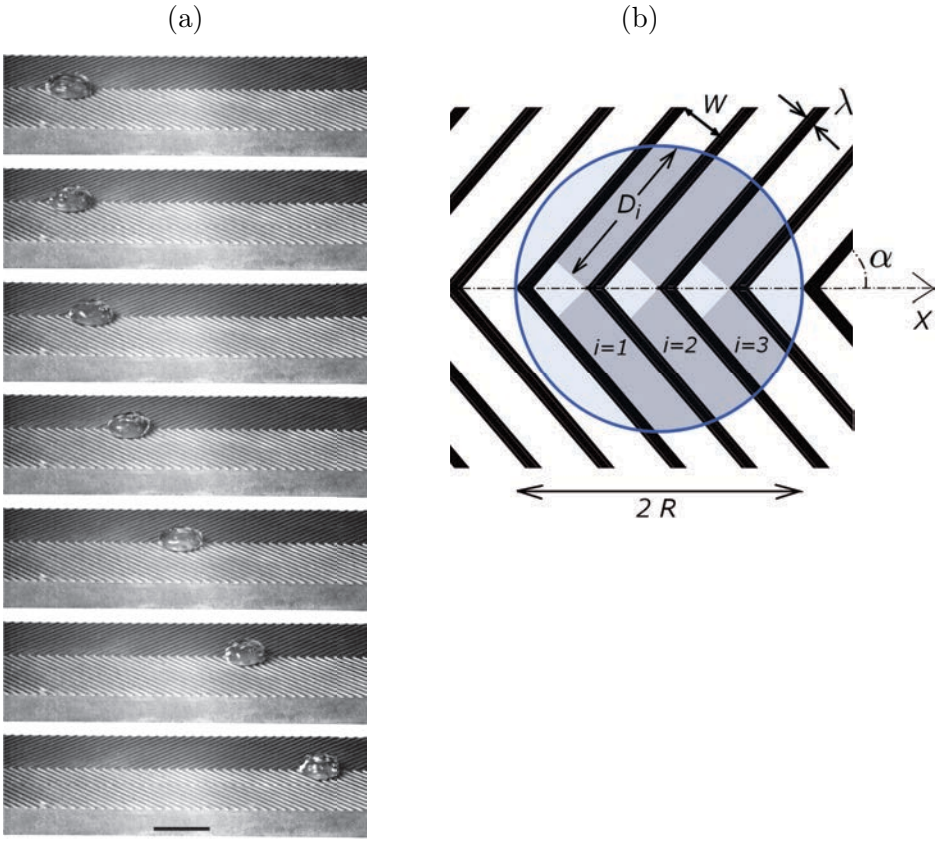

Figure II.8 – (a) Placed on the symmetry axis of a hot herringbone made of brass (angle $2\alpha = 90°$, $T = 400$ °C), an acetone drop (mass m, volume $\Omega = 200$ μL) self-propels. Images are separated by 0.2 s. The drop acceleration a is measured, from which the propelling force $F = ma$ can be deduced. Each crenel has a depth $H = 0.2$ mm and a width $W = 1$ mm. The wall thickness λ between channels is 0.2 mm. The bar shows 1 cm. (b) Top sketch of the herringbone geometry with the drop in blue and definition of the geometric parameters.

In order to force the rectification of the flow, we designed the simplest geometry we had in mind: a herringbone pattern made of grooves. As previously seen in Chapter I (section 2.4), a drop on a grooved texture will locally deform, sagging into the top of each crenel, acting somehow as a roof over a channel. Hence, the vapor has no other choice

than to follow the direction of the groove searching for the lowest point of pressure: the exit. To achieve self-propulsion we need as a second ingredient a break of symmetry. To satisfy this point, we propose to design a herringbone pattern (see figure II.9 and II.8). A drop placed on the axis of the herringbone flees in the direction opposite to the arrows of the pattern. As seen in figure II.8a where the snapshots are regularly spaced, the liquid first accelerates (with an acceleration $a \approx 10$ cm/s^2) before reaching its terminal velocity V (10 cm/s in this example) after a few centimeters. Unlike any other existing self-propelling texture, we can predict in advance the direction of the rectified flow, as it has to go from the highest point of pressure (right below the center of the drop, hence at the tip of a chevron), towards the lowest pressure point: the exit.

Experimental set-up

In order to make sure we are in the film boiling regime, we used acetone. At its boiling temperature (56 °C), it has a surface tension $\gamma = 19$ mN/m and a density $\rho_l = 751$ kg/m^3, which gives a capillary length ℓ_c equal to 1.6 mm. Its latent heat of evaporation ($\mathcal{L} \approx 520$ kJ/kg), almost four times lower than the one of the water, leads to a lower Leidenfrost temperature.

We use blocks of brass (length 100 mm, width 30 mm), and machine them with a digital Arix CNC-milling machine to create the herringbone pattern. Crenellations are parallelepipedic cavities of depth $H = 0.2$ mm and width $W = 1$ mm, separated by walls of thickness $\lambda = 0.2$ mm (figure II.8b). In order to automate the process and to increase precision, we developed a numerical code (written in G-Code language, detailed in A) resulting in a final tolerance on these values of 10 μm. A profilometer view of the surface shown in figure II.9 allows us to see the sub-millimetric herringbone texture. A much smaller roughness is also generated by the milling process, as can be seen on the bottom of each channel where circular patterns appear as a result of the rotating reamer. The angle 2α of the herringbone can be varied from 0° to 180°, where these extreme values define grooves parallel or perpendicular to the symmetry axis of the sample.

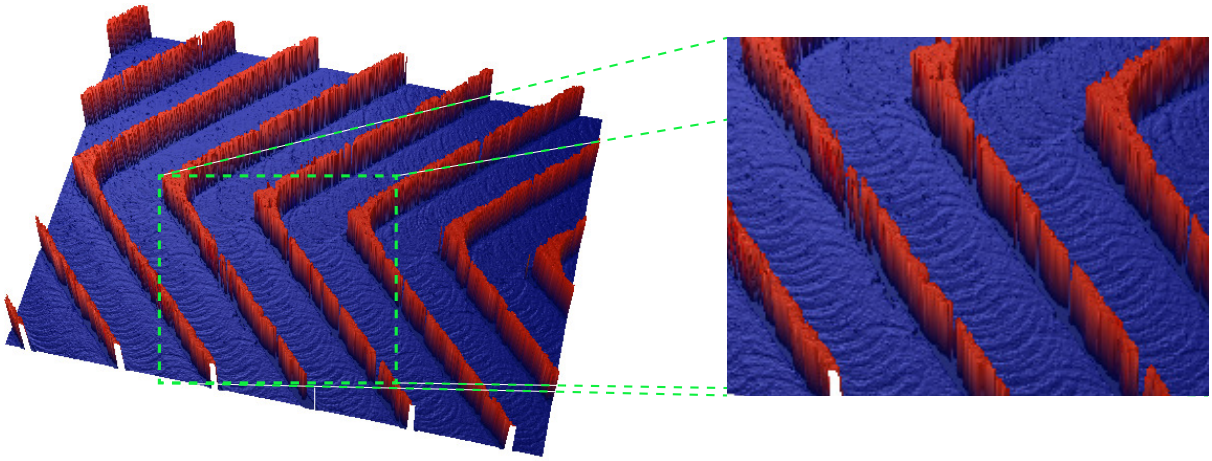

Figure II.9 – 3D Profilometer view of the herringbone surface texture. Walls' fibrous aspect is artificially due to profilometer resolution and does not depict reality. Selection zoom: a much smaller circular roughness generated by the milling process can be seen at the bottom of the grooves.

2 Force of propulsion

The herringbone texture was proved to generate self-propulsion by geometrically forcing the escaping vapor flow. We now experimentally and theoretically focus on the nature of the propelling force and on its dependency towards substrate geometry. After addressing the question of force optimization, we study questions regarding central stability and present some theoretical refinements.

2.1 Experimental measurements

Propelling force F can be deduced from the acceleration a ($F = ma$). The measurement is improved by throwing drops from a heated gutter (to make sure they stay in the axis of symmetry of the texture) at a velocity $V_0 \approx 5$ cm/s in the direction opposite to the propulsion: the liquid slows down, stops, and accelerates backwards. The trajectory $X(t)$ is parabolic ($X(t) = V_0 t - at^2/2$), from which the acceleration a and the propelling force $F = ma$ are extracted (see figure II.10). Drops typically lose 1 mg/s by evaporation, so that their mass m (of order 100 mg) can be considered as constant during experiments performed in approximately 1s.

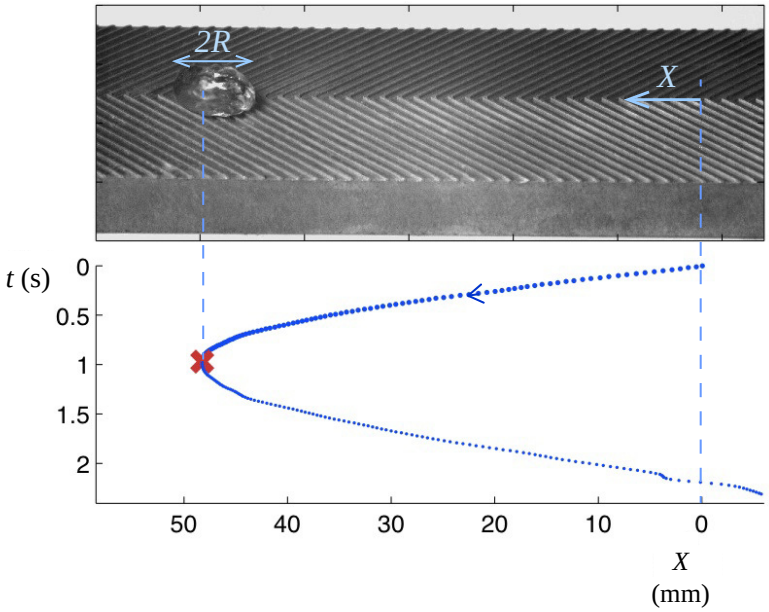

Figure II.10 – Trajectory of a drop or radius $R = 6$ mm on a herringbone surface. The drop is thrown from the right in the opposite direction of the propulsion. The liquid then slows down, stops (the top picture corresponds to this turnaround moment, marked in the bottom trajectory by a red cross), and accelerates backwards. The trajectory $X(t)$ is parabolic ($X(t) = V_0 t - at^2/2$), from which the acceleration a and the propelling force $F = ma$ are extracted.

Complementary experiments were made to measure the propelling force with a different method based on the deflexion of a fiber. We trap by capillarity a drop at the end of a wetting vertical fiber, as shown in figure II.11. We measure the fiber deflexion from its equilibrium position, as the propelling force acts on it. In thin beam theory, deflexion is proportional to the applied force, with a proportionality constant of Ed^4/L^3 where E is the Young's modulus of the fiber, d its diameter, and L its length. We can therefore deduce the force of propulsion of the drop from the fiber deflexion.

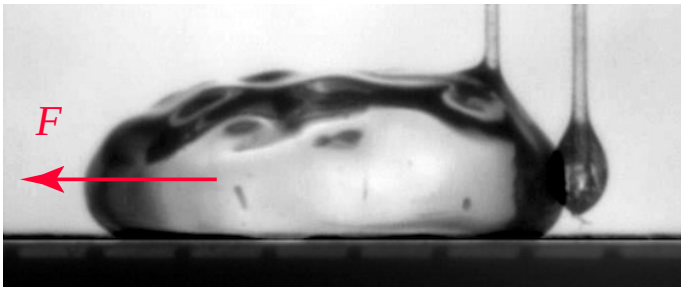

Figure II.11 – Superposition of two frames of a movie looking from the side at a wetting fiber deflected by a drop on a hot herringbone. The left fiber is in the drop of radius $R \approx 4$ mm. The right one shows the fiber at rest, after the drop has nearly evaporated. The deflexion is proportional to the propelling force.

As a great advantage of this method, we can measure the force as a function of the equatorial radius through a single experiment by taking a side movie and taking advantage of the evaporation. Measurements give results similar to the ones obtained by the first method. However, several drawbacks made us choose the first method (fitting parabola on trajectory): (i) drops vibrations generate big experimental errors; (ii) the drop stuck by capillarity to the fiber is deformed - biassing the measure. (iii) for big drops, this sticking force is not strong enough to overcome the propelling force, hence preventing the measure in the puddle regime.

We can repeat the measurement for various drop radii. We show in figure II.12a how the measured force varies with the drop's equatorial radius R. The minimum radius corresponds to drops slightly larger than the millimeter-size channel width W, a condition for achieving self-propulsion (otherwise, the drop being smaller than a groove, would fall inside). Hence, the drop radii are around or above the capillary length ℓ_c, which simplifies the liquid geometry: as seen in figures II.8a and II.10, drops are puddles of radius R and height $2\ell_c$, the thickness of puddles in a non-wetting situation (as seen in Chapter I section 2.1). It is observed in figure II.12a that the larger the drop, the stronger the force. The force typically is 5-10 μN, only a few percents of the drops' weight, yet large enough to generate velocities of a few cm/s owing to ultra-low adhesion and friction of the liquid. The force is also a function of the angle α of the herringbone. It is larger

around the "median" angle $\alpha = 45°$, which suggests that the pattern can be optimized in term of propelling force. The variation of $F(\alpha)$ is shown in figure II.12b for two drop radii, confirming the existence of a well-marked optimal angle around 45°.

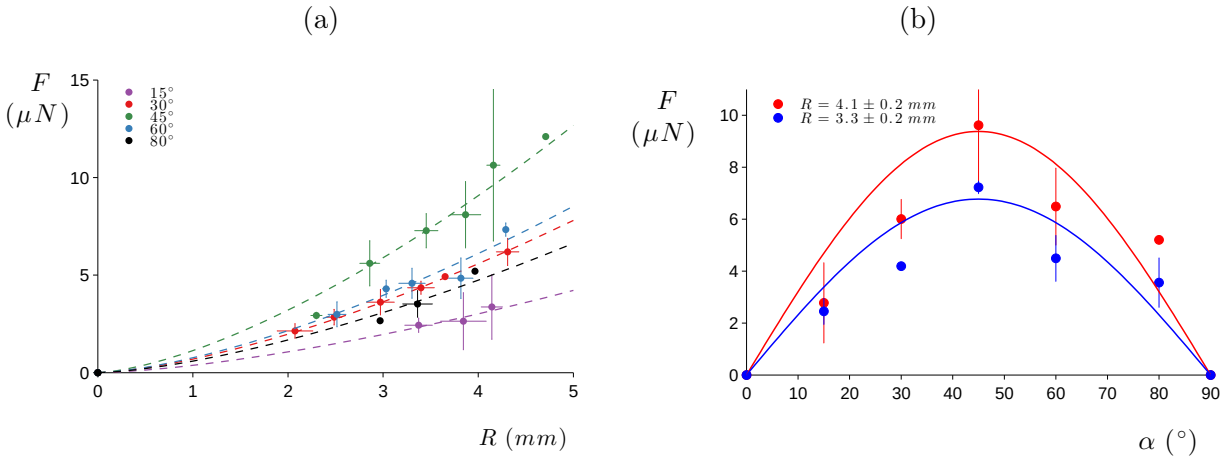

Figure II.12 – Force F propelling acetone on hot herringbones. (a) F as a function of the drop radius R. Each point is an average on 3-5 experiments, and the colors correspond to various pattern angles 2α (with $\alpha = 15°$, 30°, 45°, 60° and 80°). The channels width and depth are $W = 1$ mm and $H = 0.2$ mm, and the wall thickness between channels is $\lambda = 0.2$ mm. Dotted lines show behaviors in $R^{3/2}$, as suggested by equation II.10. (b) F as a function of the pattern angle α, for two drop volumes. The fits show equation II.10 with a numerical coefficient of 0.8 and for the radii $R = 4.1$ mm (red line) and $R = 3.1$ mm (blue line).

2.2 Analytical calculation

We now discuss these different findings, in order to understand the characteristics of drop motion on these patterns. We first focus on a single channel of length D_i (figure II.13 and II.8b) and denote the mean horizontal velocity of the vapor flow as U, and the average thickness of the vapor as h ($H - \epsilon < h < H$), as sketched in figure II.13.

On the one hand, vapor is injected at a velocity c (typically a few cm/s) from the top interface. Assuming c independent of the position x along the channel, mass conservation can be written:

$$(hU)_{x+dx} - (hU)_x = cdx \tag{II.5}$$

On the other hand, the energy balance writes per unit time and per unit area:

$$\rho c\mathcal{L} = \frac{\kappa \Delta T}{h} \tag{II.6}$$

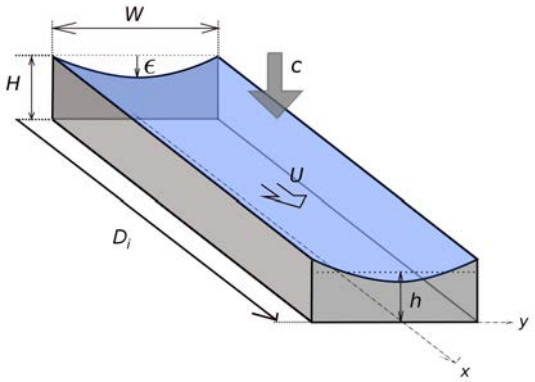

Figure II.13 – Geometry of a channel of vapor (in grey) bounded by a curved liquid/vapor interface (in blue). The vapor flows at an average velocity U, while vapor is injected at a velocity c from the top interface.

where we denote the density and thermal conductivity of the vapor as ρ and κ, the latent heat of evaporation as $\mathcal{L}$, and the difference between the substrate temperature T and liquid boiling point as ΔT. Putting together equations II.5 and II.6 yields the variation of the vapor velocity along the channel, taking the axis of symmetry of the herringbone pattern as the origin in x of the channel:

$$U = \frac{\kappa \Delta T}{\rho \mathcal{L} h^2} x \tag{II.7}$$

We expect a driving force per channel $F_i \approx \int\int \frac{6\eta U}{h} dxdy$, where the numerical coefficient corresponds to a Poiseuille flow between two solid plates. The levitating liquid has a viscosity 50 times larger than the vapor one η, justifying that we treat it as a solid for the corresponding boundary condition. Hence we get, for a channel of length D_i:

$$F_i \approx \frac{3\eta\kappa\Delta T}{\rho \mathcal{L} h^3} W D_i^2 \tag{II.8}$$

The force F_i appears to be sensitive to the design of the textured solid, via the parameters W and D_i. The total force F acting on a drop is obtained by counting the number $N(\alpha)$ of active channels below the liquid. As sketched in figure II.8b, typically 3 channels (hence, 6 half-channels, by symmetry) contribute to the motion. More generally, we can write for thin walls ($\lambda << W$): $\mathrm{N}(\alpha) \approx 4R\sin\alpha/W$. At small opening angles ($\alpha \to 0$), $N(\alpha)$ vanishes. The number of contributing channels vanishes as a consequence of the fact that we have to exclude channels open at both sides: vapor flowing on both ways produces a null total viscous force (see in figure II.8b the most left channels, or in figure II.15a the top channels). If taking the drop radius R as an average distance D_i, we get,

after projecting the different contributions on the central axis:

$$F \approx \frac{6\eta\kappa\Delta T}{\rho\mathcal{L}h^3} R^3 \sin 2\alpha \tag{II.9}$$

Until now we considered h as a constant quantity resulting from the sagging of a drop between two crenels. However, since the vapor thickness h compares to the channel depth H, the interaction with the bottom of the channel has to be taken into account. Although in our experiments we vary R on a little range (due to experimental limitations), we generally expect vapor thickness in a channel to vary with R - as observed and shown for a Leidenfrost drop on a flat solid. The relationship between h and H arises from a balance between escaping and incoming flux of vapor due to drop pressure and evaporation, respectively [11]. This leads for the geometry of channels to the relationship (see chapter I, section 2.2): $h \approx (bR)^{1/2}$, where b is a length scale defined by $b = \sqrt{\frac{3\eta\kappa\Delta T}{\rho\mathcal{L}\rho_l g\ell_c}}$. The same argument could be applied in a single groove leading to a final driving force:

$$F \approx 2\rho_l g\ell_c \, R^{3/2} b^{1/2} \, \sin 2\alpha \tag{II.10}$$

This expression is exactly the same as the very simple one $F \propto \Delta P R h$ discussed at the beginning of this section (equation II.3), where $\Delta P \sim \rho_l g\ell_c$ is the hydrostatic pressure of the drop due to its weight and $h \sim (bR)^{1/2}$ is the vapor thickness on a flat surface.

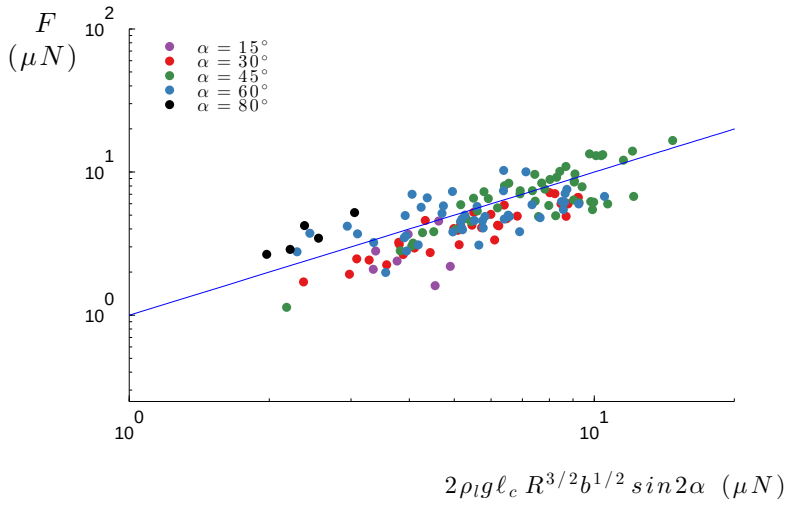

Figure II.14 – Force as a function of the theoretical expression found in equation II.10. All previous experiments are represented: radius R ranging from 2 mm to 4 mm, and opening angle $\alpha \in [15°, 30°, 45°, 60°, 80°]$. Solid line shows equation $y = x$ in log-log scale.

We show in figure II.14 the force F as a function of the theoretical expression found

in equation II.10 and see how all our data collapse on a single curve. Indeed, equation II.10 captures the different observations, and gives the correct order of magnitude of the force. Typical values for the parameters are: $\kappa \approx 13$ mW/m/K, $\eta \approx 2\,10^{-5}$ Pa.s, $\mathcal{L} \approx 520$ kJ/kg and $\rho \approx 1.8$ kg/m^3, which yields $b \approx 3$ µm and thus $F \approx 10$ μN for a drop of $R \approx 3$ mm, as measured. In addition, the force strongly increases with the drop radius, as observed in figure II.12a where the scaling law in $R^{3/2}$ (dotted lines) is found to describe the data. The small variation of the parameter R does not allow us to test quantitatively the corresponding scaling law. It is simpler (and of practical interest, since it indicates which herringbone generates the highest propulsion) to look at the variation of F as a function of α, and equation II.9 predicts a maximum for $\alpha = 45°$, as indeed observed in figure II.12b.

2.3 Further considerations

Discrete to continuous calculation

Inspired by this work, a collaboration was held with the university of Trento (Italy) in the team of Nicola Pugno [89]. To obtain the total resulting force from the contribution of each channel, they integrated the viscous stress directly on the contact area rather than on each channel. In this continuous method, the channels appear only in an indirect way: they determine the direction of the flow of vapor. Figure II.15a shows a comparison between the two methods of integration. In the channel-by-channel method, the surface of integration is approximated by rectangles of width W, whereas, a perfect half-disk is considered in the continuous method. A graphic comparison of the driving force calculated with the two methods as a function of half the angle α is given in figure II.15b.

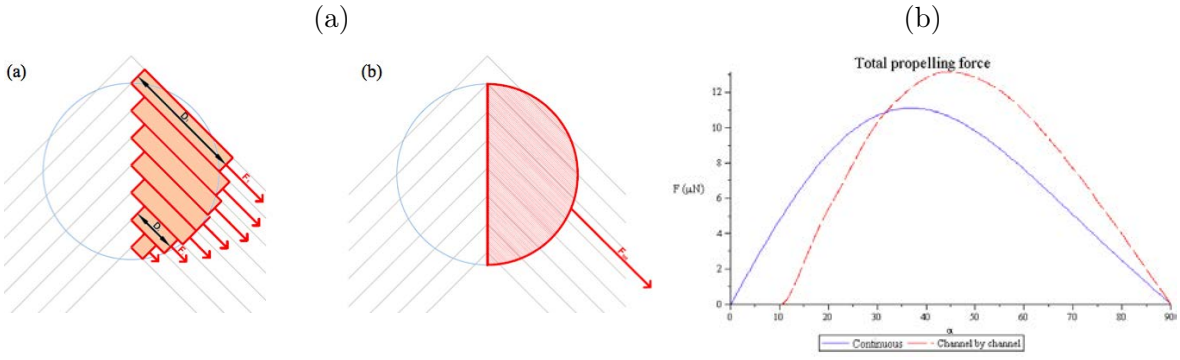

Figure II.15 – (a) Graphical representation of two methods of calculation of the driving force: channel by channel method and continuous method. (b) Force propelling a drop of radius $R = 3.3$ mm according to these two methods of calculation (Discrete in red, Continuous in blue). Figure from [89].

The difference between the results obtained by the two methods is visible; in particular, the position of the maximum is slightly shifted. However, the general characteristics of the curve (global shape and order of magnitude) are not modified.

Inspired by this continuous method we have shown a complex analytical exact solution that can be obtained by calculating the integral of viscous strain over the contact area in the frame of the corresponding grooves direction (see B for detailed calculation). Again, we find that the general characteristic of the curve are preserved.

Channel width, crenel depth and wall thickness

The discussion in Chapter I 2.4 on the deformation of a drop sitting in a crenelated surface helps us set to the optimal depth H for the channels. We saw that walls of width W must be below the critical width $W_c = 2(\sqrt{2}-1)\ell_c$ (I.31) in order to sustain the drop's weight by the top of the walls. We experimentally set $W = 1$ mm near this critical value (1.3 mm for acetone), imposing a corresponding average sagging $\epsilon \approx 140$ µm.

Once we have fixed W, we consequently choose the "right" depth channel. If we have $H >> \epsilon$, the vapor is not efficiently confined. Conversely, at small depth H, the liquid levitates far above the textures, so that the vapor flow rectification becomes negligible. Hence H must be slightly larger than ϵ, that is, 140 µm for $W = 1$ mm. In this study, H is kept constant, equal to 200 µm - larger than the typical vapor thickness $h \approx 100$ µm for a drop on a flat solid.

As the surface fraction of walls does not contribute to the propelling force, we try to get them as thin as possible. However, as we also want to avoid nucleation of boiling (enhanced by very thin walls), we experimentally set $\lambda = 0.2$ mm.

Central stability

Up to now we focused on the contribution of the viscous force to the propelling direction. Indeed, in the perpendicular direction, the projection of the force from each side of the drop compensate by symmetry. However, if the drop slightly deviates from this central position, there is no restoring force that can stabilize the drop along the axis of symmetry.

The discussion on drop deformation into a crenel suggests a way to guide the liquid. A deeper central straight channel of width $W \approx W_c$ can be etched along the symmetry axis of the herringbone. As a consequence, the drop is gravitationally trapped as sketched in figure II.16, without significantly affecting the propelling force F . We will often use this trick, in particular when curved sections appear, which could destabilize the liquid by centrifugation.

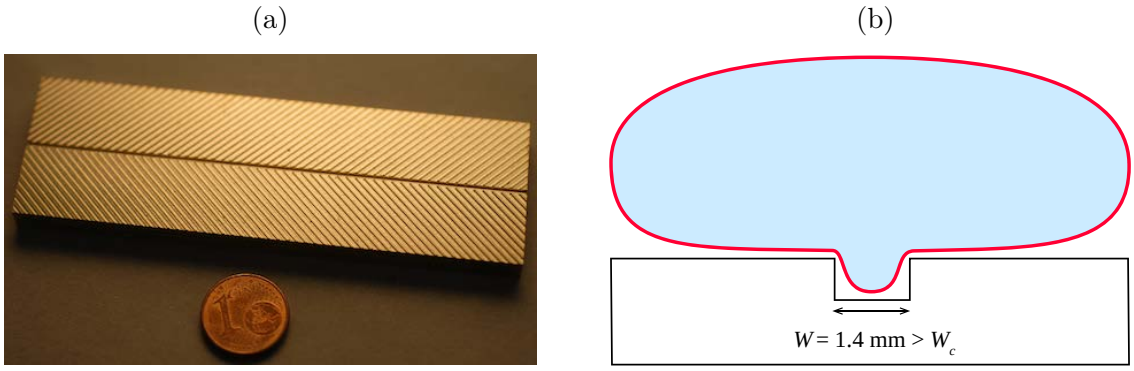

Figure II.16 – (a) Side view of a herringbone texture with a central groove of depth 0.8 mm wider than the critical width $W_c \approx 1.3$ mm. A drop completely sags in this central groove, and gets gravitationally trapped along the axis of symmetry. (b) Sketch showing the drop trapped in the central groove.

Reynolds number

Our model was based on small Reynolds number approximation and lubrication theory. In order to discuss the validity of this assumption, we replace the expressions found for the horizontal speed U (equation II.7) in the Reynolds number expression $Re = \frac{\rho_l U h^2}{\eta R}$ (discussed in chapter I), which yields:

$$Re = \frac{\kappa \Delta T}{\eta \mathcal{L}} \tag{II.11}$$

For a given liquid, the Reynolds number only depends on the differential temperature ΔT between substrate and liquid boiling point. Using typical experimental values, we obtain Reynolds numbers below 0.4, which confirms that viscous effects dominate in this vapor escaping problem.

Boundary conditions

A last point can be made concerning the boundary conditions used in each channel for our Poiseuille problem. As previously stated, we assume the liquid as behaving as a solid wall (because its density is 1000 times greater than the vapor one). The escaping vapor is trapped in a rectangular channel with solid walls. Experimentally, we measure the force by fitting the trajectory near the returning point of the drop: hence verifying the no speed condition (and by the way also avoiding any added inertial friction). However, as the drop accelerates, a moving upper wall solid condition should be set equal to the drops speed. Typical ejection speed U being 1 m/s and drops speed being ten times smaller, this will result in a slight reduction of the viscous shear at the drops' interface, hence lowering the propelling force.

3 Friction on grooved topography

As proposed by Dupeux et al., friction on large textures arise from the soft shocks of the liquid bumps on the crenellation sides [42, 40]. This scenario produces an inertial special friction $F = \beta\rho_l R^2 V^2$, denoting ρ_l as the liquid density and β a numerical coefficient explicitly characterized for normal shocks [42]. Using inclined plates with straight crenels, we checked that the friction is indeed quadratic in velocity, and deduced from measurements the friction coefficients $\beta_{\parallel} \approx 0.021 \pm 0.003$ and $\beta_{\perp} \approx 0.109 \pm 0.015$ for drops moving parallel or perpendicular to crenels. We logically have $\beta_{\parallel} << \beta_{\perp}$. The case of intermediate angles α between the grooves and the trajectory, is then experimentally and analytically explored. We finally study lateral deviation of free trajectories for drops either with initial speed moving on a horizontal substrate or initially at rest and running down inclines.

3.1 Straight trajectories

Perpendicular and parallel friction

In order to study the special friction on textured materials, we used a brass surface of 200×200 mm^2. We machined parallel crenels, with the same geometrical characteristics as for the herringbones used in our study: grooves of depth $H = 0.2$ mm and width $W = 1$ mm, separated by walls of thickness $\lambda = 0.2$ mm. The plates were heated ($T = 400$ °C) and tilted by an angle θ to the horizontal (see figure II.17), so that the levitating liquid is subjected to gravity. Acetone drops (of fixed volume $\Omega \approx 200$ μL corresponding to $R \approx 5$ mm, and density ρ_l) accelerate and reach their terminal velocity after a few cm, when the horizontal projection of the gravity $\rho_l \Omega g \sin\theta$ is balanced by friction.

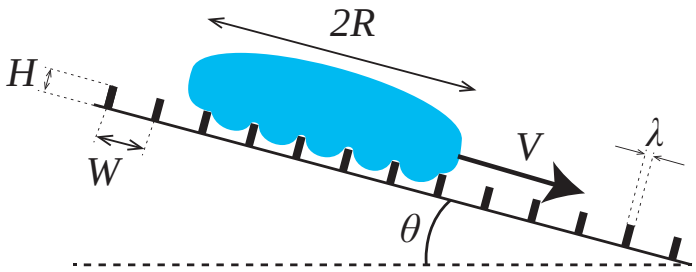

Figure II.17 – Drop of acetone of volume $\Omega \approx 200$ μL and density ρ_l descending a crenelated material inclined by an angle θ so that the gravitational force along the slope is $\rho_l \Omega g \sin\theta$. The corresponding terminal velocity is approximately 10 cm/s, comparable to the terminal velocity reached on herringbones.

The plate is first displayed with grooves perpendicular to the trajectory (figure II.17). We repeat the experiment varying the tilt θ from 1° to 12°, hence changing the drop velocity and consequently the friction force. By recording the motion, we access the terminal velocity, and plot in figure II.18a the measured friction as a function of the measured terminal velocity. The solid line represents the best parabolic fit in a log-log scale. If we consider an inertial friction $F = \beta \rho_l R^2 V^2$, as discussed above, we can deduce the friction coefficient for grooves perpendicular to the trajectory. We find: $\beta_\perp \approx 0.109 \pm 0.015$. This value is in excellent agreement with the one measured and discussed by Dupeux et al. [42].

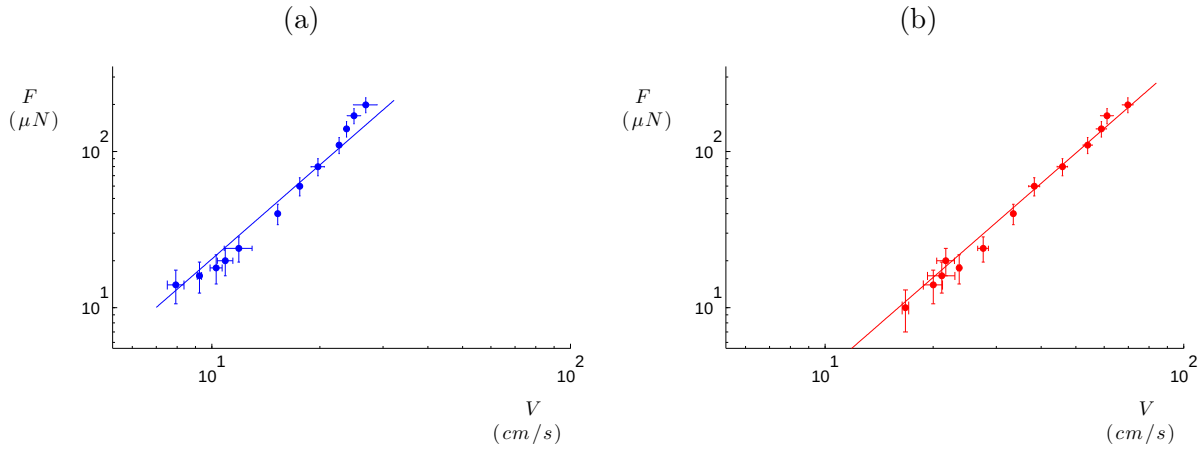

Figure II.18 – (a) Friction force as a function of the terminal velocity for grooves perpendicular to the trajectory. b) Friction force as a function of the terminal velocity for grooves parallel to trajectory. We notice that the "perpendicular friction" is an order of magnitude higher than the "parallel one". Both behaviors can be fitted by quadratic laws in velocity (inertial friction).

We can similarly measure the friction force as a function of the terminal velocity for grooves parallel to the motion (figure II.18b). Again, friction is found to be well described by a law quadratic in velocity, the signature of an inertial friction. The corresponding friction coefficient $\beta_\parallel$ can be deduced from the experiments. We find $\beta_\parallel \approx 0.021 \pm 0.003$, a value significantly smaller than $\beta_\perp$.

Intermediate angles

We repeat this experiment choosing an intermediate angle between the main groove direction and the down slope direction (denoted as α and as shown in figure II.19). Friction is logically minimized when the motion is parallel to the grooves, so that a drop will try to align with the grooves. To avoid this lateral deviation and have a straight trajectory (aligned with the slope direction), we confine the drop between two walls that compensate the projection of the friction perpendicular to the gravitational force (and represented as

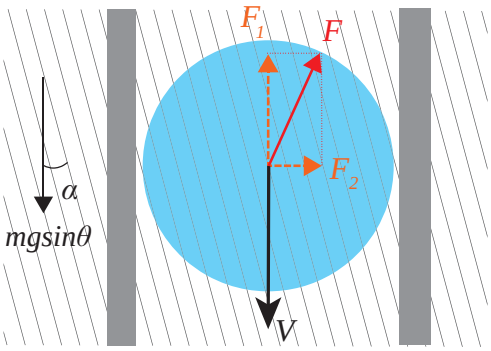

Figure II.19 – (a) Sketch of drop running down a titled crenelated surface. The angle between grooves and down slope direction is noted α. Side walls prevents the drop from laterally deviating by compensating the friction component F_2.

F_2 in figure II.19). Friction component aligned with the slope direction will be denoted as F_1 (figure II.19). We show in figure II.20a this force F_1 as a function of the drop velocity for different intermediate angles α. Each data point is an average on three experiments in order to reduce error bars. For high speeds, we can see a small systematic overestimation deviating from the parabolic law probably due to the fact that the plate is not long enough (200 mm) for the drop to fully reach its terminal speed. We show in figure II.20b the corresponding coefficient β_α assuming parabolic friction.

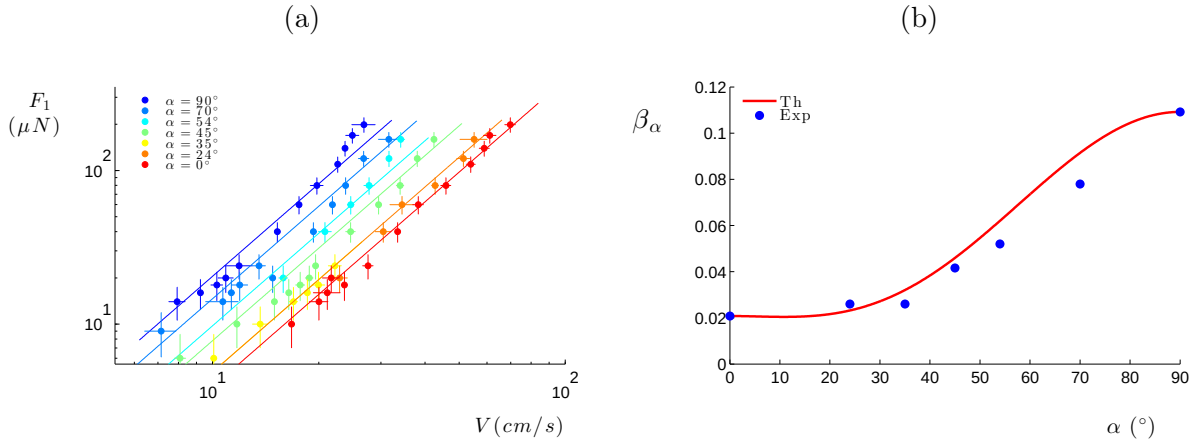

Figure II.20 – (a) Friction F_1 in the gravity direction as a function of speed for different intermediate angles α. From left to right curve, $\alpha \in [0°, 25°, 35°, 45°, 55°, 70°, 90°]$. Solid lines represent best parabolic fits. Each point is an average on three experiments. (b) Friction coefficient β_α corresponding to each angle α. Each point is deduced from data on left figure (a), assuming $F_1 = \beta_\alpha \rho_l R^2 V^2$. The red solid line shows equation II.13.

As expected, it is bound between the two previous scenarios corresponding to $\alpha = 0°$ (right curve in red in figure II.20a) and $\alpha = 90°$ (left curve in blue in figure II.20a).

Back to the herringbone

The herringbone geometry can be seen as a solution to suppress any friction "perpendicular to the motion" without modifying the friction along the central axis. We show in figure II.21 a comparison between this two scenarios.

We first focus on the friction along the axis aligned with speed V. Both geometries generate exactly the same friction. Indeed, in the herringbone case, if we "mentally" flip upside down the left half-side of the drop (shaded blue in figure II.21b), we end up with the same configuration than sketched in figure II.21a.

Then, if we now focus on the axis perpendicular to the motion, we observe that friction does not sum up for the herringbone geometry (such as in the previous case sketched in figure II.21a) but compensate by symmetry. As a direct consequence we do not need anymore to put the lateral wall to compensate F_2 and prevent deviation.

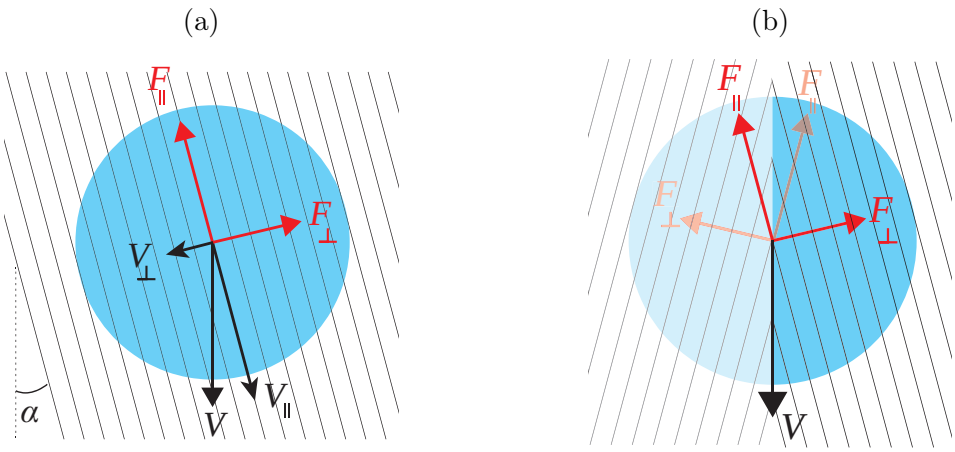

Figure II.21 – Comparison between parallel grooves (left) and herringbone texture (right). (a) Friction can be decomposed in its components parallel and perpendicular to the crenels. Friction aligned with speed writes $F_1 = F_\perp \sin\alpha + F_\parallel \cos\alpha$. Drop velocity along these directions is $V_\perp = V \sin\alpha$ and $V_\parallel = V \cos\alpha$. (b) If we flip upside down left shaded part, we see that friction F_1 along the central axis of a herringbone is the same as previously shown in figure (a). In the direction perpendicular to the motion, friction projections compensate by symmetry.

To be more quantitative we decompose the friction in its components parallel and perpendicular to the grooves, (as defined in figure II.21): $F = F_\perp \sin\alpha + F_\parallel \cos\alpha$. Since the drop velocity along these directions is $V \sin\alpha$ and $V \cos\alpha$, we end up with a strongly non-linear expression for the friction:

$$F = \rho_l R^2 V^2 (\beta_\perp \sin^3\alpha + \beta_\parallel \cos^3\alpha) \tag{II.12}$$

from which we deduce the friction coefficient β_α corresponding to each angle α:

$$\beta_\alpha = \beta_\perp \sin^3\alpha + \beta_\parallel \cos^3\alpha \tag{II.13}$$

We draw equation II.13 in figure II.20b with a red solid line, and find it is in fair agreement with experiments (blue points), provided we set $\beta_\perp$ and $\beta_\parallel$ to the experimental values obtained with $\alpha = 90°$ and $\alpha = 0°$, respectively.

3.2 Free trajectories

As a logical continuation, we wonder what happens if we do not force anymore straight trajectories (with a wall, or with a central symmetry with the herringbone). Two cases can be studied regarding the method used to set a motion. Either we use gravity with a tilted plate (as previously done), or we provide an initial speed to the drop by launching it from a tilted gutter into a perfectly horizontal plate. We explore these two possibilities, starting by the second one for the sake of simplicity.

Deviation on an horizontal plate

A 5 mm radius drop is launched from a hot straight gutter. By modifying the slope of the ramp we can select various initial speeds: $V_0 \in$ [18,24,36,42] cm/s. The angle between incoming direction and grooves axis is denoted as α, as defined in figure II.22b: for $\alpha = 0°$, ramp and grooves are aligned, while for $\alpha = 90°$, ramp and grooves are perpendicular. Chronophotography showing a typical drop trajectory can be seen in figure II.22b for $\alpha = 60°$.

The drop deviation can be modeled by adapting the argument proposed in the herringbone case. We apply Newton's second law to the drop in the frame defined by the grooves ($\vec{e_\parallel}$ being the direction along the crenels, $\vec{e_\perp}$ its perpendicular). It writes:

$$\text{along } \vec{e_\perp}: \qquad m\ddot{x} = -\beta_\perp \dot{x}^2 \tag{II.14a}$$

$$\text{along } \vec{e_\parallel}: \qquad m\ddot{y} = -\beta_\parallel \dot{y}^2 \tag{II.14b}$$

These non linear second-order differential equations can be solved using as initial speed $V_0 \cos\alpha$ and $V_0 \sin\alpha$ in the $\vec{e_\perp}$ and $\vec{e_\parallel}$ directions, respectively. Integration of equations II.14a and II.14b leads to the expression of speed:

$$\text{along } \vec{e_\perp} : \qquad \dot{x} = \frac{1}{\frac{\beta_\perp}{m}t + \frac{1}{V_0 \sin\alpha}} \tag{II.15a}$$

$$\text{along } \vec{e_\parallel} : \qquad \dot{y} = \frac{1}{\frac{\beta_\parallel}{m}t + \frac{1}{V_0 \cos\alpha}} \tag{II.15b}$$

Initial position chosen as the origin finally leads to the expression of position as a function of time[1]:

$$\text{along } \vec{e_\perp} : \qquad x = \frac{m}{\beta_\perp} \ln(1 + V_0 \sin\alpha \frac{\beta_\perp}{m} t) \tag{II.16a}$$

$$\text{along } \vec{e_\parallel} : \qquad y = \frac{m}{\beta_\parallel} \ln(1 + V_0 \cos\alpha \frac{\beta_\parallel}{m} t) \tag{II.16b}$$

Combining equations II.16a and II.16b we can get rid of speed V_0, resulting in the following trajectory equation:

$$y = \frac{m}{\beta_\parallel} \ln(1 + \frac{\beta_\parallel}{\beta_\perp \tan\alpha}(e^{\frac{\beta_\perp}{m}x} - 1)) \tag{II.17}$$

Equation II.17 is independent of initial speed V_0, although it still depends on the incoming orientation angle α. This means that initial speed V_0 will only dictate at which speed we scan the trajectory.

For small x, this equation greatly simplifies and can be approached by equation $y \approx x/\tan\alpha$, expected as we know that the drop enters the grooved plate with an incoming angle α. For long runs, where $x \to \infty$, trajectory equation can be approached by equation $y \approx \frac{\beta_\perp}{\beta_\parallel} x/\tan\alpha$. Since $\beta_\perp > \beta_\parallel$, this means that in the end, the drop tends to follow the grooves. We can reason also in terms of speed: at long times ($t \to \infty$), the ratio of terminal speeds along each direction $\dot{x}_\infty/\dot{y}_\infty$ is equal to the ratio of friction coefficients $\beta_\parallel/\beta_\perp$. Again, since $\beta_\perp > \beta_\parallel$, this means the drop speed is mainly aligned along $\vec{e_\parallel}$, that is, along the grooves.

Equation II.17 gives the trajectory in the frame of study $\vec{e_\perp}$, $\vec{e_\parallel}$ associated to the grooves. However, if we want to have the trajectory in the frame $\vec{e_x}$, $\vec{e_y}$ (sketched in figure II.22b) aligned with the incoming speed direction, we need to re-express $\vec{e_\perp}$ as $\vec{e_\perp} = -\cos\alpha\,\vec{e_x} + \sin\alpha\,\vec{e_y}$ and $\vec{e_\parallel}$ as $\vec{e_\parallel} = \cos\alpha\,\vec{e_x} + \sin\alpha\,\vec{e_y}$, resulting in the following change of frame matrix:

[1]This simple model also allows to have the analytical expressions of friction in both axes, deduced from the speed solutions.

$$T(\alpha) = \begin{pmatrix} -\cos\alpha & \sin\alpha \\ \sin\alpha & \cos\alpha \end{pmatrix}$$

We show in figure II.22a in dashed lines the analytical trajectory solution in this new frame of study, in fair agreement with the set of experiments done at initial speed $V_0 = 42$ cm/s. Changing the slope of our launching ramp (hence varying initial speed V_0) should have no impact on the trajectory. However, we have noticed that for low initial speeds, at some point the drop eventually gets trapped by the textures, aligning with them instead of deviating. Indeed, as previously mentioned (Chapter I, section 2.4), the drop deforms into the crenels, lowering its potential energy. As a consequence, there will be a critical speed for which the drop will not be anymore able to overcome this trapping force, hence being forced to follow the grooves.

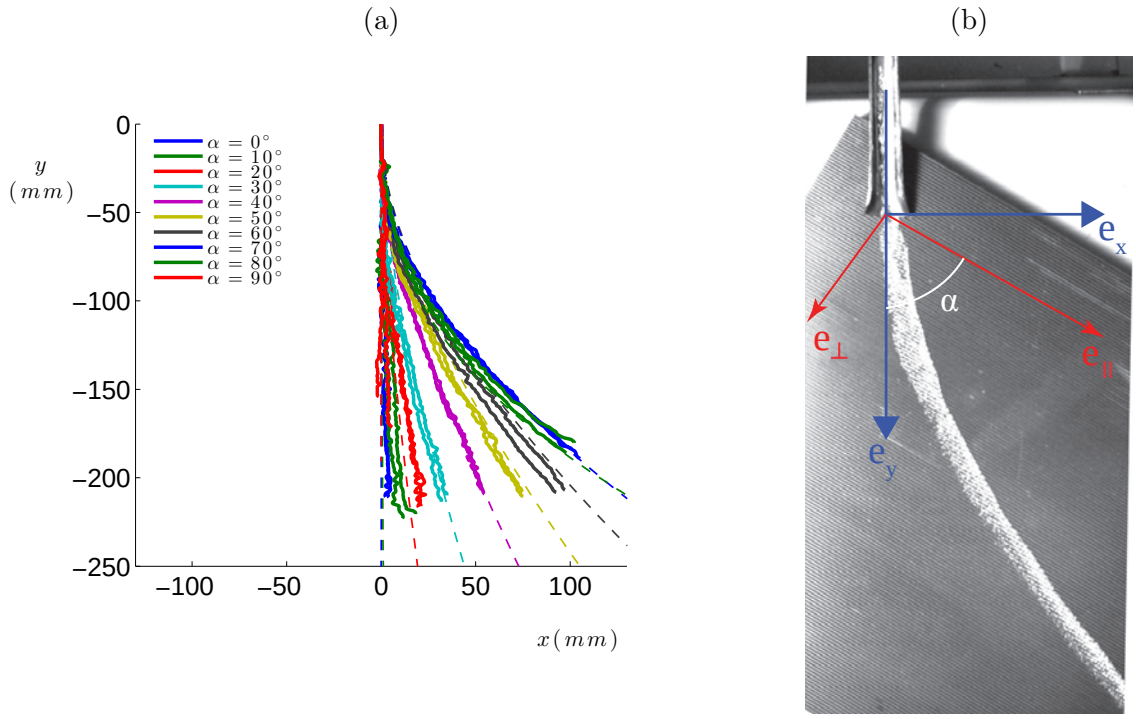

Figure II.22 – (a) Trajectory in the frame of reference $\vec{e_x}$, $\vec{e_y}$ of the gutter, for a 5 mm radius drop with initial speed $V_0 = 42$ cm/s on a horizontal crenelated plate. This plate has a square shape of dimensions 200×200 mm^2, (approximatively) corresponding to the size of the x- and y-axis. Incoming speed direction α ranges from 0° to 90° by steps of 10°. Experiments (in solid line) are in good agreement with model from equation II.17 (thin dashed line). (b) Drop launched from a tilted gutter enters a horizontal hot crenelated plate with an angle $\alpha = 60°$ (corresponding to black curve in left figure II.22a).

Deviation of gliding drops on crenels

We explore here the second method to observe moving liquid puddles: a drop running down the slope by gravity on a hot crenelated plate. As a consequence, we have to adapt previous governing equations II.14a and II.14b by adding a constant force $mg\sin\theta$. The new corresponding differential equations are now non-homogeneous and write:

$$\text{along } \vec{e_\perp}: \qquad m\ddot{x} = -\beta_\perp \dot{x}^2 + mg\sin\theta\sin\alpha \tag{II.18a}$$

$$\text{along } \vec{e_\parallel}: \qquad m\ddot{y} = -\beta_\parallel \dot{y}^2 + mg\sin\theta\cos\alpha \tag{II.18b}$$

The addition of the constant driving force implies that we are not anymore able to show an analytical solution.

Nevertheless, if we focus on the terminal regime (defined as having no acceleration $\ddot{x} = \ddot{y} = 0$), we get the following expression for the terminal speed in the frame of reference of the grooves:

$$\text{along } \vec{e_\perp}: \qquad \dot{x}_\infty = \sqrt{\frac{mg\sin\theta\sin\alpha}{\beta_\perp}} \tag{II.19a}$$

$$\text{along } \vec{e_\parallel}: \qquad \dot{y}_\infty = \sqrt{\frac{mg\sin\theta\cos\alpha}{\beta_\parallel}} \tag{II.19b}$$

Hence, the ratio of the terminal speed along each axis is:

$$\frac{\dot{x}_\infty}{\dot{y}_\infty} = \sqrt{\frac{\beta_\parallel}{\beta_\perp}\tan\alpha} \tag{II.20}$$

Equation II.20 (independent of $mg\sin\theta$) predicts an analogous behavior compared to what we have previously seen: since $\beta_\perp > \beta_\parallel$, once the drop reaches its terminal speed, there is almost no speed in the perpendicular direction $\vec{e_\perp}$ ($\dot{x}_\infty \to 0$) so that the drop moves mainly along the grooves. However, in opposition to the previous horizontal case (where we found $\dot{x}_\infty/\dot{y}_\infty = \beta_\parallel/\beta_\perp$), equation II.20 depends on the angle α. As a consequence, a special situation is found for α close to 90° (for which $\tan\alpha$ diverges, hence equivalent to $\dot{y}_\infty \to 0$) where drops can move perpendicular to the grooves.

In addition, equations II.18a and II.18b can also be numerically solved. We show in figure II.23b the numerical solution obtained for different orientation angles α. However, it is experimentally difficult to accurately set the initial position of the drop while generating it on a slope. As a consequence, arbitrary vertical shifting appears in experiments, making

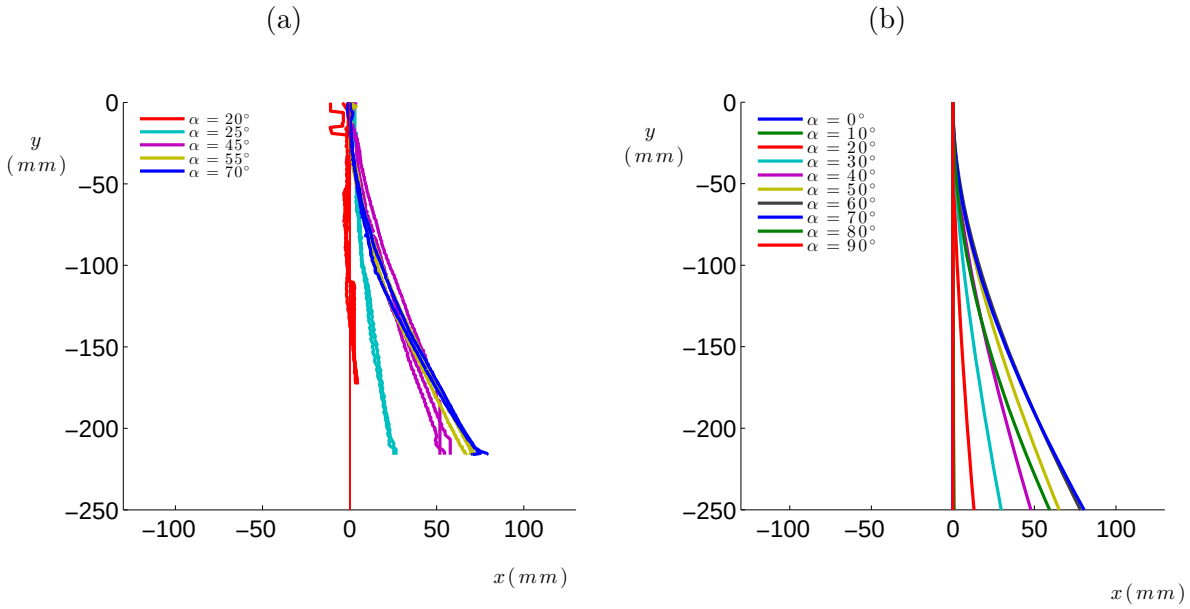

Figure II.23 – Trajectory in the frame of reference $\vec{e_x}$, $\vec{e_y}$ (associated to the direction of slope) for a 5 mm radius drop on a tilted crenelated plate. (a) Experimental trajectory: arbitrary vertical shifting is due to experimental limitations when forming the drop. (b) Numerical solution of differential equations II.18a and II.18b for a plate tilted by an angle θ: each color corresponds to a different incoming angle α ranging from 0° to 90° by steps of 10°.

it difficult to quantitatively compare numerical results with experiments. Anyhow, a fair qualitative agreement is observed in figure II.23 between experiments (left) and theory (right).

4 Terminal speed

Once propulsion and friction forces have been discussed, we have all ingredients to address the question of the terminal velocity. Before making an analytical model, we experimentally access this final speed, where friction force balances with the propelling one.

4.1 Experimental results

In order to see the drop accelerate and reach its terminal regime we need enough textured substrate length. Such long samples are difficult to manufacture keeping crenel depth precision below 10 µm. Typical length of our samples being 100 mm, we designed circuits consisting of two straight herringbones with a stabilizing channel at the center, joined by semicircular tracks bounded by lateral walls as sketched in figure II.24a. Drops hardly decelerate in the curved sections, so that the liquid quickly reaches its terminal velocity (around 10 cm/s), and keeps it for several rounds (figure II.24b), until evaporation makes its size comparable to the width W_c, which stops the motion.

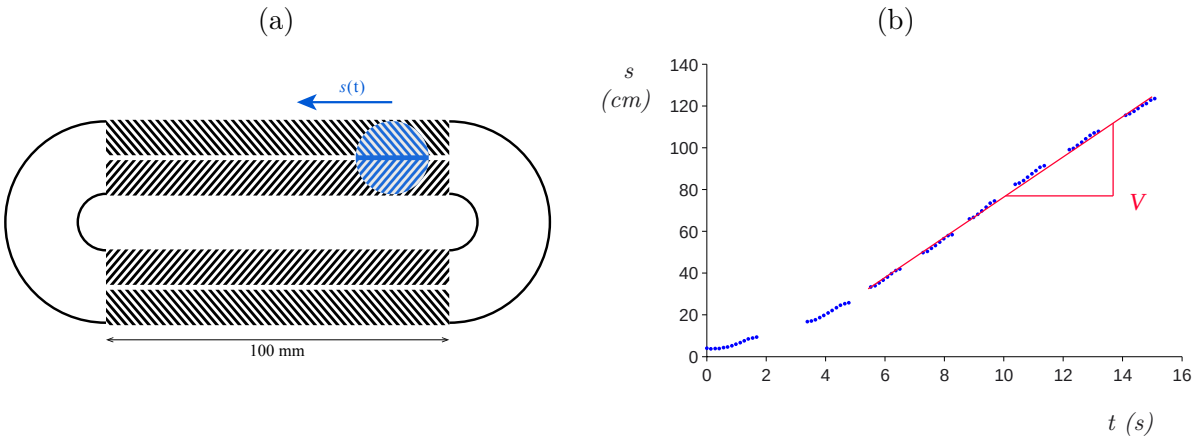

Figure II.24 – (a) Long races can be observed by displaying two herringbones in series (top view) connected by flat hemicircular paths, allowing us to determine the terminal velocity reached by the drop. The hemicircular lines are lateral walls that guide the liquid in this region. (b) Drop position along its race, as a function of time. Data are recorded on the patterned section of the device (blue points), which shows that the velocity V is reached after approximately one herringbone. Here we find $V \approx 10$ cm/s, for acetone drops of radius at mid-race $R = 3$ mm and for a herringbone angle $\alpha = 45°$.

The device shown in figure II.24a can be used to probe the optimum angle in term of terminal velocity V. This speed was measured for drops of radius $R = 3 \pm 1$ mm and was found to decrease by a factor 3 as α increases from 15° to 75°, as seen in figure II.25. Contrasting with $F(\alpha)$ (see figure II.12b), the function $V(\alpha)$ is strongly asymmetric, showing a maximum between 15° and 30°. This maximum is roughly equidistant between

45°, where we observe the maximum driving force (figure II.12b) and 0°, where the grooves are aligned with the motion, so that we expect a minimum friction (figure II.20b).

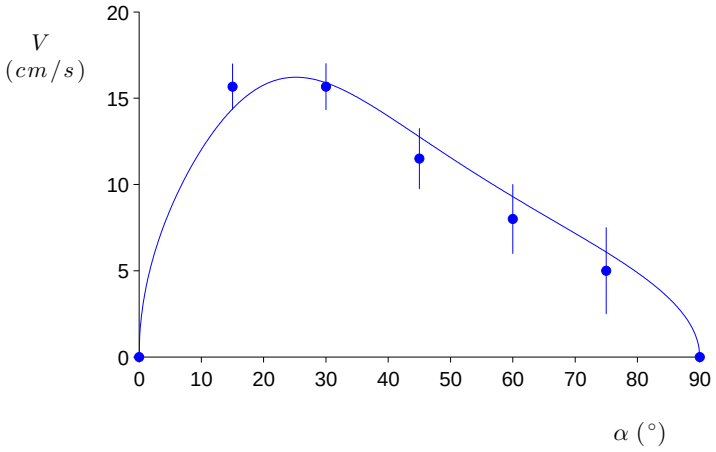

Figure II.25 – Drop terminal velocity on hot herringbones, as a function of the pattern angle. Drops are made of acetone, substrate temperature is 400°C, and the terminal velocity is measured on circuits consisting of successive herringbones (figure II.24a), allowing us to reach and measure the terminal velocity even if large. Each data point corresponds to an average done on a distance of about 1 m, and the fit shows equation II.21 with a coefficient of 0.8, drawn for $R = 3$ mm, the typical size of the drop at mid-race.

4.2 Analytical calculation and speed optimization

Balancing the propelling force (section 2, equation II.10) with the resisting force (section 3, equation II.12) yields the expected terminal velocity of drops:

$$V \approx (2g\ell_c)^{1/2}(\frac{b}{R})^{1/4}[\frac{\sin 2\alpha}{\beta_\perp \sin\alpha^3 + \beta_\parallel \cos\alpha^3}]^{1/2} \qquad \text{(II.21)}$$

Equation II.21 is drawn with a full line in figure II.25 for $R = 3$ mm with a coefficient of 0.8, as done in figure II.12b. It is found to agree well with the data, having in particular a maximum clearly displaced to small acute angles, as observed experimentally. The magnitude of the velocity also fits with the calculation.

Maximizing equation II.21 according to α implies that the optimum angle should be a function of the ratio $\beta_\parallel/\beta_\perp$. At small α, the function of α in equation II.21 becomes $2\alpha/(\beta_\perp\alpha^3+\beta_\parallel)$, whose maximum is $(\beta_\parallel/2\beta_\perp)^{1/3}$, that is in our geometry, $\alpha \approx 25°$ (within 2% of the value obtained by numerical integration), in good agreement with the observations.

5 A basic unit of a wider picture

We just discussed how we can loop two herringbones through curved sections in order to achieve a Leidenfrost racing track. Further on, we propose to see herringbones as elementary units of a larger device, which opens new applications and perspectives.

5.1 The drop trap

Two herringbones can be displayed with opposite polarization as sketched in figure II.26a. As a consequence, drops thrown on this device oscillate, as it can be observed in figure II.26b where drop position along the drops' race is plotted as a function of time. The oscillations are damped by the action of the herringbones, so that the levitating liquid eventually gets immobilized at the center of the device: opposite herringbones constitute efficient traps for these elusive drops.

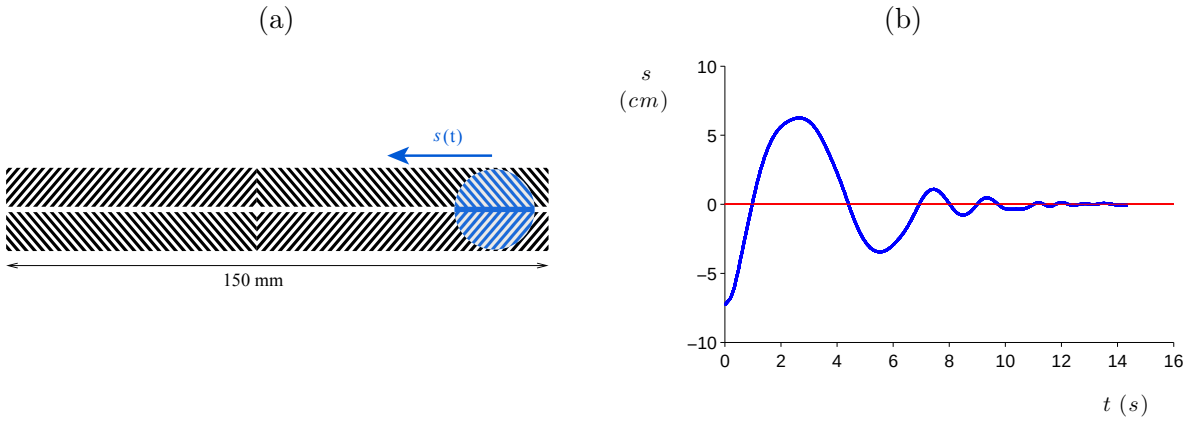

Figure II.26 – (a) Opposite polarization herringbone facing each other will trap a drop at its center. (b) Damping of oscillations for a drop of 3 mm radius at mid-race, launched into the device at 10 cm/s. After a few oscillations (during typically 10 s, smaller than the life time of an evaporating drop), the drop gets trapped in the middle.

At each side of the center line, the drops undergoes two different regimes. A first one (just after crossing the center), where inertial friction and viscous entrainment add up and oppose the movement, resulting in a very effective slow down. A second one, after the drops make a U-turn, where these forces are opposite and the drop re-accelerates in the opposite direction. Inertial friction ensures energy dissipation resulting in a final still position while the viscous entrainment acts as a restoring force attracting the drop towards the center.

If we look closer to the central pattern (see figure II.27 and II.26a), we see concentric squares or diamonds (whose 2 diagonals are the axis of symmetry of two herringbones).

We can therefore imagine a Leidenfrost chessboard in which each box would be made of concentric squares. If we were to spread a liquid sheet over this special chessboard, the liquid sheet would destabilize resulting on the trapping of a puddle on each single box.

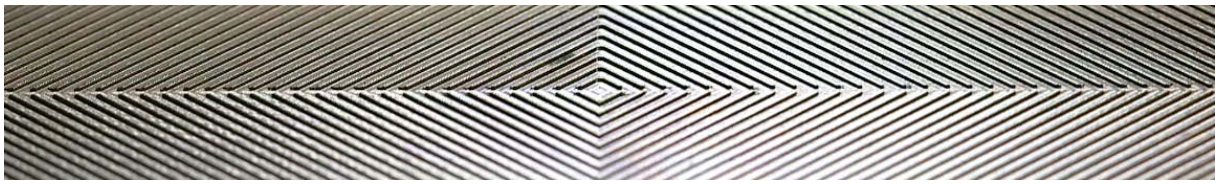

Figure II.27 – View of the texture resulting from joining two herringbones of opposite polarization and facing each other: we see concentric squares whose diagonals are the axis of symmetry of the herringbones.

5.2 The active herringbone: the switch

An other direction has been theoretically explored by our Italian collaborators ([89]) by straining an elastic substrate on which a herringbone pattern is etched. Using a very simple model of linear deformation, they expect two kinds of deformation regarding if the imposed stress is itself symmetric. The deformations which preserve the symmetry allows a modification of the geometrical parameters, as shown in right side of figure II.28. An example of deformation not preserving the symmetry of the pattern is shown on the left side of figure II.28.

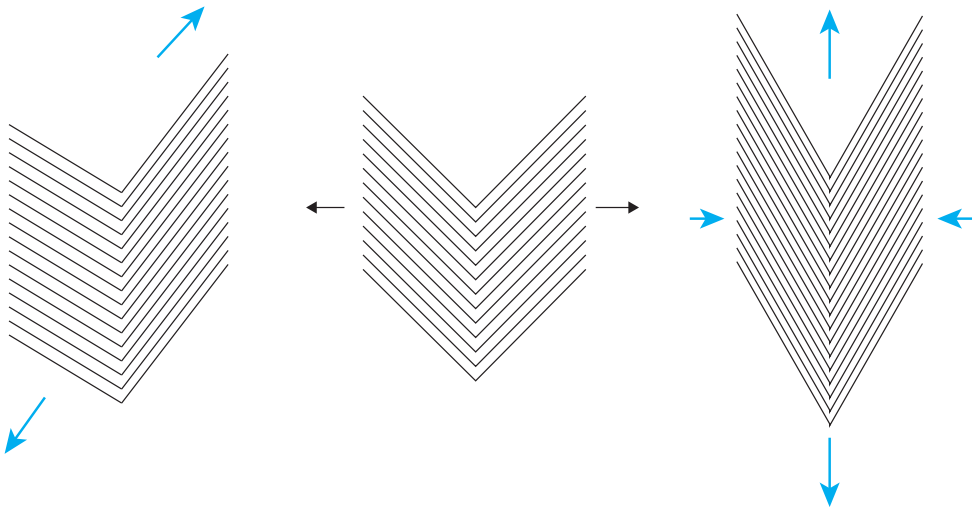

Figure II.28 – (Left) Example of elastic deformation that does not preserve the symmetry of the pattern: uniaxial tension along an oblique direction (inclination of 60° with the horizontal, blue arrows represent the applied stress). (Right) Example of elastic deformation decreasing α. From [89].

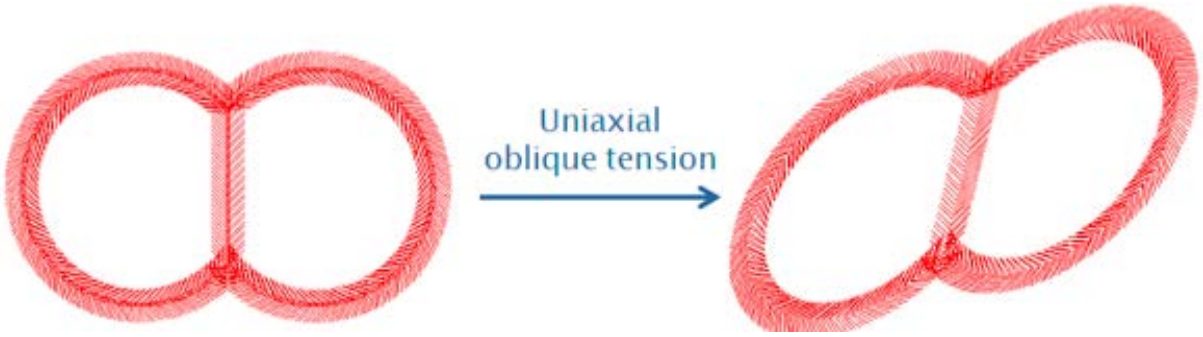

Figure II.29 – Diagram of a 'Leidenfrost switch'. Courtesy of Charlotte Rasser.

When symmetry is not preserved, they consider the asymmetric pattern as the union of two half-herringbones with different half-top angles α. Using the previous model for the propelling force with the "continuous" method of calculation, they evaluate the x-component of the propelling force on each half side of the drop (the x-axis being orthogonal to the axis made by the vertices of the arrows) as a function of the half-top angle α. They conclude that a drop placed on the axis of an asymmetric herringbone pattern will tend to deviate towards the side in which the channels have the biggest angle α (where the perpendicular projection is bigger). Taking advantage of this asymmetry, they suggest an idea of application presented in figure II.29 where a straight textured central segment joins two circular paths patterned with a herringbone texture and a central channel. A self-propelling drop moving along the straight central segment will have an equivalent probability to go each side. However, if the substrate is elastic, an asymmetry can be introduced by stretching it, systematically making the drop deviated to one side. They conclude that this active pattern could work as a switch.

Conclusion

Herringbone patterns on solids are found to propel Leidenfrost drops, which can be seen as a geometrical proof of the scenario suggesting that viscous drag should generally be responsible for such motions on asymmetric solids. Contrasting with ratchets, the geometry and the resulting vapor flows are simple and controllable, allowing us to produce quantitative models for both the propelling and the friction forces, and to discuss how the design can be optimized. Maximizing the force is useful if it is desired to oppose an existing force (such as gravity, if the solid is inclined); in other cases, it is interesting to optimize the drop speed to enhance the motion. The corresponding optimal angles are not the same, but both properties emphasize the role of geometry in these devices. Hence, any pattern polarizing the vapor flow should generate propulsion.

We just have proved that searching new textures can lead to new questions. Always using a flat substrate, we can imagine other macroscopic geometries such as curved chevrons. The question of textures on substrates that are not flat (hence exploring macroscopically the third space dimension) is also to be addressed. A good starting point would be the study of Leidenfrost self-propelled drops squeezed between two parallel textured planes (a situation recently studied by Celestini and coworkers without textures [20]). Then, the case of textures inside or outside a cylinder would lead to new questions. We show in figure II.30 an example of a herringbone texture on a (red stone) cylinder seal of the Jemdet Nasr period (4th-3rd millennium BC). We see how this simple texture was already used long ago and how the cylindrical substrate was naturally seen as the logical counterpart of the herringbone texture on a flat substrate.

Figure II.30 – Herringbone textures on the external face of red stone cylinder seal. Anatolian, 4th-3rd millennium BC, Jemdet Nasr period. Steatite or chlorite, 1.9 x 1.6 cm. Harvard Art Museums/Arthur M. Sackler Museum.

Smaller temperatures could also be tested, in particular after coating the solid with hydrophobic micro-textures, which preserves the Leidenfrost state down to the boiling point of the liquid.

Another way to extend the effect to cold(er) systems consists of etching chevrons in an

air-hockey table: blowing air through the holes generates levitation, and experiments (see Chapter III) confirm that plastic cards can indeed self-propel on such patterned tables.

Chapter III

Self-propulsion on an air hockey table

Contents

In collaboration with Hélène de Maleprade. Countless technical advice was provided by Xavier Benoit Gonin (PMMH engineer) regarding laser cutter possibilities and 3D printing.

1 When vapor is replaced by compressed air

1.1 The air hockey table

Limitations of Leidenfrost Herringbones

Two main limitations can be stressed in the Leidenfrost herringbone device. The first one dwells on the liquid nature of the self-propelled object. As a drop is deformable, it sags into the crenels generating a special friction. This deformation also implies that it is difficult to clearly define the vapor thickness h. Our best solution was to approach the local deformation by a circular geometry and then average the height over the channel width. In addition, if we want to study the effect of the object geometry on the propelling force, we are constrained by experimental limitations: large drops would destabilize (owing to chimney instability, see chapter I, 2.3) and puddle thickness cannot be varied since it is fixed to $2\ell_c$ by the competition between gravity and capillarity.

The second constraint dwells on the thermal origin of the effect. The substrate has to be brought at a high temperature, significantly above the boiling point of the liquid. Hence, the liquid itself is at its boiling temperature. Besides the high energetic cost, high temperature can be an issue if we think of transporting living media inside these moving droplets. Finally, we are also constrained by the range of temperatures we can explore, making it difficult to easily vary the height of levitation.

A new levitating device

We designed a new device allowing us to get rid of these limitations by replacing vapor by injected air. As a consequence, the liquid used to act as a vapor reservoir is no longer needed. We can from now on consider glass lamellae of controlled geometry (length a, width b, thickness c, density $\rho_g = 2130\ \mathrm{kg/m^3}$, corresponding mass $M = \rho_g abc$) to play the role of the self propelling object. By these means, we suppress both the high temperature and deformable nature of the object.

The slider is maintained in levitation by injecting a constant airflow from below through a porous media, somehow like an air-hockey table. To supply this constant flow, we inject compressed air (pressure P_2) from the bottom of a Plexiglas box device, as sketched in figure III.1. The top of this box is closed by a porous Plexiglas plate of thickness $e = 2$ mm. In order to control the characteristics of this porous wall, we manufacture it with a laser cutter (Epilog Helix 24) where we cut a square matrix of through-holes of radius $r = 100$ µm spaced by a pitch $p = 400$ µm. The velocity of air escaping from the pores is denoted as w.[1]

[1]For a detailed study, see Gary Leal [66]. In his book, he has theoretically tackled the problem of height levitation h for a given imposed pressure in the case of a circular levitating "puck".

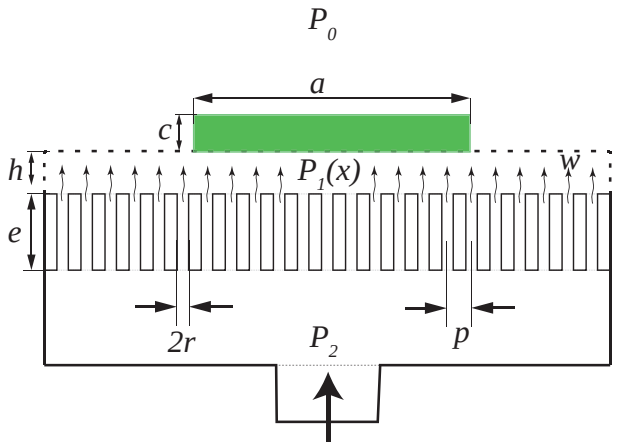

Figure III.1 – Side view of the air hockey table device. On top of a texture of height $h = 160$ μm, we place a glass lamella of thickness c, width b and length a. Air is injected through a porous floor consisting in vertical parallel tubes of length $e = 2$ mm and radius $r \approx 100$ μm, spatially distributed in a square array of pitch $p = 400$ μm. Air injected at a pressure P_2 from the bottom of the box, escapes from the pores at a speed w. The pressure in the texture (beneath the glass lamella and above the porous floor) is denoted as $P_1(x)$.

1.2 Propulsion with herringbone textures

In order to make the levitating object horizontally move, we use again the laser cutter to engrave a herringbone texture on top of the porous substrate, similar to the one done in the Leidenfrost case (see figure III.3b). The texture is made of rectangular channels of width $W = 1$ mm, depth $h = 160$ μm and walls of thickness $\lambda = 0.3$ mm. The angle between the main direction of the channel and the axis of symmetry of the chevrons is denoted by α. The air escapes from the pores into the bottom of each channel.

We start all experiments with a pressure inside the box P_2 equal to the atmospheric one P_0. We then slowly increase P_2 (hence injecting air in the channels) until the plate takes off. At this point, the top of the walls do not touch the plate anymore. The levitating height is close to the wall texture height $h = 160$ μm: the slider is skimming over the top of each channel. As soon as the plate takes off, it accelerates in the same direction as seen in the Leidenfrost case and shown in figure III.3b. We record this motion with a camera from the top view (figure III.3a). Once the plate has reached the end of the device, we push it back several times, resulting in a typical position curve as a function of time shown in figure III.2. We decompose the parabolic trajectory in two phases: in green (III.2) the slowing down phase, and in red the re-accelerating one. For each round trip we get an average acceleration from which we deduce the propelling force by multiplying it by the mass plate. To reduce uncertainty, the force is averaged over the successive parabolas.

The special friction due to the sagging of the liquid into the grooves has been here

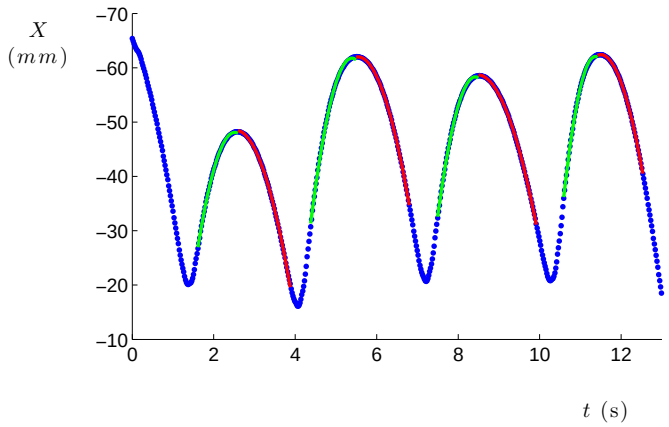

Figure III.2 – Position of the center of mass of the slider as a function of time. The plate ($a = 37$ mm, $b = 12$ mm, $c = 160$ µm) is launched several times against the air levitating herringbone texture. Green lines show deceleration phases while reaccelerating phases are shown in red. The corresponding force $F = M\ddot{X}$ is averaged over the series of round trips. Here, the obtained acceleration is $\ddot{X} = 5$ cm/s^2, which yields $F = 7$ μN.

suppressed by the use of a rigid slider. An unfortunate consequence is that we cannot anymore etch a central wide groove to gravitationally trap and guide the plate. As there is no restoring force keeping it in the plane of symmetry, we were obliged to put lateral walls to ensure central stability (see figure III.3a).

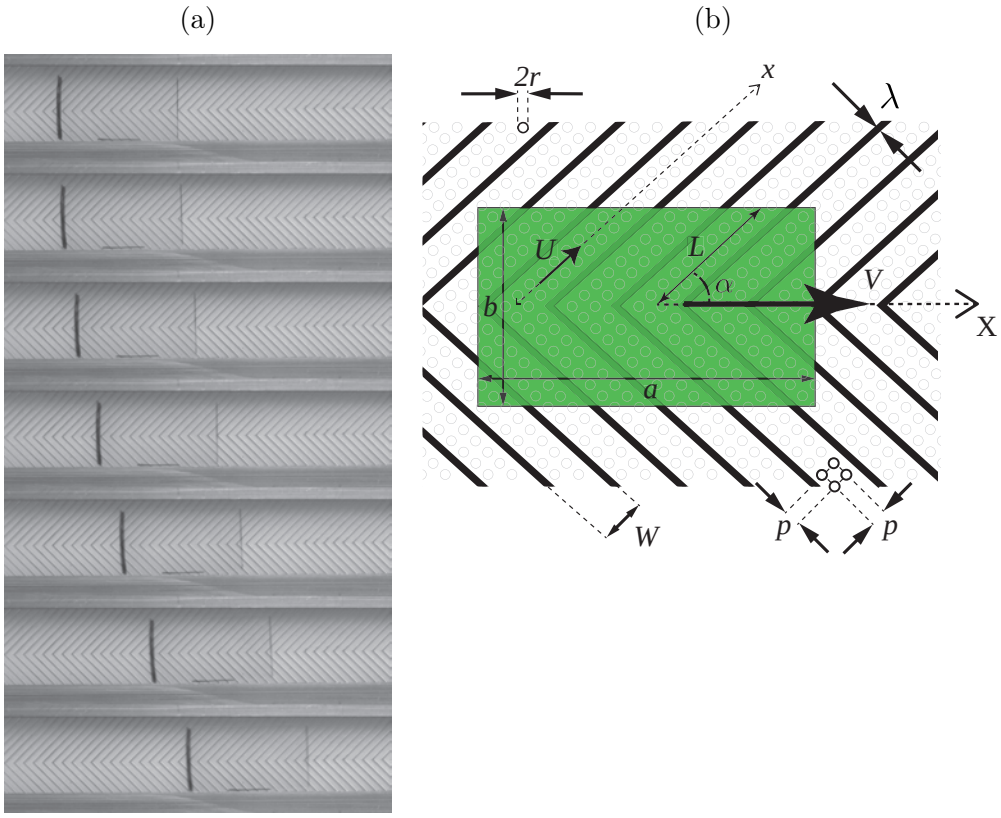

Figure III.3 – (a) Top view chronophotography (images spaced by 0.2 s) showing the acceleration of a glass lamella of length $a = 23$ mm, width $b = 12$ mm and thickness $c = 160$ µm. The slider is skimming over a herringbone texture engraved over a porous substrate through which air is blown. (b) Sketch of the herringbone texture: width of the channel $W = 1$ mm, thickness of the walls separating each channel $\lambda = 0.3$ mm, angle between half-channels and axis of symmetry α. The texture is above the porous substrate and below the glass lamella (length a, width b and thickness c). Inside each channel, we can observe a square array of circular through-holes of radius $r = 100$ µm and pith $p = 400$ µm. The horizontal ejection speed along a channel of axis x is denoted as U. The channel length below the plate is $L = b/(2\sin\alpha)$. As soon as the airflow is strong enough to make the lamella levitate slightly above the wall height h, the slider accelerates in the X direction and moves at speed V.

2 Force of propulsion

We focus in this section on the propelling force. A scaling law analysis shows how we can identify all physical ingredients in order to explain the experiments. Then we produce a quantitative model that allows us to predict the pressure needed to generate levitation and compare it to experimental observations. A new horizontal length scale σ arising from this more sophisticated model permits us to define what a "wide" or "narrow" slider is.

2.1 Experimental observations

Lamellae geometry dependency

We first discuss how the propelling force depends on the lamella geometry. We conduct our experiments with a fixed herringbone texture: $h = 160$ µm, $\alpha = 45°$. For two different thicknesses of our lamellae ($c = 160$ µm and $c = 1000$ µm), we repeat the experiment varying a and b. We show in figure III.4a the force of propulsion F deduced from acceleration measurements for each geometry.

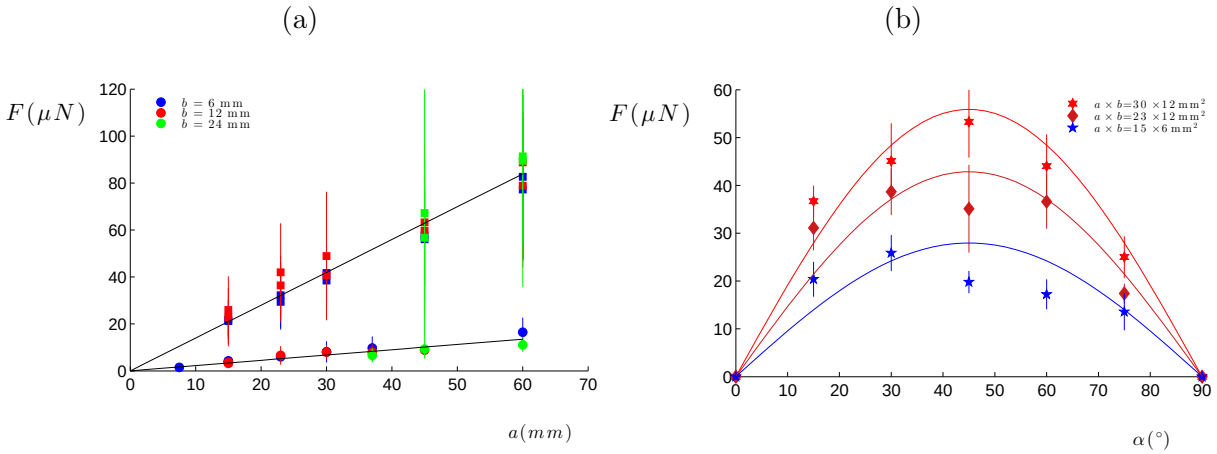

Figure III.4 – (a) Force of propulsion as a function of the length a of the glass lamella. Each color corresponds to different widths $b \in [6, 12, 18]$ mm. The two markers stand for two glass thicknesses: "circles" for $c = 160$ µm, and "squares" for $c = 1000$ µm. Straight solid lines correspond to a linear fit as suggested by equation III.1 or III.13. (b) Force of propulsion as a function of the opening angle α of the herringbone pattern. Each curve corresponds to a fixed lamella geometry of thickness $c = 1000$ µm: "stars" a x b = 30 x 12 mm^2, "diamonds" a x b = 23 x 12 mm^2, "pentagons" a x b = 15 x 6 mm^2. The solid line shows equation III.13.

We can observe in figure III.4a that the propelling force seems to be proportional to the lamella length a and independent of its width b. The ratio between the slopes of the two linear fits is 6.25, very close to the ratio between both thicknesses c (equal to 6.2), suggesting that the propelling force is also proportional to c.

Impact of the herringbone opening

Then we observe how the force depends on the geometry of the herringbone pattern, particularly on the opening angle α (figure III.4b). We measure the force for various opening angles $\alpha = [15°, 30°, 45°, 60°, 75°]$ for three plate geometries. They all have the same thickness $c = 1000$ µm, but have different areas: a x $b = 30$ x 12 mm^2 ("stars"), a x $b = 23$ x 12 mm^2 ("diamonds") and a x $b = 15$ x 6 mm^2 ("pentagons"). We report F as a function of α in figure III.4b. As previously seen in the Leidenfrost case, we observe a clear maximum around $\alpha = 45°$ and force vanishing as α tends towards 0° and 90°.

2.2 Model

In order to quantitatively capture all the results, we suggest a model based on a viscous entrainment scenario (similar to the one seen in previous chapter).

Scaling argument

Air injected from the bottom of a channel has no other option than escaping in the direction of channels of length $L = b/(2\sin\alpha)$. Denoting the gas viscosity as η and the horizontal speed as U, as shown in figure III.3b, this Poiseuille flow will create on each channel a stress $\tau \sim \eta\frac{U}{h}$ that will apply to the bottom of our glass lamella over a surface area $a\,b$. The resulting propelling force only includes the contributions which do not compensate, namely a $\cos\alpha$ projection in the plane of symmetry. Hence, we get $F \sim \eta\frac{U}{h}\,ab\cos\alpha$, where U is still unknown. Lubrication theory links the Laplacian of speed to the horizontal pressure gradient through: $\frac{\eta U}{h^2} \sim \frac{\delta P}{L}$ where L is the length of a covered channel and δP is the difference of pressure between the inside of a channel and atmospheric pressure (see figure III.3b and III.1). If we consider that the pressure beneath the plate has to support its weight, we can assume that δP scales as $\rho_g g c$. Hence, we get an expression for the gas velocity ($U \sim \frac{\rho_g g c h^2}{\eta L}$), which gives, once injected in the expression of the force:

$$F \sim \rho_g g c\, ah\, \sin 2\alpha \tag{III.1}$$

This equation is exactly the same as the one obtained in chapter II (equation II.10) if we replace the density ρ by ρ_g, the thickness $2\ell_c$ by c, the horizontal characteristic length

scale R by a and the film thickness $\sqrt{bR}$ by h.

This comparison emphasizes an advantage of the air levitated device compared to Leidenfrost case: the film thickness h is now an imposed geometrical characteristic and not a variable difficult to model.

Equation III.1 predicts a linear dependency of the force towards length a and thickness c, as observed in figure III.4a. In addition, it also explains the existence of a maximum of force for $\alpha \approx 45°$, as seen in figure III.4b. To ensure the validity of our scaling law analysis, we show in figure III.5 all our data as a function of the force predicted by equation III.1. All the data collapse in a single curve of slope 1.

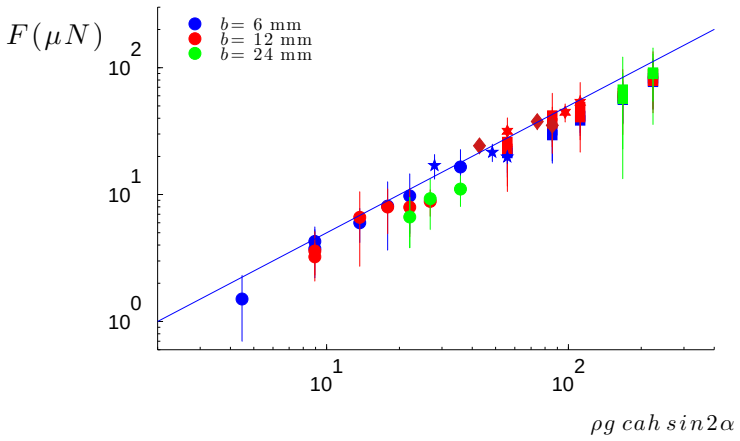

Figure III.5 – Force of propulsion as a function of the expression expected theoretically (equation III.1). Each point is an average of at least 5 experiments (typically 8). Data displayed in this figure correspond to different lengths a = [7.5, 15, 23, 30, 37, 45, 60] mm, width b = [6, 12, 24] mm (expressed by the color map), thickness c = [160, 1000] µm ("circles" and "squares", respectively). We also added experiments where we vary α = [15°, 30°, 45°, 60°, 75°] for three different geometries (same markers and colors as in figure III.4b). The blue straight line represents the line of equation $y = 1/2\,x$, that is, equation III.1 for the scaling and equation III.13 for the coefficient.

Analytical resolution

Although the scaling law argument captures all the underlying physics, we can go further, taking advantage of the fact that we control the geometry of the porous through which air is injected. Darcy law tells us that the volumetric flow rate of mean velocity w through a single hole $Q = w\pi r^2$ is proportional to the pressure jump between the inside of the box P_2 (experimentally controlled and constant) and the pressure $P_1(x)$ at a given position x below the slider:

$$Q = \frac{P_2 - P_1(x)}{R_h} \tag{III.2}$$

where R_h is the hydrodynamic resistance, equal to ${}^{8\eta e}/_{\pi r^4}$ for circular cross-section channels (e being the thickness of the porous plate as sketched in figure III.1). This expression is formally the analog of the electrokinetic law between voltage difference and current, $U = RI$. Conservation of mass gives us a second equation that links the injection speed w and the horizontal escaping speed U; $h\frac{\partial U}{\partial x} = \frac{Q}{p^2}$. These two equations can be rewritten as a single one. We have:

$$h\frac{\partial U}{\partial x} = \frac{P_2 - P_1(x)}{p^2 R_h} \tag{III.3}$$

Finally, Stokes equation in a channel writes:

$$12\eta\frac{U}{h^2} = -\frac{\partial P_1}{\partial x} \tag{III.4}$$

Equations III.3 and III.4 form a system of two equations with two variables. They can be rewritten as: $\frac{\partial^2 U}{\partial x^2} = \frac{U}{\sigma^2}$ and $\frac{\partial^2 [P_1(x)-P_2]}{\partial x^2} = \frac{[P_1(x)-P_2]}{\sigma^2}$. Both the horizontal speed U and the pressure along the channel P_1 are hyperbolic (exponential) functions that decay over a characteristic distance $\sigma = \sqrt{{}^{2ep^2h^3}/_{3\pi r^4}}$. This distance only depends on the porosity of the plate and on the height h of the wall textures: it is fixed in our experiments and its value calculated for the parameters of our system is 3 mm.

In order to have an exact solution, we consider as the boundary conditions a zero speed U at the origin of the channel x=0 and a pressure P_0 at the exit $x = L = b/(2\sin\alpha)$. We get:

$$U(x) = (P_2 - P_0)\frac{h^2}{12\eta\sigma}\frac{sh\frac{x}{\sigma}}{ch\frac{L}{\sigma}} \tag{III.5a}$$

$$P_1(x) - P_0 = (P_2 - P_0)[1 - \frac{ch\frac{x}{\sigma}}{ch\frac{L}{\sigma}}] \tag{III.5b}$$

A similar calculation was done by Gary Leal in [66], in the case of a flat porous substrate with a circular levitating puck, in relationship with the question of levitation height of a flat (non-textured) body above a hockey table. The corresponding differential equations (Bessel differential equation) are more complicated in this circular geometry, resulting in a solution that required to be evaluated numerically.

Needed pressure to propel

It is useful to bear in mind that we have $L = b/(2\sin\alpha)$, hence L and b play a similar role. We do not know "a priori" the value of the imposed pressure $P_2 - P_0$ needed to make the slider levitate at height h. We need to take into account that the pressure profile below the plate has to compensate the weight. We can limit this argument to a single wall and channel, which can be written:

$$\rho_g g c\, L(W+\lambda) = W \int_0^L [P_1(x) - P_0]dx \tag{III.6}$$

After integration and introducing the function $G(x) = \frac{1+\frac{\lambda}{W}}{1-\frac{thx}{x}}$ we get an expression for the overpressure needed to make a lamella levitate just above the texture:

$$\Delta P = P_2 - P_0 = \rho_g g c\, G(\frac{b}{2\sigma\sin\alpha}) \tag{III.7}$$

Equation III.7 confirms that the overpressure needed to induce levitation is proportional to $\rho_g g c$, anticipated in the scaling analysis. The mathematical study of the function G (for σ around 3 mm in our case) gives two regimes:

(i) for long channels ($b > \sigma$), function G scales as $G(x) \sim 1$ explaining the saturation regime $P_2 - P_0 \approx \rho_g g c$ shown in figure III.6 at large b.

(ii) for short channels ($b < \sigma$), function G scales as $G(x) \sim \frac{3}{x^2}$ leading to $G(\frac{L}{\sigma}) \propto \frac{3\sigma^2}{b^2}$, explaining the divergence of the pressure at small b: since $b \to 0$, pressure has to diverge to be able to compensate the weight of the slider.

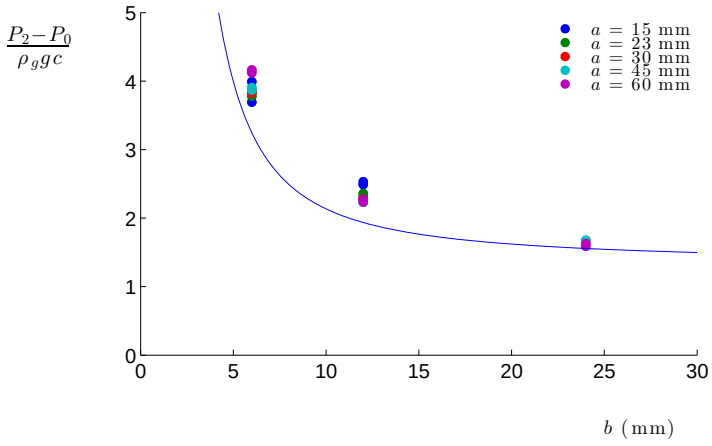

Figure III.6 – Normalized overpressure $P_2 - P_0$ imposed to induce levitation, as a function of the horizontal width b for plates of thickness $c = 1000$ μm and different lengths $a = [15, 23, 30, 45, 60]$ mm. We show equation III.7 in solid blue line with no adjustable parameter. As $b \to 0$, pressure has to diverge to compensate the weight of the slider.

We show in figure III.6 experimental measurements of this overpressure as a function of the width b for a plate of thickness $c = 1000$ μm and different lengths $a = [15, 23, 30, 45, 60]$ mm. We observe almost no dependency towards the distance a. The pressure increases as the width b decreases, in good agreement with the model (equation III.7) represented with a solid line in figure III.6. The slight systematic underestimation by the theory may be due to the fact that there are some pressure losses, so that actual pressure must be larger than estimated.

Pressure and speed profile inside the groove

Analytical solution We can now inject the expression of $P_2 - P_0$ (equation III.7) in our previous profile solutions for the pressure $P_1(x)$ and speed $U(x)$ along the channel, leading to:

$$P_1(x) - P_0 = \rho_g g c \, G(\frac{L}{\sigma}) \, [1 - \frac{ch\frac{x}{\sigma}}{ch\frac{L}{\sigma}}] \tag{III.8a}$$

$$U(x) = \rho_g g c \, \frac{h^2}{12\eta\sigma} \, G(\frac{L}{\sigma}) \frac{sh\frac{x}{\sigma}}{ch\frac{L}{\sigma}} \tag{III.8b}$$

Again, two regimes can be explored depending on the width b of the plate compared to the characteristic decay length σ.

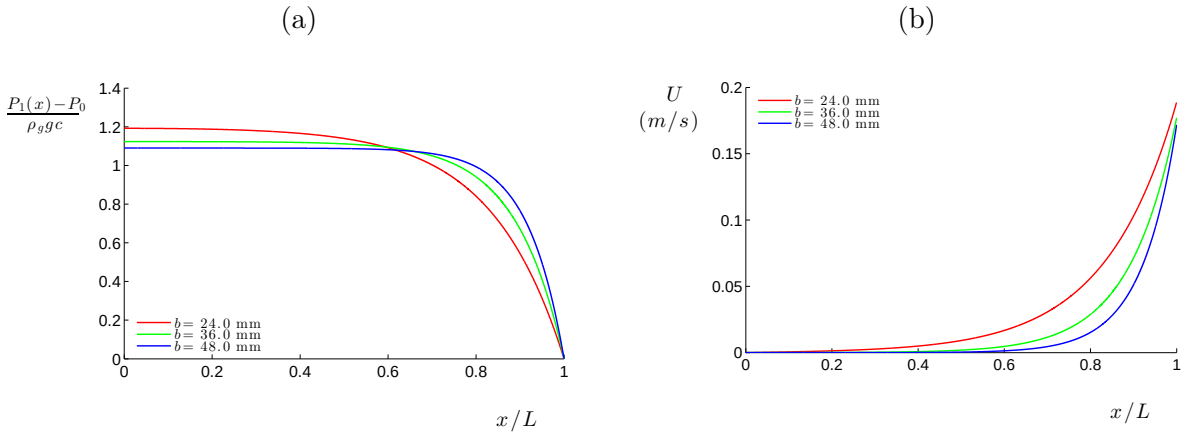

Figure III.7 – (a) and (b): Pressure $P_1(x)$ and speed $U(x)$ profile obtained from equation III.8a and III.8b respectively, as a function of the relative position x in the channel of length $L = \frac{b}{2\sin\alpha}$. Three different width $b \in [24, 36, 48]$ mm are shown. Plate thickness is set to $c = 160$ µm, length $a = 15$ mm and wall texture thickness $\lambda \to 0$. The characteristic decay length σ (independent of b) is fixed to 3 mm, so that we are in the "wide" plate regime.

(i) "Wide" plates: $b > \sigma$ We show in figure III.7a and III.7b the analytical profile solution in a channel for pressure $P_1(x)$ (equation III.8a) and speed $U(x)$ (equation III.8a) respectively, for three different widths $b \in [24, 36, 48]$ mm $> \sigma$. We fix $c = 160$ µm, length $a = 15$ mm and wall thickness $\lambda \to 0$ (in order to verify $1+\lambda/W \to 1$). A taylor expansion of equations III.8a and III.8b gives the following approximate solution (for the sake of simplicity, we will assume here $1 + \frac{\lambda}{W} = 1.3 \approx 1$):

$$\frac{P_1(x) - P_0}{\rho_g g c} \approx 1 - exp^{\frac{x-L}{\sigma}} \tag{III.9a}$$

$$U(x) \approx \rho_g g c \, \frac{h^2}{12\eta\sigma} \, exp^{\frac{x-L}{\sigma}} \tag{III.9b}$$

The characteristic decay length σ (independent of b, and set to 3 mm in our experiment) governs the pressure and velocity profile. The smaller this length, the shorter compared to the channel length L, the sharper the evolution of pressure and speed near the exit of the channel - visible in figure III.7, where the blue curve is sharper than the red one. Two channel positions are of particular interest: the exit of the channel ($x = L$) and its origin ($x = 0$). At the exiting side of the channel, pressure is $P_1(L) = P_0$ (this is merely the imposed boundary condition used for the integration). At the origin (corresponding to the tip of a chevron), pressure is a function independent of L (hence of b): $P_1(0) \approx P_0 + \rho_g g c$.

(ii) "Narrow" plates: $b < \sigma$

Taylor expansion of pressure and speed results in this case in:

$$\frac{P_1(x) - P_0}{\rho_g g c} \approx \frac{3}{2}[1 - (\frac{x}{L})^2] \tag{III.10a}$$

$$U(x) \approx \rho_g g c \, \frac{h^2}{4\eta L^2} \, x \tag{III.10b}$$

We show in figure III.8a and III.8b the corresponding speed and pressure profiles for width $b \in [0.3, 1, 3] < \sigma$. Pressure is a parabolic decaying function of the ratio x/L. As a consequence, all pressure profiles are the same if we plot them as a function of the proportional channel position x/L: all solid lines in figure III.8a superimpose to each other. Speed, in turn, is a linear function of x, whose slope is proportional to $1/b$, as can be seen in figure III.8b.

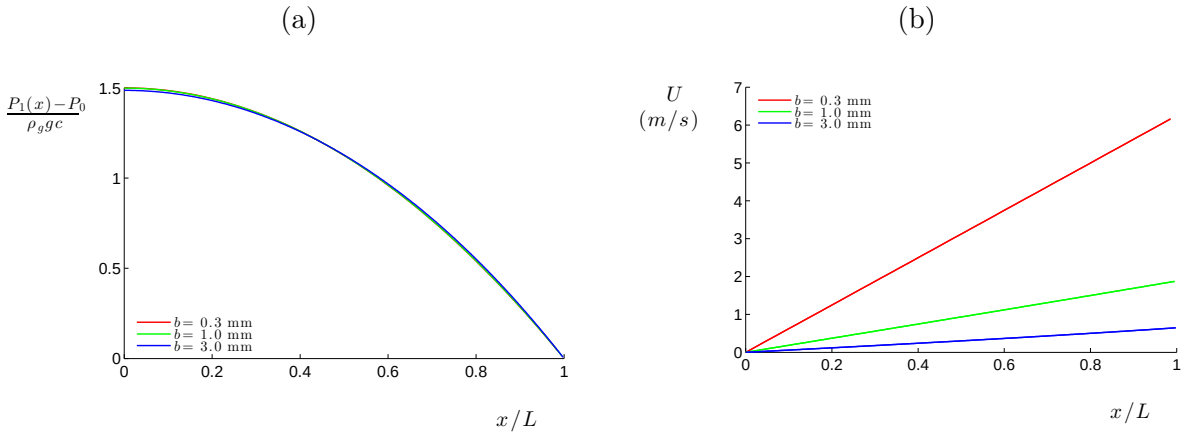

Figure III.8 – (a) and (b): Pressure $P_1(x)$ and speed $U(x)$ profiles obtained from equation III.8a and III.8b, respectively, as a function of the relative position x in a channel of length $L = \frac{b}{2\sin\alpha}$. Channel length (proportional to $b \in [0.3, 1, 3]$ mm) here is smaller than the characteristic decay distance σ, resulting in a parabolic expression for the pressure and a linear profile for speed, as described by equations III.10 for the "narrow" plate regime.

General remarks The choice of the geometrical characteristics of the porous plate allows us to play on distance σ, hence move from a "narrow" plate regime to a "wide" plate one. For all our experiments, we deliberately chose the regime of "wide" plates where the required pressure ΔP (see figure III.6) does not diverge and remains relatively small.

In all cases, maximum overpressure $(P_1(0) - P_0)/\rho_g g c$ - right below the plate (in the axis of symmetry) - ranges between $[1, 3/2]$. This means that although the imposed pressure $P_2 - P_0$ diverges, the pressure inside the channel is always finite.

In order to obtain an expression for the needed external overpressure $P_2 - P_0$, we stated that the integral over the surface of the internal channel overpressure $\int_0^L [P_1(x) - P_0]dx$ must balance the weight $\rho_g g c L$ (equation III.6). By doing a simple change of variable in this integral expression $y = \frac{x}{L}$, we get:

$$S = \int_0^1 [P_1(y) - P_0]dy = \rho_g g c \tag{III.11}$$

As a direct consequence, the surface beneath all curves in figure III.7a and III.8a are equal to unity.

Exact solution for the propelling force

Since we have an analytical solution for the speed (and the pressure) in each channel, we can make the exact calculation of the viscous force applied by the air to the plate. Knowing that the stress of a Poiseuille flow in a channel is $\tau = 6\eta U/h$ and using Stokes equation

III.4, we get: $F_i = -\int_0^L \int_0^W \tau dx dy = \frac{Wh}{2} \int_L^0 \frac{\partial P_1(x)}{\partial x} dx$. By recalling that $P_1(L) = P_0$, we obtain:

$$F_i = \frac{Wh}{2}[P_1(0) - P_0] \tag{III.12}$$

As done in the Leidenfrost situation, we have to take into account the number of contributing channels $N(\alpha) = 2a/(\frac{\lambda+W}{\sin\alpha})$ and express the projected propelling force along the central axis. Given that all our experiments are performed in the "wide" plate case ($b > \sigma$), we have $P_1(0) - P_0 \approx \rho_g g c$. We finally get the total propelling force:

$$F = \frac{1}{2} a h \, \rho_g g c \, \sin 2\alpha \tag{III.13}$$

Equation III.13 has the same behavior as the scaling law (equation III.1), but it also yields the numerical prefactor, found to be equal to $1/2$. Looking back to figure III.5, the solid line which nicely matches the data is equation $y = 1/2\, x$ (a straight line of slope $1/2$) predicted by equation III.13.

3 New geometries, new functionalities

3.1 The truncated herringbone

The model introduces a characteristic distance σ, which physically represents the exit distance over which pressure and speed changes mainly take place. Since all our experiments were made in the "wide" plate regime ($b > \sigma = 3$ mm), we expect almost all viscous entrainment to take place near the 3 last mm of the channel.

As a consequence, the central geometry of the texture should not play a key role. We have tested this idea by comparing forces between the "classic" herringbone and a "truncated" version. This new texture is shown in bottom of figure III.9 and consists in a herringbone pattern where the tip is now replaced with a straight section of length b_T (fixed to 10 mm) perpendicular to motion:

Figure III.9 – Comparison between two textures entraining a glass slider of length $a = 30$ mm, width $b = 15$ mm and thickness $c = 1$ mm (resulting in a weight M around 1 mg). Top texture is the "classical" herringbone. Bottom one corresponds to the "truncated" herringbone, which has a central straight section of length b_T (fixed to 10 mm) perpendicular to motion, hence having a null viscous propelling contribution.

We show in figure III.10 the comparison of the trajectory of a glass slider (length $a = 30$ mm, width $b = 15$ mm and thickness $c = 1$ mm) launched against the entrainement force direction (launched from left to right on the texture represented in figure III.9) for both textures. As already discussed, the entrainment force will first slow down the slider, eventually stop it and finally reaccelerate it resulting in a parabolic trajectory (friction is negligible). We qualitatively see that the trajectories are very similar, indicating that both devices have a similar propelling efficiency although they have very different textures. In more detail, we also observe that it take less time to cover the same distance to the "classical" herringbone (in blue) than to the "truncated" herringbone (in red), indicating that "classical" herringbone texture is slightly more efficient.

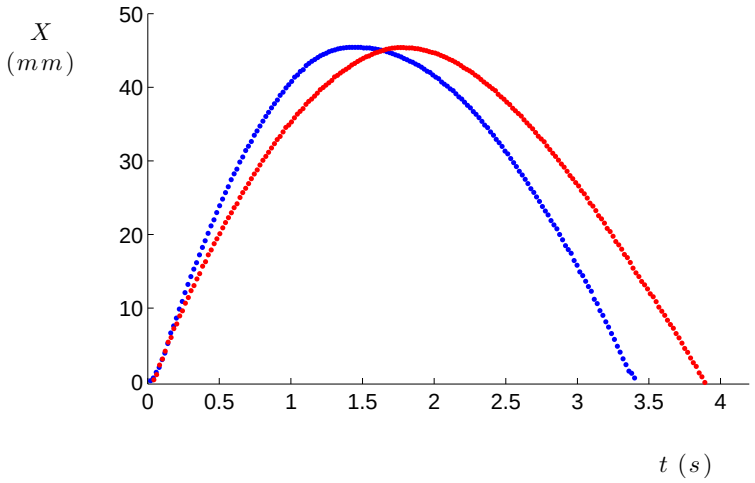

Figure III.10 – Trajectory comparison between the two propelling textures exposed in figure III.9. In red, the trajectory corresponding to the "truncated" herringbone, shown to be slower than the one in blue (corresponding to the "classical" one).

This strong similarity is in good agreement with the assumption that only the last section of each channel plays a role in the propulsion, hence the central part of the texture (either a pointed tip or a straight one) do not have a strong contribution to propulsion.

More quantitatively, we can deduce from a quadratic fit of the trajectory the acceleration equal to $\ddot{X}_T \approx 3$ cm/s^2 and $\ddot{X} \approx 4.5$ cm/s^2 for the "truncated" and the "classical" herringbone, respectively. Since the plate is the same in both situations (and has a weight M around 1 mg), we deduce a corresponding force F equal to $F_T = 30$ μN and $F = 45$ μN for the "truncated" and the "classical" herringbone, respectively. If all surface area contributed to propulsion, we could expect a reduction in propulsion proportional to the reduction of area breaking the symmetry scaling as $(b - b_T)/b$, that is, around 30 %. However, as qualitatively discussed previously, the ratio of propelling forces F_T/F is much higher (around 70 %) which confirms our assumption of viscous entrainment contribution to propulsion being concentrated at the end of each channel.

3.2 Climbing up a slope

From the expression of the propelling force (equation III.13), we deduce the expression of acceleration $\ddot{X}$ for a plate:

$$\ddot{X} \approx g\frac{h}{2b}\sin 2\alpha \tag{III.14}$$

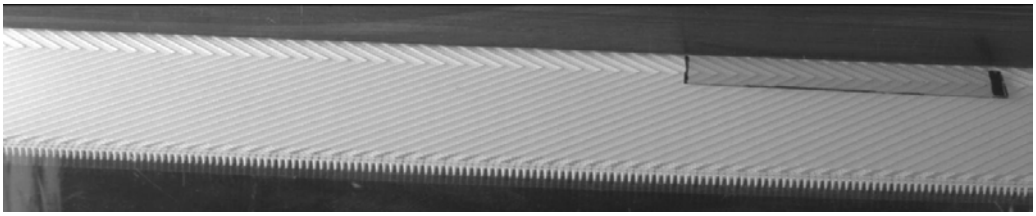

Figure III.11 – Lamella (a = 30 mm, b = 6 mm, c = 160 µm) withstanding a slope of 2% owing to viscous entrainment. From this lateral view we can distinguish the holes through which air is injected at the bottom of each chevron.

For the sake of simplicity, we assume $\alpha = 45\,^\circ$, the optimum angle in term of propelling force. Then, equation III.14 tells us that plates can climb slopes up to $\theta \approx \frac{h}{2b}$, that is, up to several % in our typical geometries. To draw a comparison, no mountain stage in the world famous "Tour de France" exceeds a 10 % slope. For instance, we show in figure III.11 a plate of width $b = 6$ mm withstanding a slope of 1.3 % where viscous entrainment balances the weight.

3.3 The viscous entrained mill

All propulsion movements seen up to now lead to straight translation. The longer we want to observe the movement, the larger textured substrate we need. In the case of drops, we solved this problem by looping two straight textured surfaces through flat semicircular sections. In addition, we used a central deeper groove to gravitationally trap the drop and be able to guide it, allowing us to reach (and study) the terminal velocity regime. In the case of non deformable glass lamellae, this set-up is much more complicated to achieve. In contrast, rotation offers great possibilities since the moving objects remain in place and can be observed as long as we want. Based on this idea, we developed the texture similar to a windmill visible in figure III.12. A plane is divided in four equal sections in which parallel grooves are engraved. Between each quadrant, a 90° rotation of the main direction of the grooves is imposed. Consequently, viscous entrainment acts on the levitating plate in a different direction for each portion (see arrows in figure III.12a), which generates a rotation.

The previous scaling argument gives us the propelling force generated by one channel: $F_i \sim \rho_g g c\, h W$. If we denote as $2b$ the side length of a square plate (see figure III.12a), each forth of the plate has $N(\alpha) = b/(\lambda + W)$ channels beneath it. The total resulting force in each quarter being: $F_{1/4} \sim \rho_g g c\, h b$. Total torque experienced by the plate will therefore scale as:

$$\mathcal{M} \sim \rho_g g c\, h b^2 \tag{III.15}$$

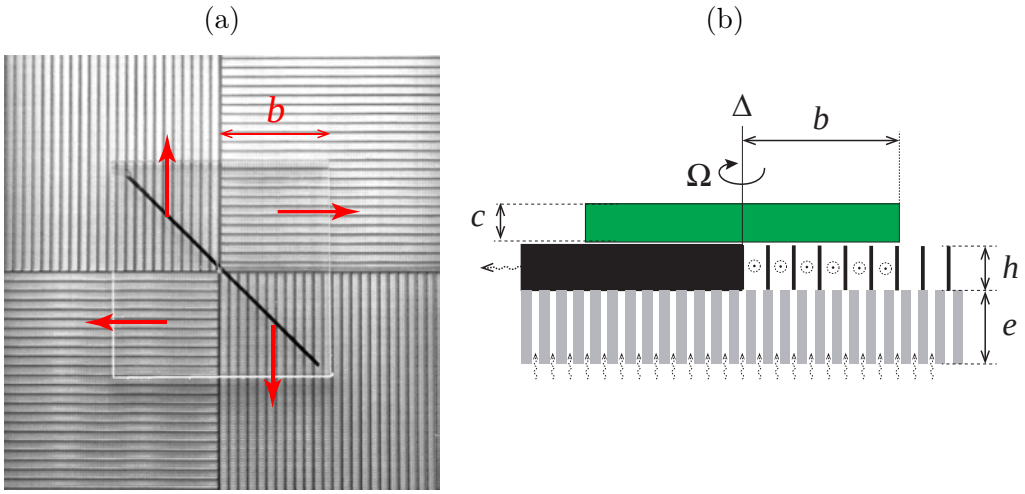

Figure III.12 – (a) Windmill texture consists of four square sections textured with parallel grooves of width $W = 1$ mm, walls of thickness $\lambda = 0.3$ mm and depth $h = 160$ µm. A vertical glass fiber acting as central axis (Δ) keeps centered a PMMA plate of density 1190 kg/m^3, thickness $c = 2$ mm and side $2b =$ 30 mm. Red arrows show viscous entrainment direction in each quadrant resulting in rotation (terminal angular speed denoted as Ω). (b) Sketch: side view of the setup. Three vertical lengths are indicated: e stands for the porous plate thickness, h for the walls' height and c for the slider thickness.

The moment of inertia J of a square plate scales as mb^2 and the second Newton's law gives us a relation between torque and angular acceleration $\ddot{\theta}$: $\mathcal{M} = J\ddot{\theta}$. Hence we get:

$$\ddot{\theta} \sim g\frac{h}{b^2} \tag{III.16}$$

If we put numbers in this equation, we obtain $h/b^2 \sim 1\ m^{-1}$ and typical angular acceleration of 10 rad/s^2 - quite large indeed!

As of now, imposed differential pressure $\Delta P = P_2 - P_0$ (between the external atmospheric pressure P_0 and the inner one P_2) was fixed and carefully chosen to match levitation height and wall texture height h, as sketched in figure III.12b. This new setup allows us to easily probe the role of imposed pressure (remained unexplored up to now). We show in figure III.13a the terminal speed of rotation as a function of this overpressure. Two regimes separated by a critical transition can be observed:

(i) a first regime (below 35 mbar in figure III.13a) where the imposed pressure is not strong enough to induce levitation. Owing to solid friction, there is no movement at all.

(ii) a second regime (above 35 mbar) where pressure is strong enough to withstand the plate's weight, which generates rotation. If we increase air injection, the plate levitates at height z higher than the walls' height h. From a side view (see figure III.13b), we can consider that the flow is divided in two regions. A lower one (flow in dotted blue),

rectified by the walls of height h and an upper one (between h and z, marked with red dotted arrows), where the flow is free and will have a symmetric pattern, resulting in a decrease of the propelling force.

Terminal speed and propelling force are optimized when the slider completely seals each channel, i.e. when it levitates at height $z = h$ (around 40 mbar in figure III.13a).

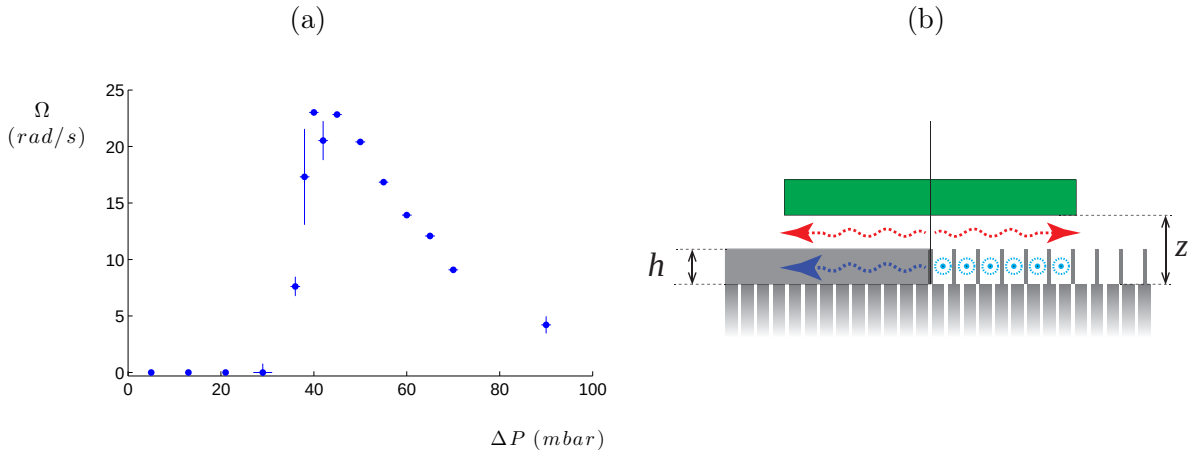

Figure III.13 – (a) Terminal angular speed $\Omega = \dot{\theta}$ of a plate on a windmill pattern, as a function of the imposed differential pressure $\Delta P = P_2 - P_0$ for a square PMMA plate of side $2b = 30$ mm and thickness $c = 2$ mm. Optimum of speed is found around 40 mbar, where the slider levitates just above the walls, hence efficiently confining and rectifying the flow. (b) Side view of the rotating slider: as the imposed pressure increases, the levitating height z increases. As a consequence, rectification of the flow is less efficient and terminal speed decreases. Red dotted arrows show the isotropic flow above the textures. Blue dotted arrows show the main direction of the flow rectified by the textures.

4 Channel depth h and Reynolds number

In all our experiments, the crenel depth h is fixed and constant. Increasing the object's thickness (or analogously increasing the crenel depth h) results in an increase of the needed injection speed w. Eventually, there will be a point where the horizontal speeds will be so high that the low Reynolds number approximation will not be satisfied anymore. From the speed solution obtained in equation III.8b, we can calculate the maximum horizontal speed. By injecting it in the Reynolds number expression $Re = \frac{\rho U h^2}{\eta L}$, we get its explicit expression:

$$Re = \frac{\rho \rho_g g c h^4}{12 \eta^2 L^2} \, H(\frac{L}{\sigma}) \tag{III.17}$$

where the function H is $H(\frac{L}{\sigma}) = \frac{L}{\sigma} G(\frac{L}{\sigma}) th \frac{L}{\sigma}$. We show in figure III.14 this expression as a function of the channel depth h for different widths b and a fixed thickness $c = 1$ mm. Two asymptotic regimes can be observed:

For "narrow" plates $b << \sigma$ ($\propto h^{3/2}$) we have $H(\frac{L}{\sigma}) \sim 3$, leading to a Reynolds number proportional to h^4 (dotted line in figure III.14):

$$Re_{b<\sigma} \propto h^4 \tag{III.18}$$

For "wide" plates $b >> \sigma$ ($\propto h^{3/2}$), $H(\frac{L}{\sigma})$ reduces to $\frac{L}{\sigma}$, hence we have (dashed line in figure III.14):

$$Re_{b>\sigma} \propto h^{5/2} \tag{III.19}$$

Our model is based on a low Reynolds number assumption (region below the horizontal solid black line in figure III.14). In our experiments, the worst scenario (where the Reynolds number is highest) corresponds to the thickest and most narrow plate ($c = 1$ mm and $b = 6$ mm, red curve in figure III.14), for which we indeed have Re $\lesssim 1$ (given that we have fixed $h = 160$ µm). All other plates have smaller Reynolds number (Re ≤ 0.3), validating our assumption of viscous scenario.

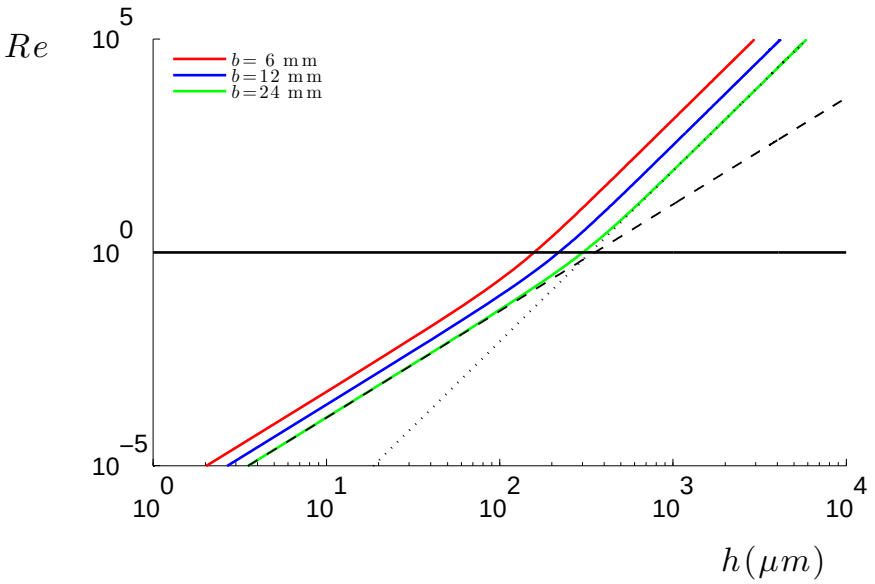

Figure III.14 – Reynolds number as a function of channel depth h as predicted by equation III.17 . Thickness is fixed to $c = 1$ mm (corresponding to our thickest plates, hence highest experimental Re numbers) and three plates of width $b \in [6, 12, 24]$ mm, as indicated with colors. The dashed black line shows asymptotic behavior $h^{5/2}$ described in equation III.19 for "wide plates" (also corresponding to shallow crenels). The dotted black line shows asymptotic behavior h^4 predicted in equation III.18 for "narrow" plates (corresponding here to deep crenels).

5 Switching roles: the texture patterned on the slider

We thank Steffen Hardt and Tobias Baier for enlightening discussions concerning this section.

5.1 Experimental set-up

For heavier plates or deeper textures, we expect to switch to a regime where inertial effects can dominate viscous ones. To generate movement, inertial thrust need a surface upon which to exert pressure: a role in our case played by the walls of the herringbone pattern. If walls are bound to the air levitating table we do not expect anything to happen. Since forces are in the range of μN, table's weight would be too big to move. Conversely, if walls are anchored to a light glass lamella, we see the textured slider move in the opposite direction compared to the one observed up to now, as shown in figure III.15:

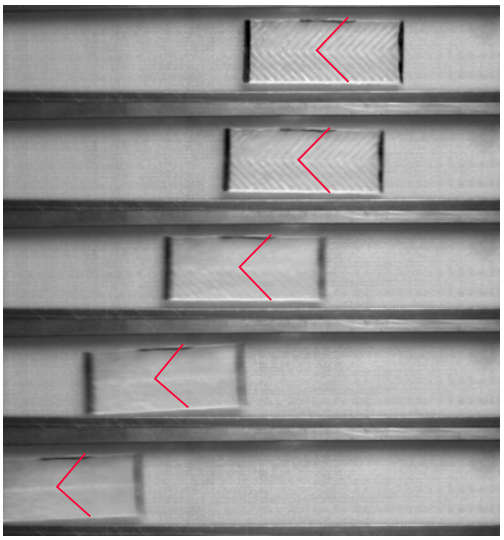

Figure III.15 – Chronophotography of a textured slider of width $b = 12$ mm, length $a = 30$ mm and glass thickness $c = 1160$ µm moving on an air-hockey table. Herringbone texture has been added to the lamellae by creating walls of depth $h = 800$ µm (resulting in a total thickness of $c+h = 1960$ µm). For visibility reasons, we have highlighted in red one of the channels of the slider. Plate levitates and moves due to air that is blown from the underlying substrate through holes of same dimension as previously (pitch $p = 400$ µm, radius $r = 100$ µm). Each image is separated by 0.2 s. Movement takes place in the opposite direction than for viscous entrainment.

This experiment could be viewed as similar to the previous situations. However, a slight difference dwells on the fact that air was previously injected from the bottom of the channels. Now, we blow air onto the whole textured slider, in particular also on the walls.

As a consequence, it is more difficult to make the slider raze to the ground, hence needing higher pressure to start levitation and allowing secondary symmetric flows to exist.

In order to create a texture on the slider, we tried several techniques:

(i) we first engraved on a plexiglass lamella the texture with the laser cutter. However, we faced a main problem since the plate bends after engraving the pattern (when the texture was engraved on the air-hockey table this problem was avoided by fixing the extremities of the plate to the substrate with screws, ensuring perfect horizontality).

(ii) we then tried 3D-printing technology (Fortus 250mc printer). The technology is Fused Deposition Modeling (FDM) where objects are produced by extruding material which harden immediately to form layers. A thermoplastic filament that is wound on a coil is unreeled to supply material to an extrusion nozzle head. The nozzle head heats the material and turns the flow on and off. The nozzle can be moved in both horizontal and vertical directions by a numerically controlled mechanism. The object is built bottom up, one layer at a time following the designed 3D pattern (see figure III.16). The highest resolution we could get using acrylonitrile butadiene styrene as construction material (ABS-P430) did not allow us to make walls thinner than 350 µm, that is, too large. In addition, the final surface was too rough, generating high solid friction against the air blowing substrate.

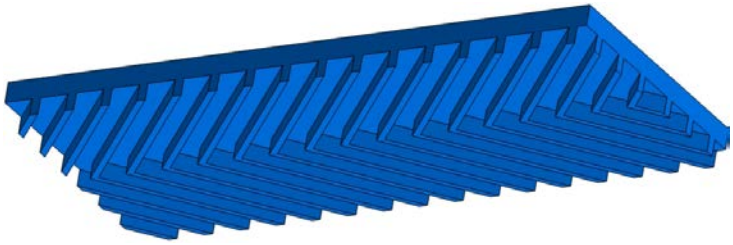

Figure III.16 – 3D image of herringbone slider designed with Computer Assisted Conception software (Catia®). The solid body has a thickness $c = 1$ mm, a width $b = 12$ mm and a length $a = 30$ mm. A herringbone texture of height $h = 800$ µm is added on the bottom.

(iii) we finally followed a two steps method based on creating a negative stamp of our brass herringbones (see [14] for additional information). A mixture (10:1 in weight) of Polydimethylsiloxane (PDMS, a liquid organosilicon compound) and cross linking agent RTV-Silicone (Room Temperature Vulcanizing silicone) is poured over the master mould (namely the brass herringbone) and placed in a furnace at 70 °C for 1 hour. Once the PDMS is hardened, we obtain a negative replica of our master mould. We recreate the initial texture by pouring UV curing optical adhesive (NOA-61)[2] in the PDMS mould.

[2]NOA-61 is designed to give the best possible bond to glass surfaces and may be polished after curing. To cure these optical adhesives, they must be exposed to UV light. Recommended energy required for

After recovering it with a glass lamella of dimension a x b x c, we expose it for 30 s under an UV light of power 100 mW/cm^2. As a consequence, we obtain a glass lamella of the desired dimension on which walls are bond to the glass forming a herringbone texture. With this technique, we avoid bending, thick walls and roughness problem previously encountered.

5.2 Force measurements

We made a set of plates with different geometrical characteristics. Four widths were generated: $b \in$ [6, 12, 18, 24] mm. For each one, three glass thicknesses were produced: $c \in$ [160, 1160, 2160] µm. Lamellae length a was not varied and was set to 30 mm. Regarding the herringbone texture, wall thickness was fixed to $\lambda = 0.2$ mm, spacing to $W = 1$ mm and opening angle α to 45°. Wall height varied in the range of $h \in$ [150, 250, 400, 800, 1600] µm. With this set of 48 different plates, we measured the propulsion force with the same method as previously used. Once again, air injected pressure was carefully chosen: we start all experiments from no overpressure and keep increasing it until the very first moment the textured plate starts to levitate (and move). We show in figure III.17 this force as a function of wall height h for the whole set of sliders.

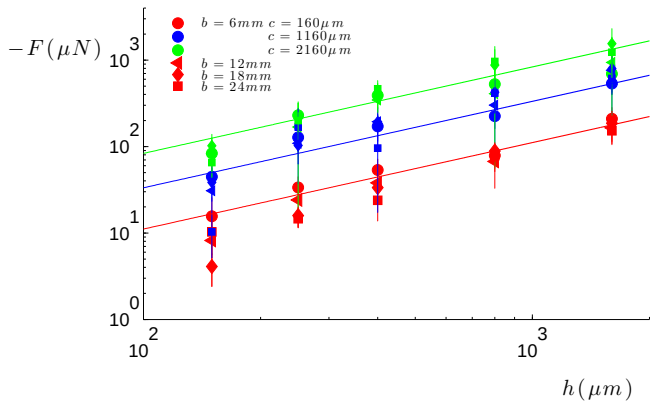

Figure III.17 – Force of propulsion as a function of wall height h. Each color represent a thickness $c \in$ [160, 1160, 2160] µm. Each symbol represent a width b (circles for $b = 6$ mm, triangles for $b = 12$ mm, diamonds for $b = 18$ mm, squares for $b = 24$ mm). Length a is fixed to 30 mm and $\alpha = 45°$. For a given plate thickness c (i.e. a given color), each cluster corresponds to a wall height $h \in$ [150, 250, 400, 800, 1600] µm. Compared to previous viscous entrained experiments, the propulsion direction is opposed, hence the negative sign of F. Solid lines show best linear fit, as suggested by equation III.21. Each point is an average of at least 5 measurements.

full cure is 3 J/cm^2 in the range of 350 nm wavelength.

In these experiments, the propulsion direction is opposed to the one observed when the herringbone texture was patterned on the air blowing device. Experiments suggest a linear dependency of the force as a function of wall height h and glass thickness c, and width b seem to play little role.

A simple argument based on inertial scenario can be produced to qualitatively capture all these results. If we first focus on a single crenel as shown in figure III.18, the underlying pressure has to compensate the weight of both the glass plate ($\rho_g cg$) and the walls ($\rho_N hg\,\frac{\lambda}{W+\lambda}$, where ρ_N is the density of NOA and the term $\frac{\lambda}{W+\lambda}$ takes into account the surface density of walls). Assuming all the vertical momentum is transformed in horizontal one, the same dynamic pressure acts on a surface area perpendicular to the plate scaling as Wh (see red and blue surfaces in figure III.18).

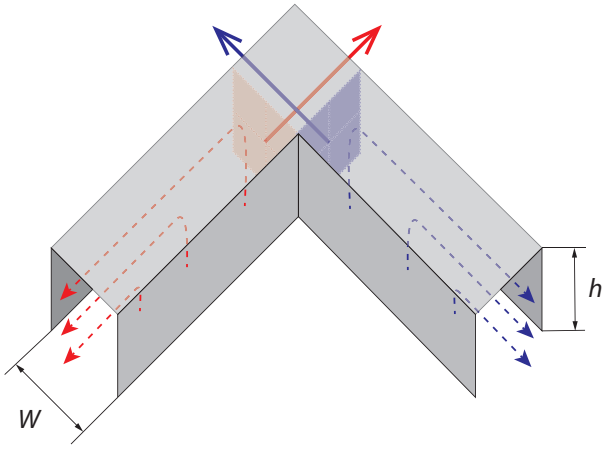

Figure III.18 – Sketch of the flow in a single crenel. Dotted lines indicate air direction. Solid arrows show the direction of the force resulting from the dynamic pressure acting over the vertical colored surfaces. By symmetry, all (absolute) magnitudes are equal between red and blue colors.

Total propelling force along the axis of symmetry is obtained by multiplying the projected force in a single crenel by the number of contributing channels $N(\alpha) \sim \frac{a\,\sin\alpha}{\lambda+W}$. Hence we get:

$$F \sim (\rho_g c + \rho_N h\,\frac{\lambda}{W+\lambda}) g\,ah\,\sin 2\alpha \qquad \text{(III.20)}$$

which is independent of b. For the sake of simplicity, the term corresponding to the weight of NOA walls can be neglected. Indeed, the surface density of walls $\frac{\lambda}{W+\lambda}$ is small (around 10%), and we have usually $h < c$ (except for very thin plates). Hence, the force is just proportional to h:

$$F \sim \rho_g c g\, a h \, \sin 2\alpha \tag{III.21}$$

This inertial argument allows us to qualitatively capture all experimental observations: we see all the experimental points collapse in a single curve in figure III.19.

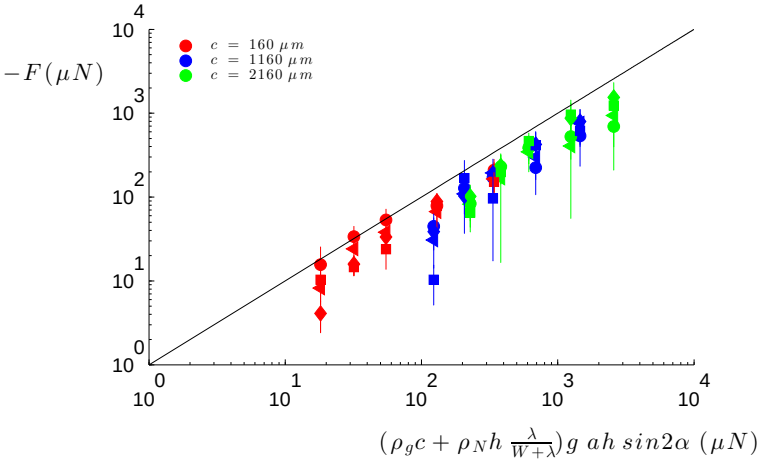

Figure III.19 – Force of propulsion as a function of the theoretical expression expected from equation III.20. The solid black line represents equation y = x. Each color correspond to a lamella thickness. Markers are the same as the ones used in previous figures.

Deviation for shallow textures (first cluster of points for each color) In the previous discussion (see section 4), we showed how the Reynolds number strongly depends on the channel depth (as $h^{5/2}$), in the viscous regime. In the case of our lamellae geometries, we saw that viscous effects would dominate only up to $h \approx 200$ µm. For texture walls higher than that, inertial effects would take over. Since $h \in$[150, 250, 400, 800, 1600], we are clearly in an inertial case for all our points excepted for $h = 150$ µm ($h = 250$ µm is also discutable). That corresponds to the first cluster of points of each color curve in figure III.17 and III.19. We expect a smaller force where both inertia and viscous effects (opposing inertial effects) are comparable. This effect is less visible for the thickest plate (green points): weight is so large that we need strong airflows to generate levitation, so that inertia completely dominates, regardless of height h.

6 Conclusion

All this work, based on air levitated objects, confirms the propelling viscous entrainment scenario discussed in the case of Leidenfrost textures. We have seen how this "cold Leidenfrost" setup overcomes the problem of high temperatures and deformable interfaces. An analytical model has paved the way to new geometries. Given that we can freely increase the air injection, we were able to explore the effect of heavier sliders or deeper textures (this time engraved on the slider itself). As a consequence, a whole new propelling mechanism based on an inertial scenario was found, and observed to reverse the direction of propulsion.

Although these two regimes (low versus high Reynolds number) are based on different physical mechanisms (viscous effects versus inertial ones) they surprisingly obey the same scaling law for the force $|F| \sim \rho_g c g\, ah \sin 2\alpha$. This is somehow explained by the fact that we experimentally chose to impose the same pressure in both regimes, that is, the one exactly compensating the objects weight. Since flow onset is pressure governed, it is not so surprising to find same scaling.

Inertial propulsion has open multitude of new questions that are currently being under study in the lab (PhD of Hélène de Maleprade). A first one would be to produce a quantitative analytical model for the inertial regime taking into account the geometrical parameters of the porous plate (as done when textures were engraved on the air blowing table) - hence involving the external imposed overpressure ΔP. The question of special friction would lead to the study of terminal speed of these objects and would require a new set up allowing to reach such velocities. All our experiments have been made with air as the injected liquid/gas phase. It will be mostly interesting to change the nature of the entraining material (hence probing the role of viscosity η) by replacing air by a liquid such as water. Another interesting question concerns the regime of $\mathrm{Re} \approx 1$, where both viscosity and inertia are comparable. Would it be possible (at small airflow injection) to entrain by viscosity the slider in one direction and make it propel in the opposite direction (at higher airflow injection)?

This experiment shows that provided we satisfy the main ingredients to achieve self-propulsion (i.e. gas rectification, break of symmetry), we can imagine a new zoology of self-propelling devices. More generally, the herringbone geometry was discussed in a wide range of different domains and applications. It was recently used in microfluidic channels for mixing liquids [109]. It has been widely used in gear technology in order to smoothly transfer power (the logo of the car maker Citroën is a graphic representation of a herringbone gear, reflecting French André Citroën's earlier involvement in the manufacture of these gears). Finally, this pattern, greatly used in artwork, can even be found in ancient Bactria back in time as far as 5000 years ago. Astonishing objects as the hairpin shown

in figure III.20 already displayed almost all explored textures of this chapter: herringbones, herringbone sections facing each other and in the center a windmill texture! With our current manufacturing techniques (easier, faster and cheaper), we should be highly encouraged to search for new geometrical patterns.

Figure III.20 – Bactria hairpin, open work, bronze. We can observe in the middle a windmill pattern and, circling it, a herringbone loop.

Chapter IV

Drop impacting a sieve

Contents

In this chapter, section 4 was done in collaboration with Pr. Robert Cohen and Siddarth Srinivasan.

1 Impact on a solid plate: a brief review

A naive method to generate a non-wetting drop is simply to suppress its substrate. However, as a price to pay for such an easy method, nothing sustains the liquid anymore, which is just a falling drop. By nature, this contactless state cannot be maintained and the globule will inevitably encounter a substrate at the end of its fall. In this chapter, we focus on this catastrophic event: the impact of a drop. We focus on the interesting situation of an impact on a mesh. A grid, that is, a mixture of holes and closings, is an intermediate case between a solid plate (i.e. a mesh with no holes) and no obstacle (a grid with holes only). In order to remain as close as possible to a contactless situation, we consider non-wetting sieves, either Leidenfrost or superhydrophobic. We privilege a qualitative description of this rich system, even if we also make at some point more quantitative models.

Impact of a drop on a solid substrate has been lately studied due to its ubiquity in everyday life. For printing, coating or spraying, from pesticides to rain [26, 134], it is essential to understand the collision mechanisms of a drop. This problem is more complex than appears at first sight. We can decompose the whole impact process in four main stages for a non-wetting substrate:

(i) at the very first moment of contact we have a singularity problem that arises many questions regarding pressure and speed profiles [45], short time dynamics [44], compressibility effects [119, 26, 79] or bubble entrapment [33, 116, 125, 117] among others,

(ii) a second spreading phase follows this early stage. Two main scenarii have then been reported [95]: splashing at high speed [130, 100, 54, 132, 131, 106, 75, 123, 118] and a strong deformation at contact at slower speed, [91],

(iii) after the drop spreads up to a maximum radius [24, 2], it eventually retracts due to capillary forces,

(iv) depending on the wetting properties of the substrate, retraction can lead to several scenarii such as equilibrium, rebound [6], or even singular jets [7].

Many other aspects have been, and are still, explored [134, 130]. Special attention has been given to the influence of the substrate [122, 55, 123, 36, 72, 78, 80, 54], to the role of the surrounding gas [132, 131, 75, 136, 106], or to the nature of the liquid (Newtonian, shear thinning, polymeric [8]).

In what follows, we will focus on the spreading phase where neither splashing nor jetting are present and where the surrounding gas can be neglected in the dynamics. We will give particular attention to two key features: the maximal spreading radius, and the height shape profile.

1.1 Maximal impacting radius

We adopt here the description of Clanet and collaborators [24], who focused (among others) on the maximal extension of an impinging drop - a question of practical importance since it defines the mark made on a solid by such drops. Two regimes are discussed according to the liquid viscosity:

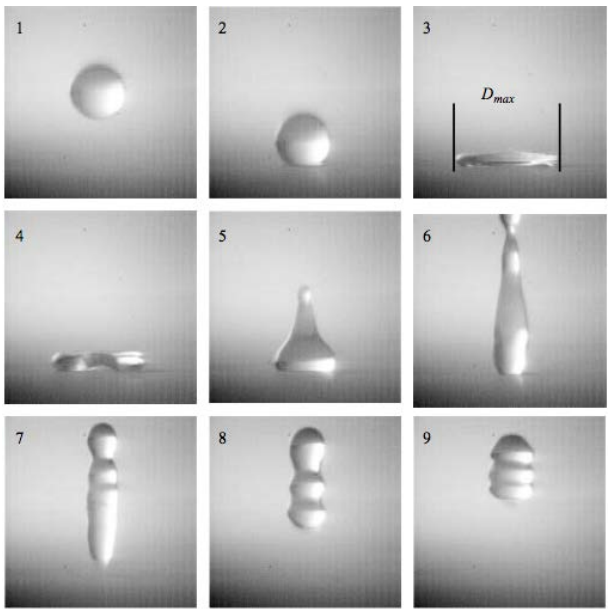

Figure IV.1 – Impact of a water drop ($2R_0 = 2.5$ mm, $V_0 = 0.83$ m s^{-1}) on a super-hydrophobic surface. The drop spreads (image 2 and 3) until it reaches its maximal diameter $D_{max} = 2R_{max}$. After a recoiling phase (image 4 to 6), a rebound (images 7 to 9) is observed, together with strong vibration. Time interval between the pictures: 2.7 ms. Figure from [24].

Low viscosity drops In the limit of low viscosity and low wettability (water on a super-hydrophobic surface), the maximum radius R_{max} of the drop was found to scale as $R_0 \mathrm{We}_0{}^{1/4}$, where R_0 is the drop's radius before impact and We_0 the so-called Weber number. This dimensionless quantity compares kinetic and surface energy. For a drop of radius R_0, a liquid of surface tension γ and density ρ, and an impact velocity V_0, the Weber number is:

$$\mathrm{We}_0 = \frac{\rho V_0^2 R_0}{\gamma} \tag{IV.1}$$

This scaling was found to hold on more wettable surfaces, and interpreted as resulting from the equation of motion: during the shock the drop experiences an effective acceleration $g^* \sim V_0^2/R_0$ (since it slows down from impact speed V_0 to rest in a characteristic

crashing time $\tau \sim 2R_0/V_0$), much more intense than the gravity field: g^* flattens the liquid and fixes its thickness to a capillary length where gravity field g is replaced by deceleration g^*. Hence a thickness: $\ell_c^* \sim \sqrt{\frac{\gamma}{\rho g^*}}$. Conservation of volume ($R_0^3 \sim R_{max}^2 \ell_c^*$) yields:

$$R_{max} \sim R_0 \, \mathrm{We}_0{}^{1/4} \tag{IV.2}$$

Recent work by Tran et al. [122] extended this study to impacts on super heated surfaces. Similar to static Leidenfrost drops, the impact behavior can be separated into three regimes: contact boiling, gentle film boiling, and spraying film boiling. In the two last regimes (both occurring when the surface temperature is higher than Leidenfrost temperature T_L), the maximum deformation displays universality ($R_{max} \sim R_0 \mathrm{We}_0{}^{2/5}$) regardless of the variation in surface temperature and liquid's properties. In the latter situation, spreading is lubricated by a gas layer between the drop and the solid surface. Tran and coworkers suggest that this steeper scaling law may be due to an extra driving mechanism caused by the evaporating vapor radially shooting outwards and taking liquid along.

Although equation IV.2 describes the experimental observations, it has been verified for a small range of We numbers. S. Chandra and C. Avedisian [22] suggested another scenario describing their measurements based on energy conservation: initial kinetic and surface energy of the spherical drop $4\pi R_0^2\gamma + \frac{1}{2}\frac{4\pi R_0^3}{3}V_0^2$ is transformed after impact into deformation $2\gamma\pi R_{max}^2$.

High viscosity drops The case of more viscous liquids was also analyzed, and a criterion for predicting if the spreading is limited by capillarity or by viscosity was derived. Kinetic energy of the impinging drop (on the order of $\rho R_0^3 V_0^2$) being dissipated by viscosity during impact (and indeed there is no more any rebound), the associated energy scales as $\eta\frac{V_0}{h_d}R_{max}^3$, h_d being the thickness of the maximal drop. Together with volume conservation ($R_0^3 \sim R_{max}^2 h_d$), this yields:

$$R_{max} \sim R_0 \, \mathrm{Re}_0{}^{1/5} \tag{IV.3}$$

where the Reynolds number is $\mathrm{Re}_0 = \frac{\rho R_0 V_0}{\eta}$ ([22, 90]).

Impact Parameter In order to differentiate between the inviscid case ($P < 1$) and the viscous case ($P > 1$), an impact number $P = \mathrm{We}_0/\mathrm{Re}_0{}^{4/5}$ can be defined. The transition between the capillary and the viscous regime is shown in figure IV.2, where the dimensionless viscous extension $R_{max}/(R_0 \, \mathrm{Re}_0{}^{1/5})$ is plotted as a function of the impact number P. The transition between the two regimes is very clear. It occurs around $P = 1$,

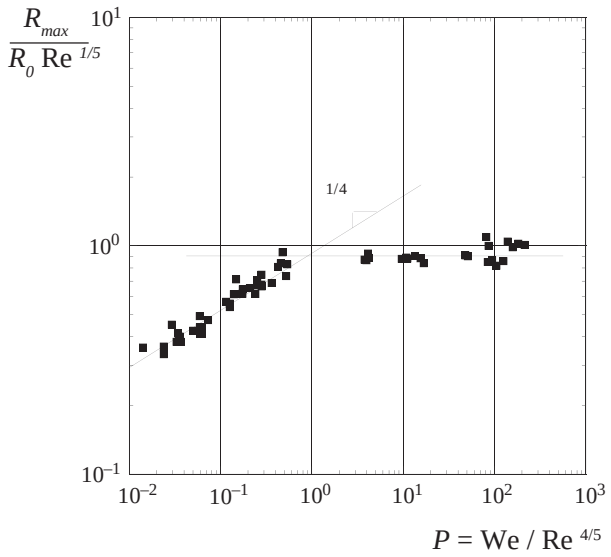

Figure IV.2 – Dimensionless deformation of an impinging drop (where the maximal extension R_{max} is normalized by the maximal deformation in the viscous regime $R_0\,\mathrm{Re}_0{}^{1/5}$), as a function of the impact number $P = \mathrm{We}_0/\mathrm{Re}_0{}^{4/5}$. Two regimes are successively followed, which corresponds to the capillary and viscous regimes (equations IV.2 and IV.3 respectively). The transition occurs around $P = 1$. Figure from [24].

as expected, since all the numerical coefficients were (experimentally) observed to be close to unity. The capillary regime ($P < 1$) is likely to be observed at small velocities, for small viscosities and large surface tension.

1.2 Drop shape profile

Lagubeau et al. [63] recently measured the drop shape during impact (over a solid surface) using space-time-resolved Fourier Transform Profilometry technique (FTP). They observe three distinct dynamical regimes of spreading for the time evolution of the film thickness at the center of the drop $h_c(t)$, as shown in figure IV.3.

These three regimes have been theoretically and numerically described by Roisman [96] and Eggers [45], and will be discussed below:

$\mathbf{t < \tau/2}$ The early time regime is a linear decrease corresponding to the free fall of the top of the drop (black solid line in figure IV.3). The apex continues falling at speed V_0 until the pressure impact reaches the top of the drop (approximatively at $\tau/2$).

$\mathbf{\tau/2 < t < t}_p$ We have an intermediate phase (red solid line in figure IV.3) where the interface velocity $-\frac{dh_c}{dt}$ decreases. In this regime, Eggers et al. [45] predicted a self-similar solution for the surface profile based on a hyperbolic (inviscid and potential) flow solution:

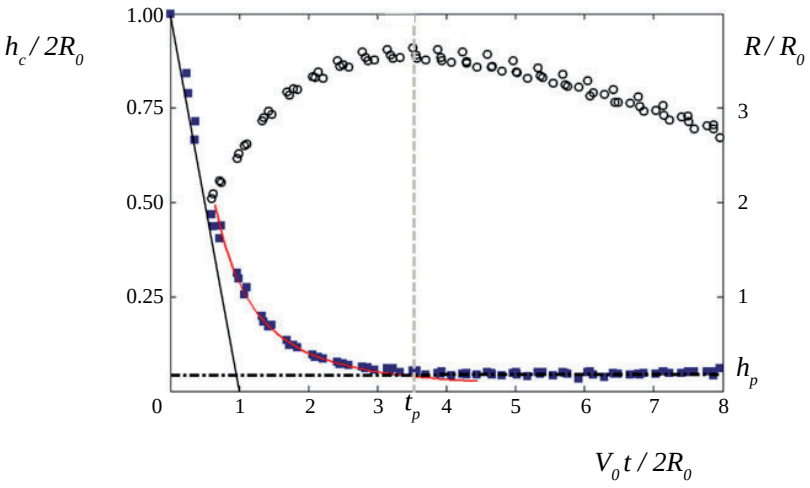

Figure IV.3 – Squares and left vertical axis: height h_c of the top of the central point of the drop surface as a function of time for $We_0 = 214$ and $Re_0 = 2690$. Circles and right vertical axis: radius of expansion $R(t)$ of the same drop. The solid line indicates the free fall regime. Red curve is the best fit of $h_c(t)$ (equation IV.4) during the self-similar regime from which $H(0)$ and t_0 are experimentally obtained. Black dashed-dotted line corresponds to the final plateau height h_p. Vertical dashed line is the crossing time t_p between the two previous regimes. Figure from [63].

$h(w,t) = 2R_0 \frac{\tau^2}{(t+t_0)^2} H(\frac{w}{V_0(t+t_0)})$. Here w denotes the radial position in the drop and t_0 is an unknown parameter whose physical significance is the time it takes for the pressure to decay and for the hyperbolic flow to establish: the flow at intermediate times is no longer pressure driven. This theoretical prediction is in good agreement with experimental measurements realized by Lagubeau et al. From the self-similar solution, we can deduce the time evolution for the central height of the drop: $h_c(t) = h(w = 0, t)$.

$$h_c(t) = 2R_0 \frac{\tau^2}{(t + t_0)^2} H(0) \tag{IV.4}$$

We can get rid of t_0 by re-expressing it in terms of the total drop volume[1]. We show in red solid line in figure IV.3 the best fit of equation IV.4, from which the two unknown parameters t_0 and $H(0)$ have been experimentally calculated by Lagubeau and coworkers: $t_0 \approx \tau/2$ and $H(0) \approx 1/2$. For $t = \tau/2$, this solution verifies $h_c(\tau/2) = R_0$ ensuring height continuity with the free fall regime.

$t > t_p$ At large time (black horizontal dashed-dotted line in figure IV.3), h_c tends to a plateau value h_p (if the drop rebounds, this plateau naturally disappears). A viscous boundary layer is found to grow from the substrate with a thickness scaling as $h_l(t) \sim \sqrt{\nu t}$

[1]See [63] for proper calculation.

(where $\nu = \eta/\rho$ is the kinematic viscosity). The asymptotic plateau film thickness h_p is obtained as the growing boundary layer meets the drop surface. The intersection of this two thicknesses defines a new characteristic plateau time t_p (vertical dashed line in figure IV.3). For $t >> t_p$, the equality $h_l(t_p) = h(w,t_p)$ scales as: $\sqrt{\nu t_p} \sim R_0 \frac{\tau^2}{t_p^2}$, hence:

$$t_p \sim \tau Re_0^{1/5} \tag{IV.5}$$

The theoretical prediction is again in good agreement with the observations by Lagubeau et al. We see that t_p scales as τ (where $t_p > \tau$) with a small dependance over the Re number (power $1/5$) and we always have $t_p > \tau$. For a millimetric water droplet, typical Reynolds range around 1000 so that we have $t_p \sim 4\tau$.

2 Impact on a plate with a single hole

As first step towards the study of impacts on grids has been done by Lorenceau and collaborators. They studied the configuration [77] of a plate of thickness e pierced with a circular hole of radius r smaller than the drop and the capillary length (see figure IV.4). This set up can be seen as a mixture of two opposite conditions: the hole allowing the liquid to flow freely, the substrate forcing it to deviate.

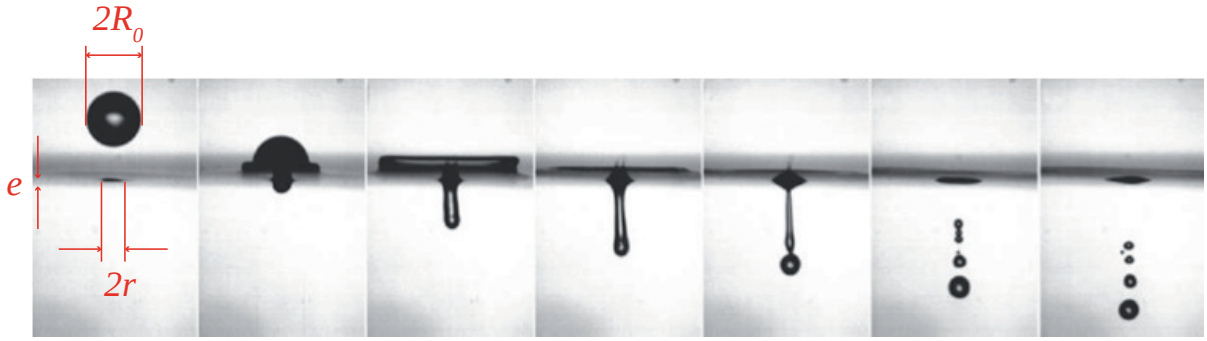

Figure IV.4 – Set of pictures taken each 2 ms apart. Drop of radius $R_0 = 1.75$ mm, hole radius $r = 450$ µm, impact speed $V_0 = 70$ cm/s, plate thickness $e = 250$ µm. Liquid (silicone oil) is ejected from the surface and forms several droplets. Figure from [77].

2.1 Critical speed V^*

In this problem, liquid inertia is always the driving force opposed by two forces: on the one hand, viscous friction related to the crossing of the hole, and on the other hand, capillary forces which oppose the formation of a liquid filament. To highlight the contribution of these two forces, the natural parameters to consider are the Reynolds number and the Weber number (associated to the hole dimension r and not to the drop radius R_0), defined as:

$$\mathrm{Re} = \frac{\rho V_0 r}{\eta} \qquad \mathrm{We} = \frac{\rho V_0^2 r}{\gamma} \tag{IV.6a}$$

In both cases, there is a threshold velocity V^* above which inertia overcomes the resisting forces and liquid passes through the hole. Lorenceau et al. focused on these two numbers at the threshold velocity V^* and reported in figure IV.5 the variation of We^* as a function of Re^* for various liquids and hole radii. Three regions can be observed in figure IV.5:

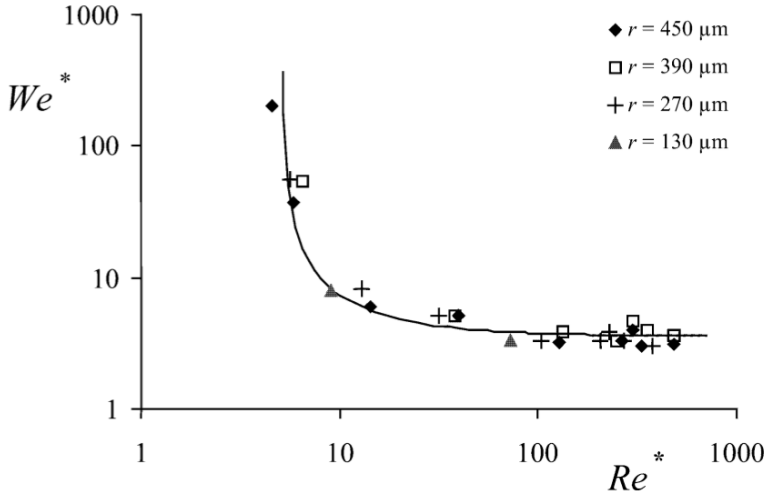

Figure IV.5 – Threshold velocity of capture: the Weber number at threshold is plotted as a function of the Reynolds number at threshold. The data are obtained using a $e = 250$-µm-thick plate, different hole radii, and various liquids (silicone oils of viscosity ranging between 0.5 and 300 mPa s, ethanol, acetone, heptane, and water). The thin line is the curve Re^* (We^* - 3.6) = 5.1 We^*, where the scaling comes from equation IV.7. Figure from [77].

Low Re number: viscous-inertial regime In the limit of small Re, the viscous force is dominant and it is responsible for the capture of the drop: this leads to a vertical asymptote $\mathrm{Re}^* \approx 5$ in figure IV.5.

Intermediate Re number For intermediate Re ($5 < \mathrm{Re} < 100$), the two numbers are observed to depend on each other. Both the capillary and the viscous forces play a role. In the limit of very thin plates ($e < r$), the viscous force associated with the crossing of the hole can be dimensionally written $\eta V_0 r$ (the velocity gradients taking place on a size of order r). The capillary force opposing the formation of a liquid finger scales as γr. Balancing these two forces with inertia gives an equation for the threshold: $\rho {V^*}^2 r^2 \sim \eta V^* r + \gamma r$. This yields:

$$\mathrm{Re}^* \sim \frac{\mathrm{We}^*}{\mathrm{We}^* - 1} \tag{IV.7}$$

where all the numerical coefficients have been ignored. An equation of the type IV.7 is indeed found to describe fairly well the data in figure IV.5, where the equation $\mathrm{Re}^*(\mathrm{We}^* - 3.6) = 5.1\,\mathrm{We}^*$ is drawn with a thin line.

Large Re number: capillary–inertial regime At large Re ($\mathrm{Re} > 100$), the critical Weber number is found to be constant, of about 3.5: the critical speed does not depend on viscosity and is set by a balance between inertia (dynamic pressure $1/2\rho V_0^2$) and capillarity

(resisting pressure γ/r). Hence a critical speed:

$$V^* = \sqrt{\frac{2\gamma}{\rho r}} \tag{IV.8}$$

The We number can be re-expressed as $\mathrm{We} = (\frac{V_0}{V^*})^2$. Therefore, the threshold condition $V_0 = V^*$ is $\mathrm{We} = 1$.

This speed threshold can be also interpreted in terms of speed of retraction of a liquid finger. As explained by Taylor [114] for thin planar liquid sheets, the speed of retraction is driven by capillary forces, scaling as $2\pi r\gamma$ in the case of a cylindrical geometry.

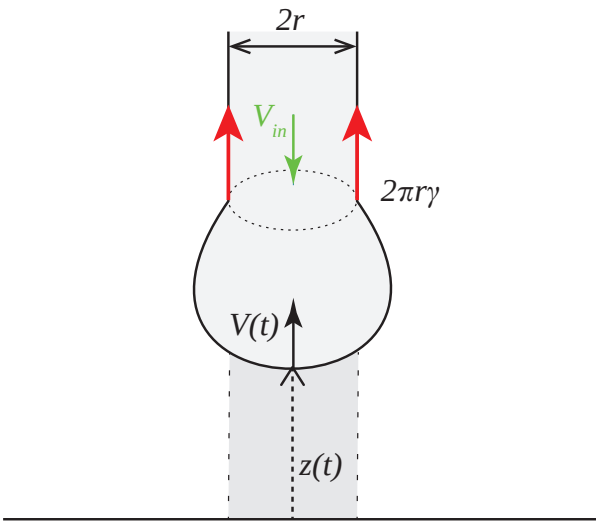

Figure IV.6 – Sketch of retracting liquid finger while liquid is injected at speed V_{in} from the top in the opposite direction. Due to mass conservation, during retraction mass accumulates forming a liquid blob.

By denoting $z(t)$ the position of the bottom of the retracting extremity (where mass is accumulating, see figure IV.6), we get the following equation of motion:

$$2\pi r\gamma = \frac{d}{dt}(M\frac{dz}{dt}) \tag{IV.9}$$

Mass accumulated at the bottom end of the finger M, is equal to the mass previously distributed in a cylinder of section πr^2 (shaded in figure IV.6), hence $M = \rho\pi r^2 z(t)$. Inserting the conservation of mass in the equation of motion yields:

$$\frac{d^2z^2}{dt^2} = \frac{4\gamma}{\rho r} \tag{IV.10}$$

Assuming finite speed and initial position $z(0) = 0$, we get after integration a speed of retraction independent of time:

$$V(t) = V^* \tag{IV.11}$$

Clanet et al. [25] refined this model in order to explain the transition between dripping and jetting. They take into account the possibility of vertical injected speed V_{in} (in green in figure IV.6, in direction opposite to retraction). The equations are consequently modified and we consider here the particular case where we can neglect gravitational forces (a fair assumption if the mass accumulated has size negligible compared to the capillary length). We have to add a dynamic pressure term $\rho\pi r^2 V_{in}(V(t) + V_{in})$ to the equation of motion IV.9, now becoming:

$$\rho\pi r^2 V_{in}(\frac{dz}{dt} + V_{in}) + 2\pi r\gamma = \frac{d}{dt}(M\frac{dz}{dt}) \tag{IV.12}$$

The conservation of mass being now $M = \rho\pi r^2(z(t) + V_{in}t)$, we finally get[2]:

$$\frac{d^2z^2}{dt^2} + 2V_{in}t\frac{d^2z}{dt^2} + 4V_0\frac{dz}{dt} = \frac{4\gamma}{\rho r} - 2V_{in}^2 \tag{IV.13}$$

Which has the following exact solution[3]:

$$V(t) = V^* - V_{in} \tag{IV.14}$$

We see that if $V_{in} = V^*$, we have $V(t) = 0$. In the case of a drop impacting a hole, V_{in} is the impact speed V_0. If $V_{in} > V^*$, the speed $V_{ej} = -V(t)$ of the ejected liquid finger becomes :

$$V_{ej} = V_{in} - V^* \tag{IV.15}$$

2.2 Role of plate thickness

In the same capillary–inertial regime, Lorenceau et al. also tested the influence of the plate thickness e on the critical speed V^*. They compared two plates of respective thickness 0.25 mm and 1.7 mm and found that the threshold of capture is weakly affected by thickness. It was observed that the critical speed is slightly higher for a thicker plate, which can be due to an additional viscous dissipation along the hole.

[2]If we take V_{in}=0, we get back to equation IV.10.

[3]To see more model refinements such as variable cylinder radius or role of gravity, see [25].

2.3 Several time scales

This problem has a multitude of different time scales. Two of them are associated to impact itself: the time of rebound T_{reb} and the time τ it takes the drop to impact. A last timescale concerns the liquid passing through the hole, namely the characteristic time T_{des} of destabilization of the liquid cylinder. In what follows we will discuss each time in more detail.

Time of rebound: $\mathbf{T_{reb}}$

The impact of a water drop on a super-hydrophobic substrate (or on a Leidenfrost surface) is generally followed by a rebound [52]. The restitution coefficient of the shock can be very large (around 0.9), so that a drop can bounce many times before stopping [94]. A rebound is possible because the kinetic energy of the impinging (non-viscous) drop can be stored in deformation during impact. The contact time has been studied [93, 87] and shown to scale[4] as $\sqrt{\rho R_0^3/\gamma}$. This variation, independent of the impact velocity V_0, can be understood by considering (globally) the rebound as an oscillation: the drop is a spring of stiffness γ and mass ρR_0^3, which oscillates with a constant period:

$$T_{reb} \sim \sqrt{\frac{\rho R_0^3}{\gamma}} \tag{IV.16}$$

For millimetric water droplets this time is typically 10 ms.

Time of finger destabilization: $\mathbf{T_{des}}$

In the capillary–inertial regime, the mechanism of transformation of a liquid cylinder into droplets was explained by Plateau and Rayleigh more than a century ago. Surface tension tends to minimize surface area, hence transforms cylinders into spheres. For a liquid column of small viscosity, the destabilization takes place in a time T_{des} obtained by balancing inertia (on the order of $\frac{\rho r}{T_{des}^2}$) with capillarity (on the order of $\frac{\gamma}{r^2}$), which yields:

$$T_{des} \sim \sqrt{\frac{\rho r^3}{\gamma}} \tag{IV.17}$$

It is interesting to see T_{des} as the time to close a cavity of size r at the Culick speed V^*: $T_{des} \sim \frac{r}{V^*}$. Destabilization time T_{des} has the same capillary-inertial nature than the time of rebound T_{reb}, hence a similar scaling law. The main difference dwells in the characteristic length scale: destabilization occurs on a distance scaling as the hole radius r, whereas rebound implies the drop radius R_0. Since T_{reb}/T_{dis} scales as $\sqrt{R_0^3/r^3}$ and

[4]This rebound time has naturally the same scaling as the period of spontaneous oscillation of drops (discussed in chapter I, section 2.3) since it is also based on inertia/capillarity balance.

$R_0 > r$ we always have: $T_{des} < T_{reb}$. For holes ten times smaller than the drop size (which is typically the case in our experiments), rebound is approximatively thirty times slower than liquid filament destabilization.

Crash time: τ

The time of rebound T_{reb} can also be compared to the time τ it takes for the drop to crash. The apex of the drop has to cover a distance $2R_0$ at speed V_0, so that τ can be defined as:

$$\tau = \frac{2R_0}{V_0} \tag{IV.18}$$

We typically have $R_0 \approx 10\ r$, hence $\tau > T_{des}$. For instance, a millimetric water drop arriving at $V_0 = 1$ m/s has a crash time of 1 ms. For a mesh with holes of size $r \approx 100\ \mu$m, the destabilization time is $T_{des} \approx 0.1$ ms, which means that the liquid cylinder destabilizes much faster (here 10 times faster) than it takes the drop to completely crash.

2.4 Transmitted mass

We suggest a simple scaling law giving the amount of liquid that passes through the hole. The finger is being ejected at a typical speed $V_{ej} = V_0 - V^*$. The total transmitted volume per unit time will scale as $\pi r^2 V_{ej}$. We now have to discuss which is the right timescale over which we have to integer this flow rate to access the transmitted mass. Three different regimes can be considered regarding the ratio $\frac{\tau}{T_{des}} \sim \frac{2R_0}{V_0}\frac{V^*}{r}$:

$T_{des} << \tau$

The liquid finger destabilizes faster than it takes for the drop to crash. The liquid jet is permanently pinching off, we are in a kind of dripping regime. As a consequence, the destabilization of the finger will not affect the amount of transmitted mass but only its geometry[5]. Mass will be transmitted all along the crashing time τ, hence transmitted mass m_T scales as $\rho R_0 r^2(1 - \frac{V^*}{V_0})$, an increasing function of the impact speed V_0. Its saturation value $m_T^{max} \sim \rho R_0 r^2$ is naively the mass contained in a cylinder of surface area πr^2 and height $2R_0$, that is, the drop height. Rescaling by the initial drop mass $m_0 \sim \rho R_0^3$ we get:

[5]An asymptotic scenario can be proposed by taking an imaginary drop of infinite radius R_0 (i.e. a continuous jet), ensuring the condition $\tau > T_{des}$.

$$\frac{m_T}{m_0} \sim \frac{r^2}{R_0^2}\,(1 - \frac{V^*}{V_0}) \tag{IV.19}$$

$T_{des} >> \tau$

Liquid is injected through the hole during a time τ smaller than the time of destabilization: the finger never pinches off. We form a liquid finger that will eventually stop falling and retract owing to capillary forces (following the Culick/Taylor speed of retraction V^*). As a consequence, no mass will be transmitted. Hence, two conditions have to be satisfied in order to transmit liquid through a hole. First, we need the liquid to have enough inertia to form a liquid finger (i.e. $V_0 > V^*$). Then the liquid has to pinch off (governed by the Rayleigh-Plateau destabilization mechanism) and detach avoiding to be retracted and recaptured due to capillary effects.

A marginal case: $T_{des} \sim \tau$

A very particular situation is observed when $T_{des} \approx \tau$ where we observe a unique pinch-off event. Several cases can be foreseen:

- if $T_{des} \lesssim \tau$ the liquid finger will pinch off shortly before the end of the impact. After this first pinch-off, even if the drop is still crashing (hence a small fraction of liquid still being injected), liquid will retract before a second pinch-off happens. Even if this effect is marginal, less mass will be transmitted and the correct time to be considered here is T_{des}.

- if $T_{des} \gtrsim \tau$ the liquid finger will pinch off shortly after the end of the impact. In a situation where there is a downwards driving force (such as inertia or gravity), the liquid finger can continue to fall and entrain supplementary liquid from the upper drop, increasing the transmitted mass. We can even imagine a situation where the finger falls and partially retracts before the first pinch-off occurs, the ultimate situation being a complete retraction (i.e. $T_{des} >> \tau$, previously addressed).

In this context, Lorenceau et al. proposed an alternate model based on the pinch-off time as characteristic timescale. The critical time should hence be the Rayleigh-Plateau time T_{des} (instead of τ). The arising scaling law gives: $m_t \sim \rho r^3(\frac{V_0}{V^*} - 1)$. Once rescaled by the initial mass, it yields:

$$\frac{m_T}{m_0} \sim \frac{r^3}{R_0^3}\,(\frac{V_0}{V^*} - 1) \tag{IV.20}$$

This second scenario predicts a transmitted mass increasing linearly with impact speed that does not saturate for any value. We show in figure IV.7, experimental data from Lorenceau et al.: transmitted mass (rescaled by ρr^3) as a function of the normalized

impact speed. The red region corresponds to a destabilization time faster than impact, modeled by equation IV.19 (red line) and capturing the steep slope for $V_0 \sim V^*$. The blue region corresponds to the case where pinch-off time dominates. It is modeled by equation IV.20 (blue line). A fair agreement is observed with the data.

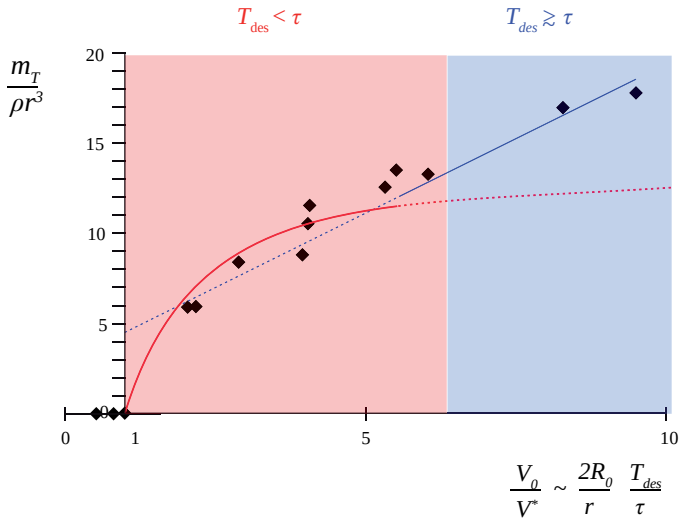

Figure IV.7 – Volume of ejected liquid (rescaled by ρr^3) as a function of the ratio V_0/V^* for different radii. Red and blue lines show equation IV.19 and IV.20, respectively. Data extracted from [77].

2.5 Final comment

The study of drop impacting a plate with a single hole shows that the key timescale in this problem is the crashing time $\tau \approx 1$ ms. Indeed, we have seen that rebound phenomenon is to slow (characteristic time typically on the order of 10 ms) to play any role and destabilization of liquid filament into droplets (characteristic time typically on the order of 0.1 ms) only modifies the shape of the enveloppe of passing liquid (but not its amount).

Nonetheless, marginal situations (where τ is not anymore the key time) can be observed by playing with the other timescales of the problem: T_{reb} and T_{des}. A whole new (and quite complex) zoology of regimes can be discussed. For instance, for low We numbers (where capillarity dominantes inertia) and non wetting plates, we can imagine that a drop will bounce faster than it crashes ($T_{reb} < \tau$), hence the limiting time now being T_{reb}. As a direct consequence, we expect an amount of transmitted mass lower than the one predicted by our previous scaling law.

3 The Leidenfrost sieve

We now have all elements to study impacts on a grid. After discussing the experimental details of our set-up, we wonder how much liquid we can grate through a sieve. A scaling law will allow us to qualitatively predict the amount of transferred mass. A more refined analytical model will lead us to focus on the deformation of the drop during impact due to horizontal evacuation of the liquid: as a consequence, we observe an increase in the section through which liquid is transferred and an ejection speed decrease at the end of the crash. We finally discuss how lateral spreading plays a role in the formation of a cone of ejected droplets.

3.1 Experimental set-up

We study in this section the impact of a drop on a Leidenfrost grid. We use a mesh of plain-woven brass wires of diameter $d = 0.17$ mm and square holes of lateral size $l = 0.37$ mm (see figure IV.16a). The corresponding surface fraction of square holes is $\phi = \frac{l^2}{(l+d)^2} = 47\%$. Since liquid avoids corners (where curvature is high), we assume that liquid ejected from this square holes will have a circular shape. The associated characteristic radius[6] is $r = l/2 \approx 0.19$ mm, which yields a slightly smaller surface fraction for the circular holes: $\phi^* = \frac{\pi}{4}\phi$.

We avoid all wetting phenomenas by heating the mesh to the Leidenfrost state. We qualitatively control the mesh temperature by heating it with a Bunsen burner until it reaches red-hot metal. To avoid any perturbation of the flame, we turn it off just before the drop impacts the grid. A simple argument allows us to estimate the proportion of mass loss due to evaporation. During an impact of characteristic time $\tau \sim 2R_0/V_0$, we get an evaporated mass scaling as $\delta m \sim \rho S_e c_e \tau$, where S_e denotes the surface of evaporation - scaling as $(1-\phi)\ R_0^2$ - and c_e denotes the speed of evaporation. Normalized by the initial mass of the drop, we get $\delta m/m_0 \sim (1-\phi)c_e/V_0$. For impact speeds of several m/s and typical evaporation speed c_e of 10 cm/s we get a loss of a few percent, allowing us to neglect mass losses due to evaporation. We can also try to estimate the thickness of the insulating layer around a hot wire using the classical Leidenfrost thickness equation (seen in Chapter I, section 2.2, equation I.18). The squeezing pressure will be the one generated by capillarity (γ/r, where $1/r$ is the local curvature radius of the liquid finger) and the characteristic escaping length scale will be d. As consequence, we expect typical local vapor thickness e_L of several tens of μm, slightly thinner than the vapor film beneath

[6]This hole length is slightly smaller than the one studied by Lorenceau and coworkers where their biggest hole was $r \approx 0.5$ mm.

a Leidenfrost puddle. As a consequence of the presence of this vapor film, the surface area through which liquid is injected becomes smaller. The corresponding critical speed should now be $V^* = \sqrt{\frac{2\gamma}{\rho(r-e_L)}}$. Since $r/e_L << 1$, the change in critical speed remains small (within measurement scattering): in what follows, we keep the definition of the critical speed unchanged (i.e. defined without e_L).

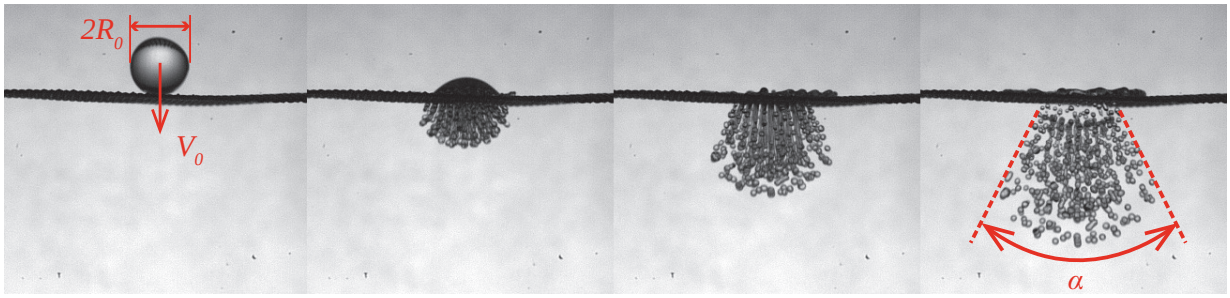

Figure IV.8 – Side view of a drop of radius $R_0 = 1.9$ mm impacting a hot grid at speed $V_0 = 1.6$ m/s. First image is used to define origin of time as being the first moment the bottom of the drop touches the grid. Second and third images represent the time it takes for the drop to crash: $\tau = 2R_0/V_0$. This time being larger than the Rayleigh-Plateau time, liquid filaments destabilize in tiny droplets. On the last image, there is no vertical momentum at the upper part of the mesh and no mass is transmitted. Grated droplets fall conserving their momentum and form a cone of angle α. Image are separated by 2 ms.

Drops in this study are formed by means of a syringe and a needle (internal diameter $d_{int} = 1.16$ mm, external diameter $d_{ext} = 1.7$ mm), which provides a drop radius $R_0 = 1.9$ mm. The syringe is fixed to a vertical beam and its height varies as to generate different impact speeds V_0 ranging between typically 0.5 m/s to 5 m/s. We record the impact from the side with a fast camera (typical frame rate 10000 fps), using backlighting to enhance contrast.

A typical impact is shown in figure IV.8 where we observe that part of the liquid passes through the sieve while the rest remains on top. On the upper part of the grid, everything happens as if we had an impact on a non-wetting substrate: we first see a spreading phase (together with liquid passing through the holes), followed by a recoiling phase (were mass is conserved) and a rebound (not shown on figure IV.8). On the lower part of the grid, we observe liquid filaments with a radius comparable to the size of the holes, which quickly destabilize in tiny droplets. They form a very well defined 3D cone characterized by an angle α (see figure IV.8).

3.2 Transmitted mass

Experiments

As previously stated, drops hitting the grid have only two possibilities: they pass through the holes, or they are stopped and horizontally redirected. We measure the transmitted mass by positioning a plastic sheet parallel to the grid at approximatively 10 cm below it. By this means, we harvest immediately after impact the transmitted droplets and weight them with a high precision scale. We repeat this experiment for each falling height (hence several impact speeds V_0).

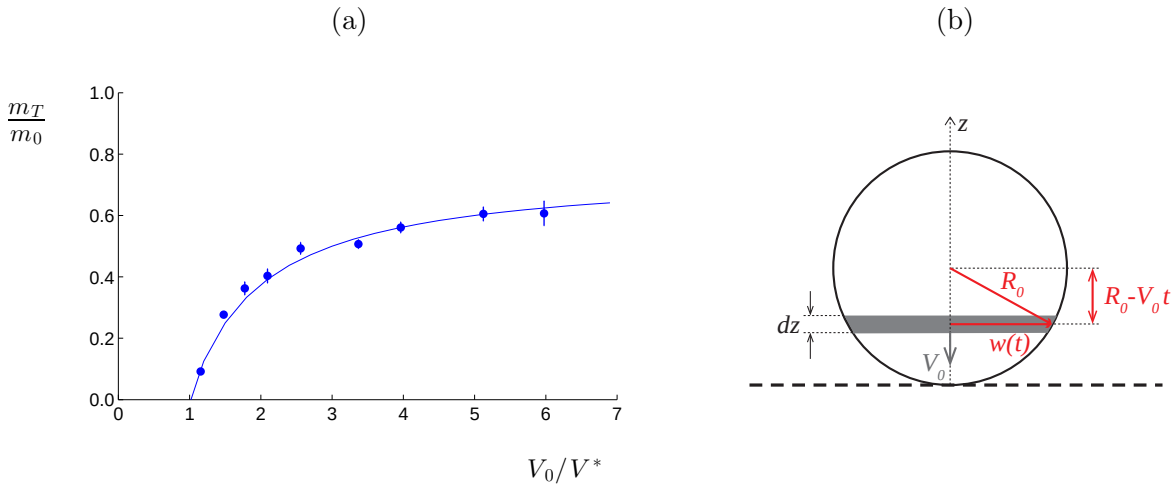

Figure IV.9 – (a) Percentage of transmitted mass as a function of impact speed normalized by the inertio-capillary speed $V^* = 0.65$ m/s. The solid blue line is equation IV.21 multiplied by a factor 3/2. (b) Sketch of drop at initial time $t = 0$. Since drop falls at speed V_0, slice at position z will reach the mesh at $t = z/V_0$. Pythagorus theorem yields the expression of $w(t)$ as a function of time, initial speed and drop radius.

We show in figure IV.9a the transmitted mass fraction m_T/m_0 ($m_0 = 4/3\pi R_0^3$ being the initial mass of the liquid) as a function of impact speed. Three regimes are clearly visible:

(i) for $V_0 < V^*$, the drop has not enough inertia to overcome capillary forces ($V_{ej} < 0$), hence even if small filaments transiently sag into the holes, they retract and no mass is transmitted ($m_T = 0$),

(ii) just above V^*, we observe a fast increase of transmitted mass,

(iii) for $V_0 >> V^*$, we get a saturation value below $m_T/m_0 = 1$.

In order to better understand these observations, we need to specify and compare the value of all the different timescales. Since drop radius $R_0 = 1.9$ mm and hole size $r = 0.19$ mm are fixed, we get: $T_{des} \approx 0.3$ ms, $T_{reb} \approx 10$ ms and $\tau \in$ [1,10] ms (in our

range of impact speeds). Liquid cylinder destabilization being much faster than the crash time $\tau > T_{des}$, the characteristic time to be considered to calculate the transmitted mass is τ (as discussed in section 2.5).

Crash time being always smaller than the rebound time, we can ignore bouncing effects. In addition, Reynolds number ranges between 100 and 2000 (validating the inertia-dominated assumption), and Weber number ranges from 0.5 up to 100.

Scaling law

To explain these behaviors we suggest the following simple scaling law. For $V_0 > V^*$, we expect the flow rate through a single hole to scale as $r^2(V_0 - V^*)$. By multiplying this flow by the number of holes N (scaling itself as $\phi R_0^2/r^2$) and the crash time $\tau = 2R_0/V_0$, we get for the total transmitted volume: $\Omega \sim \phi R_0^3 \frac{V_0 - V^*}{V_0}$. As a consequence, the fraction of transmitted mass scales as:

$$\frac{m_T}{m_0} \sim \phi \left(1 - \frac{V^*}{V_0}\right) \tag{IV.21}$$

We show in figure IV.9a that equation IV.21 is in very good agreement with the data, provided we chose a numerical factor of 3/2. Indeed:

(i) equation IV.21 is defined only above V^*,

(ii) it predicts a local slope $\frac{dm_T}{dV_0} = \phi \frac{V^*}{V_0^2}$. This slope rapidly decreases (as $1/(\frac{V_0}{V})^2$), hence being maximum for $V_0 = V^*$, which explains the fast increase of transferred mass just above V^*,

(iii) for high impact speed V_0, it predicts a saturation towards $m_T/m_0 \sim \phi < 1$.

Analytical model

We now move a step further, and produce an analytical model. We adapt the equation giving the transmitted mass through a single hole (equation IV.19) by imagining the drop as being a vertical assembly of discs of radius $w(t)$ and thickness dz (see figure IV.9b). Each slice arrives onto the grid at speed V_{in}. Since $V_{ej} = V_{in} - V^*$, the flow rate through a single hole is $\pi r^2 V_{ej}$. Mass is transferred through $N(t) = \frac{\pi w^2}{(2r+d)^2} = \frac{\pi}{4}\frac{w^2}{r^2}\phi$ holes. Factor $\frac{\pi}{4}$ reflects the fact that even though our holes are square, mass is transmitted through cylinders, hence not filling all the available space.

Total mass is calculated by integration over the crash time τ, hence:

$$m_T = \phi^* \rho \int_0^\tau V_{ej}(t)\, \pi w^2(t) dt \tag{IV.22}$$

For instance, if we assume the drop does not deform and remains perfectly spherical during impact, we have $V_{ej} = V_0 - V^*$ independent of time. From Pythagorus theorem

(applied to the triangle described by red arrows in figure IV.9b), we get: $w^2(t) = 2R_0V_0t - (V_0t)^2 = V_0^2(t\,\tau - t^2)$. Hence:

$$\int_0^\tau \pi w^2(t)dt = \frac{4\pi R_0^3}{3}\frac{1}{V_0} \tag{IV.23}$$

and

$$\frac{m_T}{m_0} = \phi^*\,(1 - \frac{V^*}{V_0}) \tag{IV.24}$$

We retrieve the same scaling as predicted by equation IV.21. In addition, this analytical model gives a geometrical prefactor equal to unity. However, equation IV.24 assumes the drop remains spherical during all impact time. Hence, this would be close to the case of hole surface fraction close to unity (almost no obstacle), which is not the case in our experiment. We conclude that the experimental higher prefactor (of 3/2) arises from the deformation of the interface at impact.

3.3 A deformable interface

For low mass transfer, falling liquid has to be strongly evacuated in the horizontal direction, resulting in the deformation of the drop's interface. The lower the transferred mass, the closer we are to a situation of impact on a solid plate. We try here to explore the consequences of this deformation and its effect on the transmitted mass. To do so, we focus on the speed of ejection $V_{ej}(t)$ and the spreading radius $w(t)$, two time-dependent quantities integrated over time to obtain the transferred mass (equation IV.22).

Speed profiles

Experimental observations In order to access the different speeds of the problem, we extract from each frame of impact movies the vertical line of pixels that passes through the axis of symmetry of the drop. We then horizontally concatenate them, resulting in an image (commonly called "reslice") where x-axis represents time and y-axis represents vertical distance. Typical curves are shown in figure IV.10. We can deduce speed as the local slope (schematically represented in green or red in figure IV.10). To increase accuracy, we developed a Matlab routine to access impact speed V_0 at the exact moment when the bottom of the drop first touches the grid, (which defines the time origin $t = 0$).

We observe two regimes depending on the impact speed: (i) for $V_0 < V^*$ (left image in figure IV.10), no liquid passes through the hole, hence $V_{ej} = 0$, (ii) for $V_0 > V^*$ (center and right image in figure IV.10), we first have $V_{ej} \approx V_0$ and then we observe a decrease in time of the ejection speed (shown by a slope decrease in figure IV.10).

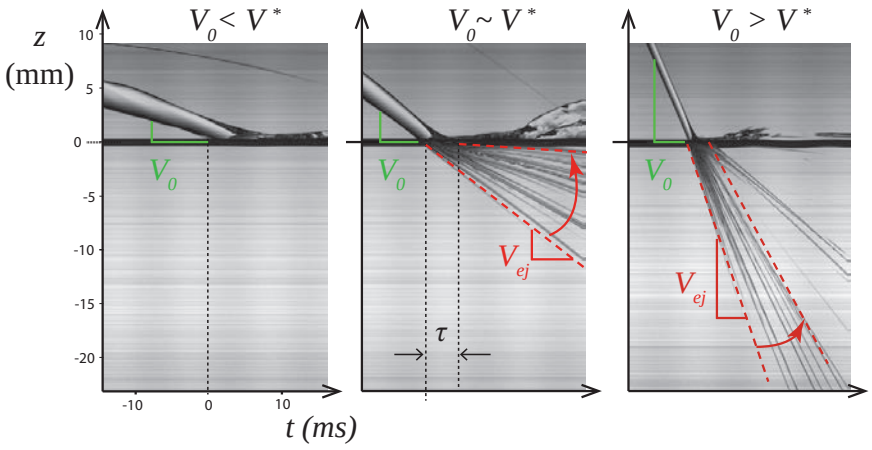

Figure IV.10 – Spatiotemporal diagram for drops impacting a sieve. (Left) Inertia is not strong enough to overcome capillary effects, hence no liquid passes below the grid (placed at $z = 0$). Local slope in green gives impact speed V_0. (Center) Inertial and capillary forces are comparable. In red, trajectory of ejected droplets whose slope is V_{ej}. As time goes on, from $t = 0$ to $t = \tau \sim 2R_0/V_0$, we see this speed decrease. (Right) Inertial regime. Speed V_{ej} of ejected daughter droplets is almost the same than V_0 the mother one.

The limit case: impact on a solid plate As observed, smaller transferred mass implies stronger speed decrease. The asymptotic limit (almost no mass transferred) was described by Lagubeau et al. for an impact on a solid plate. We deduce the injection speed V_{in} from the speed of the apex of the drop $h_c(t)$ (equation IV.4): $V_{in} = V_c(t) = \frac{dh_c(t)}{dt}$. Finally, we get:

$$V_{in}(t) = \begin{cases} V_0 & \text{if } t < \tau/2 \\ V_0 \frac{1}{(\frac{t}{\tau}+\frac{1}{2})^3} & \text{if } t > \tau/2 \\ 0 & \text{if } t > t_p \end{cases} \qquad \text{(IV.25)}$$

We represent equation IV.25 in figure IV.11 where speed profile of the apex of the drop (rescaled by the critical speed V^* for a hole of size $r = 190$ µm) is a function of normalized time for different impact speeds $V_0 = 0.9$; 1.4; 1.9; 2.4; 2.9 and 3.4 m/s, and for a drop radius $R_0 = 1.9$ mm.

These speed variations teach us that even if V_{in} is initially above the critical speed V^*, it eventually goes below it before the end of the crash. The moment at which liquid stops to flow through the hole is denoted as t_s. Its expression is given by the condition

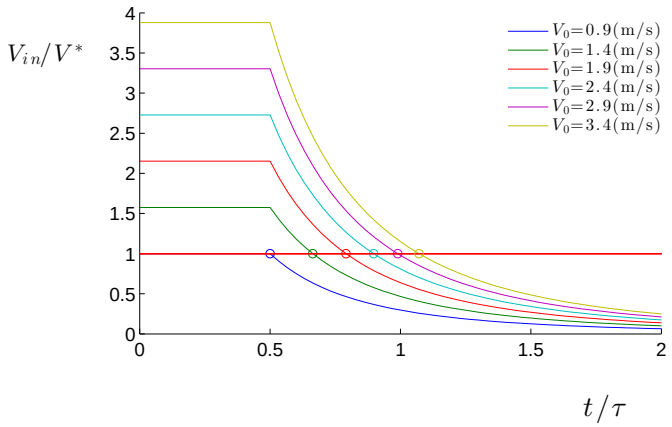

Figure IV.11 – Representation of equation IV.25: speed of the apex of an impacting drop on a plain solid (rescaled by the critical speed V^* for a hole of size $r = 190$ µm) as a function of normalized time for impact speeds $V_0 = 0.9$; 1.4; 1.9; 2.4 and 2.9 m/s. Circles on the red horizontal line shows for each curve the moment when the speed of injection is not strong enough to pass through the hole. Since in this case $t_p/\tau \gtrsim 4.5$, t_p is not visible in the figure.

$V_{in}(t_s) = V^*$, which yields:

$$t_s = \tau\,[(\frac{V_0}{V^*})^{1/3} - \frac{1}{2}] \tag{IV.26}$$

We indicate t_s in figure IV.11 for different impact speeds (circles on red horizontal solid line).

Although this model describes the decrease of vertical speed observed for drops impacting a solid plate, we assume that the same physical ingredients remain qualitatively unchanged for the case of pierced plates.

Transfer section

Another quantity varying with time during impact is the horizontal distance by which mass is injected. Owing to lateral deformation of the drop, we expect a transfer surface greater that πR_0^2, as shown in figure IV.12 where the red horizontal arrow denotes the maximum real surface πw_{max}^2 through which mass is transmitted.

We expect $w(t)$ to vary from 0 to w_{max} during impact, where w_{max} cannot exceed the maximal spreading radius R_{max} discussed in section 1.1. Although we have not done any quantitative measurements, we observe that w_{max} is a function of transferred mass. For high mass transfer, almost no liquid is horizontally evacuated, hence there is almost no lateral spreading and we have: $w_{max} \approx R_0$. For low mass transfer, liquid has to be horizontally redirected and we expect w_{max} to be a fraction of R_{max}.

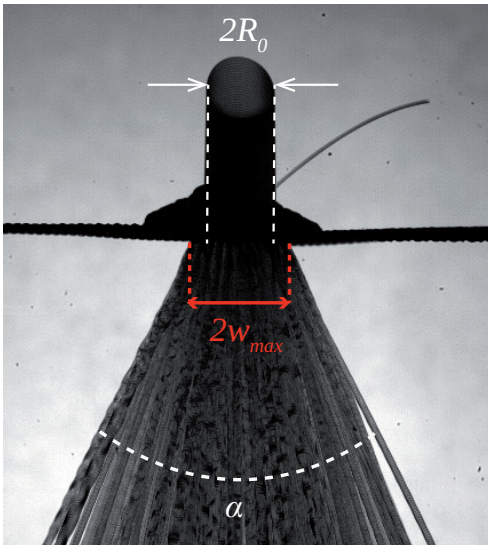

Figure IV.12 – Chronophotography (image superposition) of drop of radius $R_0 \approx 2$ mm impacting a grid at $V_0 = 1.6$ m/s. Red symbols show that mass is transmitted through a surface πw_{max}^2 larger than πR_0^2.

We experimentally observe that w_{max} can be as high as $3/2R_0$. Since transferred mass depends on the square of w_{max}, this corresponds to an increase of mass as high as a factor 2, justifying that the geometrical prefactor obtained experimentally can be higher than predicted with a perfect spherical assumption.

The mesh: a mixture in between a hole and a solid plate

Previous discussions on speed profiles and transfer section were mainly based on the study of two known asymptotic situations: almost no transferred mass (modeled by an impact on a solid plate), and high transferred mass (modeled by almost no obstacle). Even though they qualitatively explain the speed decrease and the lateral increase of transferred section, we would need an analytical solution for the shape and speed profile in this intermediate case in order to correctly model the transferred mass. A good starting point would be to adapt and extend the hyperbolic solution proposed by Eggers et al. to the particular case of the grid.

3.4 Splash pattern

Another measurable quantity characterizing the impact is the angle α of the cone formed by the passing droplets. We show in figure IV.13 a series of chronophotography for different impact speeds (obtained by adding all frames of an impact movie for a given speed). We observe that the higher the impact speed, the wider the opening angle. More quanti-

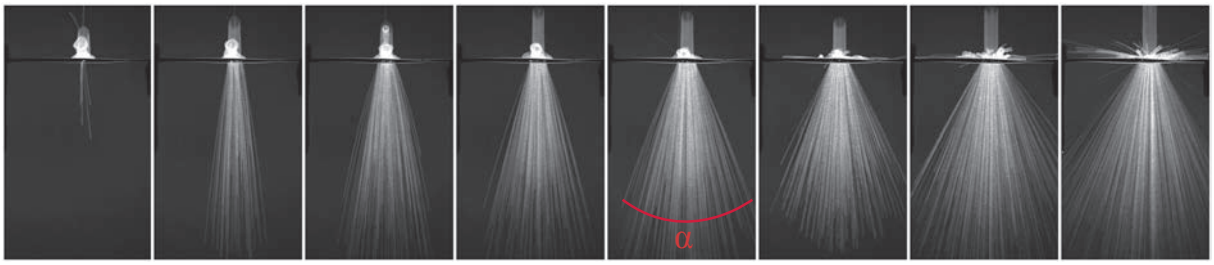

Figure IV.13 – Image set-up showing a chronophotography of the impact for different speeds $V_0 = 0.4$; 0.8; 1.1; 1.2; 1.6; 2.1; 2.5 and 3.1 m/s.

tatively, we show in figure IV.14a α as a function of impact speed V_0.

To understand the origin of the opening cone, we first discuss the filament ejection from a single hole. Since all the mass does not pass through the grid, liquid has to be horizontally redirected. Hence, injected liquid has both a vertical and horizontal component as sketched in figure IV.14b. The more the hole is off-centered from the axis of symmetry, the stronger the accumulation of horizontal redirected mass and the larger the horizontal component of the ejected liquid. As for the ejection cone, α is given by the ejection angle of the outer holes of the transmitting surface (the farther away from the center). As previously discussed, this transfer surface depends on impact speed V_0: the higher the impact speed, the the wider the transfer section, hence the larger the opening angle α (this justifies the behavior observed in figure IV.13). In other words, we can see the measure of the opening angle as an indirect measure of the maximal spreading radius!

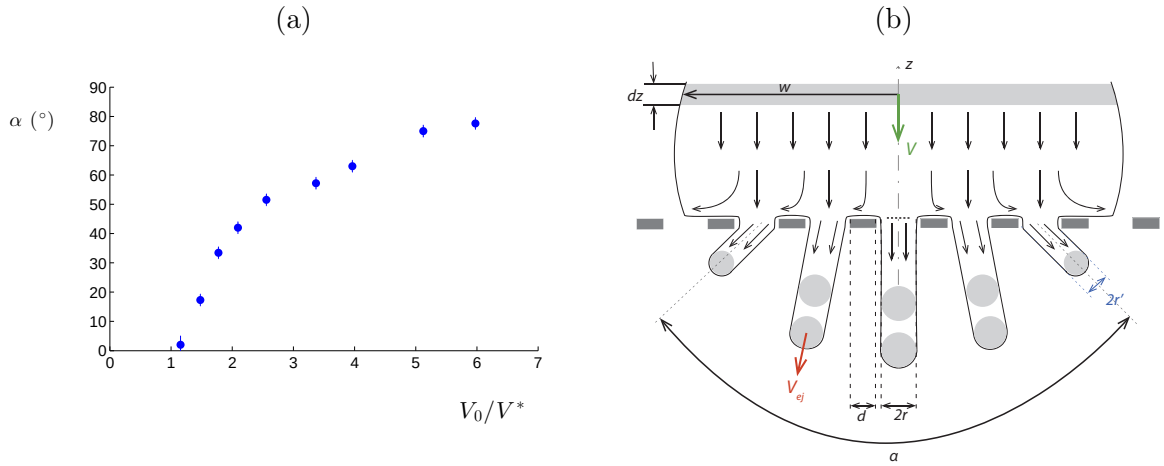

Figure IV.14 – (a) Ejection angle α as a function of normalized impact speed. (b) Sketch describing liquid injection through the holes: the more the hole is off-centered, the stronger the horizontal flow, and the horizontal ejection speed. In addition, al large α, the effective cross section $\pi r'^2$ (in blue) of ejected filaments becomes smaller.

Other features can be deduced from splashing patterns. For instance, Katsuhiko Yoneta from Hokkaido studied in 1932 the diffraction pattern made by a drop falling on a net [135]. He was struck by the regularity of the splash pattern analogous to the one seen for a diffraction pattern of X-rays through a crystal. He showed that splash pattern symmetry depends on the position of drop impact regarding mesh holes. He suggested three categories regarding if the center of the drop impacted on the middle of a hole, on the crossing of two fibers or on a combination of both. The different possible outcomes are shown in figure IV.15. The dotted circles of the left side of each figure indicate the initial size of the drop. If the volume of drop corresponds to circle n (on the left hand side), the corresponding splash pattern consists of spots 1 to n (on the right hand side). In our study we observed similar splash patterns. However, we were in the case where the circular radius of the drop was much bigger than the grid hole spacing. Hence, our patterns consisted on a multitude of spots splashed over a circular area, losing the memory of the square symmetry of the grid (somehow showed by K. Yoneta in figure IV.15 for big drop volumes).

A last comment can be made regarding the droplet sizes. We notice in figure IV.15c that the outer spotted drops are smaller than the center ones (observation also made in our experiments). This may be explained by the fact that, as the outer ejected filaments made an angle $\alpha/2$ with the vertical axis, the effective cross section of hole becomes $\pi r'^2 = \pi(\cos\frac{\alpha}{2}r)^2$ (in blue in figure IV.14b). As a consequence, ejected liquid finger has a smaller section resulting in smaller daughter droplets (of typical length scale r'). For instance, ejection of a filament with an angle α equal to $\pi/2$ will be twice smaller than if ejected vertically.

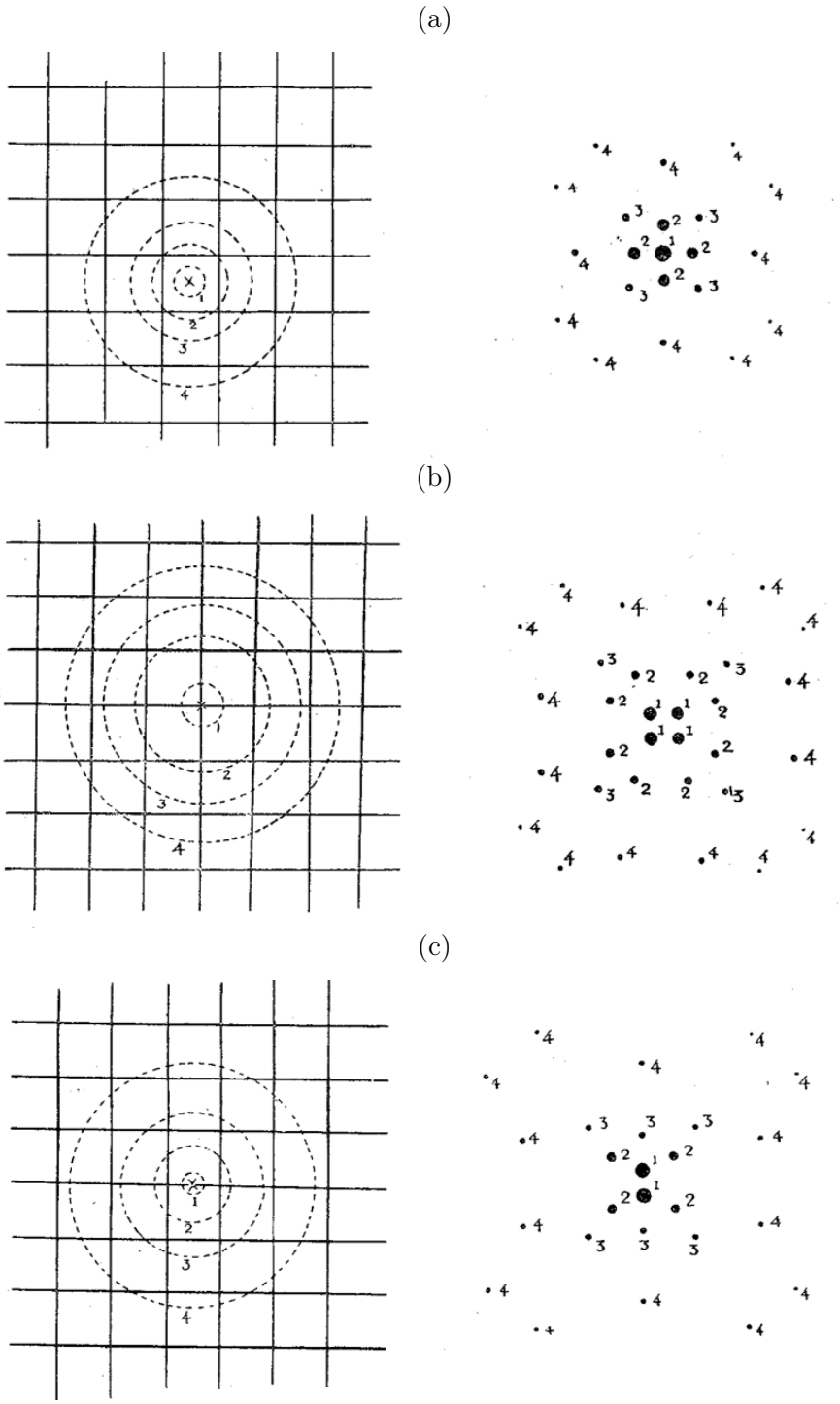

Figure IV.15 – Possible splash patterns (on a surface positioned below and parallel to the mesh) showed by Katsuhiko Yoneta. (a) Odd pattern: the center of the drop impacts on the center of a hole. (b) Even pattern: the center of the drop aligns on the intersecting point of two fibers. (c) Combined pattern: the center of the drop impacts in a mixed situation. For all figures, if the volume of the drop corresponds to circle n (on the left hand side), the spots of splash pattern become spots numbered 1 to n (on the right hand side). Figures from [135].

4 Exploring different meshes

Work in this section was motivated and done in collaboration with Professor Robert Cohen and Siddarth Srinivasan.

All our experiments were previously conducted with a unique Leidenfrost grid. Here, we want to explore the role of different parameters such as the wetting properties of the substrate or the role of the surface density ϕ of holes. The non-wetting state was formerly generated by heating the mesh above the Leidenfrost point, and we did not really control temperature or mass loss due to evaporation. In addition, meshes deformed due to thermal expansion. To avoid these problems, we now generate contactless substrates by coating the grids superhydrophobic.

(a)

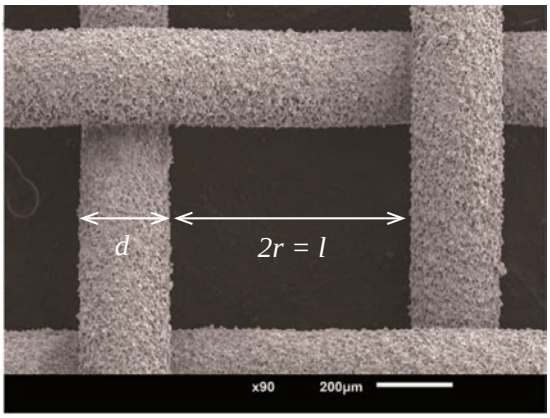

(b)

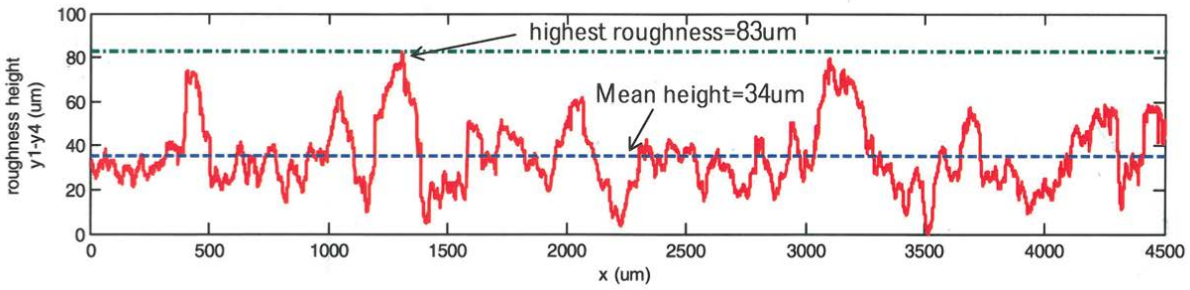

Figure IV.16 – (a) Scanning electron microscopy image of a spray-coated stainless steel mesh ($d = 254$ µm and $r = 330$ µmcorresponding to mesh C') which forms a surface with hierarchical texture (scale bar: 200 µm). The sprayed textures have a diameter around 20 µm. Figure from [60]. (b) Surface roughness information: the mean thickness of the superhydrophobic coating is found to be around $e_c \approx 30$ µm. Figure courtesy of Pr. Robert Cohen.

We created a panel of different meshes described in table IV.1 and denoted A, B,

C, D and J (previous brass Leidenfrost mesh is denoted as E). Meshes were provided by the group of Robert Cohen: each one came in two samples of same geometry but different wetting properties. The first sample made of stainless steel (McMaster-Carr) is further on referred as "plain mesh"[7]. The second sample, elaborated from the same grid, is coated superhydrophobic (referred as "SH mesh", and identified by an apostrophe sign). Coating was manufactured by Siddarth Srinivasan (from Robert Cohen group's) by spraying a PMMA and fluorodecyl POSS solution (low surface tension polymers) dissolved in Asahiklin AK-225 (protocol similar to the one done in [60]). The result of this spray is a thin coating of spherical structures of typical size 20 µm. The surface topography was investigated and shown in figure IV.16b. The coating slightly modifies the geometrical dimensions of the grid by increasing the wire diameter d and decreasing the hole radius r - each approximatively by $e_c \approx 30$ µm. For grid E, we have three samples: plain sample E, superhydrophobic sample E' and Leidenfrost sample E_L (the one studied in previous section).

Name	Wire diameter d (µm)	Hole size r (µm)	$\phi = \frac{1}{(1+d/2r)^2}$	$D^* = \frac{d+2r}{d}$	Mesh # (in^{-1})
A, A'	343	407	0.495	3.73	22
B, B'	140	229	0.586	4.27	42
C, C'	254	330	0.518	3.57	28
D, D'	508	452	0.410	2.78	18
E, E', E_L	170	190	0.477	3.24	46
J, J'	254	190	0.361	2.50	40

Table IV.1 – Table describing the geometrical properties of each mesh. Samples coated superhydrophobic are marked with an apostrophe. Values in three last columns are deduced from the dimensions r and d. They provide different criteria to characterize the meshes: ϕ is the surface fraction of square holes, D^* is the dimensionless spacing ratio of the texture, and the mesh number # represents the number of openings per (linear) inch. Colors are respected in the following figures.

4.1 Role of wetting conditions

We show in figure IV.17 a comparison of transmitted mass for the same mesh E, E' and E_L (mesh number # 46) and different wetting properties. Even if they have a similar physical behavior, we observe two main differences:

[7] Although there is a wide commercial choice of samples, we were not completely free to vary r and d independently, hence the arbitrary choice of geometrical parameters.

(i) the minimum critical speed for which mass is transferred is not the same (although they remain comparable). The superhydrophobic grid has the lowest speed V^*, then the Leidenfrost grid has a higher one and finally the regular wetting grid has the highest threshold speed,

(ii) for higher impact speeds the total amount of transferred liquid slightly differs. For example, taking the superhydrophobic grid as reference and focusing on impact speed $V_0 = 4$ m/s, regular plate has an increased transfer of 20 % while Leidenfrost grid has a decrease of 10%.

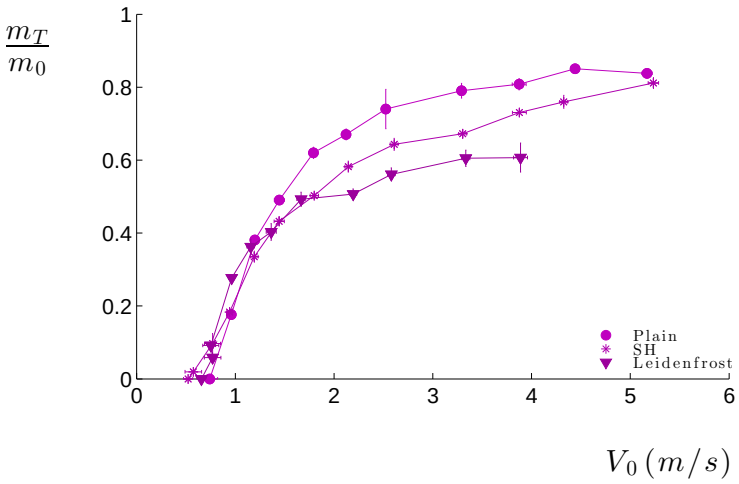

Figure IV.17 – Percentage of transmitted mass a function of impact speed. Three different wetting conditions are shown for the same mesh grid of wire size $d = 0.17$ mm and hole size $r = 0.19$ mm (meshes E, E' and E_L). The wetting brass mesh is denoted by "solid dots", the mesh treated superhydrophobic is denoted by "stars" and the Leidenfrost mesh is denoted by "solid triangles".

Previous remarks suggest the following explanations:

Square versus circular holes The first argument explaining the differences in liquid transfer is based on the square geometry of the holes (of side length l, see figure IV.16a). For a non-wetting mesh, we assumed that the surface through which liquid is injected is circular with a surface area πr^2, (where $r = l/2$), leading to a surface density ϕ^* corresponding to circular holes. This is a fair assumption for non-wetting liquids which avoid the corners generated by the crossing of two fibers - where local curvature is high. For wetting liquids, the real area to take into account is based on square holes of surface area equal to l^2, to which corresponds the surface density ϕ. As a consequence, we potentially get an increase in transmitted mass for wetting meshes up to $\frac{\phi}{\phi^*} = 4/\pi \approx 1.3$.

Coating thickness The wetting properties are modified by deposition of a small coating of thickness e_c (e_L for Leidenfrost sieves) around each wire (which reduces the

hole surface density). Taking into account this excluded thickness, the expression corresponding to the new surface density ϕ' is:

$$\phi' = \phi^* \, (1 - \frac{e_c}{r})^2 \tag{IV.27}$$

If we take $e_c \approx 30$ µm, we get $\phi' \approx 0.7\,\phi^*$, in agreement with the reduction of transmitted mass experimentally observed (between regular and super-hydrophobic grids). The same argument applies to the Leidenfrost sieve, suggesting that the vapor layer thickness e_L can even be greater than e_c.

4.2 Role of hole size r

To probe the role of hole characteristic size r, we compare in figure IV.18 the transmitted mass as a function of impact speed for meshes C and J which have same wire diameter $d = 254$ µm (in shaded gray in table IV.1) and hole size r almost twice bigger for mesh C (in red) than for mesh J (in dark green).

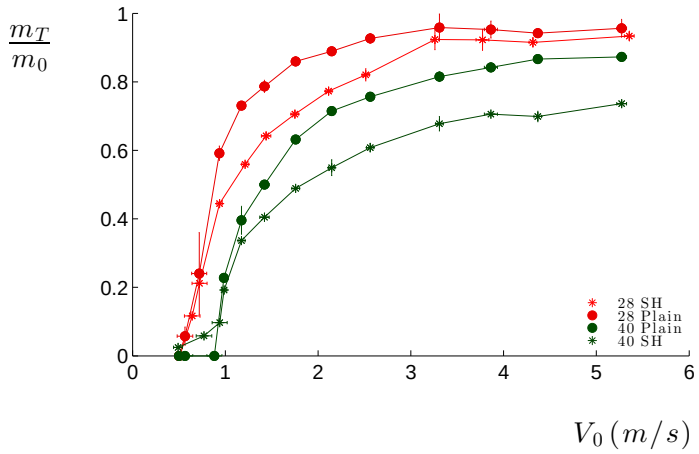

Figure IV.18 – Percentage of transmitted mass a function of impact speed for mesh C and C' in red, J and J' in dark green. "Solid dots" represent plain grids while "asterisks" represent superhydrophobic ones.

We observe a higher transmitted mass and a lower threshold speed V^* for mesh C (in red), as expected for bigger holes.

If we now focus on the difference between wetting and non-wetting properties, critical speed V^* remains almost constant for grids with big holes (mesh # 28 in red in figure IV.18). However, for small holes (mesh # 40 in dark green in figure IV.18), critical speed V^* of non-wetting grid is lower compared to the wetting one (effect also slightly visible in figure IV.17). As sketched in figure IV.19, this may be explained by the fact that the

local shape of the liquid filament near its base depends on wetting conditions.

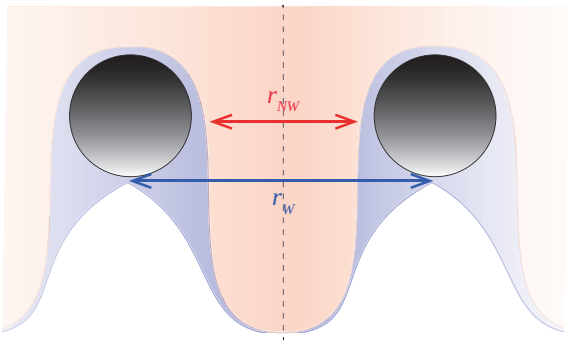

Figure IV.19 – Sketch of filament shape near its base. For impact speed $V_0 \approx V^*$, the filament slightly penetrates the texture. If the mesh is non-wetting (in red), filament has a size r_{NW} at its base. If the mesh is wetting (in blue), filament has a size $r_W > r_{NW}$ at its base.

Indeed, we assume here that pinch-off occurs at the base of the filament for impact speed V_0 close to V^*. If the mesh is wetting (situation in blue in figure IV.19), filament has a size r_W at its base. In the non-wetting situation (in red), filament has a size $r_{NW} < r_W$, facilitating the pinch-off and resulting in a lower critical speed V^*.

4.3 A single curve?

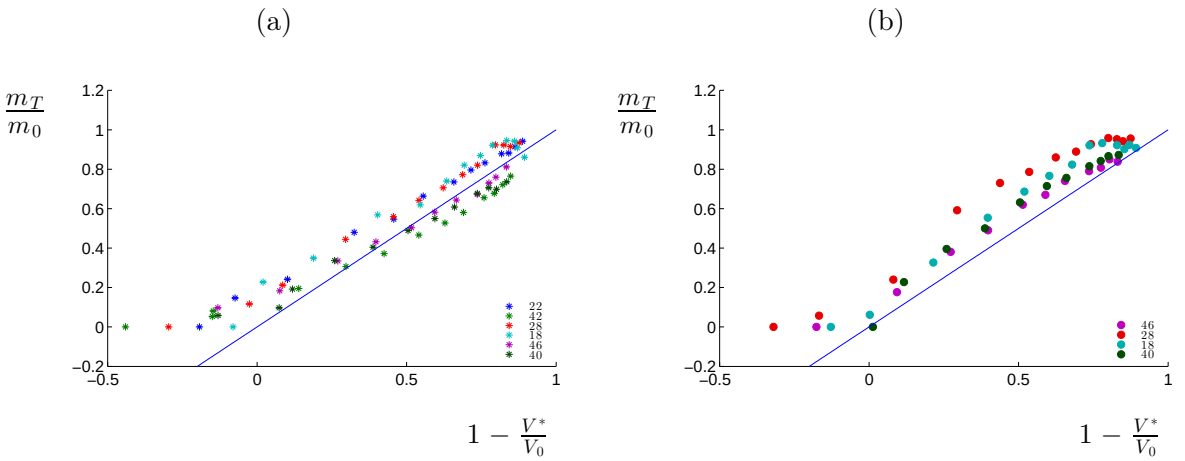

Figure IV.20 – Transferred mass as a function of impact speed, expected from scaling law (equation IV.21). Blue solid line shows equation $y = x$. (a) Superhydrophobic meshes. Mesh D' (in cyan) shows a saturation for high impact speed, probably due to the fact that we approach the marginal regime where $\tau \approx T_{des}$ (see section 2.4). (b) Regular wetting grids.

In this paragraph, we probe previous scaling (described in equation IV.21) by showing in figure IV.20 the percentage of transmitted mass as a function of $1 - V^*/V_0$. For all superhydrophobic substrates (left figure), we see all data collapse close to the line of equation $y = x$ - validating our model. However, we can also notice a slight mismatch, confirming the existence of marginal effects that stress the necessity to properly model the deformation of the interface, itself depending on the transferred mass. As discussed in section 4.1 (regarding wetting versus non-wetting effects), data for plain wetting textures (figure IV.20b) is systematically above non-wetting experiments (figure IV.20a).

4.4 Pinch-off time versus crash time

As done for a single hole, we now compare in figure IV.21 the ratio of the crashing time τ and the pinch-off time T_{des} as a function of impact speed V_0. We observe that all our experiments are in the regime where pinch-off happens faster than the crash time ($\tau/T_{des} > 1$), validating the choice of τ as the right timescale for the scaling argument.

However, meshes with big holes and small hole fraction ϕ (that is, meshes D and D', in cyan) are close to the regime $\tau/T_{des} \approx 1$ for high impact speeds. If we look back to figure IV.20, we indeed see a deviation for this mesh for high impact speed V_0, suggesting the apparition of new mechanisms, probably the ones described in section 2.4.

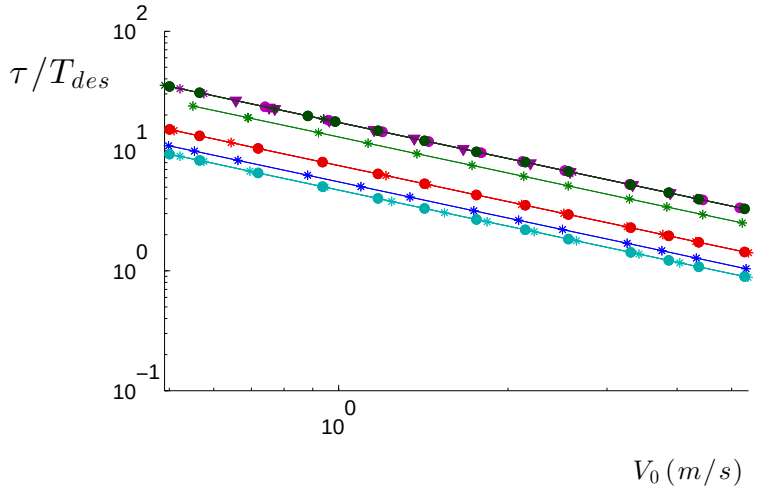

Figure IV.21 – Ratio between the crash time $\tau = 2R_0/V_0$ and pinch-off time $T_{des} \sim \sqrt{\rho r^3/\gamma}$ as a function of impact speed for each mesh (colors defined in table IV.1).

5 Conclusion and open questions

We focused in this chapter on drops impacting a grid. Experiments helped us to qualitatively differentiate the mechanisms that play a key role when liquid has to chose between flowing through a hole or being horizontally evacuated (when encountering a closing). Two main parameters were discussed: (i) the capillary speed V^* of retraction of liquid filaments forming through the holes, dictating if liquid has enough inertia to pass through a hole or not, and (ii) the time over which mass is transmitted. Although the natural time is the crash time τ, we can encounter marginal situations were the destabilization time of the liquid fingers or even the rebound time are to be considered. It will be of great interest to re-explore the experiment of an impact on a single hole (done by Lorenceau et al.) and try to experimentally shed new light on these regimes. A naive scaling law was deduced, qualitatively capturing the speed dependency of transferred mass. Since we would need to be more quantitative to model the interface deformation of the drop, a good starting point would possibly be to adapt the solution of a drop impacting a solid plate produced by Eggers et al.

We also observed that ejected liquid was confined in a cone of angle α. All our grids where thin, allowing the ejected liquid to be laterally deviated. An interesting question would be to see the effect of thicker grids on the opening angle α.

Finally, we explored the role of wetting properties. In general, suppressing liquid-solid contact greatly improves liquid mobility: we saw in previous chapters how tiny entrainment forces were able to move levitating objects. Transposing this argument to the case of drop impacts, we could have expected a greater transmitted mass for non wetting grids. However, we experimentally observed the opposite effect, confirming our assumption that viscous effects are negligible, even at relatively small length scales.

The only parameter that we have not varied is the drop radius R_0. It is experimentally difficult to vary drop size on a wide range. However, we conducted some preliminary experiments with liquid jets impacting grids. Since this new system is at dynamic equilibrium, it is a promising set up for better understanding the interaction of liquid with a mesh.

Few studies are found in the literature regarding impacts on smaller holes. Yet, Brunet et al. have tackled the problem of a superhydrophobic grid with holes of size $r \approx 5$ µm (a hundred times smaller than our experiments). For such small opening size, we should expect relatively high critical speeds: $V^* \approx 6$ m/s. However, they observed that mass is

transmitted for speeds V_0 up to 2 m/s, that is, three times smaller. Since We $= (\frac{V_0}{V^*})^2$, this means that mass was unexpectedly transferred for low We numbers - around 0.1. Similar behavior was also observed by Yarin and collaborators [70, 98] who focused on drop impacting electrospun nano fiber membranes with several micrometer non-wettable pores (porosity around 90 %). They also report transmitted mass for We smaller than unity. The origin of the discrepancy between measured thresholds and predicted ones remains unclear. However, above cited authors suggest a scenario based on collective effects leading to an additional pressure that contributes to make the liquid penetrate more easily through the grid. For instance, Yarin et al. suggest an expression of the penetration speed for a single hole scaling as $V_{in} \sim V_0 \frac{R_0}{r}$ based on a potential solution and liquid incompressibility [70]. This scaling can be interpreted as the result of the accumulation and channeling kinetic energy of a large mass of liquid through a narrow orifice.

Drop impacting a mesh can be seen as a simple set-up producing mono disperse sprays of tiny droplet. For impacts where no mass is transferred ($V_0 \lesssim V^*$), the mesh can also be seen as a tool for shaping drops. Indeed, recent work [76, 126] has shown how deformation of a drop impacting on cleverly designed superhydrophobic surfaces can lead drops to bounce from the surface with the distinct shape of a flat disc. This "pancake bouncing" is due to the storing of capillary energy in shape deformation during spreading phase. Before retraction sets in, it is restituted vertically into kinetic energy as sketched in figure IV.22.

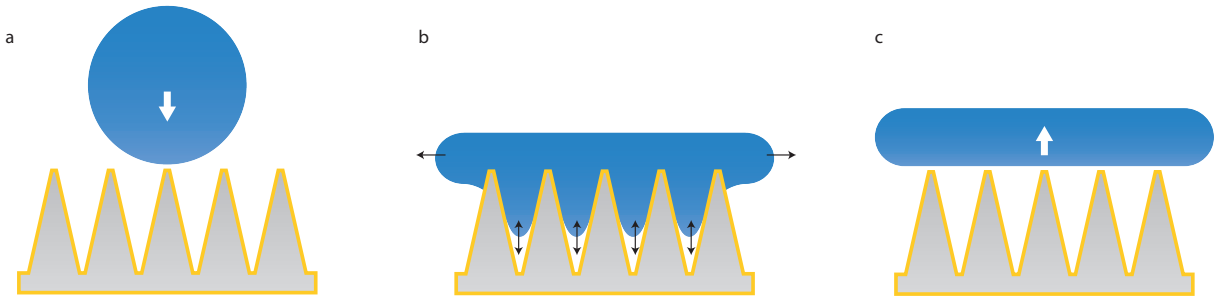

Figure IV.22 – Liu et al. [76] showed that a drop can lift-off from a surface before retraction sets in. This greatly reduces the contact time of the drop with the substrate. (a) A spherical drop just before hitting the structured surface. (b) Spreading and retraction dynamics can be modeled as a Hooke spring in both the horizontal and vertical directions. To decrease friction with the walls, the surface of the posts is coated with a superhydrophobic layer (yellow). (c) Lift-off. Figure adapted from [126].

Our grids represent a new way to shape drops in a similar way. They have the added advantage of having limited lateral walls and not having any bottom closings. Therefore, they represent a perfect alternate system for studying pancake bouncing.

Conversely, the situation of bigger holes (than studied here) has been recently addressed by de Jong and collaborators [32] who look at droplet impact near a millimeter-size hole. They showed that the behavior of an impact near a closed pit greatly differs from one on an open-ended pore. This should inspire further work focusing on the impact of sealing the exiting section of our grids on the drop spreading dynamics.

Chapter V

Impact force of a drop

Contents

1 Compression waves

We discussed in previous chapter the spectacular impact figure of a drop hitting a mesh. It was of particular interest to address two limit situations: the plain solid plate (i.e. surface fraction of holes $\phi = 0$), and the mesh with only holes ($\phi \to 1$). For an impact on a solid plane, we saw that liquid had no other choice than to be completely deviated horizontally. Hence, it is natural to think that the obstacle in this situation (that is, the plate) endures the biggest impact force. In this chapter, we only focus on the impact force of a drop on a solid substrate, a key quantity is soil erosion [26].

It is reasonable to assume that the heavier the drop, the stronger the impact force F, so that the drop radius R and density ρ naturally arise as key parameters in the study. However, as discussed in previous chapter IV, we have a geometrical singularity at early stages of the impact. Indeed, if we zoom on the bottom part of the spherical drop (see figure V.2), the interface is tangent to the substrate. Hence, the radial spreading of the contact interface is infinite at early stages, generating huge pressures - called water hammer pressures (denoted by P_{wh}). In what follows we discuss two different scenarios regarding the compressibility in the liquid or in the surrounding air.

1.1 Water hammer in the liquid

Theoretical expression

If we focus in the liquid inside the drop and take into account compressibility effects we will have right after impact a shock wave propagating upwards at the speed of sound (denoted as c). This shock wave can be interpreted as the limit separating two domains in the drop:

(i) upstream, where information that the drop has impacted arrived;

(ii) downstream where this information is still unknown.

Once the information has reached the whole drop (in a time $2R/c$), compressible effects vanish. This effect (also called hydraulic shock) commonly occurs when a valve suddenly closes at the end of a pipeline system, and a pressure wave propagates in the pipe. In the frame of the moving shock wave (as shown in figure V.1), we have again two regions separated by the shock front:

(i) the bottom of the drop (in red in figure V.1), where liquid is at rest;

(ii) the top of the drop (in blue in figure V.1), where liquid is still falling at speed V.

Conservation of mass in the pipe leads to:

$$\rho_1 = \rho_2(1 - \frac{V}{c}) \tag{V.1}$$

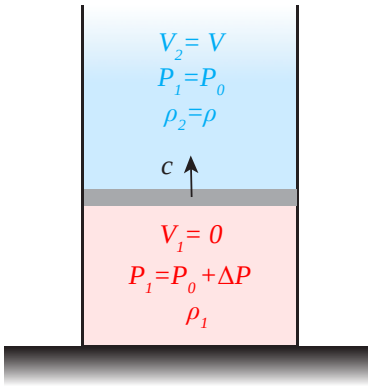

Figure V.1 – Shock wave (in grey) moving at the speed of sound c in a pipe of section S. In red, the bottom of the drop where liquid is at rest. In blue, the top of the drop where liquid is still falling at speed V.

Since $V << c$, we assume $\rho_1 \approx \rho_2 \approx \rho$. We select a volume in the pipe of section S and length L: fluid initially at speed V is stopped in a time L/c. Newton's law gives the force F needed to stop this volume : $F \sim \rho_1 SL \frac{V-0}{L/c}$. In terms of applied pressure, we can write $F = \Delta P\, S$ so that denoting ΔP as P_{wh} we get:

$$P_{wh} \sim \rho V c \tag{V.2}$$

Equation V.2 is generally referred to as the Joukowsky equation, but Tijsseling and Anderson [119] pointed out that it was actually Von Kries [127] in 1883 who first derived and validated it. In addition, Frizell (1898) and Allievi (1902) independently derived the "Joukowsky equation" in pure theoretical studies. However, it is Rankine (1870) who had already found the equation in the more general context of solids, thus preceding Kries and Joukowsky[1].

Although the scaling of water hammer pressure (equation V.2) does not predict the geometrical prefactor, Engel et al. were able to indirectly measure it [46] and found it to be around 0.2 (the same prefactor is also used in later works such as [83, 36]). Hence, we can write:

$$P_{wh} \approx 0.2\, \rho V c \tag{V.3}$$

Equation V.3 gives typical water hammer pressures on the order of MPa - relatively high pressures. The expression of speed of sound c can be obtained by using the conservation of energy. Kinetic energy $E_k = 1/2\rho V^2$ is transformed in potential energy through compression (somehow like storing elastic energy in a spring that is being compressed)

[1]These equations of conservation (V.1, V.2) are also known as the Rankine–Hugoniot relations, describing the relationship between the states on both sides of a shock wave in a one-dimensional flow.

$E_{el} = 1/2\beta\Delta P^2$, where β is the compressibility of the liquid. Balancing these energies leads to: $\Delta P \sim \sqrt{\frac{\rho}{\beta}}V$. Replacing this pressure in the Joukowsky equation V.1 yields:

$$c = \sqrt{\frac{1}{\rho\beta}} \tag{V.4}$$

Taking spherical geometry into account

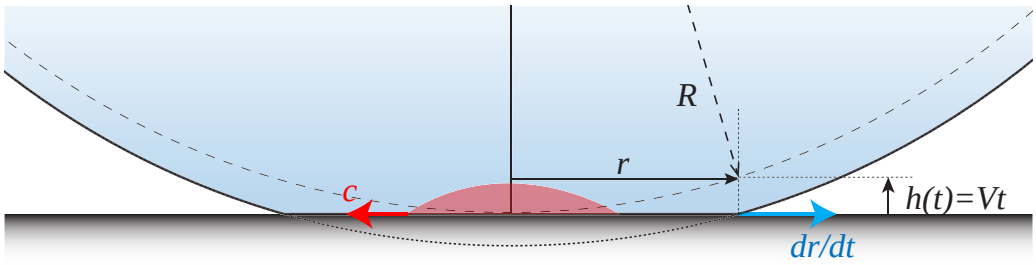

Figure V.2 – Sketch of the early stage of drop impact on a solid substrate. The contact line horizontally spreads at speed dr/dt (in blue) while the shock wave envelope moves at speed c (in red). Contact line position $r(t)$ is geometrically deduced from the impacting speed and the drop radius: $r(t) \approx \sqrt{2RVt}$.

Previous shock model was based on a "cylindrical" drop impacting a solid plate (see figure V.1). Although real drops are spherical, we can assume that this model is valid at early times due to the geometrical singularity. Indeed, the position $r(t)$ of the contact line with the plate is fixed by the falling interface of the drop (see figure V.2). We can be more quantitative by calculating the expression of $r(t)$ at height $h(t) = Vt$ (V denotes here the impact speed). Since we are only interested in the early stages of the impact, $r(t) = \sqrt{R^2 - (R - Vt)^2}$ can be rewritten as $r(t) \approx \sqrt{2RVt}$. Simple derivation leads to the horizontal speed of the contact line (in blue in figure V.2):

$$\frac{dr}{dt} \approx \sqrt{\frac{RV}{2t}} \tag{V.5}$$

Right after impact ($t = 0$), the contact line spreads at infinite speed while the shock wave envelope (in red in figure V.2) spreads at speed c. As discussed by Field and collaborators [71, 47], since the contact line speed decreases in time as $\sqrt{\frac{RV}{2t}}$, it will eventually be reached by the shock wave at time $t_c \sim \frac{2RV}{c^2}$. As a consequence, compressibility effects for a spherical drop last over a time scaling as t_c, that is, a time V/c times shorter than the time $2R/c$ previously discussed. Hence, typical shock waves last over a time on the order of the nanosecond.

Maximum impacting force in this compressible regime is obtained by multiplying

the water hammer pressure $\rho V c$ by the maximum area over which stress is applied: $\pi r^2(t_c) \approx \pi(\frac{2RV}{c})^2$. The resulting force F_{wh} is found to scale as:

$$F_{wh} \sim \rho V^2 R^2 \frac{V}{c} \tag{V.6}$$

If we put some numbers in this equation, a millimetric drop landing at several m/s generates water hammer forces on the order of a tenth of a milinewton (ten times smaller than the weight of the drop).

Recent experiments [117, 118] with a micro-second resolution and theoretical studies [79] have shown that air discs can be entrapped under the center of the drop. As a consequence, this will affect the singularity at the contact and thus the pressure and impact force at very short time.

1.2 Water hammer in the surrounding air

Compressible effects in the surrounding air also play a key role in the impact mechanism. Nagel and collaborators [132, 131, 106] have shown that splashing can be completely suppressed by decreasing the pressure of the surrounding gas. Since liquid/solid contact spreads horizontally at high speeds during early stages of impact, surrounding air is put into motion at similar speeds, generating compression waves in air. The associated pressure (referred as air hammer pressure in what follows) scales as: $P_{ah} \sim \rho_a c_a \frac{dr}{dt}$ where ρ_a and c_a denote the air density and speed of sound in air, respectively (here, the second characteristic speed to take into account is the lateral speed of the contact line, hence a characteristic speed $\frac{dr}{dt}$ as shown in figure V.2). Using equation V.5, we get:

$$P_{ah} \sim \rho_a c_a \sqrt{\frac{RV}{2t}} \tag{V.7}$$

In [132, 131], Xu et al. have measured the threshold pressure at which a splash first occurs and found it to scale with the molecular weight of the gas and the liquid viscosity. They suggest a model where the air hammer pressure P_{ah} balances capillary pressure P_γ in the thin spreading lamella. This thickness is assumed to be the boundary layer thickness (which is controlled by the diffusion of vorticity from the solid substrate), scaling as $\sqrt{\nu t}$, where ν is the kinematic viscosity of the liquid (see figure V.3). Thus we have:

$$P_\gamma \sim \frac{\gamma}{\sqrt{\nu t}} \tag{V.8}$$

Re-expressing the air density and speed of sound in air using the equation of state for an ideal gas, we get: $P_{ah} \sim \frac{PM_a}{k_B T} \sqrt{\frac{\kappa k_B T}{M_a}} \sqrt{\frac{RV}{2t}}$ (where k_B is the Boltzmann's constant, T the temperature, P the environing pressure, κ the adiabatic constant of the gas, and M_a

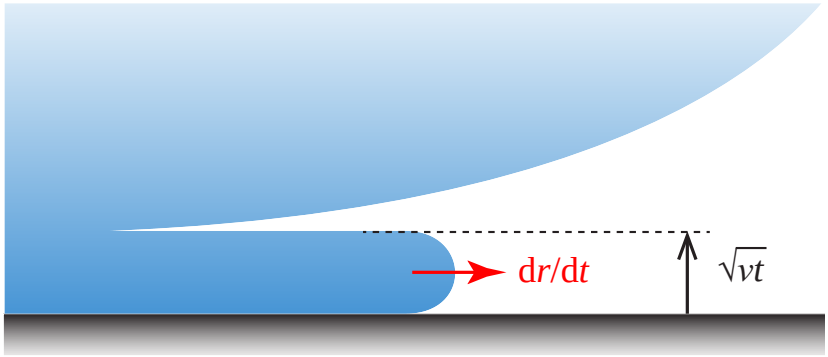

Figure V.3 – Sketch of the bottom of a drop at early stages of impact (by symmetry, we only show the right half of the drop). A liquid lamella horizontally spreads at speed dr/dt. Its thickness (controlled by the diffusion of vorticity from the solid substrate) grows as $\sqrt{\nu t}$.

the molecular weight of gas). The ratio of these two pressures is independent of time:

$$\frac{P_{ah}}{P_\gamma} \sim P\sqrt{\frac{\kappa M_a \nu R V}{\gamma^2 k_B T}} \tag{V.9}$$

Xu et al. suggest that when the two stresses are comparable, the expanding liquid rim is slowly destabilized and deflected upwards for an extended period of time, finally resulting in the ejection of droplets. Hence, equation V.9 predicts a non-intuitive result: a more viscous liquid splashes more easily than a less viscous one, that is, the threshold pressure should decrease if the liquid viscosity is raised (as experimentally observed).[2]

[2] For more information on the splashing phenomena, other regimes have been observed for higher liquid viscosities [131, 106] and numerical simulations have also been performed [75, 136].

2 Measure of impact force with a piezo-electric quartz

We just saw how compressible effects generate the so-called water hammer effect, to which corresponds high pressures, on the order of MPa. However, this phenomenon lasts over extremely short times - namely several nanoseconds. As a consequence, the generated forces (below the mN) are difficult to access experimentally. In this section, we focus only on what happens after this early stage.

2.1 Experimental Results

Drops in this study are formed by means of a syringe and various needles, which provides radii between 1 and 2 mm. The syringe is fixed to a vertical beam and its height can be changed so as to generate impact speeds V from 20 cm/s to 6 m/s (close to the terminal speed of middle-size raindrops). We record the impact from the side with a fast camera, using backlighting to enhance contrast (figure V.4a).

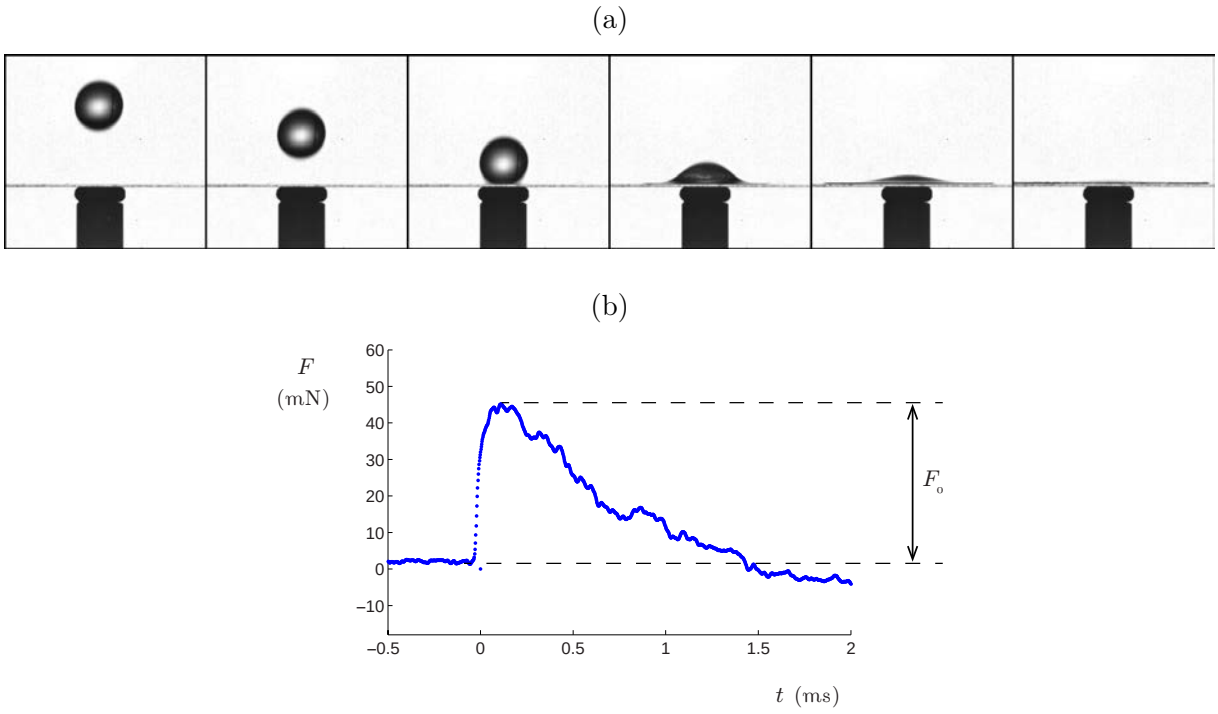

Figure V.4 – (a) Side view of a water drop of radius $R = 1.3$ mm hitting a piezoelectric quartz at $V = 3$ m/s. Images are separated by 0.5 ms from which we extract the impact velocity V. (b) Impact force F as a function of time for this experiment, measured by a piezoelectric sensor. The origin of time is chosen at contact. Impingement typically lasts 1 ms, of order $2R/V$, the time needed for the drop to travel by its own diameter. The curve is not symmetrical between the beginning and the end of the collision. The maximum force F_0 is reached after about a tenth of a millisecond.

By this means, we access the impinging speed of the drop and can check the centering of impacts. In order to control the impact position with a precision of more than 1 mm, even for high falls, two perpendicular micrometric screws are placed between the syringe and the beam.

The main specificity of this study dwells on the impulsive character of the event. A first characteristic time is the "crashing time" $2R/V$ of the drop, typically 1 ms in our experiments. We assume here that this time is smaller than the Rayleigh time of vibration of the drop, which corresponds to typical impact velocities larger than 20 cm/s.

We measure the impact force with a piezoelectric quartz: an impact hammer, PCB Piezotronics Model 086D80, is diverted from its normal usage and the signal is delivered via a Kistler charge amplifier 5015A such as used in [83, 82, 97] with a cut-off frequency of 10 kHz. The signal obtained after impact is recorded by a digital oscilloscope having a time resolution[3] on the order of 50 ms. We show in figure V.4b a typical profile of the impact force as a function of time, for a water drop with $R = 1.30 \pm 0.02$ mm, $\rho = 1000\ kg/m^3$ and an impacting speed $V = 3.00 \pm 0.02$ m/s. We observe that the typical force (50 mN for millimetric water drops) is several orders of magnitude larger than the one generated by water hammer pressure.

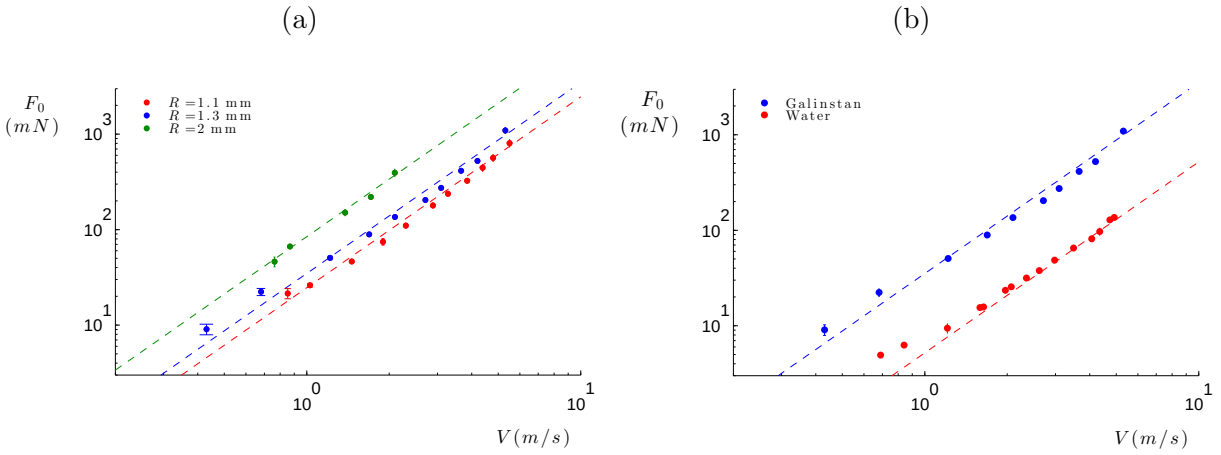

Figure V.5 – (a) Maximum force F_0 at impact as a function of the collision speed V for Galinstan, an alloy of indium, gallium and stain. F_0 is typically 300 mN, that is, about 1000 times the weight of the drop. The dashed lines show equation V.10 without any adjustable parameter. (b) F_0 as a function of V for Galinstan and water at fixed drop radius ($R = 1.3$ mm). Whatever the impact speed, forces differ by a factor 6, approximately the ratio between the two liquid densities. Again, the dashed lines show equation V.10.

From now on, F_0 denotes the maximum force of impact measured on curves similar

[3]This resolution does not allow us to extract any information regarding air entrapment (mentioned in [79, 117, 118]).

to figure V.4b. In order to obtain a larger signal, even at modest speed or small radius, we choose a liquid denser than water: an eutectic gallium–indium–stain alloy (Ga:In:Sn; 62:22:16 wt%) commonly called Galinstan [28] recently used for studying impact dynamics [133]. This liquid metal at ambient temperature is six times denser than water ($\rho = 6359$ kg/m^3) and has a viscosity of 2 mPa s, close to that of water. Repeating the experiment of figure V.4b for different drops and impact speeds yields figure V.5a where the maximum force F_0 for Galinstan is plotted as a function of V for three radii. The typical value of F_0 now becomes 300 mN, which corresponds to one thousand times the drop weight. We observe that F_0 evolves as V^2 (dotted lines in figure V.5a are parabolic fits in log–log scale), a signature of the inertial nature of the collision. Hence, the liquid density should also matter, and we compare in figure V.5b the function $F_0(V)$ for Galinstan and water, at a fixed radius $R = 1.3$ mm.

The parabolic behavior is independent of the liquid nature, and it is found that F_0 is 6 times greater for Galinstan than for water at any impact speed, corresponding to the density ratio between these two liquids. Studies in the 80s by Nearing [82, 83] and more recently by Grinspan & Gnanamoorthy [97] obtained comparable results with water only and on a much more narrow range of velocity, making it difficult to extract scaling laws in velocity. In 2012, numerical and experimental studies performed by Mangili et al. [78] produced different predictions for the force of impact. Our measurements are in good agreement with their numerical simulations assuming potential flow theory.

2.2 Analytical calculation

According to these results, we propose a model based on an inertial scenario, as postulated in [53]. During impact, the transmitted quantity is momentum: at a given time, a slice of drop of height Vdt, radius $r(t)$ (that changes from 0 to R) and mass $dm = \rho\pi r^2(t)Vdt$ decelerates from V to 0 in a time dt, which yields: $F(t) = \rho\pi r^2(t)V^2$. The maximum impact force F_0 is reached for $r(t) = R$. Hence we get:

$$F_0 = \pi\rho R^2 V^2 \tag{V.10}$$

This expression can be seen as a dynamic pressure ρV^2 applied over a surface area πR^2. It can also be understood as arising from the deceleration (from V to 0) of a mass $M = 4\pi\rho R^3/3$ in a time $2R/V$. We can now calculate the ratio between the water hammer force and the dynamic one: $F_{wh}/F_0 \sim V/c \approx 1/1000$. As previously mentioned, although water hammer pressures are extremely high, the surface over which they act is so small that the resulting force is V/c times smaller than the one expected from a dynamic pressure ρV^2 acting over a surface R^2. When compared to experiments, equation V.10

is observed (in dashed lines) to nicely fit the different data in figure V.5 without any adjustable parameter.

2.3 The case of raindrops

We can think of exploiting this result to discuss how force measurements provide an estimate of raindrops radii, a quantity of interest in meteorology where it is desired to access the polydispersity of falling rain. In other words, understanding the force F_0 may allow us to deduce drop radii for a given liquid, providing a new kind of "disdrometer" – namely, the device giving access to the size distribution of rain.

We assume that drops reach the sensor with their terminal velocity V_0 [51, 92] for which inertial friction in air balances liquid weight (discussed in chapter I, equation I.9). These two forces can be written as $4\pi\rho R^3 g/3$ and $\rho_a C_x \pi R^2 V^2/2$, respectively (where $C_x \approx 0.44$ is the drag coefficient at Re > 1000). Balancing them, we get a scaling law for the terminal speed of a raindrop: $V_0 \sim \sqrt{\rho R g/\rho_a}$. Injecting this expression in equation V.10 yields:

$$F_0 \sim \frac{\rho}{\rho_a} mg \tag{V.11}$$

This formula emphasizes how the impact force magnifies the drop weight of raindrops (by a factor ρ/ρ_a, on the order of 1000), which shows why measuring the impact force can be an accurate method to obtain the drop mass. Indeed, equation V.11 can be rewritten as: $R \sim (\frac{F_0 \rho_a}{\rho^2 g})^{1/3}$, allowing us to deduce a drop radius from an impact force measurement.

3 A cheaper sensor: the lamella

In order to complement this first method, we now consider a simpler (and cheaper) sensor, namely a thin glass lamella (Menzel-Glaser Microscope cover slip #1) of Young modulus $E = 69$ GPa, density $\rho_g = 2350$ kg/m^3, thickness $h = 160$ μm, and transverse width $b = 24$ mm. One side is clamped by squeezing 10 mm of a 60 mm-long lamella between two thick glass plates. The other side being free, we have a narrow rectangular plate of length $L = 50$ mm and mass $M = \rho_g hbL$ free to vibrate as sketched in figure V.6. Since the drop spreads at impact, the impact location is adjusted a few millimeters from the tip of the plate in order to avoid spilling.

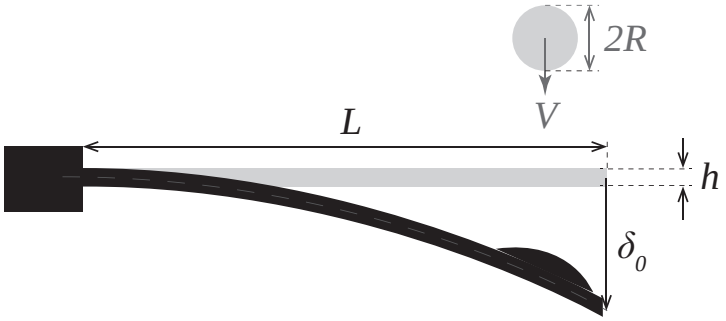

Figure V.6 – Sketch of lamella sensor. A thin glass lamella of length $L = 50$ mm, thickness $h = 160$ μm and transverse width $b = 24$ mm is clamped at one end and free to vibrate at the other one. A drop of radius R and speed V impacts a few millimeters from the tip of the plate. In grey, the system before impact; in black, the system at the maximum deflexion δ_0. We observe that the drop is sticking to the free end of the plate.

3.1 Experimental Results

We show in figure V.7 a typical side view of the impact resulting in a maximal lamella deflexion δ_0:

Figure V.7 – Galinstan drop of radius $R = 1.25$ mm and speed $V = 4$ m/s hitting the edge of a thin glass plate. Images are separated by 1 ms and only show 1/3 of the lamella. We denote δ_0 as the maximum plate deflection after impact.

From this lateral movie we observe that the dynamics of the plate are dominated by its first mode of vibration. In addition, side view of plate oscillations allow us to access the vertical position of the free end of the lamella as a function of time, as shown in figure V.8 for different impact speeds.

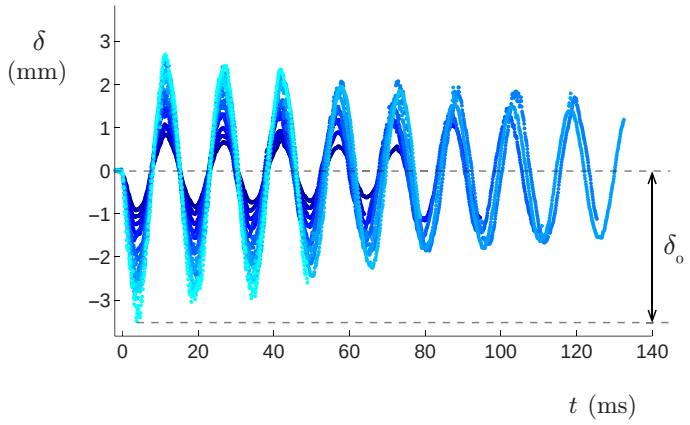

Figure V.8 – Vertical deflection δ_0 of the lamella tip as a function of time for experiments such as shown in figure V.7. Each curve corresponds to an impact speed V (the brighter the color, the higher V, which varies from 1.3 m/s to 4.9 m/s by steps of 0.3 m/s). The characteristic period of vibration of the plate is independent of V and observed here to be $\tau \approx 20$ ms.

Focusing on the maximum force, we denote δ_0 as the largest deformation of the lamella for a given impact (see figure V.6 and V.7). We plot this quantity in figure V.9a as a function of impact speed for water drops of different radii, and compare in figure V.9b the plate deflection between water and Galinstan for $R = 1.3$ mm. The results contrast with figure V.5 since we now observe that δ_0 linearly varies with both V and ρ.

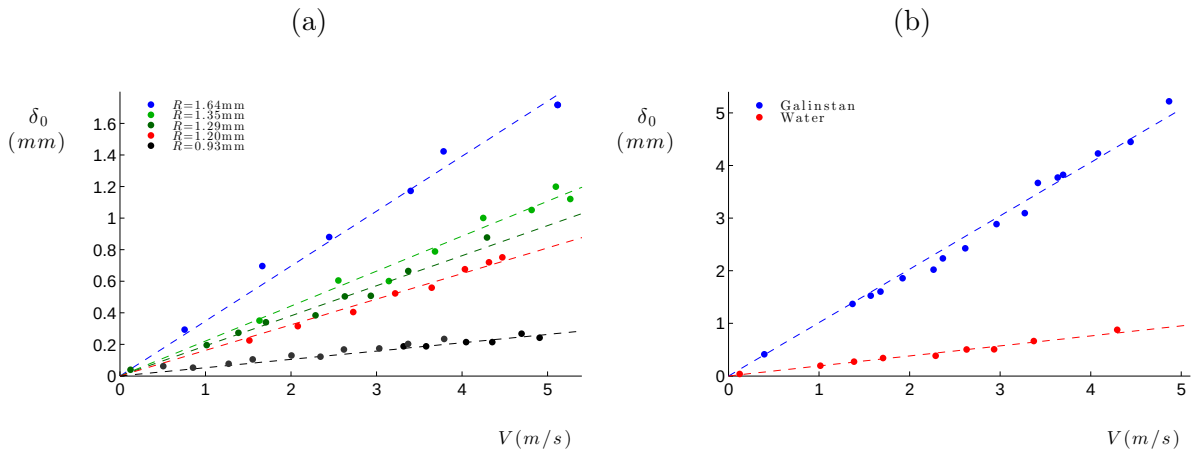

Figure V.9 – (a) Maximal deflection δ_0 of the tip of a glass lamella as a function of the impacting speed of a water drop hitting this lamella close to the edge. We do not observe a parabolic relationship between δ_0 and V, but a linear law. (b) Comparison between water (lower curve) and Galinstan (upper curve) for a radius $R = 1.3$ mm. The ratio of δ_0 between the liquids is approximately the ratio of their densities.

3.2 Model

At mechanical equilibrium, the deflection δ_0 of a thin plate is proportional to the applied force F_0. Denoting $I = bh^3/12$ as the moment of inertia of the plate, thin plate theory [120, 107] gives us the following relation between force and deflection:

$$\delta_0 \sim F_0 L^3/EI \tag{V.12}$$

With an impact force varying as V^2 (as seen before), we anticipate a deflection quadratic in velocity. It is not the case here because the plate has a slow response compared to the crashing time $2R/V$ (≈ 1 ms) of the liquid: the characteristic time $\tau_0 = 1/f_0$ of the plate in figure V.8 is about 20 ms, and it is expected to be a function of the plate parameters ($\tau_0 = \sqrt{ML^3/EI}$). Since the lamella is not at static equilibrium during an impact ten times shorter than its response time we cannot assume instantaneous proportionality between deformation and force. We propose here to understand the data using an argument based on momentum conservation. Before impact, the drop of mass m moves at speed V and the plate of mass M is at rest. After impact, the drop sticks to the plate, resulting in a system of mass $(m + M)$ vibrating at its natural frequency, independent of the collision speed V. With a uniform distribution of m along the plate, the first resonance frequency would become $f = f_0\sqrt{\frac{M}{M+m}}$. A geometrical correction could be introduced to take into account the fact that the drop is neither localized at the free end, nor homogeneously spread all over the lamella. However, since $m << M$, this correction is marginal, and we assume $f \approx f_0$. The lamella is vibrating on its natural mode, with a parabolic modal shape as a first approximation for clamped-free end conditions. Hence, its momentum can be written: $p_M = \int_0^L \rho_g bh\, 2\pi f_0 \delta_0 \frac{x^2}{L^2} \cos(2\pi f_0 t) dx = \frac{2\pi}{3} M f_0 \delta_0 \cos(2\pi f_0 t)$. On the other hand, the momentum of a drop vibrating at the tip of the lamella is: $p_m = m\, 2\pi f_0 \delta_0 \cos(2\pi f_0 t)$. Assuming that the first mode accounts for the dynamics also at $t = 0$, the conservation of momentum yields for $m << M$:

$$\delta_0 \approx \frac{3}{2\pi} \frac{m}{M} \frac{V}{f_0} \tag{V.13}$$

Equation V.13 is found to be linear in V (instead of quadratic) and sensible to the ratio of mass between the drop and the lamella. Typical mass ratio m/M in our experiments being 1/30, a millimetric drop hitting the plate at several meters per second will induce millimetric deflections to our glass lamella (which has a typical vibration frequency f_0 of 50 Hz).

3.3 Agreement between model and data

In order to explore a large range of densities, we repeated the experiment with the previous liquids (water, Galinstan) to which we added acetone (of density $\rho = 714$ kg/m^3), hexane ($\rho = 659$ kg/m^3) and a viscous silicone oil ($\rho = 970$ kg/m^3, viscosity of 500 mPa s). We show in figure V.10 how the deflection δ_0 rescaled by the distance V/f_0, as suggested by the model, varies as a function of the mass ratio m/M for all experiments. As predicted by equation V.13, data collapse on a line of slope 1.

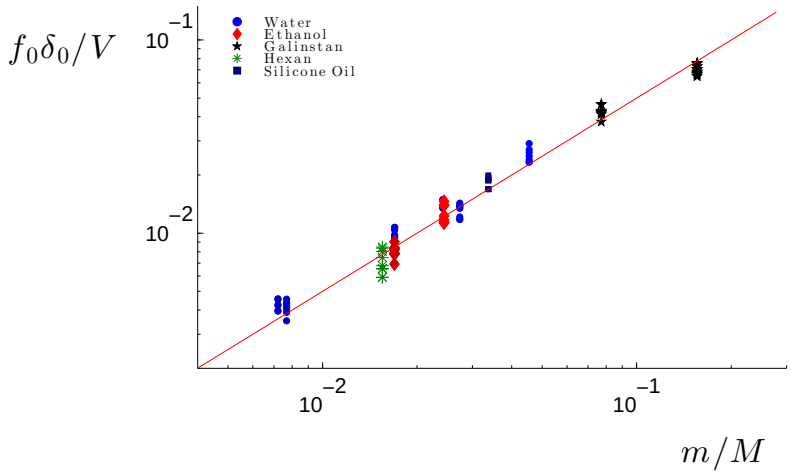

Figure V.10 – Normalized deflection $f_0\delta_0/V$ as a function of the ratio m/M between the drop and the plate mass. V varies from 20 cm/s to 6 m/s. The red line shows equation $y = (3/2\pi)x$, that is, equation V.13. Each color corresponds to a liquid, and each cluster to different radii R ranging from 0.9 mm to 1.7 mm.

3.4 The two impact regimes

According to the characteristic response time τ_0 of the substrate, we expect two regimes of impact:

(i) a fast one, where the liquid crash is faster than the response of the substrate, which leads to equation V.13 and corresponds to all our experiments,

(ii) a slow one, where impact is slower than τ_0. In this case, since the response of the plate is quasi-static (mechanical equilibrium), the deformation is proportional to the force: δ_0 scales as L^3F_0/EI (equation V.12), which yields (using equation V.10): $\delta_0 \sim \pi\rho R^2V^2L^3/EI$, quadratic in velocity.

Since τ_0 is a function of L, let us re-express the transition between both regimes in terms of substrate length: the linear regime in V occurs for $L > L_c$, and the quadratic

one for $L < L_c$ where the critical length L_c is given by:

$$L_c \sim \left[\frac{Eh^2}{\rho_g}\right]^{1/4} \left[\frac{R}{V}\right]^{1/2} \tag{V.14}$$

For glass lamellae and millimetric drops in our range of impact speeds, this critical length is around 3 cm. Since the lamella in experiments ($L = 5$ cm) is longer than L_c, we indeed expect $\delta_0(V)$ to be linear, as observed in figure V.9.

From a more general point of view, leaves can also be viewed as lamellae, and drop impact can naturally bend or even damage them [129]. We expect leaves to have a large response time τ_0, owing to an effective Young modulus E more than one thousand times smaller than for glass. For a leaf (of thickness h and width b comparable to that of our lamellae), L_c becomes about 6 mm. Most plants have leaves longer than L_c, so that equation V.13 can be used to estimate the deflection of leaves under rain. For millimetric drops on leaves of a few centimeters ($\tau_0 \approx 600$ ms, $f_0 \approx 1.5$ Hz), equation V.13 predicts centimetric deflections. But equation V.13 also exhibits the sensitivity to other parameters of the leaf: bigger drops hitting thin small leaves can generate a deflection comparable to the leaf size, which can lead to breakage after multiple impacts.

3.5 The case of raindrops

As previously done for the piezo-electric quartz, we can use a lamella to propose an alternate solution to achieve a disdrometer. Two regimes arise regarding lamellae length:

For lamellae of length $L > L_c$, we obtain after expressing the terminal velocity of raindrops in equation V.13:

$$\delta_0 \sim \frac{\rho^{3/2} g^{1/2}}{\rho_a^{1/2} M f_0} R^{7/2} \tag{V.15}$$

For lamellae of length $L < L_c$, injecting the expression of impact force of a raindrop (equation V.11) into equation V.12, we get:

$$\delta_0 \sim \frac{\rho^2 g L^3}{\rho_a E b h^3} R^3 \tag{V.16}$$

In both regimes, the deflection δ_0 is a lightly-sensitive function of R, and it can be measured from a side view video, from which we can deduce the drop radius. As a consequence, by associating several sensing plates (hydrophobically coated in order to avoid cleaning between successive impacts), we can assess the polydispersity of rain.

3.6 Energy harvesting

We can finally estimate the collision energy. The system periodically transfers bending energy $Ebh^3\delta_0^2/L^3$ into kinetic energy $E_{k-plate} = 1/5[1/2M(\delta_0 2\pi f_0)^2]$, that is, $(9m/5M)E_{k-drop}$. The kinetic energy E_{k-drop} of a raindrop is around 1 mJ and the energy of the plate after impact is typically 10^{-4} J. Assuming an efficiency of 10% when transforming bending energy into electrical energy with a piezo-sensor, and supposing that this energy is delivered for each vibration, we get a transmitted power of 10^{-3} W. In the case of rain, assuming an impact every 10 seconds, we deduce that a roof of 100 m^2 with 10^6 receivers can deliver an average power of 100 W, just enough to light a bulb – a modest amount. Even if raindrops fall from high, drag slows them down dissipating almost all their potential energy, which is not efficient if we dreamt of energy harvesting but a blessing for plants, soil or living creatures that luckily experience relatively less impact force or erosion!

4 Non-wetting impacts

In this section, we address the question of the influence of wettability in the impact problem. As we know, a substrate coated superhydrophobic generates bouncing after impact.

4.1 Deflection

We consider a drop impacting the same previous thin plate, excepted it is now coated to be non-wetting. If the time τ of crash (scaling as $2R/V$) is shorter than the period τ_0 of vibration of the plate, the drop can spill away and it will not stick anymore to the plate after impact, resulting in a lighter final vibrating system. Since we saw that this problem is based in momentum conservation and since initial momentum remains unchanged, we expect higher deflections. Indeed, if we do not neglect the drop mass compared to the plate one, our argument in section 3.2 gives:

$$\delta_0 = \frac{3}{2\pi}\frac{m}{M}\frac{V}{f}\frac{1}{1+3\frac{m}{M}} \tag{V.17}$$

In equation V.17 frequency f also depends on the final mass of the system and varies as $f = f_0\sqrt{\frac{M}{M+m}}$, so that the expression of deflection δ_0 becomes:

$$\delta_0 = \frac{3}{2\pi}\frac{m}{M}\frac{V}{f_0}\frac{1}{1+3\frac{m}{M}}\sqrt{\frac{M+m}{M}} \tag{V.18}$$

For $m < M$, we get back to equation V.13, which exactly corresponds to the situation of an impact on a super-hydrophobic substrate: the drop bouncing away from the plate, it is not anymore attached to it. Hence, the ratio between maximum deflection in a non-wetting state δ_{nw} and in a wetting state δ_w is:

$$\delta_{nw}/\delta_w = (1+3\frac{m}{M})\sqrt{\frac{M}{M+m}} \tag{V.19}$$

As expected, equation V.19 states that we have a higher deflection for a non-wetting plate. For small mass ratio $m/M < 1$, Taylor expansion leads to $\delta_{nw}/\delta_w \approx 1 + \frac{5}{2}\frac{m}{M}$. In our experiments done with water, drop mass m was much smaller than plate mass M ($m/M \approx 1/30$). As a consequence, the correction due to taking into account the mass sticking to the plate is a few percent - indeed, negligible. However, if we repeat the experience with a drop of radius twice bigger, we would expect a difference in deflection up to a factor 2 - clearly measurable and not negligible anymore. It could be an interesting challenge to experimentally probe this relation.

4.2 Force

We now think in terms of impact force (instead of maximum deflection). If the rebound time T_{reb} of the drop (scaling as $\sqrt{\rho R^3/\gamma}$) is shorter than the crashing time $2R/V$, C. Ybert and coworkers [67] suggest a new expression for the force based on transfer of momentum. Indeed, the drop will bounce before it has completely crashed. Assuming a perfect rebound (restitution coefficient of 1) the drop experiences a change of momentum $2mV$ in a time T_{reb}. Hence, the substrate experiences a force F_{nw} scaling as:

$$F_{nw} \sim \sqrt{\rho\gamma R^3 V^2} \tag{V.20}$$

Equation V.20 predicts an impact force linearly dependent on impact speed V (in the non-wetting bouncing situation). At low speed, this means a stronger force compared to the wetting case (which had a parabolic dependence).

The condition of validity $T_{reb} < 2R/V$ can be re-interpreted in terms of speed: the impacting speed V has to be smaller than Taylor-Culick speed of retraction $V^* = \sqrt{\frac{\gamma}{\rho R}}$. For a millimetric water droplet V^* is on the order of 20 cm/s - relatively small. At this maximum speed V^*, we would expect the maximum force F^*_{nw} in this linear regime to scale as:

$$F^*_{nw} \sim \gamma R \tag{V.21}$$

If we put some numbers in equation V.21, we get a force on the order of 0.1 mN - too small to be detected by our sensor. In order to increase the intensity of the signal we can think of using mercury. Indeed, this liquid metal has a surface tension approximatively six times higher than water. As a consequence, the corresponding maximal force F^*_{nw} is increased by the same factor, resulting in measurable forces, probably allowing us to experimentally bring to light this regime. Another solution to have a stronger signal would be to use rubber ballons filled with liquid. This technique, already used by Clanet et al. to study the maximal deformation of an impacting drop [24], showed that we can have an increase in apparent surface tension of a factor up to a thousand.

Surface tension is related to matter cohesiveness (or affinity between molecules) hence, a higher surface tension implies also a higher density. As a consequence, the maximum speed V^*, which is a function of the ratio ρ/γ, is relatively insensitive to a change in liquid nature: the critical speed for mercury is found to be approximatively 70% of the one of water.
If we now focus on the ratio of forces between wetting and non-wetting substrates, we get:

$$\frac{F_{nw}}{F_0} \sim \frac{V^*}{V} \tag{V.22}$$

Equation V.22 predicts a strong effect of bouncing at small impacting speeds[4]. The divergence predicted for $V \to 0$ should be difficult to probe since the corresponding forces tend towards zero.

[4]Since we can not play on wetting properties of mercury, this difference can not be experimentally probed with mercury.

5 Conclusion

Drop impacts have been extensively studied for more than one century due to their ubiquitous implication in everyday life. For printing, coating or spraying, from pesticides to rain, [26, 134], it is essential to understand the collision mechanisms of a drop. Many aspects have been and are still explored [134, 130]. Special attention has been given to the early stages of splashes [45, 132] to the dynamics of the spreading radius [122] or to the influence of the substrate [122, 55, 123, 36, 72].

However, the force experienced by a substrate hit by a drop has been less discussed, apart from early discussions about soil erosion [83, 82, 53] and more recent studies about the rain impact on small creatures [37]. Indeed, drop impacts are difficult to characterize due to their transient, non-stationary nature. We discussed in this chapter the force generated during impacts, a key quantity for animals, plants, roofs or soil erosion.

At early stages, compression waves in the liquid generate extremely high pressures (on the order of MPa). However, they last over a time so short, that the corresponding forces remain small (below the millinewton).

We measured this force through two different systems: a piezo-electric quartz sensor and a deflecting thin lamella. Although a millimetric drop has a modest weight, it can generate collision forces on the order of thousand times this weight. We modeled this amplification considering natural parameters such as drop radius and density, impact speed and response time of the substrate. We proposed as well two kinds of devices allowing us to deduce raindrops size from impact forces.

Finally, we theoretically explored the influence of a superhydrophobic coating allowing the drop to bounce. We deduced that if the drop bounces faster than the response time of the lamella, the maximal deflection of the plate will be enhanced. Similarly, if the drop bounces faster than the crashing time of the drop, we expect increased impact force. Future work should lead to new experiments allowing to probe these models.

Conclusion

In this work, we discussed special dynamics experienced by non-wetting objects. We focused on two opposite phenomena: the onset of motion (due to textured substrates) and the radical stop (due to an obstacle such as a solid plate or a grid).

In 2006, Linke et al. showed that liquid drops deposited on hot solids covered by asymmetric teeth self-propel. We show that herringbone patterns on solids also propel Leidenfrost drops, which can be seen as a geometrical proof of the scenario suggesting that viscous drag should generally be responsible for such motions on asymmetric solids. Contrasting with ratchets, geometry and resulting vapor flows on herringbones are simple and controllable, allowing us to produce quantitative models for both the propelling and the friction force, and to discuss how the design can be optimized. Maximizing the force is useful if it is desired to oppose an existing force (such as gravity, if the substrate is inclined); in other cases, it can be interesting to optimize the drop speed to enhance the motion. The corresponding optimal chevron angles are not the same, but both properties emphasize the role of geometry in these devices.

We also show that viscous entrainement effects can be extended to room temperature: blowing air through the holes of an air-hockey table with etched chevrons generates both levitation and self-propulsion of plastic cards and glass platelets placed on such tables. Propulsion takes place in the same direction and with the same characteristics as in the Leidenfrost case, showing the generality and versatility of these devices. However, if we use deeper channels we lose the confinement effect. We show that we need stronger airflows in order to induce levitation. Even though we still see motion, it takes place in the opposite direction. Although these two regimes (low versus high Reynolds number) are based on completely different physical mechanisms (viscous effects versus inertial ones) they surprisingly obey the same scaling law.

Regarding the impact of a drop, we first focus on the impact on a grid. Liquid chooses to pass through a hole depending on the capillary pressure defined by the size of the hole (and by the wetting conditions). We show that the total amount of transmitted mass is

usually fixed by the time of crash. However, different timescales have to be taken into account in other marginal situations such as when bouncing is faster than crashing.

Finally, we focus on drop impacts and their transient, non-stationary nature. We show that although a millimetric drop has a modest weight, it can generate collision forces on the order of one thousand times this weight. We measure and discuss this amplification, considering natural parameters such as drop radius and density, impact speed and response time of the substrate. We finally imagine and describe two kinds of device allowing us to deduce the size of raindrops from impact forces.

Appendix A

G-code script to machine a herringbone pattern

In this appendix, we give the G-Code script used to texture a herringbone pattern on a brass substrate using a numerical CNC-Milling machine. Variables used by the machine are preceded by "#". Comments are either on the right hand side or preceded by "//". This work has been possible thanks to the valuable help of Guillaume Clermont.

```
% @MACRO
//The zero reference is on the right top side of the piece (which is horizontal)
// All units must be in mm
//N denotes the number of passings in each crenel

//Definition of variables
#1=60;                                  Herringbone half opening angle α (deg)
#2=0.1;                                 Depth pitch for each passing
#21=0.20;                               Maximum depth: h (mm), must be multiple of #2
#3=30.;                                 Width of substrate (mm)
#5=1;                                   Diamater of reamer, defining width of groove W (mm)
#6=0.2;                                 Width of wall λ (mm)
#7=190.;                                Length of substrate (mm)
#19=#5+1.;                              Safety margin (mm)

#16=(#7/(#6+#5)/SIN(#1))+1;             Number of passing to do
#8=0;                                   Loop counter

//Start
```

```
T1;                                          Name of the reamer
M3 S3700;                                    Milling speed

G00 Z5.0;                                    Go up
G00 Y(#19);                                  Go to zero
G01 Z(-#2) F100.00;                          Reamer down at translation speed 25

//Loop
WHILE #8<=(#16) DO;

    #9=-#8*((#5+#6)/SIN(#1));                Initial position of the loop
     #11=-#3/2;                              First position
     #12=#9+(#3/2+#19)/TAN(#1);              Second position
     #13=(-#3-#19);                          Third position
     #20=-#2;                                Loop counter for depth

    WHILE -#20<#21 DO;
        G01 Z#20;
        G01 X#9 Y#19;
        G01 X#12 Y#11;
        G01 X#9 Y#13;

        #20=#20-#2;
        G01 Z(#20);
        Lower reamer G01 X#12 Y#11;
        G01 X#9 Y#19;

        #20=#20-#2;

    END_WHILE

    G01 Z(-#2);                              Take reamer to next initial position
    G01 X(#9-((#5+#6)/SIN(#1)));
    #8=#8+1;                                 Loop counter

END_WHILE;
G01 Z1; M5;                                  Take reamer away
```

Appendix B

Exact calculation of viscous entrainment force

In this appendix, we present an exact calculation of the force of viscous entrainment generating self-propulsion of a Leidenfrost drop on a herringbone texture. By symmetry, projection of the forces in the plane perpendicular to the axis of symmetry of the herringbone compensate and they add up in the plane of symmetry. After projection (hence the cosine of α), total entrainement force is:

$$F = 2\cos\alpha \iint_S \frac{6\eta U}{h} dX dY \tag{B.1}$$

Here, the surface of integration S is half the circle below the drop[1]. To get an analytical solution, the best method is to use the frame $\overrightarrow{e_x}, \overrightarrow{e_y}$ defined by the direction of the grooves, sketched in figure B.1 and different from the frame $\overrightarrow{e_X}, \overrightarrow{e_Y}$ naturally associated to the plane of symmetry. Instead of first calculating the force generated by the Poiseuille flow in each channel and then adding them up, we directly integrate the stress over the whole surface (inspired by the numerical work done in [89]). We inject in equation B.2 the expression of the horizontal speed U in a single channel described in equation II.7 and obtained from conservation of mass and thermal balance: $U = \frac{\kappa\Delta T}{\rho\mathcal{L}h^2}x$. Denoting $\frac{12\eta\kappa\Delta T}{\rho\mathcal{L}h^3}$ as A, equation B.2 can be rewritten as: $F = A\cos\alpha \iint_S x\, dX dY$. We decompose the total integration in two regions:

(i) upper one, denoted as S_1 (in red in figure B.1a): $I_1 = \iint_{S_1} x\, dX dY$, and

(ii) lower one, denoted as S_2 (in blue in figure B.1b): $I_2 = \iint_{S_2} x\, dX dY$,

These notations lead to the following expression for the total entraining force:

[1]We can take into account the fact that the walls occupy a surface that does not contribute to propulsion by multiplying S by $W/(\lambda + W)$, where W is the width of a groove and λ the thickness of a wall.

$$F = A\cos\alpha(I_1 + I_2) \tag{B.2}$$

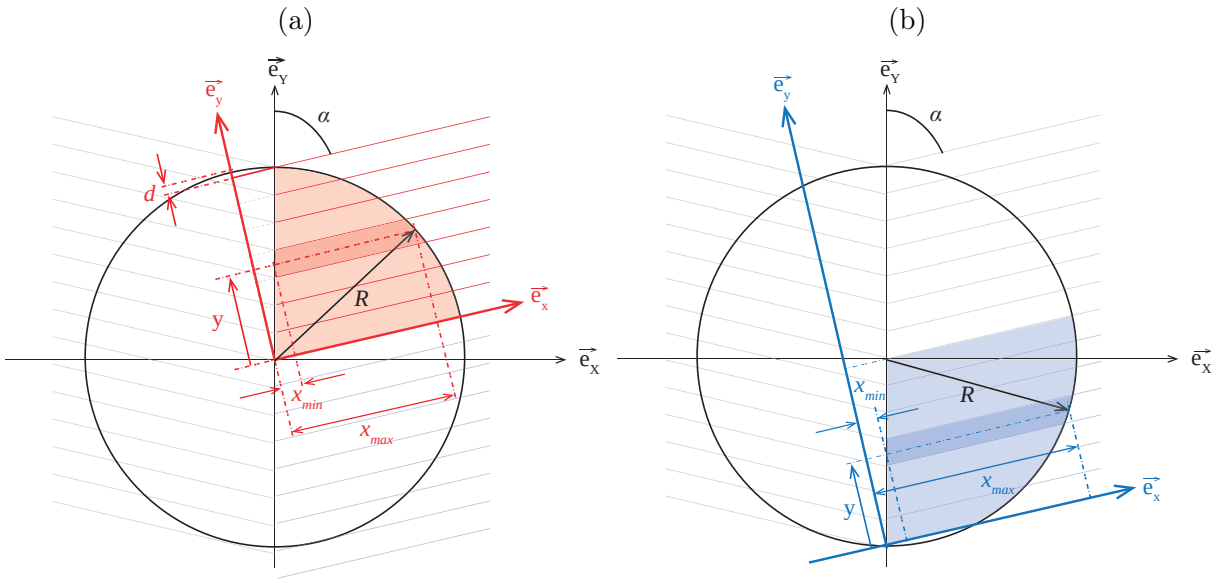

Figure B.1 – Sketch of surface over which we integrate equation B.2. (a) Upper part, in red, corresponding to area S_1 (and integral I_1). (b) Lower part, in blue, corresponding to area S_2 (and integral I_2).

Upper contribution

We focus now on the mathematical integration of $I_1 = \iint_{S_1} x\, dXdY$. Looking at figure B.1a, we have to integrate x in the $\overrightarrow{e_x}$ direction from $x_{min} = y/\tan\alpha$ to $x_{max} = \sqrt{R^2 - y^2}$ for a channel at height y. We then have to integrate this result in the $\overrightarrow{e_y}$ direction from $y_{min} = 0$ to $y_{max} = R - d = R\sin\alpha$. Hence:

$$I_1 = \int_0^{R\sin\alpha} \int_{y/\tan\alpha}^{\sqrt{R^2-y^2}} x\, dxdy \tag{B.3}$$

After integration, we get:

$$I_1 = \frac{\sin^3\alpha}{3} R^3 \tag{B.4}$$

Lower contribution

We discuss here the mathematical integration of $I_2 = \iint_{S_2} x\, dXdY$. Looking at figure B.1b, we have to integrate x in the $\overrightarrow{e_x}$ direction from $x_{min} = y/\tan\alpha$ to $x_{max} = R\cos\alpha +$

$\sqrt{R^2-(R\sin\alpha-y)^2}$ (as expected, for $y=0$, $x_{max}=2R\cos\alpha$) for a channel at height y. We then have to integrate this result in the $\overrightarrow{e_y}$ direction from $y_{min}=0$ to $y_{max}=R\sin\alpha$. Hence:

$$I_2=\int_0^{R\sin\alpha}\int_{y/\tan\alpha}^{R\cos\alpha+\sqrt{R^2-(R\sin\alpha-y)^2}} x\,dxdy \tag{B.5}$$

After integration (with the help of Mathematica software), we get:

$$I_2=\frac{6\cos\alpha(2\alpha+\sin 2\alpha)+(11\sin\alpha+3\sin 3\alpha)}{24}R^3 \tag{B.6}$$

Resulting force

Injecting solutions obtained in B.4 and B.6 in equation B.2 yields the expression of the total propelling force:

$$F=\frac{6\eta\kappa\Delta T}{\rho\mathcal{L}h^3}\,R^3\,f(\alpha) \tag{B.7}$$

where f is the function defined as $f(\alpha)=\frac{2}{3}\cos\alpha(\sin^3\alpha+\frac{1}{8}[6\cos\alpha(2\alpha+\sin 2\alpha)+11\sin\alpha+3\sin 3\alpha])$. As expected, equation B.7 nearly has the same expression as the one obtained in section 2.2, equation II.9 (provided we set $f(\alpha)\sim\sin 2\alpha$).

We show in blue in figure B.2 the function $f(\alpha)$ obtained from equation B.7. In red, the function obtained from approximation done in chapter II, leading to equation II.9. Although they have a similar allure, the maximum for the exact calculation (in blue) is slightly shifted towards lower angles (and is also slight higher).

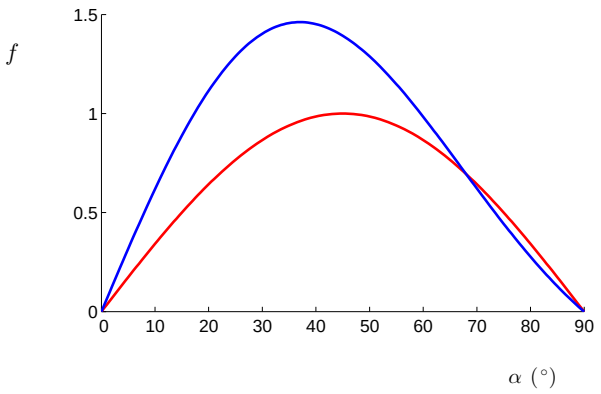

Figure B.2 – Comparison of functions $f(\alpha)$: in blue, obtained from exact calculation (equation B.7); in red, obtained from approximation done in chapter II (leading to equation II.9).

Appendix C

Résumé en Français

Cette thèse porte sur les liquides non-mouillants et leur interaction avec des textures. Elle s'articule autour de cinq chapitres. Le premier chapitre introduit clairement toutes les notions nécessaires à la lecture du manuscrit, et replace la problématique dans le contexte de la recherche internationale sur ces sujets. Les deux chapitres suivants traitent le phénomène de lévitation et d'auto-propulsion. Les deux derniers chapitres se centrent sur le phénomène d'impact d'une goutte: soit avec une grille soit avec une plaque lisse. Nous détaillons par la suite le contenu de chaque chapitre.

Le premier chapitre est consacré à la physique des objets non-mouillants (voir figure C.1). Trois méthodes permettant d'atteindre cet état sont discutés [30]. La première, propose de réduire le contact entre liquide et solide en combinant un traitement chimique et physique afin de rendre le substrat super-hydrophobe [62]. La deuxième, se centre sur la lévitation par caléfaction, c'est-à-dire, la lévitation d'objets (solides ou liquides) sur la couche de gaz qu'ils génèrent en s'évaporant [11]. La dernière, très similaire, consiste à souffler de l'air à travers le substrat poreux qui se trouve sous la goute - à l'image d'un palet qui lévite sur une table d'air-hockey [48].

On étudie par la suite les conséquences de l'existence de cette couche de gaz (isolant physiquement et thermiquement la goutte du substrat) sur la forme de ces perles liquides. N'ayant plus aucun contact avec le solide, les petites gouttes sont dominées principalement par les effets de tension de surface. Cette force interfaciale, qui essaye de minimiser la surface des objets, leur confère une forme sphérique. Pour des plus grosses gouttes, la gravité doit être prise en compte, et la goutte s'aplatit sous l'effet de son propre poids. Apres avoir discuté leur forme, nous nous intéressons au coussin de vapeur formé sous la goutte. Son épaisseur résulte d'un équilibre dynamique entre le poids de la goutte (qui est en train d'écraser le coussin de vapeur), et le liquide évaporé qui est en permanence en train de l'alimenter. La question de stabilité de ce coussin de vapeur et de la forme de la goutte y sont aussi traités. Cette thèse portant sur l'interaction de gouttes avec des

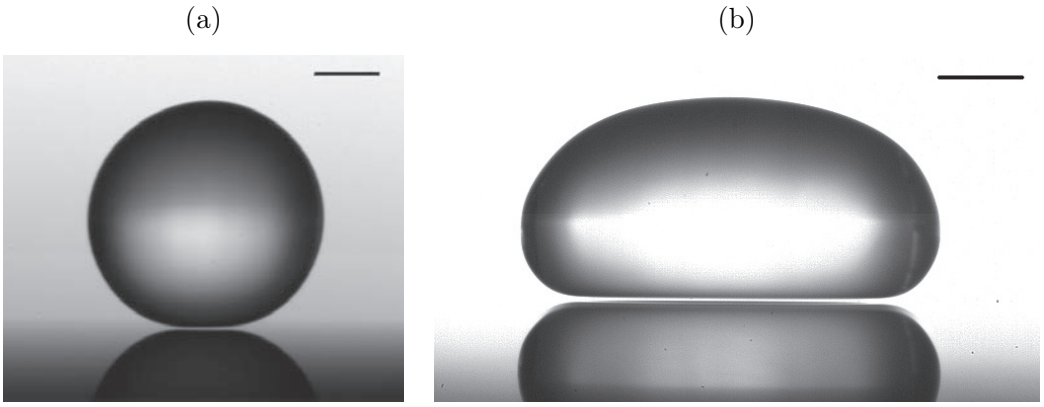

Figure C.1 – Gouttes en caléfaction (a) Les petites goutes sont soumises principalement à la tension de surface, ce qui leur confère leur aspect sphérique. L'échelle représente 1 mm. (b) Les plus grosses gouttes sont aplaties par la gravité. L'échelle représente 2 mm.

textures, nous discutons comment la forme d'une goutte posé sur une surface crénelé est modifiée (par rapport au cas du substrat lisse). Par ailleurs, l'extrême mobilité de ces objets donne toute sa richesse à ce sujet. Leur dynamique est en effet gouvernée par des forces très faibles, dont la nature et la valeur sont particulièrement difficiles à identifier et à mesurer. Ainsi, pour clore ce chapitre nous passons en revue les différentes forces qui peuvent générer de la friction sur ces aéroglisseurs: friction dans le coussin d'air, friction avec l'air environnent ou friction sur une surface crénelée.

Cette introduction, qui pose les bases de ce travail en même temps qu'elle introduit des résultats inédits, ouvre naturellement le chemin au deuxième chapitre. On y présente l'étude du mouvement d'un liquide caléfié sur un substrat texturé. En 2006, H. Linke [73] a ainsi montré qu'un liquide posé en caléfaction sur un support couvert de dents asymétriques est autopropulsé dans la direction de la pente descendante des dents. Le point essentiel est la production de vapeur sous la goutte, une vapeur évacuée par la pression qu'exerce le liquide sur le film qui le supporte. Si cet écoulement est isotrope sur un solide plan (cas de la figure C.1), il peut ne plus l'être sur un solide aux textures asymétriques (cas de la figure C.2). En disposant des microbilles de silice sur les textures, G. Dupeux [43] a réussi à mesurer le champ de vitesse dans la très fine couche de vapeur qui maintient l'objet en lévitation. Il a ainsi mis en évidence que le gaz s'écoule vers la zone la plus profonde du sillon avant d'être évacué latéralement. C'est ce flux vers les zones profondes de la texture qui entraine, par viscosité, la goutte sur le substrat. On comprend ainsi que la locomotion est activée dès que l'on canalise la vapeur dans une direction donnée – ce que fait la vapeur sur les dents à cause de leur asymétrie. Cependant, l'écoulement de vapeur dans cette texture reste extrêmement complexe. C'est cette complexité (et la difficulté qui en découle à modéliser physiquement ce problème) qui

nous a poussé à chercher des nouvelles textures permettant de générer de l'autopropulsion.

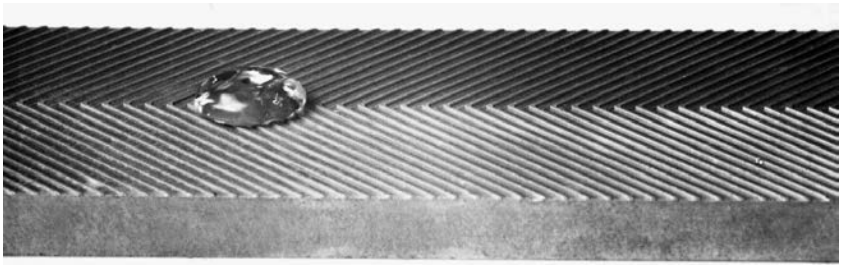

Figure C.2 – Vue de trois quarts d'une goutte en caléfaction sur une surface texturée en forme de chevron. De part et d'autre du plan de symétrie, la texture est formée par des créneaux parallèles entre eux. Pour cette texture, le demi-angle au sommet du chevron est de 45° - ce qui correspond à l'optimum en force.

Tout en respectant les ingrédients clefs pour établir ce type de mouvement (c'est-à-dire, la rectification de l'écoulement de vapeur de façon asymétrique) nous avons abouti à une nouvelle texture. Cette dernière est formée localement de cerneaux parallèles qui se rejoignent de part et d'autre d'un plan de symétrie pour créer un motif en forme de chevron (voir figure C.2 ou C.4). Cette texture peut être ainsi vue comme étant une preuve géométrique permettant de confirmer le scénario d'entraînement visqueux. En effet, dans chaque cellule, la vapeur n'a pas d'autre choix que de s'écouler le long du créneau et de suivre ainsi la direction imposée par celui-ci. La simplicité de l'écoulement dans cette configuration est traduite en loi d'échelle et conduit à une force en accord avec les résultats expérimentaux. Par la même occasion, ce modèle nous permet de discuter de l'optimisation de la force de propulsion par rapport aux différents paramètres géométriques du problème. Par exemple, en ce qui concerne le demi-angle définissant l'ouverture du chevron, nous montrons que la force est maximale pour un angle de 45° (voir figure C.2). L'absence de contact rend ces gouttes extrêmement mobiles (ce sont des aéroglisseurs) et empêche l'ébullition. Ainsi, la grande mobilité de ces objets soulève la question de la friction qu'ils subissent. Très faible sur un substrat lisse, on observe une dissipation inertielle dans l'air environnant et dans une couche limite liquide pour les gouttes. En revanche, sur un substrat crénelé, elle est fortement amplifiée par l'impact du liquide sur les textures. En utilisant comme point de départ la friction étudiée par G. Dupeux lorsqu'une goutte avance sur des rainures perpendiculaires à sa trajectoire [42], nous élargissons cette étude au cas des trajectoires formant un angle donné par rapport à l'alignement des créneaux. Nous proposons par la suite un modèle qui rend compte de la friction que subit une goutte dans le cas qui nous intéresse tout particulièrement: des textures en forme de chevron. Ayant étudié la force de propulsion et de friction, il ne nous reste plus qu'à en déduire la vitesse terminale en les équilibrant. Le modèle qui en résulte est en très bon accord avec les données expérimentales et il permet de prédire un maximum de vitesse pour un demi-angle au sommet de 21°. En effet, cet angle représente

le meilleur compromis entre l'optimisation de la force de propulsion (proche de 45°) et la minimisation de la friction (proche de 0°, correspondant à des créneaux alignés avec la trajectoire, ce qui minimise les chocs entre la goutte et les murs des rainures). Dans ce chapitre, nous proposons finalement d'utiliser cette texture comme point de départ pour de nouvelles applications: un piège à gouttes caléfiées (figure C.3a), une piste circulaire pour les observer sur des longues trajectoires (figure C.3b) ou même des textures actives afin d'interagir, en temps réel, avec nos perles liquides.

(a)

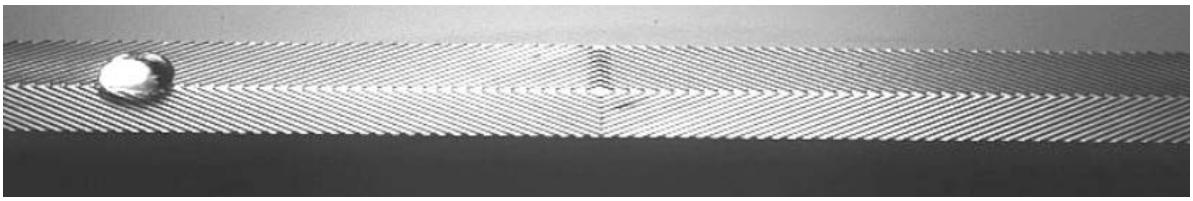

(b)

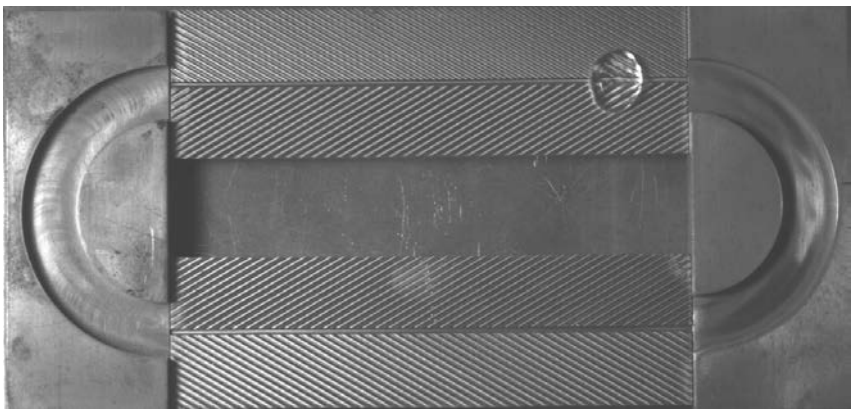

Figure C.3 – Dispositifs utilisant les textures en forme de chevron comme unité de base. (a) Deux chevrons juxtaposés avec des polarités opposées permettent de piéger une goutte à leur intersection. (b) Deux chevrons reliés par des sections circulaires vont faciliter l'observation du mouvement de la goutte sur de très longues distances.

Induire de la lévitation en utilisant la température est restrictif: un liquide non volatil ne lévitera pas, et nous ne serons pas toujours en mesure de chauffer le support. Il est donc intéressant de se demander si l'on peut caléfier "à froid" un liquide. Le troisième chapitre répond à cette question en remplaçant la goutte liquide par un objet solide (une lamelle de verre). N'ayant plus d'évaporation pour nourrir le coussin qui se trouve entre la goutte et le substrat, nous perforons ce dernier pour le rendre poreux et y injecter de l'air à travers [48]. Il en résulte une table de air-hockey (permettant la lévitation,

[69]) sur laquelle nous allons venir texturer nos motifs en forme de chevron (générant le mouvement, voir figure C.4). Le fait d'entraîner par viscosité un objet solide nous

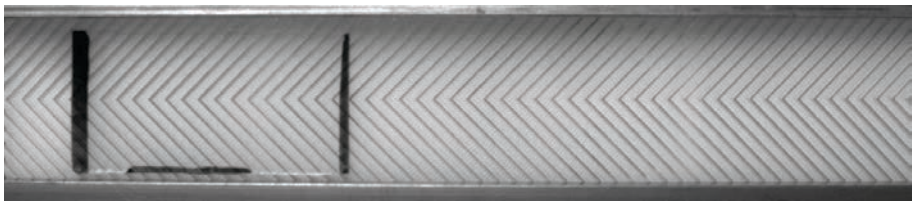

Figure C.4 – Plaque de verre (épaisseur 1 mm, largeur 24 mm, longueur 45 mm) posée sur une substrat poreux texturé. Au fond de chaque créneau, un réseau de trous permet de souffler de l'air, ce qui va induire la lévitation de la plaque.

aide à comprendre comment la force de propulsion dépend de la géométrie de l'objet (dans le cas liquide, ceci était impossible à cause de l'apparition d'instabilités liées à l'aspect déformable de l'interface). Nous pouvons dès lors proposer un modèle en parfait accord avec les mesures expérimentales. L'existence d'une solution analytique décrivant l'écoulement dans les canaux nous permet, par la même occasion, de remonter à la pression nécessaire à imposer sous le poreux pour démarrer la lévitation.
Jusqu'ici nous avons réussi uniquement à induire des mouvements de translation sur un plan horizontal. Par la suite nous démontrons qu'il existe une pente maximum (non négligeable) que peuvent remonter ces objets (voir figure C.5b) ou que l'on peut créer des mouvements de rotation avec des textures en forme de "moulin" (voir figure C.5a).

Pour finir, nous étudions les conséquences de travailler avec des objets plus lourds (ou des textures plus profondes). On comprend intuitivement qu'afin de faire léviter un objet plus lourd, il faut augmenter les pressions mises en jeu. Par conséquent, la vitesse du gaz dans les rainures augmente aussi et le scénario d'entrainement visqueux (basé sur des effets inertiels négligeables par rapport aux effets visqueux, à savoir, des bas nombres de Reynolds) n'est plus valable. Nous montrons alors que, pour des pressions de lévitation élevées (i.e. des haut nombre de Reynolds), les effets inertiels dominent et les objets avancent en sens opposé à celui observé dans le cas visqueux: c'est l'effet fusé (conservation du moment) qui est à l'origine de cette nouvelle propulsion.

Une façon extrêmement naïve de générer des situations de non-mouillage consiste tout simplement à supprimer le substrat sur lequel repose le liquide. Il s'en suit un régime de chute libre puis, inévitablement, un impact avec un substrat qui met fin à cette belle aventure. La situation est quelque peu moins dramatique lorsque le substrat sur lequel la goutte impacte est une grille non-mouillante (voir figure C.6).

En effet, ce mélange de trous passants et sections bouchées va arrêter une partie du liquide (qui sera redirigé latéralement), mais il va aussi laisser passer une partie du liquide (sous forme de filaments liquides, qui, à leur tour, vont se déstabiliser en petites gout-

(a)

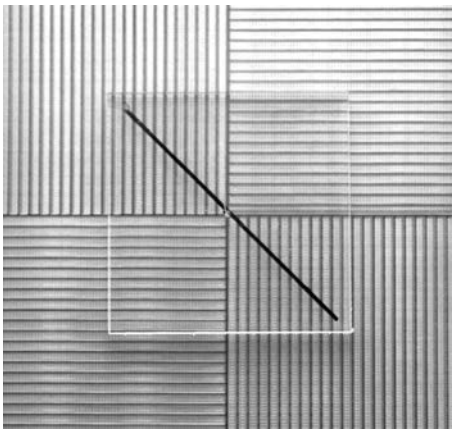

(b)

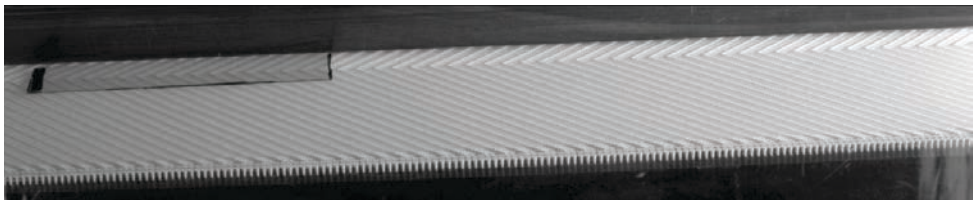

Figure C.5 – (a) Moulin visqueux: son motif est basé sur des rainures parallèles disposées dans une direction qui varie sur quatre quadrants différents. L'écoulement d'air entraîne par viscosité chaque section d'une plaque en verre (épaisseur 1 mm, longueur et largeur 30 mm), ce qui induit un mouvement de rotation. (b) Vue de trois quarts d'une lamelle montant une pente de 2% grace aux effets d'entraînement visqueux.

telettes). Le quatrième chapitre, qui porte sur cette interaction goutte/grille, commence donc par une brève introduction au monde des impacts. On s'attarde en particulier sur les impacts sur des substrats solides non-mouillants [24, 63]. Un point de départ idéal au problème de la grille, se trouve dans les travaux de E. Lorenceau [77] et collaborateurs. En effet, ils traitent le cas de l'impact d'une goutte sur une plaque avec un seul trou. Cette situation, plus simple que la grille mais renfermant des ingrédients physiques similaires, nous permet d'isoler des paramètres clefs tels que la vitesse de rétraction d'un filament visqueux ou le temps que met la goutte pour complètement s'écraser. Dès lors, nous proposons un modèle qui nous aide à prédire la masse transmise en fonction de la vitesse d'impact, le rayon de la goutte et la taille du trou. On s'attaque ensuite au problème d'une plaque avec une multitude de trous - la grille. En utilisant les mêmes principes que ceux utilisés pour un seul trou, nous adaptons le modèle pour aboutir à une loi d'échelle qui explique qualitativement les différents régimes observés expérimentalement. Apparaît alors le besoin de modéliser la déformation de la goutte pendant l'impact afin de rendre compte des mesures quantitativement. Nous explorons finalement différentes configura-

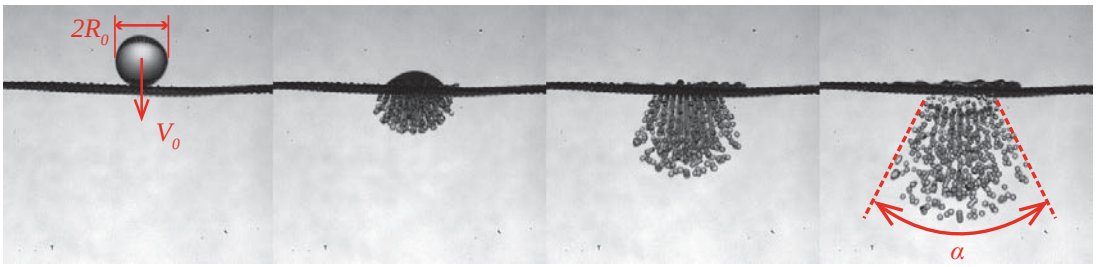

Figure C.6 – Vue latérale d'une goutte de rayon $R_0 = 1.9$ mm impactant à vitesse $V_0 = 1.6$ m/s sur une grille (trous circulaires de rayon approximatif 200 μm). La première image représente le début de l'impact. La deuxième et troisième image représentent le temps nécessaires à la goutte pour complètement s'écraser. Grâce à l'inertie, une partie du liquide passe à travers chaque trou sous forme de jet liquide. Ces doigts cylindriques n'étant pas stables, ils donnent naissance à un ensemble de petites gouttes. Sur la dernière image, les gouttelettes continuent leur trajectoire en formant un cône d'angle α. Chaque image est séparée par 2 ms.

tions possibles (nous faisons par exemple varier la nature mouillante ou non-mouillante de la grille, ou bien, nous modifions la porosité de la grille) et nous vérifions que le comportement physique reste qualitativement bien décrit par notre loi d'échelle.

L'étude des impacts sur grille nous a amené, dans le dernier chapitre, à nous pencher sur la question de la force subie par un substrat lisse à l'impact d'une goutte. On s'est tout d'abord intéressé aux phénomènes d'ondes de choc existant juste après le début de l'impact, à très court terme [119, 71]. En effet, ces ondes génèrent des pressions tellement élevées (de l'ordre du MPa) que l'on pourrait s'attendre à des forces associées considérables. Cependant, leur temps de vie est si bref (de l'ordre de la nanoseconde [47]) que la surface sur laquelle elles agissent est tellement réduite que les forces restent relativement faibles (de l'ordre du μN). Par ailleurs, il convient de tenir compte des effets de compressibilité dans l'air environnant si l'on veut comprendre le phénomène d'apparition des "splashs" [130, 132, 106].

On s'intéresse, dans un deuxième temps, aux forces qui ont lieu dès que les effets de compressibilité disparaissent. Ces forces d'origine inertielle sont mesurées à l'aide d'un capteur piézo-électrique (figure C.7a). On observe (figure C.7b) des profiles atteignant des forces maximums de plusieurs dizaines de mN - bien plus élevées que les forces liées aux ondes de choc. Un modèle analytique basé sur le transfert de quantité de mouvement rend parfaitement compte des données expérimentales.

Nous proposons par la suite l'utilisation d'un capteur bien moins couteux basé sur l'étude de la déflexion d'une lamelle de verre (pincée à une extrémité, libre de l'autre côté) suite à l'impact d'une goutte (voir figure C.8). Cette fois-ci, c'est la conservation de la quantité de mouvement qui décrit la déflexion maximale δ_0 (définie sur figure C.8)

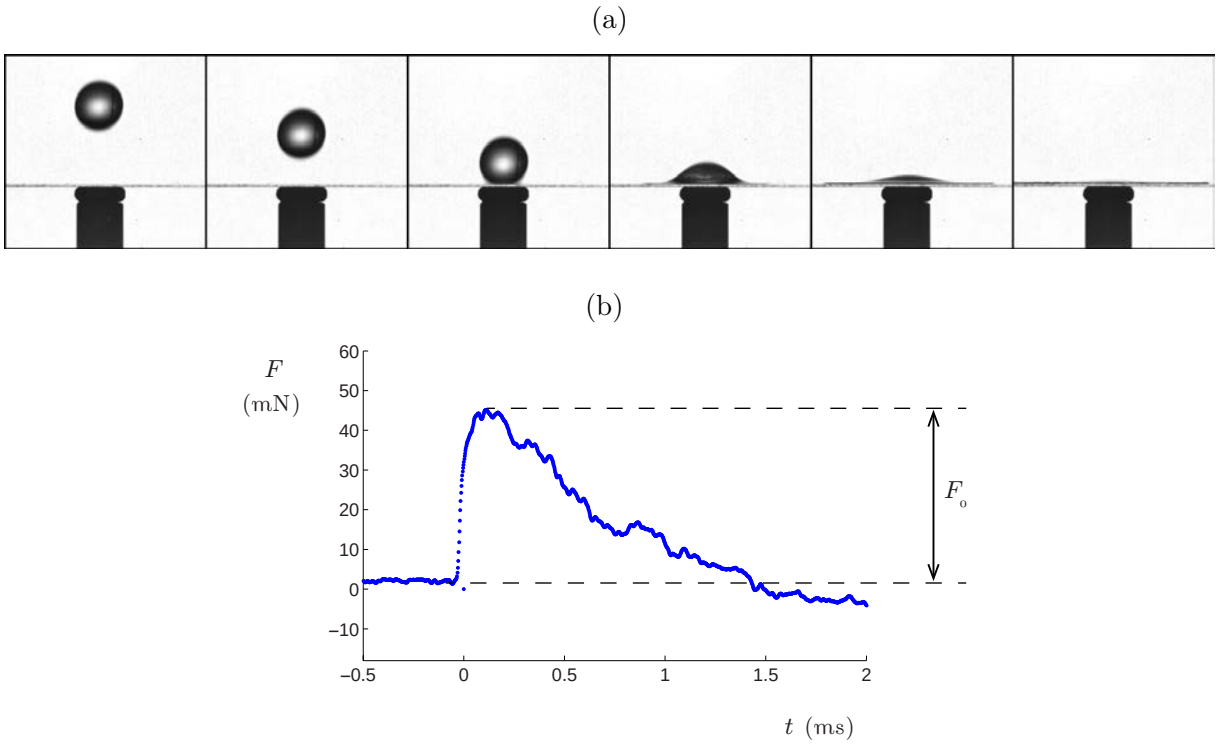

Figure C.7 – (a) Vue latérale d'une goutte de rayon $R = 1.3$ mm impactant un quartz piézo-électrique à vitesse $V = 3$ m/s. Chaque image est séparée par 0.5 ms. (b) Force d'impact mesurée par le capteur piézo-électrique en fonction du temps. La force maximum F_0 est atteinte environ un dixième de milliseconde après le début de l'impact.

en fonction des propriétés intrinsèques de la plaque ainsi que la vitesse et le rayon de la goutte. Ainsi, deux régimes ("lent" et "rapide") sont mis en évidence en fonction du temps de réaction de la plaque comparé au temps d'écrasement de la goutte.

Figure C.8 – (a) Goutte de rayon $R = 1.25$ mm et vitesse $V = 4$ m/s impactant sur le bord libre d'une lamelle de verre. Chaque image est séparée par 1 ms et ne montre que le dernier tiers de la plaque. δ_0 représente la déflexion maximum de la plaque après impact.

Ces deux différents capteurs (piezo et lamelle de verre) nous permettent ainsi de discuter le cas particulier de la force d'impact des gouttes de pluie. En effet, leur vitesse terminale étant fixé par un équilibre entre le poids et la trainée inertielle dans l'air, l'expression de la force d'impact peut être simplifiée.

Tout en gardant cette optique de non-mouillage au coeur de notre démarche, nous explorons en dernier lieu l'effet d'un traitement super hydrophobe sur la physique de ces impacts. Cette étude théorique prévoit une augmentation de la force d'impact (ainsi

que de la déflexion maximale de la lamelle en verre). Elle ouvre la voie à de futurs travaux comme, par exemple, la vérification expérimentale des ces différentes predictions théoriques.

Bibliography

[1] R. S. Alex Grounds and K. Takashina. Enhanced droplet control by transition boiling. *Scientific Reports*, 2:720, 2012.

[2] S. An and S. Lee. Maximum spreading of a shear-thinning liquid drop impacting on dry solid surfaces. *Experimental Thermal and Fluid Science*, 2011.

[3] C. Antonini, I. Bernagozzi, S. Jung, D. Poulikakos, and M. Marengo. Water drops dancing on ice: How sublimation leads to drop rebound. *Physical review letters*, 111(1):014501, 2013.

[4] T. Baier, G. Dupeux, S. Herbert, S. Hardt, and D. Quéré. Propulsion mechanisms for leidenfrost solids on ratchets. *Physical Review E*, 87(2):021001, 2013.

[5] W. Barthlott and C. Neinhuis. Purity of the sacred lotus, or escape from contamination in biological surfaces. *Planta*, 202(1):1–8, 1997.

[6] D. Bartolo, C. Josserand, and D. Bonn. Retraction dynamics of aqueous drops upon impact on non-wetting surfaces. *Journal of Fluid Mechanics*, 545:329–338, 2005.

[7] D. Bartolo, C. Josserand, and D. Bonn. Singular jets and bubbles in drop impact. *Physical review letters*, 96(12):124501, 2006.

[8] V. Bergeron, D. Bonn, J. Y. Martin, and L. Vovelle. Controlling droplet deposition with polymer additives. *Nature*, 405(6788):772–775, 2000.

[9] B. Bhushan, Y. C. Jung, and K. Koch. Micro-, nano-and hierarchical structures for superhydrophobicity, self-cleaning and low adhesion. *Philosophical Transactions of the Royal Society A: Mathematical, Physical and Engineering Sciences*, 367(1894):1631–1672, 2009.

[10] A. Biance, F. Chevy, C. Clanet, G. Lagubeau, and D. Quéré. On the elasticity of an inertial liquid shock. *Journal of Fluid Mechanics*, 554(1):47–66, 2006.

[11] A. Biance, C. Clanet, and D. Quéré. Leidenfrost drops. *Physics of Fluids*, 15:1632, 2003.

[12] A. L. H. Biance. Gouttes inertielles : de la caléfaction à l'étalement. *PhD Thesis, Université Paris 7-Denis Diderot*, 2005.

[13] H. Boerhaave. Elémens de chymie. *Chez Durand, rue du Foin, au Griffon*, 2:279–281, 1732.

[14] P. Bourrianne. Evaluations de formulations asp pour la récupération d'huiles extralourdes sur des micromodèles. *Technical report, ESPCI, Paris*, 2011.

[15] W. Bouwhuis, K. G. Winkels, I. R. Peters, P. Brunet, D. van der Meer, and J. H. Snoeijer. Oscillating and star-shaped drops levitated by an airflow. *arXiv:1305.5736*, 2013.

[16] P. Brunet and J. H. Snoeijer. Star-drops formed by periodic excitation and on an air cushion-a short review. *The European Physical Journal-Special Topics*, 192(1):207–226, 2011.

[17] J. C. Burton, A. L. Sharpe, R. C. A. van der Veen, A. Franco, and S. R. Nagel. The geometry of the vapor layer under a leidenfrost drop. *Phys Rev Lett*, 109(074301), 2012.

[18] A. Cassie and S. Baxter. Wettability of porous surfaces. *Transactions of the Faraday Society*, 40:546–551, 1944.

[19] T. A. Caswell. Dynamics of vapor layer under a leidenfrost drop. *arXiv:1401.4424*, 2014.

[20] F. Celestini, T. Frisch, A. Cohen, C. Raufaste, L. Duchemin, and Y. Pomeau. Two dimensional leidenfrost droplets in a hele shaw cell. *arXiv:1311.4264*, 2013.

[21] F. Celestini, T. Frisch, and Y. Pomeau. Take off of small leidenfrost droplets. *Physical Review Letters*, 109(3):034501, 07 2012.

[22] S. Chandra and C. Avedisian. On the collision of a droplet with a solid surface. *Proceedings: Mathematical and Physical Sciences*, 1991.

[23] S. S. Chhatre, W. Choi, A. Tuteja, K.-C. Park, J. M. Mabry, G. H. McKinley, and R. E. Cohen. Scale dependence of omniphobic mesh surfaces. *Langmuir*, 26(6):4027–4035, 2009.

[24] C. Clanet, C. Béguin, D. Richard, and D. Quéré. Maximal deformation of an impacting drop. *Journal of Fluid Mechanics*, 517:199–208, 2004.

[25] C. Clanet and J. C. Lasheras. Transition from dripping to jetting. *Journal of Fluid Mechanics*, 383(1):307–326, 1999.

[26] S. Cook. Erosion by water-hammer. *Proceedings of the Royal Society of London. Series A*, 119(783):481–488, 1928.

[27] Y. Couder, E. Fort, C. Gautier, and A. Boudaoud. From bouncing to floating: Noncoalescence of drops on a fluid bath. *Physical review letters*, 94(17):177801, 2005.

[28] R. Dadashev, R. Kutuev, D. Elimkhanov, and Z. Bichueva. Surface tension of indium-tin-gallium melts. *Russian Journal of Physical Chemistry A, Focus on Chemistry*, 81(11):1734–1737, 2007.

[29] S. Daniel, M. K. Chaudhury, and P.-G. De Gennes. Vibration-actuated drop motion on surfaces for batch microfluidic processes. *Langmuir*, 21(9):4240–4248, 2005.

[30] B. Darbois-Texier, G. Dupeux, G. Lagubeau, M. L. Merrer, K. Piroird, D. Soto, C. Clanet, and D. Quéré. La caléfaction. *Reflets de la Physique*, 37, 2012.

[31] P.-G. de Gennes, F. Brochard-Wyart, D. Quéré, M. Fermigier, and C. . . Clanet. Gouttes, bulles, perles et ondes. *Belin Paris*, pages Ch. 9– 203, 2002.

[32] R. de Jong, O. R. Enríquez, and D. van der Meer. Droplet impact near a millimetre-size hole: closed pit versus open-ended pore. *arXiv preprint*, 2014.

[33] J. de Ruiter, J. Oh, D. van den Ende, and F. Mugele. Dynamics of collapse of air films in drop impact. *Physical Review Letters*, 108(7):74505, 2012.

[34] P. Dell'Aversana, J. R. Banavar, and J. Koplik. Suppression of coalescence by shear and temperature gradients. *Physics of Fluids (1994-present)*, 8(1):15–28, 1996.

[35] P. Dell'Aversana and G. P. Neitzel. When liquids stay dry. *Physics today*, 51(1):38–41, 2008.

[36] T. Deng, K. Varanasi, M. Hsu, N. Bhate, C. Keimel, J. Stein, and M. Blohm. Nonwetting of impinging droplets on textured surfaces. *Applied Physics Letters*, 94(13):133109, 2009.

[37] A. Dickerson, P. Shankles, N. Madhavan, and D. Hu. Mosquitoes survive raindrop collisions by virtue of their low mass. *Proceedings of the National Academy of Sciences*, 109(25):9822–9827, 2012.

[38] L. Duchemin, J. R. Lister, and U. Lange. Static shapes of levitated viscous drops. *Journal of Fluid Mechanics*, 533(1):161–170, 2005.

[39] A. Duchesne, C. Savaro, L. Lebon, C. Pirat, and L. Limat. Multiple rotations of a drop rolling inside a horizontal circular hydraulic jump. *EPL (Europhysics Letters)*, 102(6):64001, 2013.

[40] G. Dupeux. Propulsion et friction d'objets non mouillants. *PhD Thesis, Paris*, 2014.

[41] G. Dupeux, T. Baier, V. Bacot, S. Hardt, C. Clanet, and D. Quéré. Self-propelling uneven leidenfrost solids. *Physics of Fluids*, 25:051704, 2013.

[42] G. Dupeux, M. Le Merrer, C. Clanet, and D. Quéré. Trapping leidenfrost drops with crenelations. *Phys Rev Lett*, 107(11):114503–114503, 09 2011.

[43] G. Dupeux, M. L. Merrer, G. Lagubeau, C. Clanet, S. Hardt, and D. Quéré. Viscous mechanism for leidenfrost propulsion on a ratchet. *EPL (Europhysics Letters)*, 96:58001, 2011.

[44] A. Eddi, K. G. Winkels, and J. H. Snoeijer. Short time dynamics of viscous drop spreading. *Physics of Fluids*, 25:013102, 2013.

[45] J. Eggers, M. Fontelos, C. Josserand, and S. Zaleski. Drop dynamics after impact on a solid wall: theory and simulations. *Physics of Fluids*, 22:062101, 2010.

[46] O. Engel. Waterdrop collisions with solid surfaces. *J. Res. NBS*, 5:281–298, 1955.

[47] J. E. Field, J.-J. Camus, M. Tinguely, D. Obreschkow, and M. Farhat. Cavitation in impacted drops and jets and the effect on erosion damage thresholds. *Wear*, 290:154–160, 2012.

[48] M. Goldshtik, V. Khanin, and V. Ligai. Liquid drop on an air cushion as an analogue of leidenfrost boiling. *Journal of Fluid Mechanics*, 166:1–20, 1986.

[49] A. Gomez Marin, D. Arnaldo del Cerro, G. Romer, B. Pathiraj, and D. Lohse. Capillary droplets on leidenfrost micro-ratchets. *Physics of fluids*, 24(12):1–10, 2012.

[50] B. Gottfried, C. Lee, and K. Bell. The leidenfrost phenomenon: film boiling of liquid droplets on a flat plate. *International Journal of Heat and Mass Transfer*, 9(11):1167 – 1188, 1966.

[51] R. Gunn and G. Kinzer. The terminal velocity of water drops and raindrops in stagnant air. *Journal of Meteorology*, 6:243–248, 1949.

[52] G. Hartley and R. Brunskill. Reflection of water drops from surfaces. *Surface phenomena in chemistry and biology*, 214, 1958.

[53] A. C. Imeson, R. Vis, and E. de Water. The measurement of water-drop impact forces with a piezo-electric transducer. *CATENA*, 8(1):83–96, 1981.

[54] C. Josserand and S. Zaleski. Droplet splashing on a thin liquid film. *Phys. Fluids*, 15(1650), 2003.

[55] R. Kannan and D. Sivakumar. Drop impact process on a hydrophobic grooved surface. *Colloids and Surfaces A: Physicochemical and Engineering Aspects*, 317(1):694–704, 2008.

[56] A. Karl and A. Frohn. Experimental investigation of interaction processes between droplets and hot walls. *Physics of Fluids (1994-present)*, 12(4):785–796, 2000.

[57] H. Kim, J. Buongiorno, L.-W. Hu, and T. McKrell. Nanoparticle deposition effects on the minimum heat flux point and quench front speed during quenching in water-based alumina nanofluids. *International Journal of Heat and Mass Transfer*, 53(7):1542–1553, 2010.

[58] H. Kim, G. DeWitt, T. McKrell, J. Buongiorno, and L.-w. Hu. On the quenching of steel and zircaloy spheres in water-based nanofluids with alumina, silica and diamond nanoparticles. *International Journal of Multiphase Flow*, 35(5):427–438, 2009.

[59] H. Kim, B. Truong, J. Buongiorno, and L. Hu. On the effect of surface roughness height, wettability, and nanoporosity on leidenfrost phenomena. *Applied Physics Letters*, 98:083121, 2011.

[60] J. A. Kleingartner, S. Srinivasan, J. M. Mabry, R. E. Cohen, and G. H. McKinley. Utilizing dynamic tensiometry to quantify contact angle hysteresis and wetting state transitions on nonwetting surfaces. *Langmuir*, 2013.

[61] G. Kozyreff and P. Howell. The instability of a viscous sheet floating on an air cushion. *Journal of Fluid Mechanics*, 2004.

[62] A. Lafuma and D. Quéré. Superhydrophobic states. *Nature materials*, 2(7):457–460

[63] G. Lagubeau, M. A. Fontelos, C. Josserand, A. Maurel, V. Pagneux, and P. Petitjeans. Spreading dynamics of drop impacts. *Journal of Fluid Mechanics*, 713:50–60, 2012.

[64] P. S. Laplace. Traité de mécanique céleste, supplément au dixième livre du traité de mécanique céleste. *Imprimerie de Crapelet*, 4:1–79, 1805.

[65] I. A. Larmour, S. E. Bell, and G. C. Saunders. Remarkably simple fabrication of superhydrophobic surfaces using electroless galvanic deposition. *Angewandte Chemie*, 119(10):1740–1742, 2007.

[66] L. G. Leal. *Advanced transport phenomena: fluid mechanics and convective transport processes*, volume 7. Cambridge University Press, 2007.

[67] C. Lee, H. Lastakowski, A.-L. Biance, C. Pirat, C.-J. Kim, and C. Ybert. Two types of cassie-to-wenzel wetting transitions on superhydrophobic surfaces during drop impact. *Submitted to Langmuir*, 2014.

[68] J. G. Leidenfrost. On the fixation of water in diverse fire. *Int. J. Heat Mass Transfer*, 9:1153–1166, 1966.

[69] J. Lemaitre, A. Gervois, H. Peerhossaini, D. Bideau, and J. Troadec. An air table designed to study two-dimensional disc packings: preliminary tests and first results. *Journal of Physics D: Applied Physics*, 23(11):1396 0022–3727, 2000.

[70] A. Lembach, H. Tan, I. Roisman, T. Gambaryan-Roisman, Y. Zhang, C. Tropea, and A. Yarin. Drop impact, spreading, splashing, and penetration into electrospun nanofiber mats. *Langmuir*, 26(12):9516–9523, 2010.

[71] M. Lesser and J. Field. The impact of compressible liquids. *Annual review of fluid mechanics*, 15(1):97–122, 1983.

[72] X. Li, X. Ma, and Z. Lan. Dynamic behavior of the water droplet impact on a textured hydrophobic/superhydrophobic surface: The effect of the remaining liquid film arising on the pillars' tops on the contact time. *Langmuir*, 26(7):4831–4838, 2010.

[73] H. Linke, B. Alemán, L. Melling, M. Taormina, M. Francis, C. Dow-Hygelund, V. Narayanan, R. Taylor, and A. Stout. Self-propelled leidenfrost droplets. *Physical Review Letters*, 96(15):154502, 2006.

[74] J. R. Lister, A. B. Thompson, A. Perriot, and L. Duchemin. Shape and stability of axisymmetric levitated viscous drops. *Journal of Fluid Mechanics*, 617:167–185, 2008.

[75] J. Liu, H. Vu, S. S. Yoon, R. A. Jepsen, and G. Aguilar. Splashing phenomena during liquid droplet impact. *Atomization and Sprays*, 20(4), 2010.

[76] Y. Liu, L. Moevius, X. Xu, T. Qian, J. M. Yeomans, and Z. Wang. Pancake bouncing on superhydrophobic surfaces. *Nature Physics*, 2014.

[77] É. Lorenceau and D. Quéré. Drops impacting a sieve. *Journal of colloid and interface science*, 263(1):244–249, 2003.

[78] S. Mangili, C. Antonini, M. Marengo, and A. Amirfazli. Understanding the drop impact phenomenon on soft pdms substrates. *Soft Matter*, 8(39):10045–10054, 2012.

[79] M. Mani, S. Mandre, and M. P. Brenner. Events before droplet splashing on a solid surface. *Journal of Fluid Mechanics*, 647:163–185, 2010.

[80] M. Marengo, C. Antonini, I. V. Roisman, and C. Tropea. Drop collisions with simple and complex surfaces. *Current Opinion in Colloid and Interface Science*, 16(4):292–302, 2011.

[81] P. T. Nagy and G. P. Neitzel. Optical levitation and transport of microdroplets: Proof of concept. *Physics of Fluids (1994-present)*, 20(10):101703, 2008.

[82] M. Nearing and J. Bradford. Relationships between waterdrop properties and forces of impact. *Soil Science Society of America Journal*, 51(2):425–430, 1987.

[83] M. Nearing, J. Bradford, and R. Holtz. Measurement of force vs. time relations for waterdrop impact. *Soil Science Society of America Journal*, 50(6):1532–1536, 1986.

[84] G. P. Neitzel and P. Dell'Aversana. Noncoalescence and nonwetting behavior of liquids. *Annual review of fluid mechanics*, 34(1):267–289, 2002.

[85] P. C. Nordine, J. Weber, and J. G. Abadie. Properties of high-temperature melts using levitation. *Pure and applied chemistry*, 72(11):2127–2136, 2000.

[86] J. Ok, E. Lopez-Oña, D. Nikitopoulos, H. Wong, and S. Park. Propulsion of droplets on micro-and sub-micron ratchet surfaces in the leidenfrost temperature regime. *Microfluidics and nanofluidics*, pages 1–10, 2011.

[87] K. Okumura, F. Chevy, D. Richard, D. Quéré, and C. Clanet. Water spring: A model for bouncing drops. *EPL (Europhysics Letters)*, 62(2):237, 2003.

[88] D. Quéré. Leidenfrost dynamics. *Annual Review of Fluid Mechanics*, 10 2012.

[89] C. Rasser. Contact angles and leidenfrost drops on strained materials. *M.S. Thesis Ecole Polytechnique,*, 2013.

[90] M. Rein. Phenomena of liquid drop impact on solid and liquid surfaces. *Fluid Dynamics Research*, 12(2):61, 1993.

[91] Y. Renardy, S. Popinet, L. Duchemin, M. Renardy, S. Zaleski, C. Josserand, M. Drumright-Clarke, D. Richard, C. Clanet, and D. Quéré. Pyramidal and toroidal water drops after impact on a solid surface. *Journal of Fluid Mechanics*, 484:69–83, 2003.

[92] E. Reyssat. Gouttes, films et jets : quand les écoulements modèlent les interfaces. *PhD Thesis, Université Paris 7-Denis Diderot*, 2007.

[93] D. Richard, C. Clanet, and D. Quéré. Contact time of a bouncing drop. *Nature*, 417(6891):811, 2002.

[94] D. Richard and D. Quéré. Bouncing water drops. *EPL (Europhysics Letters)*, 50(6):769, 2000.

[95] R. Rioboo, C. Tropea, and M. Marengo. Outcomes from a drop impact on solid surfaces. *Atomization and Sprays*, 11(2), 2001.

[96] I. Roisman. Inertia dominated drop collisions. ii. an analytical solution of the navier–stokes equations for a spreading viscous film. *Physics of Fluids*, 21:052104, 2009.

[97] A. Sahaya Grinspan and R. Gnanamoorthy. Impact force of low velocity liquid droplets measured using piezoelectric pvdf film. *Colloids and Surfaces A: Physicochemical and Engineering Aspects*, 356(1-3):162–168, 2010.

[98] R. Sahu, S. Sinha-Ray, A. Yarin, and B. Pourdeyhimi. Drop impacts on electrospun nanofiber membranes. *Soft Matter*, 8(14):3957–3970, 2012.

[99] E. G. Shafrin and W. A. Zisman. Upper limits for the contact angles of liquids on solids. *American Chemical Society, chapter 10*, pages 145–157, 1963.

[100] J. Shin and T. McMahon. The tuning of a splash. *Physics of Fluids A: Fluid Dynamics*, 2:1312, 1990.

[101] A. Snezhko, E. B. Jacob, and I. S. Aranson. Pulsating-gliding transition in the dynamics of levitating liquid nitrogen droplets. *New Journal of Physics*, 10(4):043034, 2008.

[102] J. H. Snoeijer and B. Andreotti. Moving contact lines: Scales, regimes, and dynamical transitions. *Annual review of fluid mechanics*, 45:269–292, 2013.

[103] J. H. Snoeijer, P. Brunet, and J. Eggers. Maximum size of drops levitated by an air cushion. *Physical Review E*, 79(3):036307–, 03 2009.

[104] K. Sreenivas, P. De, and J. H. Arakeri. Levitation of a drop over a film flow. *Journal of Fluid Mechanics*, 380:297–307, 1999.

[105] S. Srinivasan, W. Choi, K.-C. Park, S. S. Chhatre, R. E. Cohen, and G. H. McKinley. Drag reduction for viscous laminar flow on spray-coated non-wetting surfaces. *Soft Matter*, 9(24):5691–5702, 2013.

[106] C. S. Stevens, A. Latka, and S. R. Nagel. Comparison of splashing in high and low viscosity liquids. *arXiv preprint*, 2014.

[107] W. F. Stokey. Vibration of systems having distributed mass and elasticity. *Shock and vibration Handbook*, pages 7–1, 1988.

[108] D. Strier, A. Duarte, H. Ferrari, and G. Mindlin. Nitrogen stars: morphogenesis of a liquid drop. *Physica A: Statistical Mechanics and its Applications*, 283(1):261–266, 2000.

[109] A. D. Stroock, S. K. Dertinger, A. Ajdari, I. Mezić, H. A. Stone, and G. M. Whitesides. Chaotic mixer for microchannels. *Science*, 295(5555):647–651, 2002.

[110] R. Takaki and K. Adachi. Vibration of a flattened drop. ii. normal mode analysis. *Journal of the Physical Society of Japan*, 54(7):2462–2469, 1985.

[111] R. Takaki, N. Yoshiyasu, Y. Arai, and K. Adachi. Self-induced vibration of an evaporating drop. *KTK Scientific Publishers*, 1984.

[112] M. Taormina. Leidenfrost ratchets. *B.S. Thesis, University of Oregon*, june 2006.

[113] G. Taylor. The instability of liquid surfaces when accelerated in a direction perpendicular to their planes. i. *Proceedings of the Royal Society of London. Series A. Mathematical and Physical Sciences*, 201(1065):192–196, 1950.

[114] G. Taylor. The dynamics of thin sheets of fluid. iii. disintegration of fluid sheets. *Proceedings of the Royal Society of London. Series A. Mathematical and Physical Sciences*, 253(1274):313–321, 1959.

[115] J. W. J. Thomas R. Cousins, Raymond E. Goldstein and A. I. Pesci. A ratchet trap for leidenfrost drops. *J. Fluid Mech*, 2011.

[116] M. Thoraval, K. Takehara, T. Etoh, and S. Thoroddsen. Drop impact entrapment of bubble rings. *arXiv preprint arXiv:1211.3076*, 2012.

[117] S. Thoroddsen, T. Etoh, K. Takehara, N. Ootsuka, and Y. Hatsuki. The air bubble entrapped under a drop impacting on a solid surface. *Journal of Fluid Mechanics*, 545:203–212, 2005.

[118] S. Thoroddsen, K. Takehara, and T. Etoh. Micro-splashing by drop impacts. *Journal of Fluid Mechanics*, 706:560–570, 2012.

[119] A. Tijsseling and A. Anderson. A precursor in waterhammer analysis - rediscovering johannes von kries. *Proceedings of the 9th International Conference on Pressure Surges*, 2004.

[120] S. Timoshenko, S. Woinowsky-Krieger, and S. Woinowsky-Krieger. *Theory of plates and shells*, volume 2. McGraw-hill New York, 1959.

[121] N. Tokugawa and R. Takaki. Mechanism of self-induced vibration of a liquid drop based on the surface tension fluctuation. *Journal of the Physical Society of Japan*, 63(5):1758–1768, 1994.

[122] T. Tran, H. J. J. Staat, A. Prosperetti, C. Sun, and D. Lohse. Drop impact on superheated surfaces. *Physical Review Letters*, 108(3):036101, 01 2012.

[123] P. Tsai, M. Hendrix, R. Dijkstra, L. Shui, and D. Lohse. Microscopic structure influencing macroscopic splash at high weber number. *Soft Matter*, 7(24):11325–11333, 2011.

[124] I. Vakarelski, N. Patankar, J. Marston, D. Chan, and S. Thoroddsen. Stabilization of leidenfrost vapour layer by textured superhydrophobic surfaces. *Nature*, 489(7415):274–277, 2012.

[125] R. van der Veen, T. Tran, D. Lohse, and C. Sun. Direct measurements of air layer profiles under impacting droplets using high-speed color interferometry. *Physical Review E*, 85(2):026315, 2012.

[126] D. Vollmer and H.-J. Butt. Fluid dynamics: Shaping drops. *Nature Physics*, 2014.

[127] J. von Kries. On the relations between pressure and velocity which exist in the wave-like motion in elastic tubes. *Festschrift der 56. Versammlung deutscher Naturforscher und Ärzte gewidmet von der Naturforschenden Gesellschaft zu Freiburg i. B*, Supplement zu Band VIII der Berichte, 1883.

[128] L. Wachters, L. Smulders, J. Vermeulen, and H. Kleiweg. The heat transfer from a hot wall to impinging mist droplets in the spheroidal state. *Chemical Engineering Science*, 21(12):1231–1238, 1966.

[129] W. Wirth, S. Storp, and W. Jacobsen. Mechanisms controlling leaf retention of agricultural spray solutions. *Pesticide science*, 33(4):411–420, 1991.

[130] A. M. Worthington. The splash of a drop. *Society for Promoting Christian Knowledge, London*, 1895.

[131] L. Xu. Liquid drop splashing on smooth, rough, and textured surfaces. *Physical Review E*, 75(5):056316, 2007.

[132] L. Xu, W. Zhang, and S. Nagel. Drop splashing on a dry smooth surface. *Physical Review Letters*, 94(18):184505, 2005.

[133] Q. Xu, E. Brown, and H. M. Jaeger. Impact dynamics of oxidized liquid metal drops. *Physical Review E*, 87(4):043012, 2013.

[134] A. Yarin. Drop impact dynamics: splashing, spreading, receding, bouncing.... *Annu. Rev. Fluid Mech.*, 38:159–192, 2006.

[135] K. Yoneta. Diffraction of falling drop by plane net part i. *Journal of the Faculty of Science, Hokkaido Imperial University.*, 1(4):121–147, 1932.

[136] J. Zhen, C. Josserand, S. Zaleski, S. Popinet, and P. Ray. Gas influence in drop impact on dry solid substrates. *2nd ECCOMAS Young Investigators Conference*, 2013.

Abstract

We investigate through several experiments the special dynamics generated by non-wetting objects. On a substrate textured with grooves forming a herringbone pattern, a Leidenfrost levitating liquid is propelled: the textures channel the vapor flow in a well-defined direction so that the slider above is driven by vapor viscosity. These deformable objects undergo very little friction on flat surfaces. However, on crenelated substrates, impacts on the texture sides greatly enhance dissipation. We extend this entrainment scenario to other situations where the liquid (and its deformable nature) is not involved anymore. A solid plate can levitate over a porous substrate through which air is blown. Again, escaping flow can be rectified by the textures and entrain the plate, leading to translation movement or even to rotation. If we create deeper channels (hence losing flow confinement), we observe motion in the opposite direction due to "rocket effect" (conservation of momentum).

We are also interested in an extreme non-wetting situation: the falling drop. Indeed, all along the fall, the drop only experiences air drag friction, easily reaching high speeds. We tackle the problem of the dramatic issue of this fall: the impact. We first study the impact of a drop on a sieve. In this situation intermediate between a solid wall and no obstacle at all, mass either passes through the holes or gets stopped by the closings. We then focus on the impact force experienced by the substrates and characterize the force as a function of the drop and impact properties, but also of the nature of the solid on which impact takes place.

Keywords: interface, non-wetting drop, Leidenfrost effect, texture, self-propulsion, friction, levitation, impact, grid.

Résumé

Nous étudions à travers plusieurs expériences la dynamique spéciale engendrée par des objets non mouillants. Un liquide en état Leidenfrost est autopropulsé lorsqu'on le pose sur un substrat texturé avec des rainures formant un motif à chevrons: les textures canalisent l'écoulement de vapeur dans une direction bien définie de sorte que ces aéroglisseurs liquides sont entraînés par la vapeur sous-jacente. Ces objets déformables subissent très peu de friction sur une surface plane. Toutefois, sur des substrats crénelés, les impacts sur les textures créent une friction spéciale qui est également étudiée. Nous étendons ce scénario d'entraînement visqueux dans d'autres situations où le liquide (et sa nature déformable) est remplacé par une plaque solide. Pour permettre la lévitation, on le place sur un substrat poreux à travers lequel de l'air est soufflé. Une fois de plus, l'écoulement est rectifié par des textures permettant l'entraînement d'une lamelle de verre dans un mouvement de translation ou même de rotation. Si nous augmentons la profondeur des textures, le confinement est perdu et on observe un mouvement dans la direction opposée dû à "l'effet fusée".

Nous nous sommes également intéressés à une situation de non mouillage particulièrement simple: la goutte en chute libre. Tout au long de sa chute, la goute ne subit que la trainée de l'air, ce qui lui permet d'atteindre des vitesses élevées. Nous abordons le problème de l'issue de cette chute: l'impact. Nous étudions d'abord l'impact d'une goutte sur un tamis. Dans cette situation intermédiaire entre un mur solide et aucun obstacle, le liquide passe à travers les trous ou est arrêté par les sections bouchées. Nous nous concentrons ensuite à la force d'impact subie par le substrat. Nous la mesurons et la calculons en fonction des caractéristiques du liquide, de l'impact, et de la nature du substrat.

Mots-clés: interface, goutte non mouillante, caléfaction, texture, autopropulsion, friction, lévitation, impact, grille.